DANMARKS OG GRØNLANDS GEOLOGISKE UNDERSØGELSE RAPPORT 2016/43

Targeting: Prospectivity mapping for orogenic gold in South-East Greenland

Bo Møller Stensgaard & Björn H. Heincke

GEOLOGICAL SURVEY OF DENMARK AND GREENLAND
DANISH MINISTRY OF ENERGY, UTILITIES AND CLIMATE

GEUS

DANMARKS OG GRØNLANDS GEOLOGISKE UNDERSØGELSE RAPPORT 2016/43

Targeting: Prospectivity mapping for orogenic gold in South-East Greenland

Bo Møller Stensgaard & Björn H. Heincke

GEOLOGICAL SURVEY OF DENMARK AND GREENLAND
DANISH MINISTRY OF ENERGY, UTILITIES AND CLIMATE

GEUS

Content

Introduction

To support new activities in mineral exploration and to exploit the new knowledge from recently acquired geochemical and geophysical data from South-East Greenland, it was decided to carry out a regional reconnaissance-scale prospectivity analysis. For this a mineral system approach for orogenic gold mineralisation was used in an integration of geological-geochemical-geophysical studies carried out by fuzzy logic methods.

The study area in South-East Greenland encompasses the Archaean North Atlantic Craton (NAC; 62°–64°30'N) and the Palaeoproterozoic Nagssugtoqidian Orogen (also referred to as the Ammassalik Mobile Belt; 64°30'–66°N), including part of the northern Archaean foreland that mostly comprising rocks from the Rae Craton to the north. To the south, the study area is affected by deformation and intrusives of the Palaeoproterozoic Ketilidian Mobile Belt. The lower crustal, predominately mafic-ultramafic granulites, and the orthogneisses of the NAC are named the Thrym Complex. This complex is characterised by intrusions of the 2785–2664 Ma Skjoldungen Alkaline Province (SAP). The main deformation events and stages within the craton are named the Timmiarmiut (>2700 Ma) and Skjoldungen (2790-2700 Ma) Orogenies. The Palaeoproterozoic Nagssugtoqidian Orogen in southern East-Greenland comprises reworked Archaean rocks from both cratons, as well as slivers and belts of Palaeoproterozoic formed meta-volcanic, meta-sedimentary and intrusive rocks. Based on differences in lithologies and tectonometamorphic history, the orogen is divided into four terranes from south to the north. These are: the Isortoq Terrane, the Ammassalik Intrusive Complex (AIC), the Kuummiut Terrane and the Schweizerland Terrane. The orogenic events include subductions and magmatic arc-related magmatism as well as the formation of supracrustal successions. Later post-orogenic ~1670 to 1600 Ma granites and diorites occur within both the Kuummiut and Isortoq terranes. Nickel-copper±platinum group elements±gold sulphide mineralisation occurs in the Thrym Complex and within the AIC, and iron-vanadium-oxide mineralisation occur within mafic intrusions of the SAP. Graphite mineralisation occurs within the surpracrustal successions in the Kuummuit Terrane and gemstones in the form of corundum occur in association with ultramafic in the Isortoq Terrane. To date, no in-situ gold mineralisations have been found in the study area. However, for the Palaeoproterozoic orogenic part of the study area, a relatively high number of gold-bearing samples have been acquired within the public hunt for mineral program, Ujarassiorit, and a couple of areas stand as being anomalous in gold and pathfinder elements for gold. No indication of gold exists within the cratonic part of the study area.

In this prospectivity study, the mineral system models for orogenic gold were assessed and targeting elements, which may mirror certain geological processes of the gold mineralising system, were selected. The geological, geochemical and geophysical data were processed and a number of evidential datasets and maps believed to reflect the target elements was produced. The targeting maps were integrated by the use of a knowledge-driven fuzzy logic model. The results of the resulting prospectivity analysis were finally briefly discussed and the limitations, uncertainties and technical aspects of this work were summaries.

Geological and tectonic history of South-East Greenland

The geology and mineral potential of the study area in South-East Greenland have recently been described by Kolb *et al.* (2016). Furthermore, a newly revised 1:500 000 scale geological map have also been published digitally (Stensgaard *et al.* 2016). For more details on the geological settings and environments encountered in South-East Greenland beyond those given in the following sections, please refer to the references given above.

The North Atlantic Craton

The region between c. 61°45’ N and c. 64°30’ N forms the eastern part of the North Atlantic Craton in Greenland (Fig. 1) (Andrews *et al.* 1971; Andrews *et al.* 1973; Escher & Nielsen 1983; Kolb *et al.* 2013).

Thrym complex and the Skoldungen Alkaline Province

(Andrews *et al.* 1971, 1973; Escher & Nielsen 1983; Kolb *et al.* 2013). The craton is dominated by migmatitic orthogneiss with intercalated narrow bands and belts of mafic granulite, ultramafic, and in smaller volumes, probably less than 1% of the craton, possible meta-sedimentary rocks, and alkaline-carbonatitic intrusive rocks of the Skjoldungen Alkaline Province. The rocks represent a lower crustal section of a Meso- to Neoarchaean craton; also referred to as the Thrym Complex (Fig. 2; Bagas *et al.* 2013).

The mafic, ultramafic and meta-sedimentary units can be up to 1 km wide although the majority are less than 1 km thick. These units can often be followed for tens of kilometres. The ultramafic bands and belts are widespread in the northern part of the craton region and may represent mantle-like intrusive rocks emplaced as sheets in the lower crust (Kolb *et al.* 2013). The Skjoldungen Alkaline Province (SAP), one of the oldest alkaline provinces in the world, comprises more than 20 individual intrusions (Blichert-Toft *et al.* 1995; Nielsen & Rosing 1990).

The regional metamorphism within the craton varies from peak amphibolite-facies to peak granulite facies. The oldest orthogneiss yields an age of around 2850 Ma (Kolb *et al.* 2016). The protolith for these rocks appear to have intruded mafic granulite, ultramafic and meta-sedimentary rocks that are older than 2865 Ma. Inherited zircons with ages of 3450 Ma in the orthogneiss suggest that Meso-archaean parts of the craton exist. Metamorphic zircons ages cluster around 2800-2780 Ma suggesting that the older orthogneisses were formed at the time of regional high grade granulite facies metamorphism (Kolb *et al.* 2016). The SAP intrusions are constrained to two intrusive phases; one at 2785-2730 and a second at 2720-2700 Ma (Kolb *et al.* 2013). The carbonatite of the Singertât Complex have yielded an intrusive age of ca. 2664 Ma (Blichert-Toft *et al.* 1995).

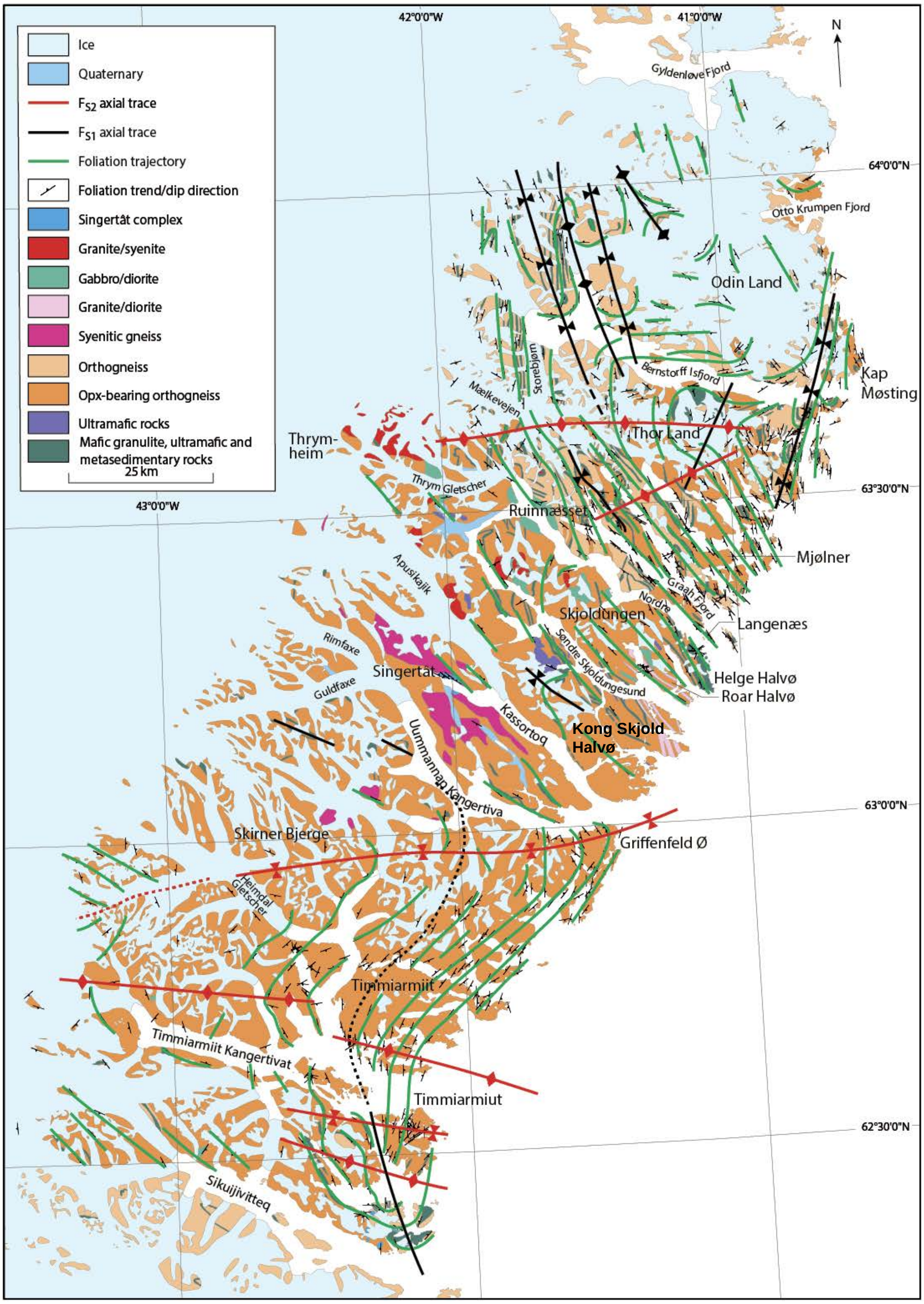

Figure 1. *Geological map of the North Atlantic Craton, the Skjoldungen region in South-East Greenland, with foliation trajectories and fold axial traces outlined, indicating a complex fold interference pattern and general structural uniformity in the Thrym Complex (figure from Kolb et al. 2013).*

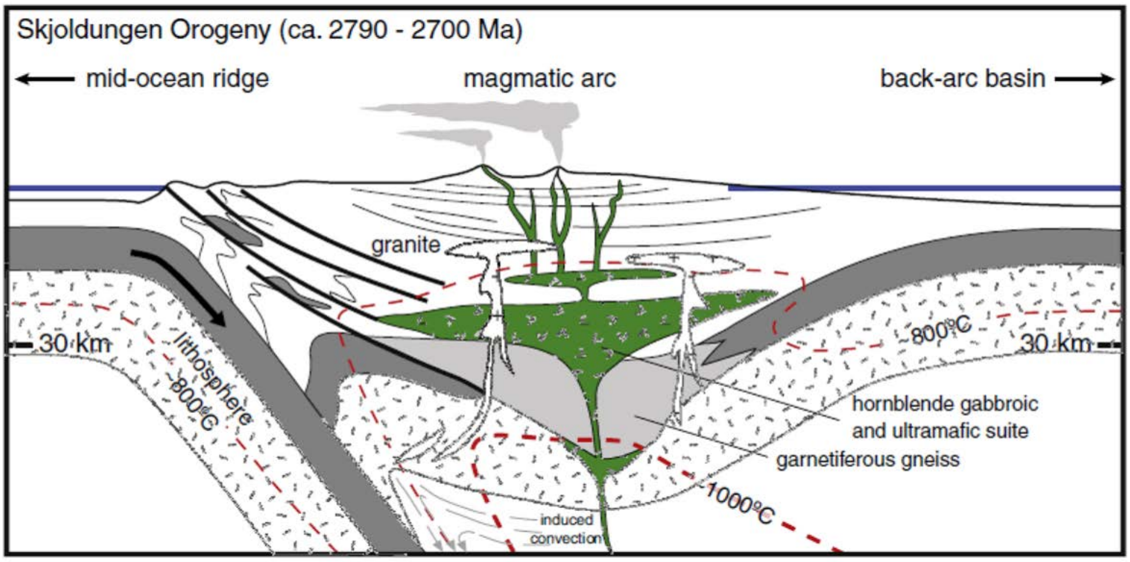

Figure 2. *The conceptual model suggested by Bagas et al. (2013) for the formation of the protoliths for the ca. 2720 Ma granulites and gneisses in the Thrym Complex of South-East Greenland. The mafic-ultramafic granulites and the orthogneisses are interpreted to represent the relict root zone of a magmatic-arc during the Timmiarmiut Orogeny in which the granulites and the gneisses formed at the base of continental collision thickened crust (re-laminated) at 800–1000°C, 1–1.5 GPa and depths of between 35–50 km.*

Timmiarmiut and the Skjoldungen orogenies

The deformation events and stages within the craton have be categorized by Kolb *et al.* (2013) (Fig. 3) into an early deformation (>2700 Ma) with foliation preserved in mafic and ultramafic rocks and early- to syn-tectonic orthogneiss. This fabric is best preserved in the Timmiarmiut area and has been named the Timmiarmiut Orogeny (D_T). The fabric of the D_T is subsequently at 2790-2700 Ma folded into regional-scale upright to reclined isoclinal fold during the Skjoldungen Orogeny (D_S). During the D_S event shear zones are developed, e.g. as tens of meter wide shear zones in the contact between orthogneiss and mafic granulite, as discrete cm-m wide northeast-southwest trending, near vertical, sinistral shear zones and as <20 cm wide, east-west trending, near vertical, dextral shear zones. The near-vertical shear zones form a conjugate set together with syn-tectonic pegmatite dikes. These shear zones and pegmatites are common features found together with SAP intrusions and can be followed over several 100s of meters to kilometres. The orientations of the D_S structural features suggest a north-south compression and east-west extension during this event. At the Singertât Complex, a conjugate set of up to 1 km wide, near vertical, sinistral, southeast- and dextral northeast-trending shear zones is present in the 3 km wide complex. These shear zones are formed under retrograde greenschist-facies conditions, and the orientation of the zones is indicative of north-south extension and east-west compression during deformation, which is denoted the Singertât Stage by Kolb *et al.* (2013). South-southeast-northnorthwest and north-south trending up to 100 m thick dolerite dikes are common within the craton. Thicker dikes of this set have sheared margins and are cut by southeast-northwest trending brittle faults. These dikes are assumed to be of part of the 2200-2050 Ma Umîvik dike swarm (Bridgwater *et al.* 1990).

The craton is bounded to the south at c. 61°45’N by Meso- and Neoarchaean rocks affected by deformation and intrusives of the Palaeoproterozoic Ketilidian Mobile Belt (Garde *et al.* 1999) before the Ketilidian subduction-related Julianehåb Batholith appears. To a lesser extent also smaller intrusives and dykes related to mid-Proterozoic Gardar Igneous Province in South-West Greenland, which developed in a continental rift-related environment straddle the zone between 61°45’N to around 62°30’N. Dykes related to the Gardar Province are also encountered within the southern part of the craton itself (Bartels 2015).

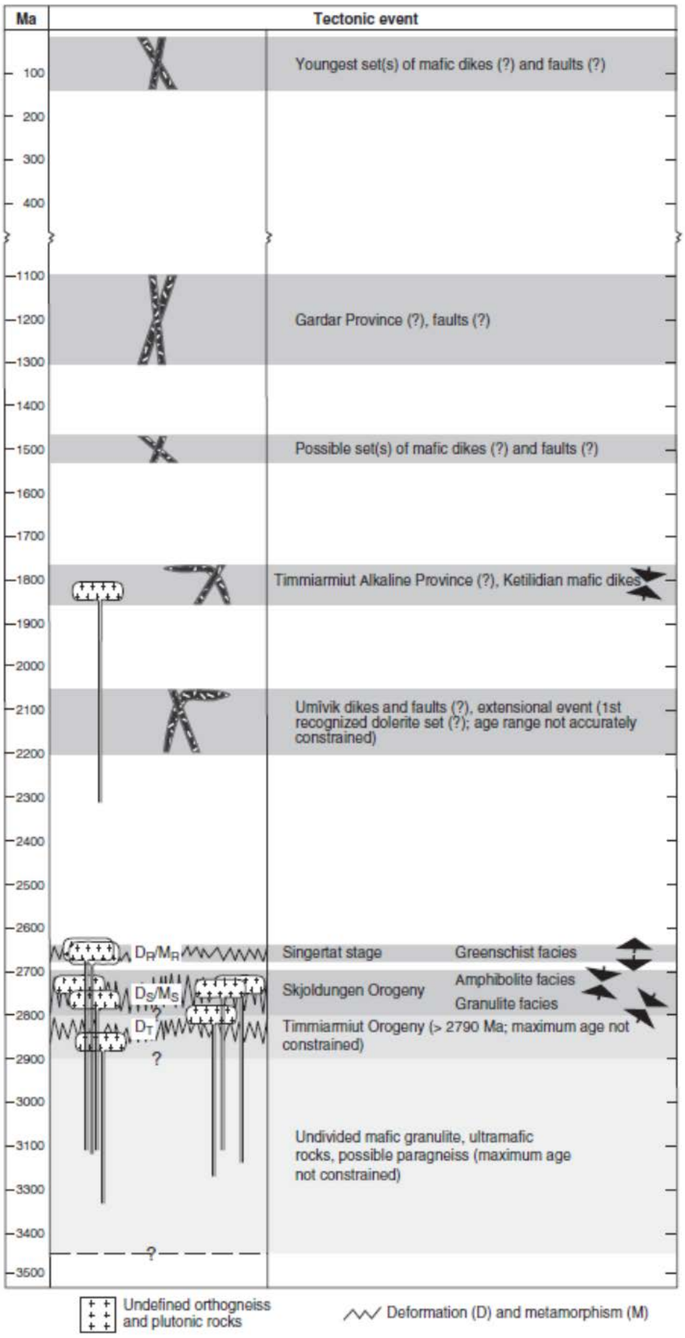

Figure 3. *Tectonometamorphic and magmatic event and stages as defined by Kolb et al. (2013) within the North Atlantic Craton between ca. 62°N–64°30’N. The main metamorphic and magmatic events took place from 2900-2650 Ma during the Timmiarmiut and Skjoldungen orogenies. Figure is taken from Kolb et al. 2013.*

To the north, the craton is affected by Palaeoproterozoic deformation related to the collisional East Greenland Nagssugtoqidian orogen which formerly was referred to as the Ammassalik Mobile Belt (Chadwick *et al.* 1989; van Gool *et al.* 2002). The deformation to the north seems to be irregular but gradually increasing from around 64°45’N towards the north and the centre of the orogen around Tasiilaq (65°30’N). In places, the craton is also affected by Proterozoic and Mesozoic-Cenozoic deformation. However, this deformation is restricted to narrow structural zones/faults.

The East Greenland Nagssugtoqidian Orogen (Ammassalik Mobile Belt)

The Palaeoproterozoic Nagssugtoqidian Orogen in southern East-Greenland comprises Archaean rocks from the Rae Craton to the north, the North Atlantic Craton to the south and Palaeoproterozoic meta-volcanic, meta-sedimentary and intrusive rocks. Kolb (2014) has, based on differences in lithologies and tectonometamorphic history, and divided the Orogen into four terranes, viz. from south to north: the Isortoq Terrane, the Ammassalik Intrusive Complex (AIC), the Kuummiut Terrane and the Schweizerland Terrane (Fig. 4). The Thyrm Complex of the North Atlantic Craton to the south forms the substrate and the southern hinterland of the Orogen; from around 64°45’N and towards the north these rocks gradually become more and more deformed and affected by the Palaeoproterozoic orogenic event.

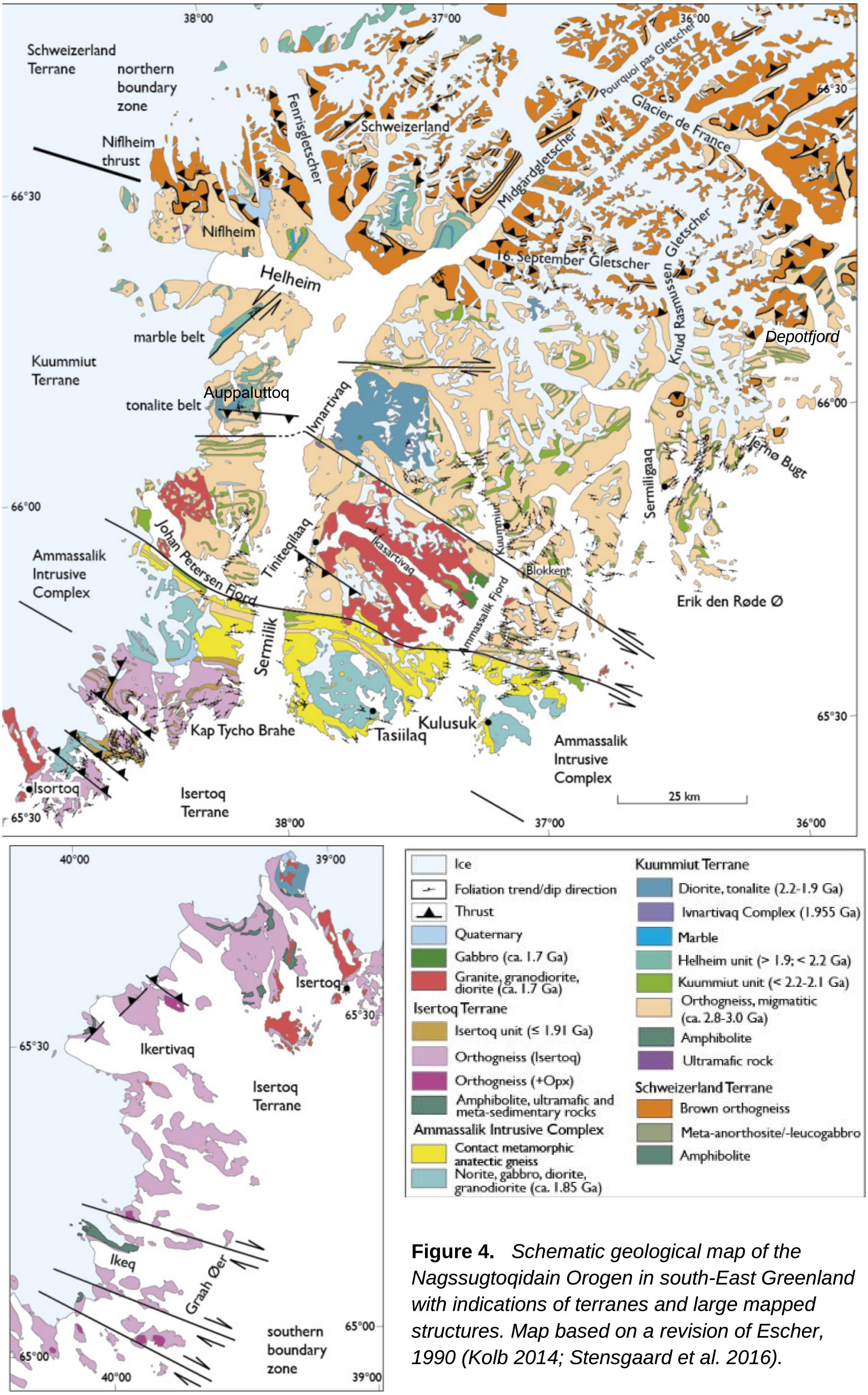

Figure 4. *Schematic geological map of the Nagssugtoqidain Orogen in south-East Greenland with indications of terranes and large mapped structures. Map based on a revision of Escher, 1990 (Kolb 2014; Stensgaard et al. 2016).*

Isortoq Terrane

The Isortoq Terrane is defined as the region between Graah Øer to the south and the area immediately south of the AIC (Fig. 4); it consists of polyphase, mainly quartzo-feldspathic granodioritic granulite facies orthogneiss with narrow bands of mafic and ultramafic rocks. Locally, the rocks have been retrogressed to the amphibolite facies. The orthogneisses have yield ages up to 3050 Ma (Sm-Nd whole rock model age; Kalsbeek *et al.* 1993).The Isortoq Terrane hosts the Síportôq Supracrustal Association; a supracrustal succession consisting of meta-sedimentary rocks and amphibolite with local smaller ultramafic pods or lenticular bodies (Hall *et al.* 1989). They occur as doubly folded belts and are abundant in the Síportôq area north of the Isortoq fiord. The lithostratigraphic sequence, here termed the Kap Tycho Brahe unit, consists of three lower amphibolite units separated by ultramafic and calc-silicate rocks including possible marble (Wright *et al.*, 1973; Kolb 2014). The metamorphic mineral assemblage indicates a temperature range of 500-700 °C and pressures of 4–5 kbar (Kolb 2014). Several dyke swarms cut the Isertoq Terrane; these are most likely of both of Palaeoproterozoic and Palaeogene age although exact ages are pending. Diorite and granite intrusions north and south of the settlement of Isortoq is dated at 1667–1664 and 1523 Ma (Kolb *et al.* 2016).

Ammassalik Intrusive Complex

The Ammassalik Intrusive Complex (AIC;) comprises three ovoid-shaped centres of mafic to intermediate intrusives with minor felsic components aligning in a 75 km long and 20 km wide SE-trending corridor centred at Tasiilaq. The intrusions are complexly layered; they contain layers of melagabbro, anorthositic rock, intermediate diorite to granodiorite, and more mafic to ultramafic components. Diorite from Tasiilaq has been dated at 1886±2 Ma (bulk zircon analysis; Hansen & Kalsbeek 1989) with high-resolution sensitive iron microprobe Pb-Pb zircon data analysis of 1881±10 Ma (Nutman *et al.* 2008). Isotopic data indicate mixing of a juvenile magma with Archaean crustal material during the creation of the AIC (Kalsbeek *et al.* 1993). Pressure-temperature data on diorites from the AIC suggest 830–850 °C and c. 7.5 kbar (Nutman & Friend 1989). Wall rocks of the AIC are contact metamorphosed and form a distinct km wide contact aureole of migmatite characterised by banded garnet gneiss with local pods of amphibolite, calc-silicate and ultramafic rocks. Meta-pelitic rocks from the aureole yields 720–840°C and 7.5 kbar for cores and 710–570°C for rim analyses (Andersen *et al.* 1989). The meta-sedimentary rocks from the contact aureole yield mostly detrital zircon ages of 1950–1910 Ma (Nutman *et al.* 2008).

Kuummiut Terrane

The Kuummiut Terrane is complex with several intrusives and abundant slivers and belts of meta-volcanic and meta-sedimentary rocks (Fig. 4) (Kolb 2014). The Archaean orthogneiss in the terrane is migmatitic with polyphase leucosomes and pegmatitic bands (Dawes 1989a). Dated gneiss samples from the Kuummiut Terrane spans a wide range of ages from around 2630 to 3010 Ma (Kalsbeek *et al.* 1993; Nutman 2008; Kolb 2014). The gneiss consist of a suite of mafic tonalitic, granodioritic and dioritic rocks with intercalated amphibolites, which form 10 to 100 m wide lenses and layers with pinch-and-swell structures parallel to the foliation (Dawes 1989a). The narrow slivers and belts of meta-volcanic and metesedimentary are interleaved with Archean rocks in thin-skinned thrust sheets that are subsequently refolded (Kolb 2014; Nutman *et al.* 2008). Late orogenic Paleoproterozoic intrusions comprise granite and diorite (Kolb 2014; Nutman *et al.* 2008). The tract is cut by a major NW-trending, transcrustal structure, a possible suture, and several near-vertical strike-slip faults (Fig. 5; Kolb 2014).

Swarms of strongly deformed discordant mafic dykes, represented by lenses and boudins, cut the Archaean orthogneiss. Mineral reaction textures indicate high-pressure eclogite facies metamorphism and subsequent decompression with calculated PT conditions being 660–760°C and 8–11 kbar (Nutman & Friend 1989; Nutman *et al.* 2008). Imprecise Pb-Pb ages zircon ages from a high-pressure amphibolite facies dyke dating the high pressure event have yield 1867±28 Ma whereas Rb-Sr and Sm-Nd data indicate metamorphism, probably related to the decompression, at ca. 1820 Ma (Kalsbeek *et al.* 1993; Nutman *et al.* 2008). The Sm-Nd data indicate that the dykes were emplaced after 2400–2200 Ma (Kaldsbeek *et al.* 1993).

The 300×800 m large and isolated dunitic Ivnartivaq Complex, which also host a ca 230 m^2 large magnetite-lens, is located in the central part of the terrane. The emplacement age, dated by hornblende Ar-Ar, is interpreted to be 1955±28 Ma (Brooks & Stenstrup 1989). Two major and a smaller more northerly located diorite and tonalite intrusions occur in the same part of the terrane, west and east of Sermilik. The tonalite west of Sermilik has a Pb-Pb zircon age of 1901±9 Ma (Nutman *et al.* 2008).

Palaeoproterozoic belts and slivers of paragneiss and schists occur throughout the Kuummiut Terrane. They consist of quartz, biotite, muscovite, feldspar, and minor garnet, kyanite, sillimanite and graphite. In some cases graphite and/or garnet are abundant. Locally grey graphitic marble or calc-silicate layers are present within the metasedimentary packages. They are most often found as boudinaged layers less than 1 meter wide. Larger belts, up to 100 m wide, also occur in a couple of places. The marble and calc-silicate layers are often hosted by muscovite-biotite-calcite schist. Amphibolite, containing plagioclase, hornblende, biotite, garnet and minor quartz, form 0.3 to 100 m thick layers parallel to the foliation. Smaller lenses of ultramafic rocks and meta-gabbro are found locally. The metamorphic mineral assemblages indicate amphibolite facies conditions with temperature range of 500–700°C and pressures of 4–8 kbar (Kolb 2014). Isotopic age data on zircon rims suggest a metamorphic overprint between 1870 and 1740 Ma (Kalsbeek *et al.* 1993; Nutman *et al.* 2008). In situ partial felsic melt pockets indicate metamorphic conditions of higher amphibolite to granulite facies.

The Schweizerland Terrane

The glaciated mountainous region north of the fjords Sermilik and Kangertigtivatsiaq (north of ca. 66°30’N) constitute the Schweizerland Terrane (Fig. 4). It is defined by the Archaean orthogneiss and narrow bands of mafic rocks of the Rae Craton in the hanging wall of the Palaeoproterozoic Niflheim Thrust (Bridgwater & Myers, 1979; Myers, 1984, 1987; Dawes *et al.*1989b; Kolb 2014). The orthogneiss has yielded ages in the range of 2870-2700 Ma (Kalsbeek *et al.* 1993; Nutman *et al.* 2008) and has indicated a polyphase nature of the orthogneiss with no signs of Palaeoproterozoic overprint. The mineral assemblage in the orthogneiss indicates granulite facies metamorphism. Pegmatites with ages of 2630±65 Ma intruded the orthogneiss during retrograde amphibolite facies.

Large structures

Some geological observations

Large-scale structures in form of deep-seated structures in the brittle-ductile to pure ductile regime have not been recognised in the Skjoldungen region. Instead, this region is dominated by regional-scale early upright to reclined isoclinal folds formed during the Skjoldungen Orogeny (Kolb 2014).

Early locally developed small-scale minor shear zones occur throughout the region. However, these are related to shearing along the limbs of the regional-scale folds. SSE-NNW-trending lineaments in the topography and visible in geophysical data can be related to brittle structures and are probably related to Palaoproterozoic and possible also Phanerozoic tectonic events. Greenschist facies alteration is observed in some of these brittle-structures.

The boundary of the Skjoldungen region towards the north is defined by near-vertical, dextral ESE-WNW trending mylonitic shear zones located between Umivik and the northern part of Jens Munk Ø (64°30’N to ~65°; Myers, 1984, 1987; Chadwick *et al.* 1989). The deformation is in greenschist facies in the brittle/ductile transition as shown by the presence of brittle deformation along strike-slip fault planes with epidote (2015 personal communication with P. Guarnieri).

Early deformation phase large-scale thrusts juxtapose the Kap Tycho Brahe unit of the Síportôq Suprcrastal Association and Archaean orthogneiss-amphibolite rock units against each other in a compressional shallow-dipping SE-vergent imbricated thrust/reverse shear zone system south of AIC. Later deformation resulted in SW-vergent thrust zones observed near the Inland Ice south of AIC and south of Isortoq (Kolb 2014). Large-scale fold patterns are obvious by the map pattern of the Palaeoproterozoic rocks in the area around Isortoq to Kap Tycho Brahe (Fig. 4). These folds, developed between the SW-vergent thrust zones, become more open to the south and are not observed south of Ikertivaq (Fig.4). A system of early deformation phase dextral strike-slip shear zones located south of Isortoq at Graah Øer connect the reverse shear zones of the early deformation, forming a lateral and frontal ramp thrust system (Kolb 2014).

Within the Kuummiut Terrane (Fig. 4) early deformation resulted in the formation of shear zones along the contact between Archean orthogneiss and Palaeoproterozoic rocks and large-scale nappe imbrication of the two. Later deformation resulted in reverse NE-vergent, near-vertical sinistral oblique-slip and normal W-vergent shear zones. These zones are 10s of metres wide and are characterised by mylonitic orthogneiss.

A large NNW-SSE trending 7 km wide shear zone north of AIC (Fig. 4) straddles the outer part of the large partly contact-metamorphosed paragneiss unit that surrounds the intrusive complexes of the AIC. These probably mark a distinct deep-seated structural feature that may be the structural centre of a doubly-vergent collisional orogen. The zone is here referred to as the Ammassalik Shear Zone.

Structures within the Schweizerland Terrane have seen little investigations. Archaean structures present in the hanging wall of the Palaeoproterozoic shallow to moderately NW-dipping Niflheim Thrust and related thrust system (Fig. 4). However, two distinct shear zones in the coastal areas of the Schweizerland Terrane have been noted (e.g. Dawes *et al.* 1989b, p. 57, Fig. 3). At Kap Japetus Steenstrup, northern side of the fjord Kangertigtivatsiaq, retrogressed granulite facies gneiss is deformed by variable trending (ENE- and WNW) near vertical several hundred meters wide ductile shear zone (Bridgwater *et al.* 1977; Bridgwater & Myers, 1979; Myers *et al.* 1979; Dawes *et al.* 1989b). According to Dawes *et al.* (1989b), the shear zone can be followed for 20 km, where after it bifurcates and appears to die out east of the fjord Kangertigtivatsiaq. However, it is also noted, that the zone is more or less along strike with the prominent physiographic lineament followed by the fjord and the eastward continuation in Glacier de France. The fjord Kangertigtivatsiaq also host a major, brittle, E-W oriented left-lateral fault zone (P. Guarnieri, pers. com. 2015). This fault could have reused and reactivated part of the former ductile structure and have caused a displacement and termination of the ductile structure.

Mineralisations

The mineralisations in South-East Greenland are tightly linked to the tectonometamorphic Archaean, Palaeoproterozoic and Palaeogene evolution. The mineralisations encountered in the region are outlined in Table 1. The economic geology has recently been described in Kolb *et al.* (2016). The descriptions below of the different mineralisations are extracted from this publication.

Nickel-copper mineralisation

Local nickel-copper- sulphide mineralisations found within bands and lenses of mafic granulites, pyroxenite and peridotite (interpreted to represent lower crustal ultramafic intrusions) are known from several localities within the Thrym Complex of the North Atlantic Craton between the peninsula Langenæs just north of Skjoldungen Island and Odins Land (63°30’N to 64°N) in South-East Greenland (Bagas *et al.* 2016; Owen 2011; Stensgaard *et al.* 2010). In-situ SHRMP analyses on zircon grains from the mafic granulite hosting the mineralisation have given an age of 2859 ± 6 Ma (Bagas *et al.* 2016; minimum age of emplacement and crystallization for the protolith of the mafic granulite). Two styles of Ni- and Cu-rich sulfides mineralisation can be recognized; as (i) interstitial or net-textured sulphides or (ii) as metamorphic granoblastic-decussate rocks containing disseminated sulphides (Bagas *et al.* 2016; Owen 2011; Stensgaard *et al.* 2010). The first style is predominantly in peridotite and mafic granulite with greatest volume in close proximity to peridotite and contains up to 5180 ppm Ni and 2560 ppm Cu. The second disseminated style is concentrated in metre-scale shear zones and is depleted in nickel but contains comparable copper values. Bagas *et al.* (2016) interpreted the second style mineralisation to have been sourced from the first style during the late stage Skjoldungen Orogeny.

Molybdenum-tungsten mineralisation

A quartz-wolframite-molybdenite vein with phyllic alteration is known from north-western part of the Thrudvang peninsula, close to the Kangertikajik Fjord in the Skjoldungen area (Rosa & Ulrich, 2015). The approximately 30 cm wide, sub vertical vein is hosted in mafic granulite and yields up to 1.6% W and 263 ppm Mo. Molybdenite yields a Re-Os age of 2749 ± 11 Ma contemporaneous with early intrusions from the SAP, e.g. granite-monzogranite and Skirner Bjerge Syenite (Rosa & Ulrich 2015). Two rusty-weathered horizons in amphibolite (retrogressed mafic granulite) have anomalous W content (up to 0.55% W) due to scheelite mineralisation, but are low in Mo. Both mineralisation styles are spatially closely related; they are interpreted to having been formed contemporaneously by magmatic hydrothermal processes (Rosa & Ulrich 2015). The fluid inclusions in quartz of the vein are sparse and show a one-phase, high-density CO_2 composition. Whether this fluid is responsible for the mineralisation, or if it is a feature of later re-crystallization, cannot be unequivocally determined.

Iron-vanadium mineralisation

Some *c.* 2700 Ma layered intrusions of the SAP host magnetite bands and veins. The Vend Om Intrusion is a small 350 x 450 m elliptical intrusion with ≤2 m wide bands of ≤35 vol.% magnetite and hercynite, hornblende and plagioclase. Several ≤ 0.2 m wide magnetite, ilmenite and spinel bands are present in the Njords Glacier intrusions (Klausen & Kokfelt 2014). Most notable metal content is vanadium content of up to 1.7 wt% V_2O_5.

Nickel-copper-gold-platinum group element mineralisation

The Ammassalik Intrusive Complex (AIC;) has numerous Ni and Cu anomalies in stream sediment samples, which was the motivation for mineral exploration in the area since the mid-1990s.The most recent mineral exploration was concentrated on the southern rim of the Tasiilaq Intrusive Centre, the central complex in the AIC. In 1997, an approx. 90 long and 1-8 m wide mineralised lens of serpentinized ultramafic rocks was discovered, returning up to 1.0 wt% Ni, 0.5 wt% Cu, 0.4 ppm Au and 615 ppm Co in mineralised samples (Lie 1997). Similar values have been obtained in various mineral exploration campaigns up to 2012. The interstitial network of ore minerals consists of pyrrhotite, pentlandite, chalcopyrite and minor magnetite (Lie 1998). The mineralisation was interpreted to be hosted in ultramafic rocks occurring in the contact aureole of the Tasiilaq Intrusive Centre.

Reconnaissance and detailed mapping of the AIC during the joint GEUS-MMR SEGMENT project from 2009-2015 discovered several sulphide mineral occurrences hosted by intrusive rocks of the AIC. In the Tasiilaq Intrusive Centre of the AIC, pyroxenite and olivine-bearing gabbro host interstitial sulphides (Grøtner 2014). The ore assemblage is pyrrhotite-pyrite-chalcopyrite-(magnetite). Pentlandite has not been observed in the studied samples, but whole rock geochemistry returned higher Ni and Co as predicted from modal mineral abundance, which indicates presence of pentlandite (or another Ni-Co-bearing mineral). Maximum values for mineralised samples are 770 ppm Ni, 5230 ppm Cu and 433 ppb Au (Grøtner 2014).

In the Johan Petersen Intrusive Centre of the AIC, east of Sermilik Fjord, mineralisation are found in various settings within the AIC. Contact-style mineralisation of up to 5 vol.% interstitial chalcopyrite, pyrrhotite, lesser pyrite, covellite and marcasite hosted in gabbronorite and melanogabbronorite and in biotite-garnet-gneiss in the south-western marginal part of the intrusion. Mineralisation are also found mafic-ultramafic sheets and breccia with an average of 5-15 vol.% with maximum values at 30 vol.% sulphides. Pyrrhotite and pyrite with lesser chalcopyrite and pentlandite form an interstitial network and local inclusions in cumulus silicates. The sulphur isotope signature for all mineralised samples is in the range ofmantle composition and very different from the very heavy signature of the contact-style mineralisation.

Mineralisation in mingling zones occurs throughout the Johan Petersen Intrusive Centre is mainly hosted by pyroxenite, melanogabbronorite and Hbl-melanogabbro stringers. The gabbroic rocks may contain disseminated sulphides up to 10 cm away from the stringers. The sulphide content varies from a few percent up to 20 vol.% and averages at 5 vol.%. Pyrrhotite, minor chalcopyrite and traces of pentlandite are fine-grained, finely disseminated, cm-scale clusters, an interstitial network or inclusions in silicates. The recognition of hybrid igneous lithologies and K-feldspar-cordierite-garnet-graphite assemblages indicates magma mingling, and melting and assimilation of the wall rock. The favoured interpretation of the mineralisation is formation from assimilation of sedimentary sulphide in an already semi-solid magma, which was already depleted in Ni and Cu.

Shear zone-related sulphide mineralisation within or at the margin of the AIC have been found locally in 1.5-3 m wide shear zones indicated by protomylonite structures in several places. Three shear zone trends are recognized: (1) NE-trending dipping at 60°-80° SW; (2) NNE-trending dipping at 60°-80° SSW; and (3) NW-trending dipping 80° NE. Quartz veins and the hydrothermal quartz-biotite-epidote-chlorite-talc-muscovite-pyrite alteration assemblage point to hydrothermal overprint related to deformation. Pyrite occurs in quartz veins, breccia matrix and in protomylonite elongated along the main foliation. Distal to the shear zone, primary sulphides are replaced by pyrite, minor chalcopyrite, chalcocite and covellite. All sulphides show supergene alteration to hematite-goethite assemblages. Copper- and Ni-contents are generally low, with local Cu-enrichment up to 1 wt%, indicating selective transport of Cu by the hydrothermal fluid. The sulphur isotope signature is light with $\delta^{34}S$ values peaking at -3‰ to -4‰ and -10‰ to -15‰, overlapping with adjacent primary sulphide mineralisation. This indicates that hydrothermal fluids remobilized the primary magmatic sulphide mineralisation into the shear zones.

Sulphide mineralisation in the intrusions of the AIC is complex, involving several processes like magma mixing, mingling and wall rock assimilation, and later hydrothermal remobilization and supergene alteration. The mineralisation is at very low Ni-Cu-PGE-Au grade and only the mafic-ultramafic sheets formed grades that may be comparable to known deposits.

Graphite mineralisation

Flake graphite mineralisation is present in the high-grade metamorphic Kuummiut Terrane north of Tasiilaq at Auppaluttoq and Kangikajik (Fig. 4).

The rocks in the Auppaluttoq area are orthogneiss, amphibolite, paragneiss and biotite schist, which are cross-cut by pegmatite, and dolerite dykes and quartz-garnet veins. The oldest (F_1) ENE-trending folds are associated with layer sub-parallel, up to hundreds of meters long thrusts, which host the graphite mineralisation. The graphite content decreases outward from the shear zones, indicating that they acted as fluid conduits during hydrothermal mineralisation. Graphite mineralisation of > 30 vol.% graphite is hosted in 0.2 to 1.5 m-wide and 2 to 20 m long bands (Rosing-Schow *et al.* in review). The Kangikajik area consists of orthogneiss, amphibolite, grunerite-gneiss, paragneiss, quartzite and biotite schist, which show complex fold interference patterns. Graphite is concentrated in ~ 1.5 km wide D_1 shear zones, commonly forming anastomosing structures containing mineralised lenses draped around amphibolite, grunerite-gneiss and orthogneiss fragments. High-grade graphite mineralisation is up to 0.7 m wide and 20 m long and locally forms rich lenses in F_1 fold hinges. Pegmatite dykes locally contain up to 2 vol. % graphite (Rosing-Schow *et al.* in review).

The graphite mineralisation is hosted in various rocks as well as in veins and breccia, with the richest mineralisation being located in shear zones. Hydrothermal alteration of the wall rocks associated with the graphite mineralisation indicates hydrothermal processes involved in the mineral system. Three stages of graphite mineralisation are distinguished: (1) organic matter was transformed to graphite during prograde metamorphism; (2) remobilization by hydrothermal fluids during retrograde exhumation, possibly in several stages; and (3) enrichment in supergene alteration zones. The carbon source likely is in the metasedimentary rocks of the Kuummiut unit based on the relatively low $\delta^{13}C$ values. Marble has carbon isotope composition that cannot be related to the graphite signature. The shear zones acted as pathways for metamorphic fluids, which scavenged carbon from the graphitic metasediments. Graphite precipitated from these carbon-bearing hydrothermal fluids resulted from hydration of the wall-rocks causing carbon-saturation. Supergene alteration led to enrichment in an approx. 2 m thick colluvium layer.

Corundum mineralisation

Corundum was first discovered by the the Geological Survey of Greenland (GGU) in the Síportôq supracrustal belt in the 1980’s (see Hall *et al.* 1989). In 2009, corundum-bearing samples from the Nattivit Kangertiva area north-east of Isortoq (Fig. 4) won the first price in the national mineral hunt program Ujarassiorit. Subsequently follow-up and detailed work was carried out during the joint GEUS-MMR SEGMENT project in 2014-2015. The discovered corundum occurrences are of local extent and vary in size. Most of the corundum has a light pink colour with two samples having a purplish colour. However, the quality of the stones discovered so far is not of gemstone quality. Corundum mineralisation in the Nattivit area is hosted in metamorphosed, hydrothermally altered and boudinaged ultramafic rocks that represent dykes or sills emplaced in a basement of paragneiss and amphibolite. Hydrothermal alteration and corundum mineralisation occurs, where the youngest pegmatite generation cross-cuts the ultramafic rocks. Notably, earlier pegmatite that is folded by regional deformation is not related to corundum mineralisation. At the contact of metamorphosed ultramafic rocks and young pegmatite, hydrothermal alteration zones developed: (1) an outer biotite or talc zone; (2) an intermediate black or green amphibole zone; and (3) an inner corundum or plagioclase zone. The genesis of this hydrothermal alteration is interpreted to be related to fluid-assisted Si-Al exchange between the pegmatite and the metamorphosed ultramafic rocks. The amount of Si and the availability of hydrothermal fluid appear to control the style of mineralisation. The aluminium appears to come from the pegmatite and removal of silica creates new mineral zones and reaches Al_2O_3 saturation in the late-stage phases.

Gold – previous investigations

Several gold-bearing samples from the public hunt for minerals program, Ujarassorit (Fig. 6, Petersen and Thomsen 2014), as well as some anomalous gold values in stream sediment sampling campaigns by NunaMinerals A/S in 1996 (Lie 1997) might indicate a potential for gold in the Tasiilaq region.

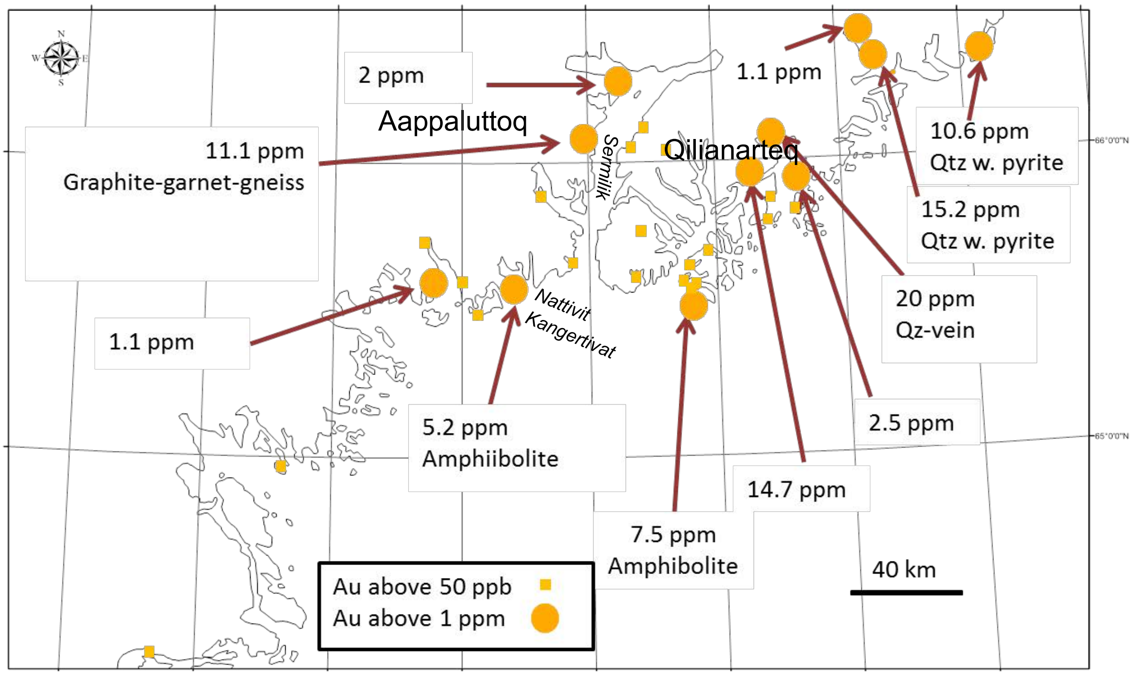

Figure 6. *Gold from analysed Ujarassiorit rock sample. The Ujarassiorit samples cover samples from the years 1989-2013. The samples are reported as being both floats and in-situ bedrock samples; due to the nature of the public hunt for minerals program, the exact sample localities are often insufficiently recorded. Figure from Petersen and Thomsen (2014).*

This is also supported by the findings in the new GEUS-MMR stream sediment geochemistry dataset in which both elevated gold and gold-pathfinder elements such as arsenic and caesium also are found (see also the section “SEGMENT Stream sediment data (T3a to T3i)” on page 55).

Especially supracrustal dominated and contact affected aureole areas south and north of the Ammassalik Intrusive Complex (AIC), as well as areas at Nattivit Kangertivat and east and west of the central part of Sermilik Fjord, are characterised by having clusters of samples with elevated gold (30-190 ppb Au) within areas also characterised by high traditional gold-pathfinders elements such as arsenic and/or caesium. Other elements, which can be considered as gold-pathfinder elements, such as molybdenum and tungsten, are also found to be elevated in some of the gold-arsenic-caesium elevated areas.

The highest encountered gold value in a stream sediment sample (190 ppb Au) within the Tasiilaq region is located in the north-western part of the contact aureole that envelope the Tasiilaq Intrusive Centre; an area that also is characterized by intense shearing. A follow-up field investigation during SEGMENT 2014 fieldwork failed to identify an in-situ gold mineralised setting in this area.

A winning gold-bearing Ujarassorit sample from Aappaluttoq (Fig. 6) in the north-eastern part of Sermilik Fjord was investigated during the SEGMENT program in 2014. The sample had been described as "*a graphite and garnet gneiss*" and had a gold content of 11.1 ppm gold. However, a detailed examination of the sample in 2016 revealed that the auriferous sample more probably should be described as a pyroxene-garnet gneiss consisting of garnet, pyroxene, biotite, pyrrhotite, quartz, plagioclase and graphite (Baden 2016).

A visit during the SEGEMNT project in 2014, while work was still based on the original description and a gold-pyroxene-garnet skarn model for the mineralisation, contact with the local finder of the winning sample from the settlement Kuummiut enabled a detailed sampling of the garnet-rich (garnetite) horizon pointed out to be the location of the winning sample. This horizon belongs to one of several discontinuous and foliation-concordant, garnet-rich bodies present within graphitic mica schist. No visible mineralisation was observed in the horizons and no elevated gold was encountered in the garnetites. However, an extensive sampling program of the other lithological units near the horizons from e.g. silicified domains of the graphitic mica-schist, quartz veins and veinlets containing sulphides or gossanised materials was carried out. The hydrothermal quartz veins and veinlets have a biotite-pyrrhotite-chalcopyrite-graphite alteration halos and are structurally controlled by the larger near-vertical shear zone systems. The 2014 sampling program identified anomalous gold values up to 463 ppb Au found in few of the quartz veins and veinlets. It was suggested that the original winning sample might also include similar veinlets and that a "gold-nugget" effects might explain the difference between the gold content in the wining sample and the vein/veinlets samples during the 2014 sampling program. Follow-up during the SEGMENT project in the Qilanarteq area, which host several gold-bearing samples from the Ujarassorit program (Fig. 6), failed to identify any gold mineralisation. Neither did heavy mineral panning in the larger drainage system reveal any anomalies.

No notable elevated gold or arsenic have been encountered in the stream sediment geochemistry from Skjoldungen region (highest content being 35 ppb Au) and no in-situ gold mineralisation have been found. However, most notable is a small cluster of stream sediment samples with elevated geochemical gold values at Timmiarmiut in the southern part of the Skjoldungen region.

Table 1. Overview of known mineralization in South-East Greenland (62°–67°N)

	Commodity	Name	Description
North Atlantic Craton	Ni-Cu	Thrym Complex Ni-Cu mineralisation	Two styles of mineralization are distinguished: (1) interstitial or net-textured and disseminated sulphides in peridotite and mafic granulite, containing up to 5180 ppm Ni and 2560 ppm Cu; and (2) disseminated sulphides concentrated in metre-scale shear zones as remobilization, being Ni-depleted but with comparable Cu contents.
	Fe- V	Skjoldungen magnetite-ilmenite mineralisation	Several of the c. 2700 Ma intrusions of the SAP host <2 m wide bands and narrow veins of magnetite-ilmenite±apatite with potential for Fe-Ti-V mineralization. Highest values being 0.6–0.7% V_2O_3,
	W-Mo	Thrudvang W±Mo mineralisation	Sub-vertical quartz-wolframite-molybdenite vein (1.6% W, 0.26 Mo) with phyllic alteration in a package of mafic granulite gneiss and two rusty amphibolite horizons (up to 0.5% W) has been found on Thrudvang peninsula, Skjoldungen region.
Nagssugtoqidian Orogen	Corundum (gemstone)	Nattivit corundum mineralisation	Corundum occurs locally in the Siportoq area as metasomatic product where late-stage pegmatite crosscuts metamorphosed ultramafic rocks.
	Ni-Cu-Au-PGE	Ammassalik Intrusive Complex Ni-Cu-Au-PGE mineralisation	Orthomagmatic Ni-sulfide mineralisation is hosted in ultramafic rocks of the AIC in zones of magmat mingling and mixing. Potential remobilization occurred along shear zones. Commercial exploration have reported up to 1.39% Ni, 0.46% Cu, 757 g/t Co, 0.25 g/t Pt+Pd, Ni^{Tenor} 4.72% from a mini-bulk sample of the mineralisation.
	Graphite	Auppaluttoq and Kangikajik graphite mineralisation	Flake graphite is hosted in shear zones in biotite-graphite schist in the high-grade metamorphic Kuummiut Terrane. Up to 53 wt%; 50 out of 75 samples have graphitic contents above 2 wt%; uniformly large graphite flake size of 3.33 ± 1.21 mm.
	Au	Tasiilaq gold mineralisation(?)	Laminated pyrite-pyrrhotite-quartz veins (up 463 ppb Au). Anomalous stream sediment geochemistry (up to 190 ppb AU). Historical Ujarassiorit samples (public hunt for mineral program) have yielded up to 11.1 g/t Au.

Prospectivity modelling

Prospectivity modelling can be defined as making “descriptions, representations or predictions about an indirectly observable and complex real-world system via (quantitative) analysis of relevant data” (Carranza 2009). In the case of mineral prospectivity modelling, the indirect observable and complex real-world system is the subsurface that is considered in terms of the targeted mineralization. The descriptions, representations or predictions are criteria in the form of explanatory, predictor, evidential variables or properties directly observable or measurable and are considered as being inter-related to each other and to the targeted system (i.e. the mineralisation).

For a quantitative prospectivity modelling, the criteria have to be transferred to a mathematical representation. The mineral prospectivity model is finally defined as the simplified numerical representation that is associated with the relationships between targeting criteria and the targeted mineralisation in the form of potential mineral deposits (Porwal et al. 2003). A variety of linear and non-linear functions can be used to approximate the relationship between the criteria and the mineralisation potential. Based on the nature of the functions used the prospectivity models can be defined as either linear (e.g. using weights-of-evidence) or non-linear (e.g. using fuzzy logic, logistic regression, neural network, Bayesian network).

Based on whether the model parameters are estimated from empirical data or from conceptual knowledge, the prospectivity models are classified into either data-driven or knowledge-driven, respectively, although overlaps and mixtures between the two exist.

The current mineral prospectivity modelling is based on an underlying mineral system approach and is carried out via knowledge-based fuzzy logic analysis.

Similar approaches to prospectivity mapping of orogenic gold considering the fuzzy logic in combination with the mineral system approach can be found in e.g. Knox-Robinson (2000), Porwal *et al.* (2003), Nykänen,& Salmirinne (2007), Nykänen *et al.* (2008), Silva *et al.* (2012), Joly *et al.* (2013) and Ford *et al.* (2016).

Knowledge-driven fuzzy logic analysis

In the knowledge-driven fuzzy logic analysis, which is used in this study, the relationships between evidential datasets and the targeted mineralisation potential are based on conceptual knowledge-based exploration criteria, which in the current work is identified from a mineral system approach (i.e. in this study orogenic gold mineral system).

The fuzzy logic analyses allow an integration of a number of evidential variables, whose impact onto the system is described by membership functions and which are differently weighted based on their relative significance estimated from expert knowledge. The evidential variables can be analysed spatially and quantitatively in a GIS platform (in this case ArcGIS™) by a stepwise procedure (Fig. 7). Only step 3, 4 and 5 will be described in this section. Step 1 and 2 are described in later sections.

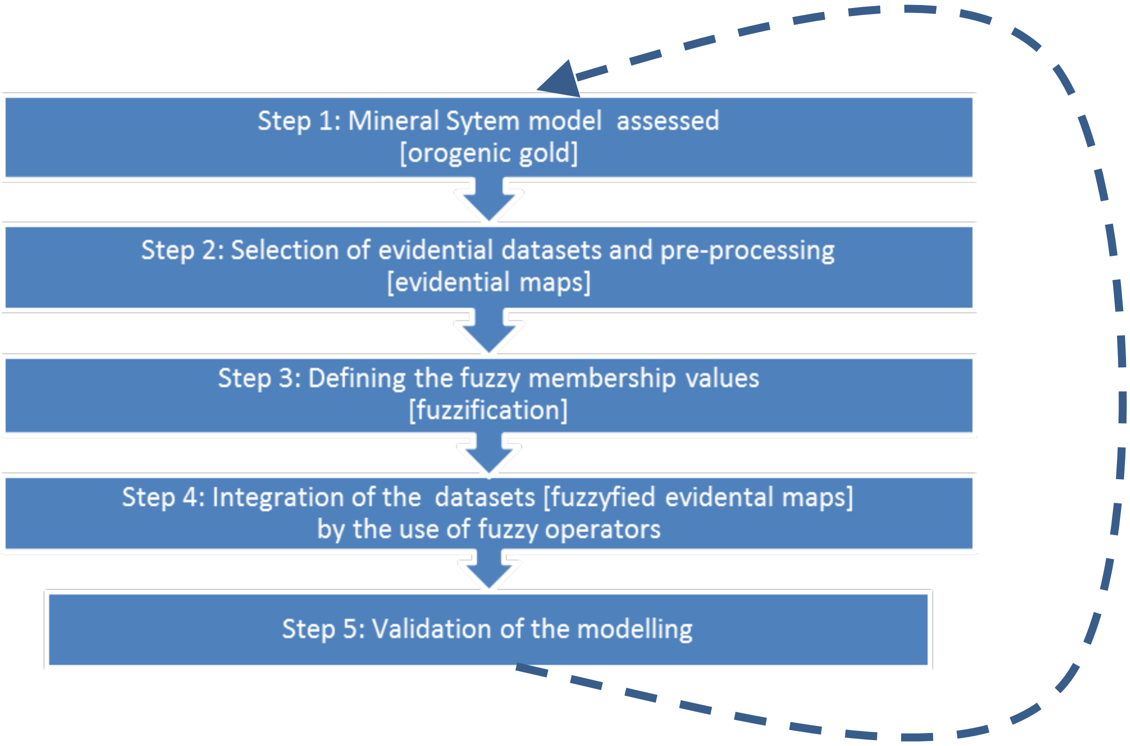

Figure 7. *Flow-chart showing the steps of the fuzzy logic procedure.*

Step 1: The mineral system approach – orogenic gold

The underlying rational of the mineral prospectivity modelling carried out in this work is based on the mineral systems approach as presented by Wyborn et al. 1994 and McCuaig *et al.* (2010). In the mineral system approach, governing geological processes assigned to different components of a system required to form and preserve an ore deposit at different scales are addressed. This is in contrast with a more mineral deposit-focused descriptive approach in which the characteristics and foci most often are the directly observable criteria at a deposit scale.

The mineral system approach provides a holistic view on the geological system that forms and preserves a mineralisation. The geological system constitutes in principle all the physiochemical processes needed for the formation and preservation of a mineralisation. The approach works under the assumption that the focal point of the system, i.e. the ore deposits itself, is a consequence of processes that have operated across a range of scales, from broad continental, regional, district, prospect down to the actual ore body. As the scale is reduced, the processes and their importance will also vary.

Wyborn *et al.* (1994) and McCuaig *et al.* (2010) define the **mineral system components** to be:

- Source
- Active pathways
- Throttles (physical)
- Trap (scrubber, chemical)
- Preservation

Referring to them, the generalised physiochemical processes related to the components of the system are:

1. Extraction of metals and, if needed, chemical ligands for metal complexation in the fluids from suitable sources
2. Establishment of energy gradients to initiate and drive the mineral system
3. Generation or availability of fluids/medium for transporting metal/metal complexation
4. Migration of metalliferous fluids/medium to the trap regions (narrow focused pathways for the fluid/medium that carry the metal/metal complexation)
5. Modification of the metalliferous fluid/medium composition in the trap region by physical and/or chemical processes, leading to the deposition of the metal
6. Preservation of the deposit through time

As the mineral system approach is a generalised process-based framework for addressing the formation and preservation, the system and its identified processes can easily be adapted to different environments and ore deposits. The processes occurred in the past and cannot be observed directly. Consequently, they need to be inferred from geological features called **targeting elements** (Joly *et al.* 2013). Targeting elements are in almost all cases not directly identifiable or mappable in the present day geology but need to be inferred/mapped from their responses through observations and available datasets. These spatial proxies of the targeting elements are in mineral prospectivity mapping termed evidential maps, predictor maps, predictor patterns, or simply predictors (Joly *et al.* 2013). They will be referred to as **evidential maps** in this work.

The evidential maps are based on various forms of geological information and/or data – they are referred to as **primary data** in this work. In several cases the primary data will be subject to a laborious processing before the targeting elements have been extracted and brought into a format that can be used as an evidential map.

The mineral system components are the same for all mineral systems, whereas the processes defined under each component and the targeting elements may vary according to the mineral deposit type and the geological environment under investigation. Also, the availability of datasets and prior knowledge from the region provide natural constrains on which evidential maps are created and addressed.

The prospectivity analysis presented here, based on the mineral system approach, is carried out for orogenic type of gold in South-East Greenland. The mineral system for orogenic gold was evaluated according to the geological settings and geoscience datasets available in South-East Greenland.

Step 2: Selection and processing of evidential datasets for orogenic gold in South-East Greenland

The targeting elements and the associated evidential maps which it was decided to produce and use are summarized in Table 2 to Table 5.

The targeting elements, the primary data and evidential maps identified and processed during the work presented here, only constitute a chosen selection of elements and evidential maps amongst many other elements and maps that could have been included. Those selected in this study aim at providing a regional to district input to narrow down the areas that could be of special interest. The amount of resources (worktime) available for the investigation and processing of existing dataset in order to produce different evidential maps, as well as which datasets are accessible, also provide constraints on which and in which form datasets can be evaluated and transformed into evidential maps. The significance and applicability of the target elements and corresponding evidential maps can always be questioned according to the mineral system and mineral deposit type in focus.

The primary data and the processing needed to extract the targeting elements and produce the evidential maps, which were used in the final prospectivity analysis for gold in South-East Greenland, are described in the section “Step 2: Used datasets, processing and resulting evidential maps” starting at page 37. The selected evidential datasets and maps used as proxies to target elements of the mineral system for orogenic and intrusive-related gold are described in the following sections.

First, the different proxies used for representing the different mineral source components and why they are considered as relevant as are summaries in the following sections.

Proxies for source

At the time of a mineralising process involving fluids ascending through the continental crust, it is proposed that the existence/thickness of the underlying sub-continental lithospheric mantle (SCLM) may represent a governing factor for the fertility for the formation of gold mineralising systems. Gold mineralising systems are more likely to develop in orogens with deducted oceanic or thin continental lithosphere (see e.g. Bierlein *et al.* 2006; Goldfarb *et al.* 2001a, b).

Even though it is difficult to deduce the thickness of the continental crust at the time of formation of possible gold mineralisation, it is believed that the entire Archaean craton and the Palaeoproterozoic orogenic parts of the study region in South-East Greenland is underlain by a Precambrian SCLM. In addition, subduction of oceanic- and back arc-related crust has been proposed during the Skjoldungen Orogeny and the Nagssugtoqidian Orogeny in South-East Greenland (Bagas *et al.* 2013; Kolb *et al.* 2016).

Table 2. *Overview of the mineral system component: Source. The short names (in bold) and, in some cases abbreviated short names (in bold and brackets), for the different proxies are given in the column for ‘Proxies’. These are used throughout the report – in some cases together with the numeral “Code” of the concerned proxy.*

		Mineral System Component: Source				
		Process	**Targeting element**	**Proxies**	**Description**	**Code**
Scale	**Regional**	**Tapping of Mantle Source ”SCLM”**	Deep seated structures tapping deep reservoir – regarded important for the access to source areas for fluids and metals	Regional gravity **“Tapping – Gravity”**	Major lineaments/shifts, calculation of distance (m) from lineaments as determined from the regional gravity (CAMP-G compilation; picked manually)	S1b
				Regional magnetic **“Tapping Magnetic”**	Major lineaments/shifts calculation of distance (m) of lineaments as determined from the regional magnetic (CAMP-M compilation; picked manually)	S1c
	District	**Magmatic input to the crust**	All intrusion – regarded important for the access to source areas for fluids and metals	Extracted from 1:500 000 geological map **“Magmatic input”**	Polygons of all intrusions; calculation of distance (m) from intrusions extracted from the geological map.	S2
		(none)	-	-	-	
	Prospect	(none)	-	-	-	

Assuming that a fertile source is present beneath the entire study region, identifying possible areas with tapping of the SCLM becomes important, when addressing the source. The tapping of fluids from SCLM is generally thought to be attributed to large-scale crustal breaks such as terrane boundaries and the largest deep-seated structures. To deduce these, distances to the major lineaments and shifts identified from anomalies in gravity and magnetic data of continental-scaled data compilations have been considered as proxies. These proxies are named “Tapping – Gravity” and “Tapping - Magnetic” (code S1b and S1c; see Table 2). The processing and extraction of these proxies are described in the section ‘Detection of first-order trends from CAMP magnetic and gravity data (S1b, S1c)’ starting on page 84.

Another source of fluids, and potentially also metal, to the gold mineralising system are magmatic input to the crust in the form of intrusions. The proxy for these is represented by distances to the polygons that define the intrusions on 1: 500 000 scale geological map (Stensgaard *et al.* 2016). This proxy is named “Magmatic input” (code S2; see Table 2).

The processing of this proxy is described in the section ‘Distribution of intrusions (S2)’ on page 45.

Proxies for pathways

Fluids and fluid-carried metals originating from the ‘Source’ component of an mineral system usually has to circulate and flow from the source to a new position; in some cases enhancing their capabilities to form a mineralisation (e.g. pick up more metals or other fluid components) or to enter a mineral system component that facilitate a deposition of metal and/or other elements of the fluid. This fluid flow and circulation is controlled by fluid pathways.

It is well-established in the models for orogenic gold that 1st order long-lived structural features act as pathways for ascending fluids through the crust, with ore systems being developed preferentially in second- and third-order structures within damage zones of misalignment and relay zones (Goldfarb *et al.* 2001a, b; Hodgson 1989, 1993; Cox 1999; Cox *et al.* 2001).

As no known gold mineralisation is present to be investigated structurally within the study region, is it impossible to delineate certain structural trends and stages of deformation as more perceptible for gold mineralisation than others.

In general, structural lineaments from shear zones, faults and thrust zones are distinct and laterally continuous signatures that are often identifiable in magnetic data. However, the large topographical variability in parts of the study area with deep fjords and steep high cliff-walls/mountains influence the data quality and can introduce artificial lineaments in the data. We have tried to consider this in the processing scheme for the potential field data. Further investigations are required to reduce the impact of the topography by using more advanced methods.

First order lineaments are picked manually from an investigation of higher-resolution aeromagnetic data; this proxy is referred to as “1st Structures” (code P1b; see Table 3. Second- to third-order structures are determined from the aeromagnetic data by means of a processing scheme for automated lineament detection and are referred to as ”2nd/3rd structures” (code P2; Table 3). The processing of these proxies is described in the section “Detection of lineaments from regional airborne magnetic data (Pb1, P2, T1, T2)” starting on page 65.

Table 3. *Overview of the mineral system component: Active Pathways. The short names (in bold) and, in some cases abbreviated short names (in bold and brackets), for the different proxies are given in the column for ‘Proxies’. These are used throughout the report – in some cases together with the numeral “Code” of the concerned proxy.*

		Mineral System Component: Pathways				
		Process	**Targeting element**	**Proxies**	**Description**	**Code**
Scale	**Regional**	**Faulting I**	First order fault/shear zones – regarded as pathways for mineralizing fluids	Fault/shear/lineament zones derived manually from aeromagnetics **“1st order structures”**	Calculation of distance (m) from 1st order lineaments as determined from the aeromagnetic data picked manually (TMI and 1st vertical derivative after reduction-of-pole).	P1b
	District	**Faulting II**	Second and/or third order fault/shear zones – regarded as pathways for mineralizing fluids	Fault/shear/lineament zones derived from automatic lineament detection on aeromagnetics **”2nd/3rd order structures”**	Calculation of distance (m) from 2nd and 3rd order lineaments as determined from the aeromagnetic data by means of a processing scheme for automated lineament detection.	P2
	Prospect	**Interface complexity**	Lithological interfaces – regarded as pathways for mineralizing fluids	Interfaces between different lithological units create a pathway **”Lithological units interface complexity”** **[”Litho. Interface complex.”]**	Number of interfaces within a certain cell size; Determine first the number of geological interface in a 5 x 5 km raster. Because information exists only in non-ice covered onshore regions, a kriging interpolation is performed afterwards to have more spatially uniform information that cover also neighboring fjord regions, offshore regions and ice regions.	P4

The 1st- and 2nd/3rd-order structures are regarded as being detectable from these geophysical data at a district to regional scale (see Table 3). At a local scale, e.g. prospect scale, pathways for fluid flow, could be enhanced at interfaces between different lithological units. As a proxy for this, the interfaces of different lithological units in the 1:500 000 geological map (Stensgaard *et al.* 2016) were extracted and the number of interfaces within cell-sizes of 5×5 km was calculated. This proxy is referred to as ”Lithological units interface complexity” (code P4; see Table 3). The processing of the proxy is described in section “Rock unit interfaces complexity (P4)” on page 47.

Proxies for physical traps / throttles

‘Physical Traps’ are physical settings or environments, into which the fluids originating from the ‘Source’ and ascending through the ´Pathways´, are throttled and focused. Fluids migrate into dilatational zones with fracture–related higher permeability. Such zones could at various scales, be related to high intensity structural damage zones, intersection of different structures or other features, crustal complexity/variability, permeability barriers, competency contrast and kinematic conditions (Wyborn *et al.* 1994; Cox *et al.* 2001; McCuaig *et al*. 2010; Joly *et al.* 2012; 2013).

At large-scale, major structures intersecting each other are thought to represent physical traps/throttles for fluids. Cross-cutting structures from the manually picked 1st order structures picked from the aeromagnetic data (proxy code Pb1; see Table 2) are identified in a GIS operation. A grid is created including the distances from these intersections. This proxy is named ”Structural intersection” (proxy code T1; see Table 4).

Second- to third-order structures intersecting with boundaries of lithological rock units are thought to provide another possible physical trap/throttle for fluids. As the interfaces of different rock units by different rheological competency already pose a contact of possible fluid flow or trapping, intersecting structures are in many cases enhance the focus and permeability. These intersections are determined from the automatically picked lineaments in the processed aeromagnetic data (proxy code P2; see Table 2) and the mapped rock units interfaces from the 1:500 000 geological map (Stensgaard *et al.* 2016). The number of intersections of structures with rock unit interfaces is calculated in a 5 x 5 km grid. This proxy is named “Structures crossing lithologies” (proxy code T2; see Table 4).

Bending on structural features may also pose a structural trap and throttle for the mineralizing fluids. The bending is determined for the structures extracted from the 1:500 000 geological map. The structures are segmented into lineaments by a 5 x 5 km grid. The bending (expressed as sinuosity) of the lineaments is then determined. The resulting proxy is named “Structural bends” (proxy code T3; see Table 4).

The number of structures in an area is also believed to be an indirect indicator of physical traps and throttles for fluids. A high number of structures in an area increase the permeability and a higher number of traps are present. The number of structures extracted from the 1:500 000 geological is determined on a 5 x 5 km grid. The resulting proxy is named “Structural complexity” (proxy code T4; see Table 4).

Table 4. *Overview of the mineral system component: Physical TrapThrottle. The short names (in bold) and, in some cases abbreviated short names (in bold and brackets), for the different proxies are given in the column for 'Proxies'. These are used throughout the report – in some cases together with the numeral "Code" of the concerned proxy.*

		Mineral System Component: Physical Trap/Thottle				
		Process	**Targeting element**	**Proxies**	**Description**	**Code**
Scale	**Regional**	**Enhance permeability, locus of**	Structure intersection	Cross-cutting structures from manually determined faults (P1b) from geophysics (distance from intersections) **"Structural intersection"** **[Struc. intersect.]**	Distances from intersections of manually derived structures from aeromagnetics; the intersections of the manually determined 1st-order lineaments from the aeromagnetic AEROMAG dataset are determined. Then a grid is created including the distances (m) from these intersections.	T1
	District		Structure intersection with lithostratigraphy interface	Structures intersecting with interfaces between different lithological units – locus of mineralisations **"Structures crossing lithologies"** **["Struc. X-ing litho."]**	Number of intersections of automatically picked lineaments from processed aeromagnetics with geological units; determine first the number of intersections of lineaments (manual lineaments from AEROMAG) with different lithostratigraphic interfaces in a 5 x 5 km raster. Because information exists only in non-ice covered onshore regions, a kriging interpolation is performed afterwards to have more spatially uniform information that cover also neighboring fjord regions, offshore regions and ice regions.	T2
			Major bends of structures	Curvature/bending on structures – locus of mineralisations **"Structural bends"** **["Struc. Bends"]**	The degree of bending of structures from the geological map (1:500 000) within a certain cell size; first structures are fragmented into sub-structures by using a 5 x 5km raster; then the bending (sinuosity: a straight line has a value of 1, but a very bended one is converging towards 0) of the sub-structures is determined and assigned to their midpoints. Because information exists only in non-ice covered onshore regions, a kriging interpolation of the midpoints is performed afterwards to have more spatially uniform information that cover also neighboring fjord regions, offshore regions and ice regions.	T3
			Structural complexity	Number of structures in an area; the higher the more favorable for the locus of mineralisation **"Structural complexity"** **["Struc. Complex"]**	Number of structures from the 1:500 000 geological map within a certain cell size; the higher, the more favorable for the locus of mineralisation; The numbers of structures are determined on a 5 x5 km raster. Because information exists only in non-ice covered onshore regions, a kriging interpolation is performed afterwards to have more spatially uniform information that cover also neighboring fjord regions, offshore regions and ice regions.	T4
	Prospect		(none)	-	-	-

Proxies for chemical traps / chemical scrubber

Regional and detailed stream sediment geochemistry are traditionally considered one of the targeting tools for gold mineralisations as elevation of certain characteristic geochemical elements reflects hydrothermal mineralising fluids as well as their associated alteration halos (e.g. Robert *et al.* 2007). In Greenland, characteristic elements in regional stream sediment geochemistry have been found that indicate elevated gold mineralisation potential (see e.g. Steenfelt 2000; Stensgaard *et al.* 2005; Stensgaard & Steenfelt 2007). Regional stream sediment geochemistry sampling has been carried out recently for the entire study area in South-East Greenland (see e.g. Stensgaard *et al.* 2010; Kolb *et al.* 2016).

Elevated to high content of elements as e.g. Au, As, Sb, Cs and Ni/Mg ratio are found to be indicative and associated with hydrothermal (mesothermal) orogenic type gold mineralisation. Elevated anomalous high gold concentrations in stream sediment geochemistry can in most cases be directly related to a geological setting, e.g. a gold occurrences that are elevated in this element. Arsenic (As), antimony (Sb) and caesium (Cs) are all characteristics pathfinder elements for gold mineralisation in which they, together with gold itself, may reflect the hydrothermal fluids and processes that are leading to their enrichments and the alteration of the country rocks that are associated with these processes. Caesium may be considered as a pathfinder element for gold mineralisation associated with granite-related hydrothermal alteration (Steenfelt 2000). Although perhaps more variable than the previous introduced elements, also W, Mo and Bi are geochemical elements that characterise hydrothermal orogenic gold mineralising systems. These are, as Cs, perhaps also more indicative for gold mineralisation associated with granite-related hydrothermal alteration than the others. In studies from the Archaean terranes in the Nuuk fjord region in southern West Greenland, the Ni/Mg ratio has found to be indicative for gold mineralised areas. The nickel enrichment was attributed to sulphide mineralisation and to calc-silicate alteration in which Ca replaces Mg and Fe. Thus, the increase in the Ni/Mg ratio was suggested to be an indicator for alteration/mineralisation that has been sufficiently widespread to leave an imprint on the stream sediment geochemistry (see Stensgaard *et al.* 2005; Stensgaard & Steenfelt 2007). Distributions of stream sediment geochemistry for Au, As, Sb, Cs, Bi, W and Mo as well as Ni/Mg are used as direct proxies for 'Geochemical Trap / Throttle / Scrubber'. These proxies are named by the element/ratio followed by "– SS" (SS = stream sediment; proxy code T3a to T3g and also T3i; see Table 5).

The typical associated host rocks in high-grade metamorphic terrains are considered to be typically mafic to ultramafic, although this is a very generalised (and debated) view of the real processes. This may be caused by the characteristics of these rocks having, relative to granitic rocks and many sedimentary rocks, a higher concentration of cations (Fe, Mn, Mg, Ca) and hereby a better potential to enhance the alteration processes that lead to the gold deposition (Kerrich & Fyfe 1981). Also, in the so-called metamorphic source model for orogenic gold type mineralisation (Powell *et al.* 1991; Phillips & Powell 2009, 2010; Wilson *et al.* 2013) it is suggested that hydrated mafic rocks are the source for fluids and gold. However, it has been shown that metamorphism of pyritic carbonaceous sedimentary rocks is also able to generate even more fertile fluids than the mafic rocks (Tomkins 2010). As a proxy for the above rock types the mafic (meta-volcanic), supracrustal-mica schist (meta-sedimentary) and carbonate (marble) rock units have been extracted from the 1:500 000 geological map of South-East Greenland (Stensgaard *et al.* 2016). These proxies are named "Mafic units", "Suprac. units" and "Marble units" (proxy codes T1a, T1b and T1c;

see Table 5). As a proxy for the lithological diversity, variability and complexity the number of different rock units within an area is determined. This proxy is named “Geological Complexity” (proxy code T1e; see Table 5).

Another utilised proxy for these rocks is mineral indices of mafic minerals and carbonate minerals rocks from processed satellite ASTER data. Quartz is almost an universal mineral of orogenic gold mineralisation and the mineral index for quartz (silica) has also been included for reflecting ‘Geochemical Trap’. However, it is acknowledge that the thermal-infrared sensor data from the ASTER data only provides a resolution of 90 m and that it is not able to distinguish between hydrothermal silica and siliceous lithologies. On the other hand, siliceous lithologies in the area may also be related to lithologies that could reflect more favourable conditions for the formation of gold, e.g. silica-rich granitic intrusions or siliceous metasedimentary units. These proxies are named “Mafic index”, “Carbonate index” and “Silica index” (proxy codes T2a, T2b and T2c; see Table 5).

Table 5. *Overview of the mineral system component: Chemical Trap/Throttle/Scrubber. The short names (in bold) and, in some cases abbreviated short names (in bold and brackets), for the different proxies are given in the column for 'Proxies'. These are used throughout the report – in some cases together with the numeral "Code" of the concerned proxy.*

		Mineral System Component: Chemical Trap / Throttle / Scrubber				
		Process	**Targeting element**	**Proxies**	**Description**	**Code**
Scale	**Regional**		(none)	-	-	-
		Chemical anomalous area	Geochemistry signature regarded favorable or indicative for mineralization "XX – SS"	Au **"Au – SS"**	Stream sediment geochemistry anomalies; To get uniform information in the area of interest, stream sediment data from all considered elements are interpolated using kriging.	T3a
				As **"As – SS"**		T3b
				W **"W – SS"**		T3c
	District			Mo **"Mo – SS"**		T3d
				Sb **"Sb – SS"**		T3e
				Cs **"Cs – SS"**		T3f
				Bi **"Bi – SS"**		T3g
				Ni/Mg ratio **"Ni/Mg – SS"**		T3i
		Chemical favorable or reactive host I	Chemical favorable host rock to mineralisation	Mafic units **"Mafic units"**	Extract polygons of the rock units from the geologically map; afterwards calculate the distances from the rock units	T1a
				Supracrustal-mica schist **"Suprac. units"**		T1b
				Marble **"Marble units"**		T1c
				Geological complexity **"Geological Complexity"** **["Geo. complex"]**	Determine the number of geologic units (change from one to the next geologic units) from the geologic map on a 1 x 1 km raster; Because information exists only in non-ice covered onshore regions, a kriging interpolation is performed afterwards to have more spatially uniform information that cover also neighboring fjord regions, offshore regions and ice regions.	T1e
		Chemical favorable or reactive host II	Chemical favorable hosts	Mafic index from ASTER data **"Mafic index"**	Mineral indices from processed ASTER data; Because ASTER data are not available at the close-by offshore areas and ice-covered areas, the ASTER data are interpolated using kriging. (Due to computational limitations, it has been required to reduce the number of points by 90% before the interpolation is performed.)	T2a
				Carbonate index rom ASTER data **"Carbonate index"**		T2b
				Silica index rom ASTER data **"Silica index"**		T2c
	Prospect		(none)	-	-	-

Step 3: Fuzzification

In a classical theory of sets, the membership functions of a component of a set (i.e. the evidential variables in the form of evidential datasets) are expressed as true or false (one or zero).

In the theory of fuzzy sets (Zadeh, 1965; An et al 1991) which is used in this work, the fuzzy membership function is defined on a continuous scale from true (full membership represented by a value of “one”) to false (full non-membership represented by a value of “zero”). The fuzzy set theory is an approach that handles uncertainty in datasets fundamentally differently from the traditional probabilistic and statistical approaches. By using the fuzzy logic, a spatial set of data can be represented in a map according to its fuzzy membership degree. The degree is expressed by using a **membership function.** The membership function “translates” the “real” values of the original evidential maps of the proxies to fuzzy values from 0 and 1. By assigning a continuous scale from true to false to the datasets is it possible to manifest the expert opinion on the importance of various ranges of the data (e.g. the expert’s opinion on the importance for a given challenge on being near, middle or a long distance from a fault). Another benefit from transferring the datasets into one common scale is that is makes it possible to integrate the different datasets. Fuzzy membership function could be expressed as linear, nonlinear, continues, discontinues analytic functions or by using numerical tables. The process of transforming the evidential maps into a representation of a fuzzy membership function is sometimes referred to as **fuzzification**.

The fuzzy membership functions enable the expert (the geologist) to transfer their expert knowledge and experience as well as their opinion on the uncertainties associated with the datasets. In the case of mineral potential the goal could be the *“definition of favourable location for mineralisation”* (Nykänen *et al.* 2008). Or rephrased; how well and when (at what values/which values) does the data indicate a favourable location for orogenic gold.

In this work, the membership functions named ‘Small’ and ‘Large’ in the ArcGIS™ menu have been used in the fuzzification (described in the section ‘Step 3: Fuzzification of evidential maps’ on page 91). The resulting fuzzified evidential maps and datasets are referred to as ‘fuzzy evidential maps’ or ‘fuzzy datasets’, respectively.

Step 4: Fuzzy integration

Fuzzy logic is based on the fuzzy set theory (Zadeh 1965) and has been used for mineral prospectivity mapping in an number of studies (e.g. Knox-Robinson 2000, Carrenza & Hale 2001, Luo & Dimitrakopoulos 2003; Porwal *et al.* 2003, Harris & Sanborn-Barrie 2006, Nykänen *et al.* 2008, Joly *et al.* 2012, 2013).

Five different arithmetic operators, or combinations of the operators, are generally considered to be useful for combining fuzzy datasets since they can reflect relative relevance of the datasets and, hence, provide an appropriately manner to integrate them in a fuzzy logic such that can finally mimic conceptualised models of interplaying geological process involved in the mineral system (Carrenza 2009).

The fuzzy operators that are commonly used are: Fuzzy AND, Fuzzy OR, Fuzzy algebraic product, Fuzzy algebraic sum, and Fuzzy gamma (γ) (An et al 1991; Bonham-Carter 1994).

The different operators integrating the different fuzzy datasets will form a fuzzy **inference network** that should constitute series of logical rules that sequentially combine the evidential maps. The interference network can also act to filter effect of ambiguous evidence.

The fuzzification and fuzzy integration were carried out using the ArcGIS™ extension toolbox “Spatial Analyst”.

Step 2: Used datasets, processing and resulting evidential maps

All data used in prospectivity analysis have to be presented in meaningful evidential maps. This is a challenge, because data are available in very different types: Stream sediment data are for instance point data, but remote sensing and geophysical data exist as grids in raster format with uniform coverage. In addition, the coverage of the individual datasets is not everywhere overlapping (e.g. geological information and remote sensing data exist only in the ice-free land region, but geophysical data are available also from the adjacent inland ice region and offshore regionsregion; the geological mapping has not everywhere the same detail; see Fig. 8). Consequently, it is important 1) to define an adequate region that is acceptably well-covered by all type of data/information, and 2) to find appropriate strategies to make grids from all data overlapping in this area.

The initial representation of the different data (e.g. made during gridding) should take into account all the available data (e.g. regional gravity data point outside of the main study area is also taken into account in the initial gridding). This means that after the initial gridding, the resulting data representation has to be evaluated and non-reliable and/or sparse in data coverage have to be excluded in a second step.

As the ‘initial study area’ a larger area was chosen, whose boundaries are outlined by red-colours in Fig. 8. All data was initially gridded to fill out this area, whether or not data coverage extended across the complete area or only covered parts of this area. The resulting data representation (both the raw, extracted information and the resulting gridded evidential maps) were subsequently evaluated according to data coverage, the obtained results and the reliability. In accordance with this evaluation, it was chosen to use the extent of the AEROMAG surveys plus a 10 km buffer zone surrounding the surveys as the targeting area for the prospectivity analysis (see green-coloured boundary in Fig. 8). Except for structural information from the digital geological map that is missing in the area north of the Sermilik, all datasets show at least some data coverage in all parts of the investigation area.

Because some datasets are sparsely spatially distributed as sampling points (e.g. stream sediments),) and because much information (e.g. remote sensing, geology) is restricted to the partly very narrow ice-free land region intersected by many fjords, there is a need for an interpolation method that reliably grid data in areas that have no or a low and/or irregular data coverage to create proper evidential maps. Kriging is based on the statistical assumption that the spatial relations of data can be properly described by a semi-variogram model (e.g. Dubrule 2003); it is a well-established interpolation method for irregular distributions of data points and for extrapolation in regions with sparse data coverage. To perform the kriging, we use for all data the ArcGIS function “Kriging” with a spherical semi-variogram model (see Fig. 9). The output sampling of the grids varies for different measures between 100 m and 2000 m dependent on the amount of available data.

However, kriging is not the interpolation method that provides the most appropriate results, if data-sampling is dense and homogeneous in a region. A number of data sets (e.g. the indices from the ASTER satellite data and parameters that are derived from the digital geological maps) show such a dense and uniform data coverage and therefore we decided to apply natural neighbour interpolation to these data to create a second set of grids as evidential maps for the associated criterion/proxy elements. Natural neighbour interpolation is based on a weighted sum of values from nearby points (by using surface contributions of Voronoi cells after Delaunay triangulation, Sambridge *et al.*,1995) and is known to provide accurate estimates where a dense and uniformly covered sampling exists. In contrast, results from natural neighbour interpolation are non-reliable in regions sparsely or not-covered with data and here results from kriging is considered as superior.

In our case, this means that natural neighbour gridding provides better estimates for densely sampled datasets in the onshore ice-free areas; but estimates 1) from the same datasets in the nearby fjord, coastal and ice-covered regions and 2) from generally sparse and ununiformed distributed datasets (e.g. stream sediments) in the whole region of interest are considered as less appropriate.

In summary, we apply the kriging to all data sets that have to be gridded and create a second version of grids for datasets that show a dense coverage in the accessible ice-free land area by using natural neighbour interpolation (data from ASTER satellite and information directly extracted from the geological map). However, for datasets having an irregular spatial coverage (e.g. stream sediments), we consider grids from natural neighbour interpolation to be less appropriate and did not generate them. This means that partly different versions of evidential maps will be created (see figures in this section and Appendix B) resulting in different versions of prospectivity maps (see section “Resulting fuzzified, intermediate maps and prospectivity maps”). We will see by means of the final results that the choice of the interpolation method not is an unimportant technical detail, but has a rather large impact onto the final outcome in prospectivity mapping.

Although the natural neighbour interpolation has no inherent limitation in the size of the gridding interval, the employed ArcGis routine limited us to use grid intervals of 3000 m; the actual reason for this restriction of ArcGIS is unknown.

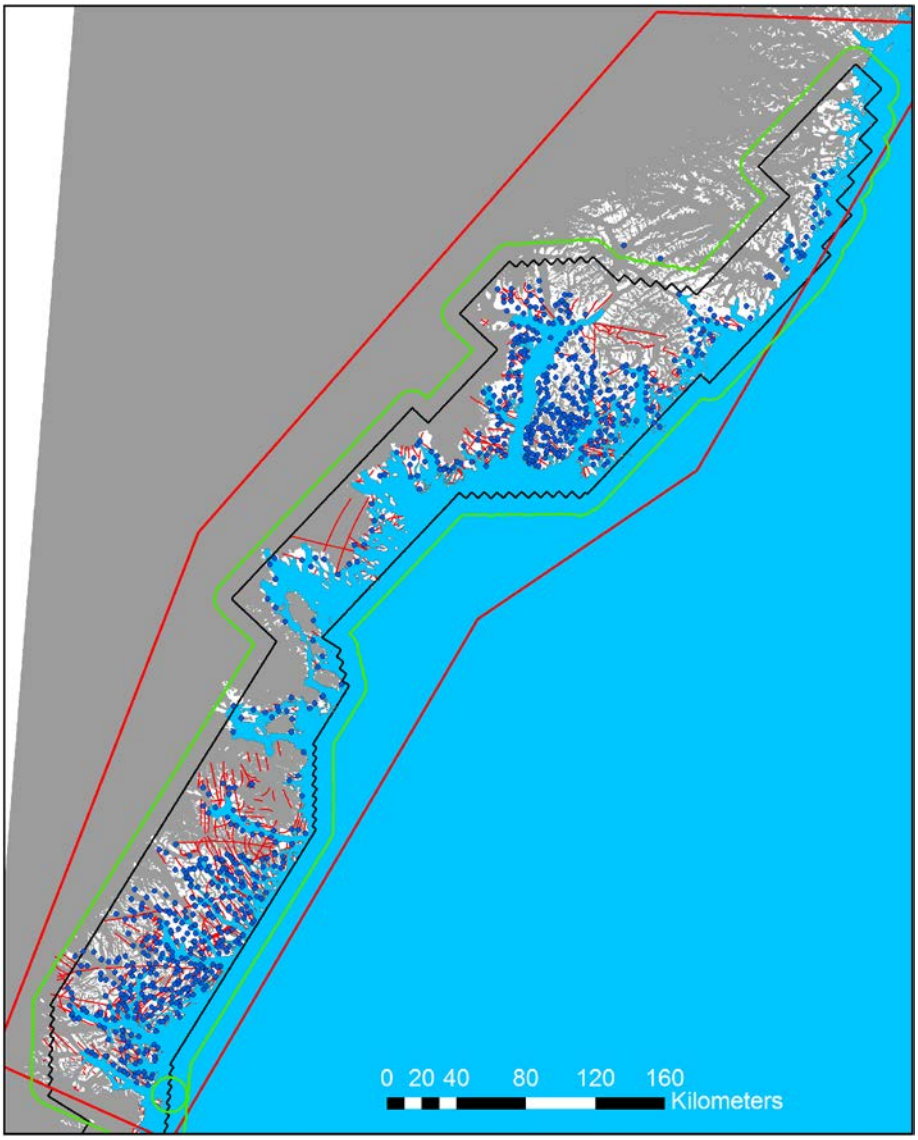

Figure 8. *Distributions of different types of data used in the prospectivity analysis. The black line outlines the surveying area of the AEROMAG surveys. The blue dots show the locations, where the used stream sediment samples are taken. Structures and lineaments from the 1:500 000 geological map (Stensgaard et al. 2016) are presented as red lines; note that no structures occur north of the Sermilik Fjord; this is partly, because this area is little visited and not well mapped. Remote sensing data and other geological information is limited to the ice-free on-shore region (white color). Based on an evaluation of all these available data and their reliability according to data coverage and resulting data representation in the evidential maps, a study area was chosen – which is outlined by the green-colored boundary in the map. This green-colored boundary corresponds to the blue-colored boundary, which is the extent of the AERO-MAG surveys plus a 10 km buffer zone in addition. The red-colored outline shows the 'initial study area' for which all data were gridded, both when data coverage extended outside of this area and when only parts of the 'initial study area' are covered. The data representations for this area (i.e. grids) were subsequently evaluated according to resulting reliability of the data-representation.*

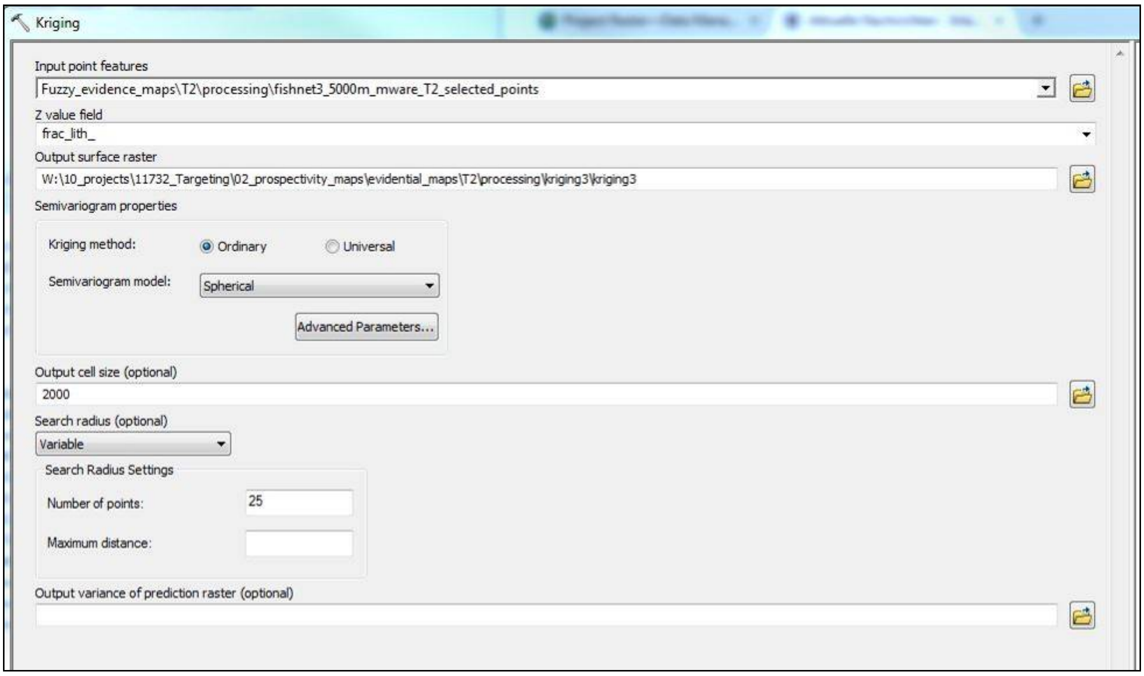

Input point features
Fuzzy_evidence_maps\T2\processing\fishnet3_5000m_mware_T2_selected_points

Z value field
frac_lith_

Output surface raster
W:\10_projects\11732_Targeting\02_prospectivity_maps\evidential_maps\T2\processing\kriging3\kriging3

Semivariogram properties
Kriging method: ● Ordinary ○ Universal
Semivariogram model: Spherical

Output cell size (optional)
2000

Search radius (optional)
Variable

Search Radius Settings
Number of points: 25
Maximum distance:

Output variance of prediction raster (optional)

Figure 9. *Snapshot of the ArcGIS "kriging" tool. Parameters are shown that are used for the kriging of the intersections of structures from aeromagnetic data with lithological units (see Fig. 17) for the evidential map T2.*

Another challenge is that there are significant topographic undulations in large parts of Southeast Greenland (Fig. 10). Several of the datasets used to make the evidential maps are affected by variations in the topography (e.g. bending of structures extracted from the digital geological map - T3 - and anomalies in the aeromagnetic data - P2 -) resulting in some bias in the targeting procedure.

To reduce the impact of topography on evidential maps created from aeromagnetic data, we modified the automated detection procedure used to identify second order lineaments from this type of data (see section "Detection of lineaments from regional airborne magnetic data (Pb1, P2, T1, t2)"). However, these modifications are not optimal yet and all erroneously identified lineaments associated with strong topography variations should be removed. This means for future studies that additional research is required to find processing strategies that minimize the impact of the topography in aeromagnetic data.

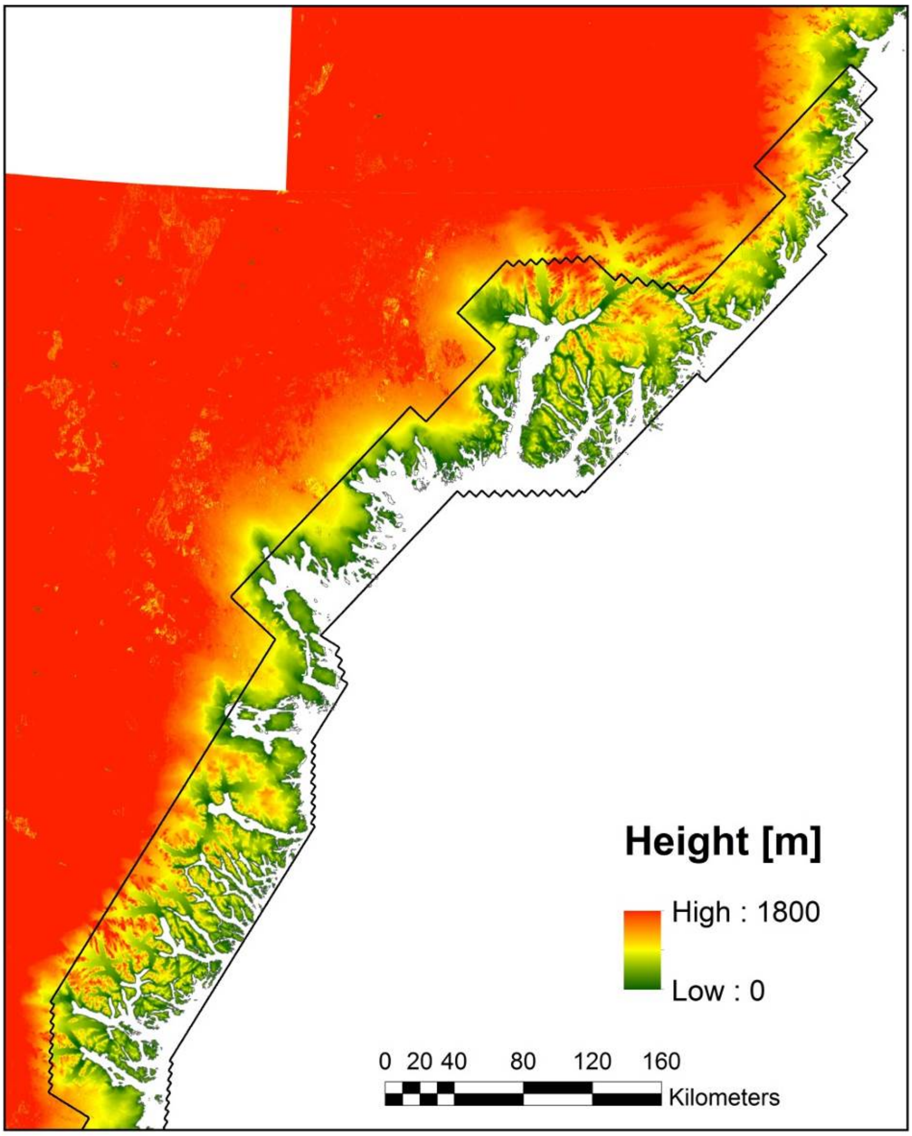

Figure 10. *DEM from ASTER satellite data. The black line outlines the area of the aeromagnetic surveys.*

Geological data

1:500 000 geological map

The digital GIS version of the 1:500 000 scale geological map (Stensgaard *et al.* 2016; Kolb *et al.* 2016), which is based on a revision of the published 1:500 000 scale geological map of South-East Greenland (Escher 1990) is used as the geological background for this study (Fig. 11). The lithological rock units and their outline were involved to create different evidential maps (proxy code numbers S2, P4, T2, T3, T4, T1a, T1b, T1c and T1e in Table 2 to Table 5).

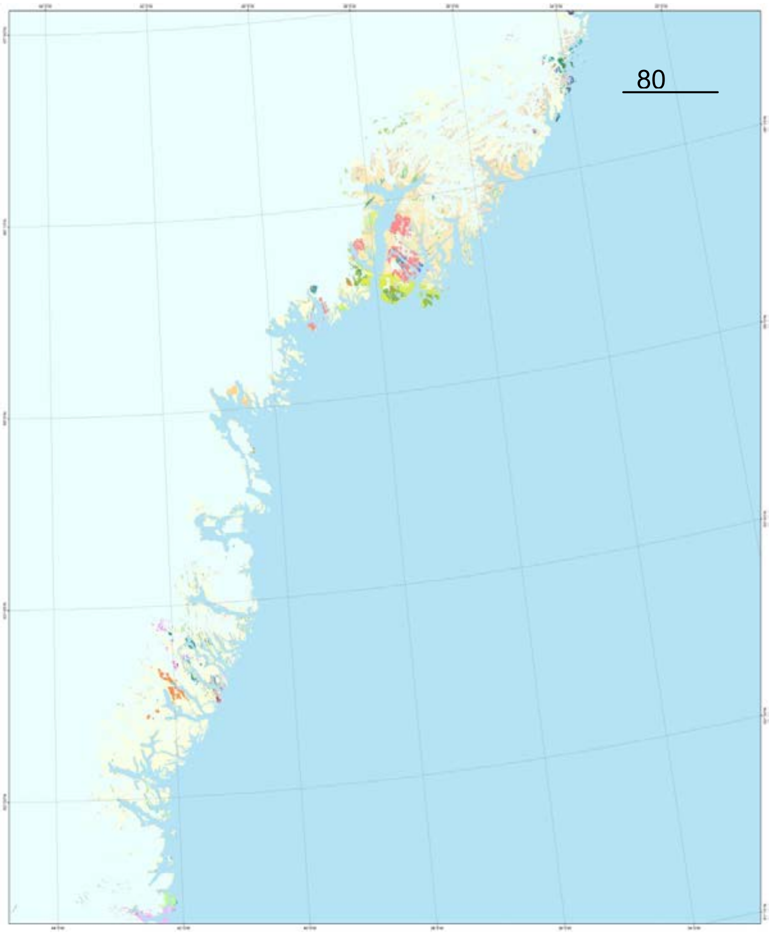

Figure 11. *Revised geological 1:500 000 scale geological map of South-East Greenland, which is used as a geological input to the construction of various evidential maps. For details, legend and description please refer to Stensgaard et al. 2016 and Kolb et al. 2016.*

Distribution of specific rock units (T1a, T1b, T1c)

A simple enquiry based on the polygon attribute information on the rock units in 1:500 000 digital geological map was used to extract supracrustal, mafic and marble rock units (Table 6). These extractions (Fig. 12) are used for the targeting elements T1a, T1b and T1c (see Proxies for Table 5)   by considering the distances from these units (Fig. 13) in the determination of the associated evidential maps.

Table 6. *Polygon attributes included in the different classes of extracted rock units (see Stensgaard et al. 2016).*

Rock units	Attributes (GM Label) of rock units included from the 1:500 000 geological map
Supracrustal	ms_s; ss
Mafic	a_k; an_s, delt_w, ga_s. gad_s, msa_s, ub. msa_s
Marble	c_s

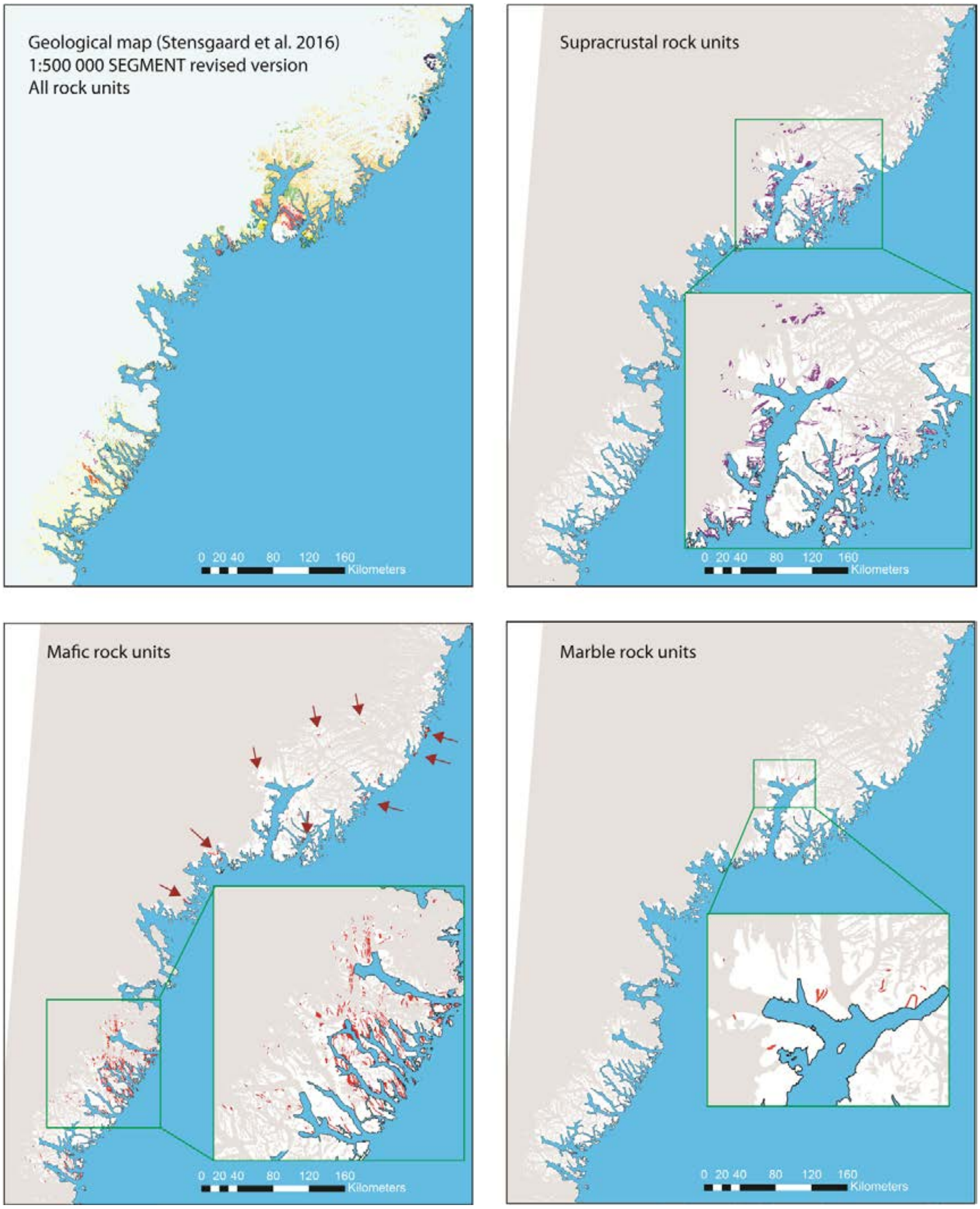

Figure 12. ***A.*** *1:500 000 digital geological map of the study area (Stensgaard et al. 2016).* ***B., C.*** *and* ***D.*** *are extracted supracrustal, mafic and marble rock units, respectively.*

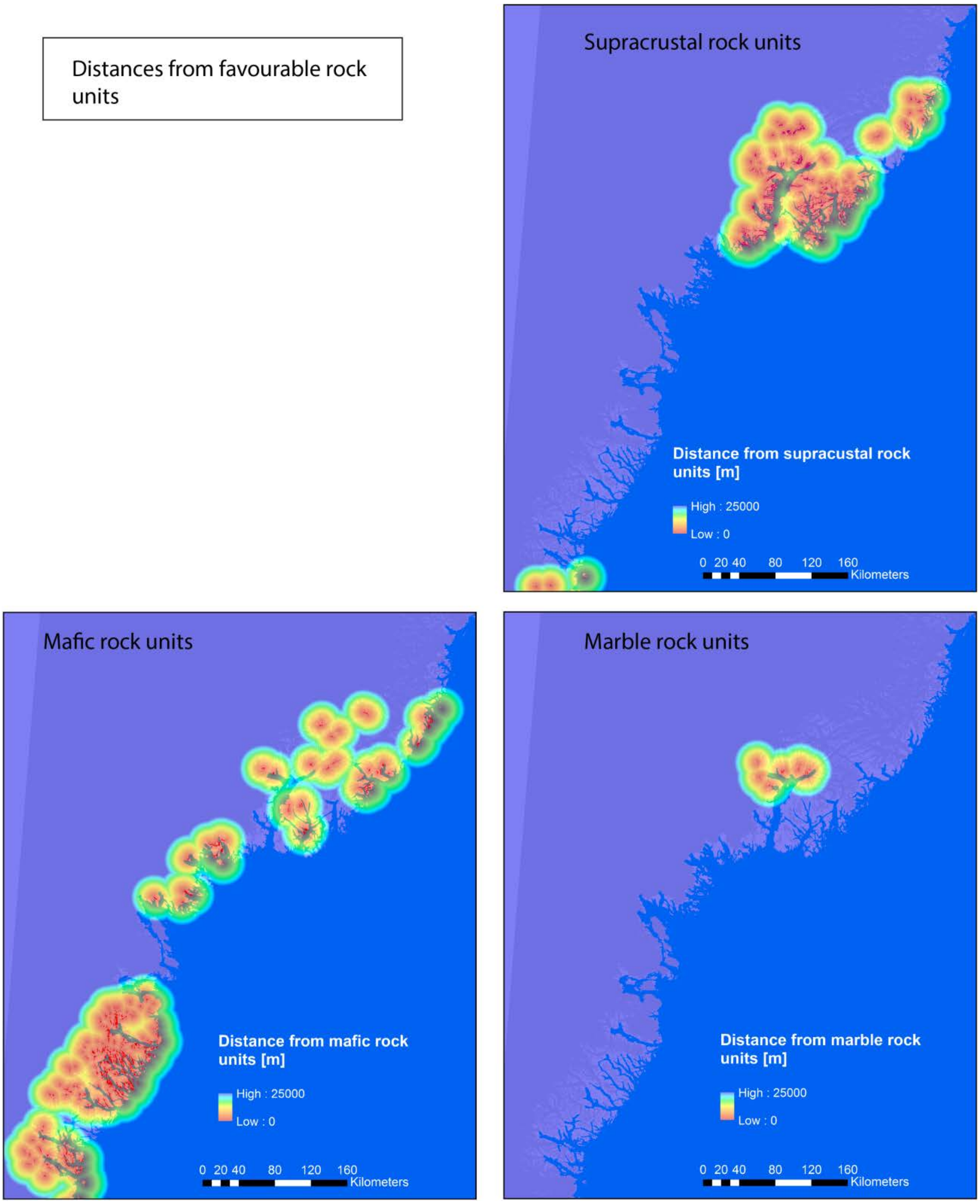

Figure 13. *Distances from favorable rock units (supracrustal rocks, mafic rocks and marble rocks) shown in Fig. 12. These distances are used for the criteria/proxy elements T1a, T1b and T1c.*

Distribution of intrusions (S2)

Intrusions are selected from the 1:500 000 digital geological map. Spatial polygons with attribute information from rock units that are associated with intrusions (Fig. 14a) are used to estimate the source areas for fluids and metals (targeting element S2; see Table 2). The associated evidential map is determining by considering the distances from these polygons (Fig. 14b).

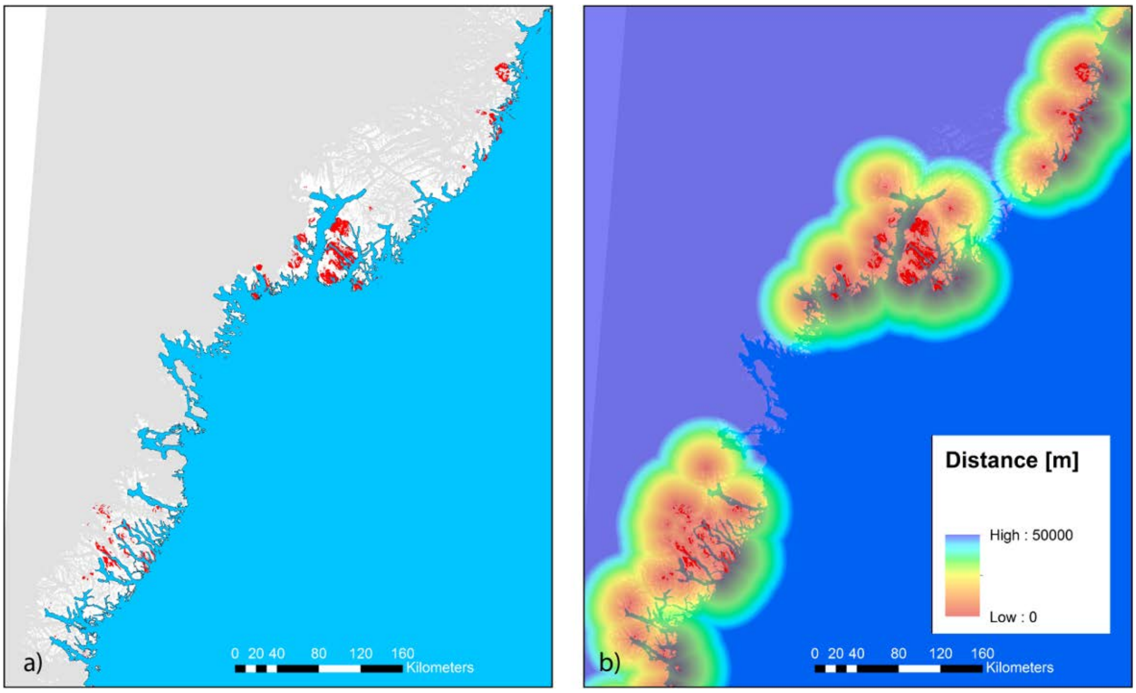

Figure 14. ***A.*** *Intrusions extracted from the1:500 000 digital geological map of the study area (Stensgaard et al. 2016).* ***B.*** *Distances from these intrusions used for the criteria/proxy element S2.*

Geological complexity (T1e)

For receiving a representation of the “geological complexity” used for the targeting element T1e (see Proxies for Table 5), different geological units were extracted from the digital geological map (Stensgaard *et al.* 2016) and the number of layers from these rock units was determined on a grid of 1 x 1 km rectangular cells. If there are two layers of the same rock unit that are separated from each other by another rock unit, they were counted separately. The cell information was then assigned to points that are located at the cell centres (Fig. 15a) to be able to interpolate the data. Two different interpolations were performed to obtain two versions of evidential maps for targeting element T1e. For the first version, interpolation was performed with kriging (Fig. 15b) to extent information to areas that are inaccessible for geological mapping (ice-covered, fjord and offshore areas). For the second version, natural neighbor gridding was performed to get more appropriate and very precise estimates in the uniformly and densely gridded ice-free onshore area (Fig. 107a).

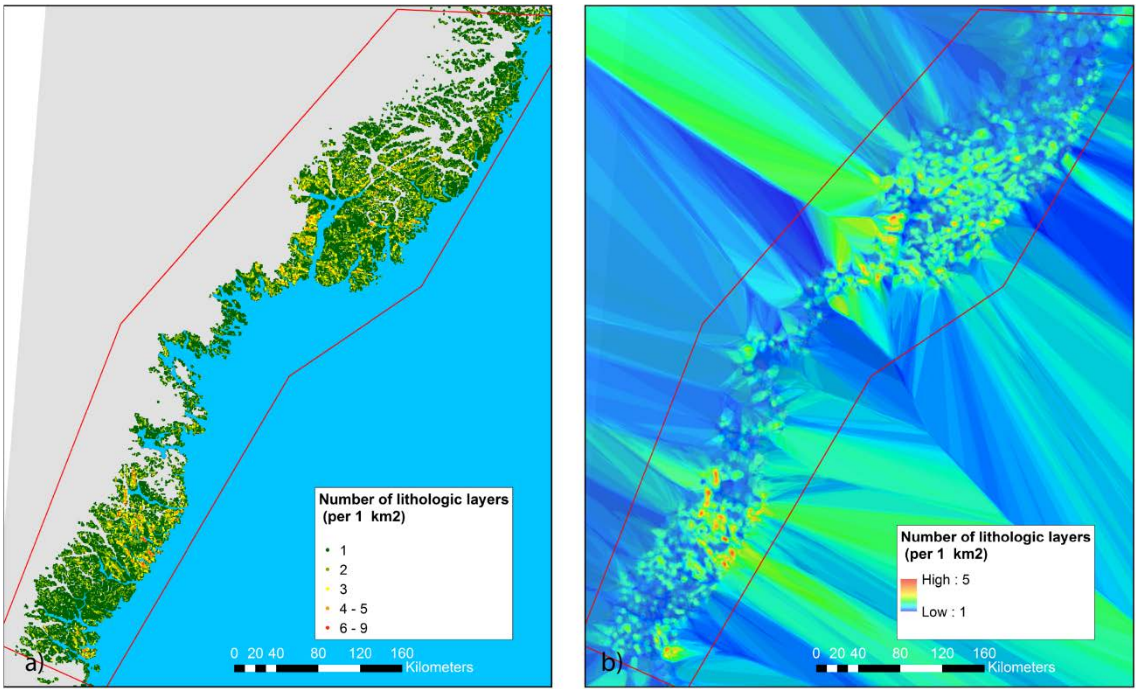

Figure 15. ***A.*** *Number of layers from lithologic units within cells of a 1 x 1km grid. The lithologic units are taken from the digital 1:500 000 geological map of the area (Stensgaard et al. 2016).* ***B.*** *Interpolation of the data in A by using kriging (interpolation parameters are described in section "Step 2: Used datasets, processing and resulting evidential maps"). The red line encompasses the area that is used in probability calculations. The interpolated grid is used for the criteria/proxy element T1e.*

Rock unit interfaces complexity (P4)

For a representation of the "interface complexity" associated with the targeting element P4 (see Table 4), the number of interfaces between different rock units (Fig. 16a) was determined in a grid of 5 × 5 km rectangular cells (Fig. 16b) and then transferred to point information by considering the centres of cells. These point data were then gridded with a kriging interpolation (Fig. 16c) to create an evidential map where information between rock units are extended to "unexposed" areas (as ice-covered, fjord and offshore areas). The interpolation of data points was then repeated with the natural neighbour method to generate a second version of the evidential map for the same targeting element P4 (Fig. 104a). The intention of this second map is to have very accurate data estimates in the ice-free onshore area characterized by dense and uniform data coverage.

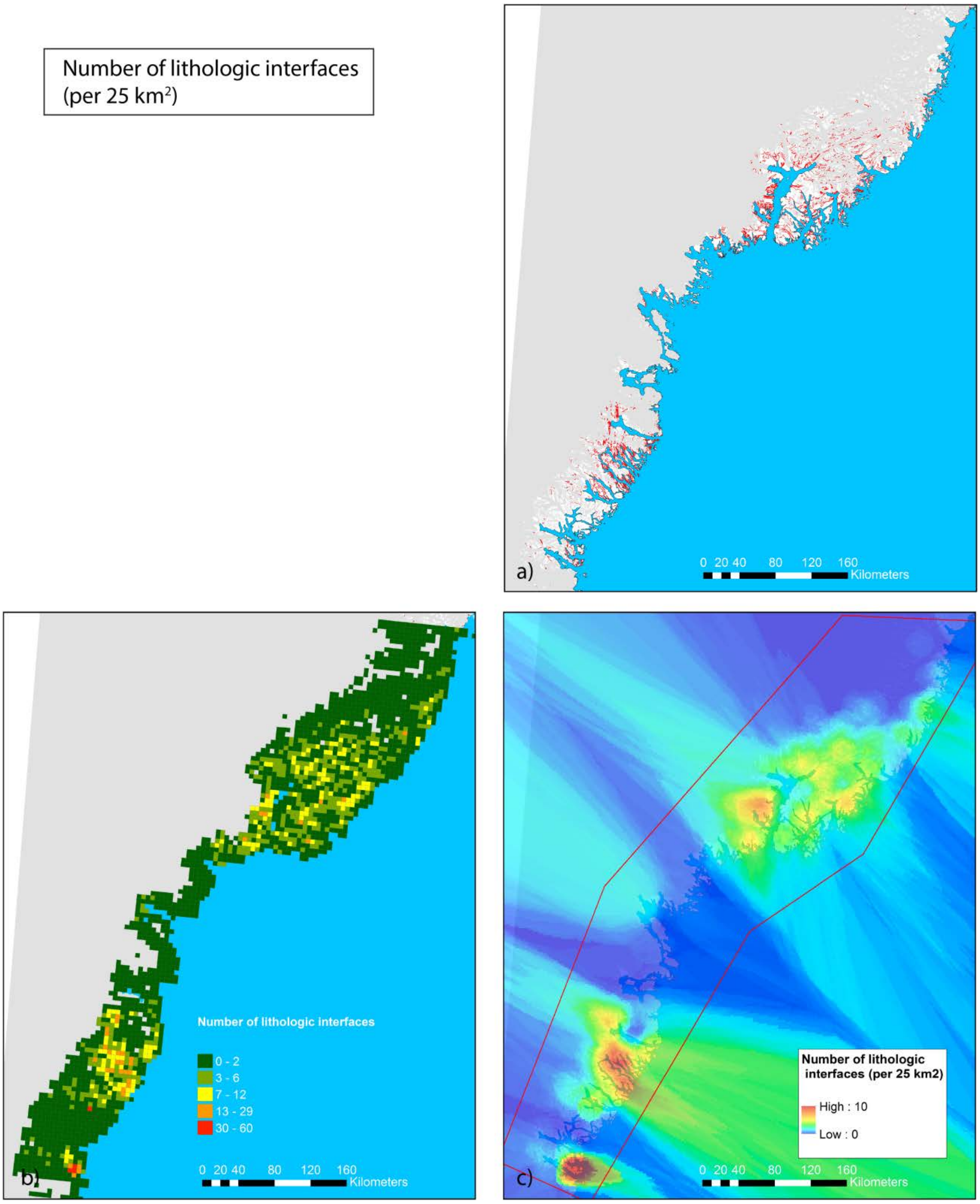

Figure 16. ***A.*** *Boundaries (outlined red lines) of individual rock units in the 1:500 000 geological map.* ***B.*** *Number of interfaces (boundaries between different rock units within cells of 5 × 5 km grid).* ***C.*** *Interpolation of the data in B by using kriging (interpolation parameters are described in section "Step 2: Used datasets, processing and resulting evidential maps"). The red line encompasses the area used in probability calculations. The interpolated grid is used for the criteria/proxy element P4.*

Intersection of structures with interfaces between rock units (T2)

There are different ways to select structures for this targeting element T2 (see Table 4); either using structures presented in geological maps or using lineaments identified in the aeromagnetic data.

Not all areas in Southeast Greenland are mapped with the same detail; particularly in the part north of the Sermilik (66° 30’ N), structural information is completely missing in the digital geological map (see Fig. 18a). Consequently, we decided not to use structural elements from the geological map. Because automated picking of lineaments is, moreover, affected by the topography (see the later section about automated lineament detection from aeromagnetic data), the manual picked lineaments (see yellow lines in Fig. 48 and green lines in Fig. 17a) seem to be more reliable and in this study we choose them as the “structures”.

Intersections of these “structures” and the lithological units (extracted from the digital 1:500 000 geological map) are shown in Fig. 17a as blue dots. The intersections are counted in each rectangular cell of a 5 x 5 km grid (see Fig. 17b) and then two interpolations of the data were carried out. In a first run, kriging interpolation is applied mainly intended to fill up areas not accessible for geological mapping (ice covered areas, fjord and nearby coastal regions; Fig. 17c). Afterwards, we repeated the gridding with the natural neighbor interpolation to obtain a second version of the evidential map, where data estimates are very precise in the uniformly covered ice-free onshore area (Fig. 105a).

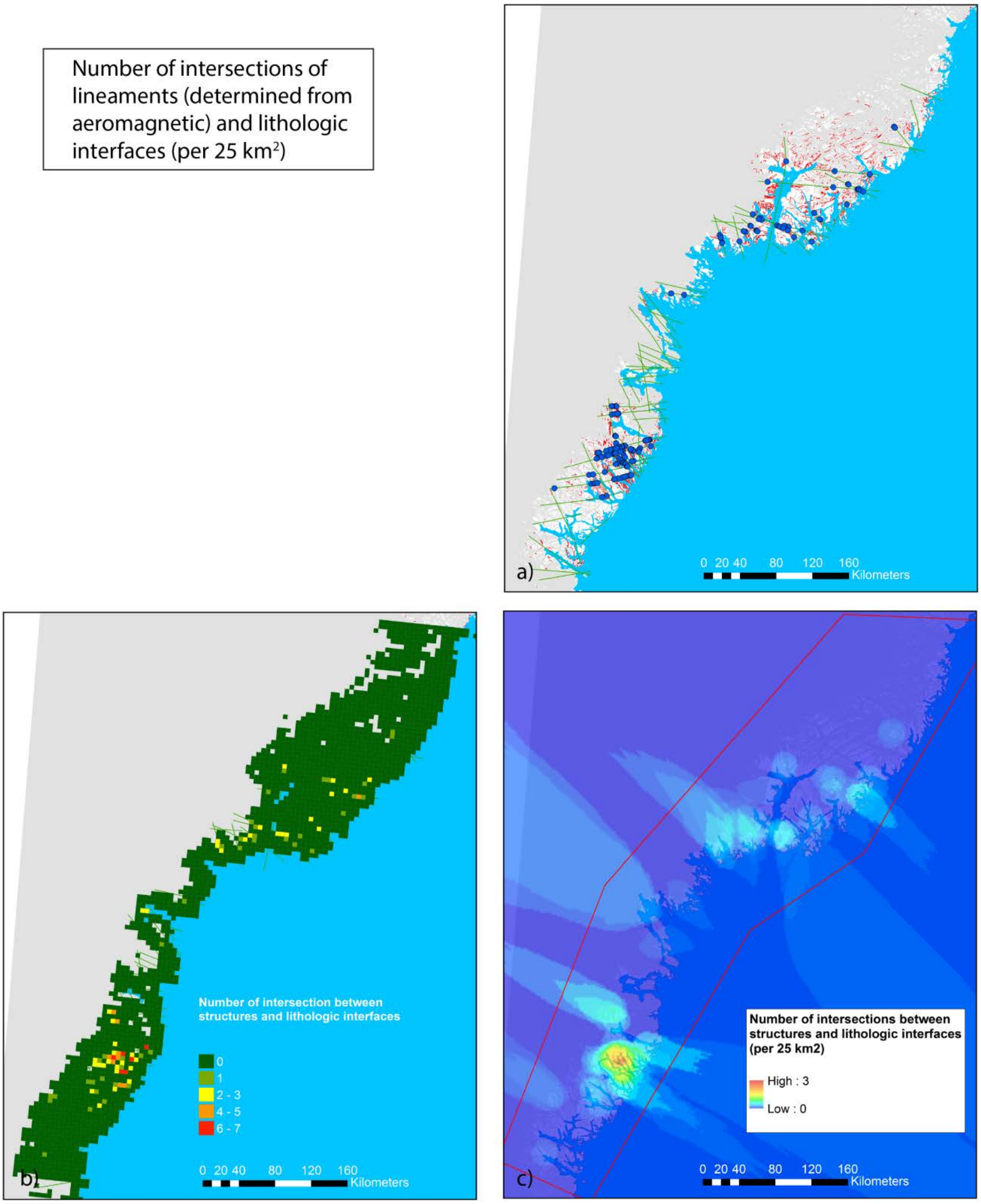

Figure 17. *A.* *Boundaries of individual rock units in the 1:500 000 geological map are shown as red lines. Green lines indicate lineaments that are (manually) identified in the aeromagnetic data (see section" Detection of lineaments from regional airborne magnetic data (Pb1, P2, T1, t2)" for details) and blue dots show locations, where the boundaries intersect with the lineaments.* ***B.*** *Number of intersections within cells of 5 × 5 km grid.* ***C.*** *Interpolation of the data in B by using kriging (interpolation parameters are described in section "Step 2: Used datasets, processing and resulting evidential maps").The red line encompasses the area used in probability calculations. The interpolated grid is used for the criteria/proxy element T2.*

Structural complexity (T4)

The “structural complexity” (targeting element T4; see Table 4) is estimated by determining the density of structural elements. As mentioned in the previous section, the structural mapping has not the same detail and north of the Sermilik (66° 30’ N) no structures are present in the digital geological map (Fig. 18a). This means the resulting evidential map derived from these data have to be considered very carefully, and it is not applicable in the northern-most part of the investigated area.

To calculate this density, the individual structures are counted in each rectangular cell of a 5 x 5 km grid (Fig. 18b). Afterwards two types of interpolations of these data points are performed. In the first run, kriging interpolation is applied intended to fill up areas that are not accessible for geological mapping (ice covered areas, fjord and nearby coastal regions) (Fig. 18c). In the second run, the natural neighbor method is used for interpolation to obtain a second version of the evidential map having very accurate estimates in the uniformly and densely covered ice-free land area (Fig. 106a).

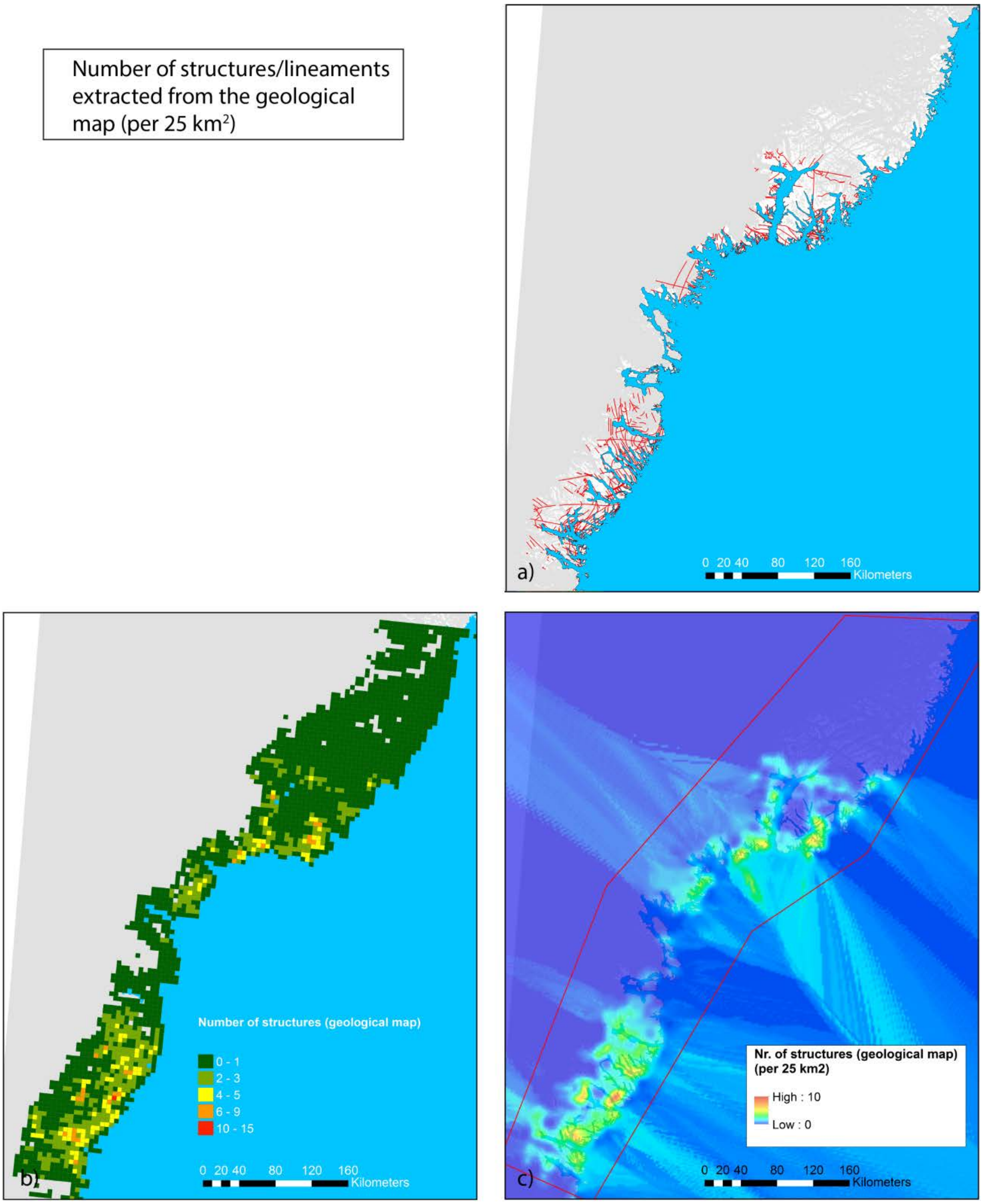

Figure 18. ***A.*** *Structures and lineaments (red lines) are extracted from the 1:500 000 geological map.* ***B.*** *Number of these structures and lineaments within cells of 5 × 5 km grid.* ***C.*** *Interpolation of the data in B by using kriging (interpolation parameters are described in section "Step 2: Used datasets, processing and resulting evidential maps"). The red line encompasses the area used in probability calculations. The interpolated grid is used for the criteria/proxy element T4.*

Major bends of structures (T3)

It is well-known that bends or splays on major first and secondary structures may act as locus or fluid-flow and trapping mechanisms in orogenic gold mineralisation. Consequently, it was decided to determine the curvature/bending of the major structures extracted from the geological map and determines this parameter (targeting element T3; see Table 4).

To determine the local curvature/bending of structures from the digital geological map (Fig. 19a) they are first fragmented into sub-structures by using a 5 x 5 km raster. Then, the sinuosity, which is the length along the curve (curvilinear length) and the Euclidian distance from the start to the end point, is calculated for all sub-structures. The sinuosity value of each sub-structure is assigned to its midpoint (Fig. 19b) and finally a kriging interpolation is performed using all midpoints to fill up areas that are not accessible for geological mapping (ice covered areas, fjord and nearby coastal regions) (Fig. 19c).

Because bending of structures is both affected by topography variations and very much dependent on the personnel doing the mapping and transferring data to the ArcGIS system, the corresponding evidential map has to be very carefully considered.

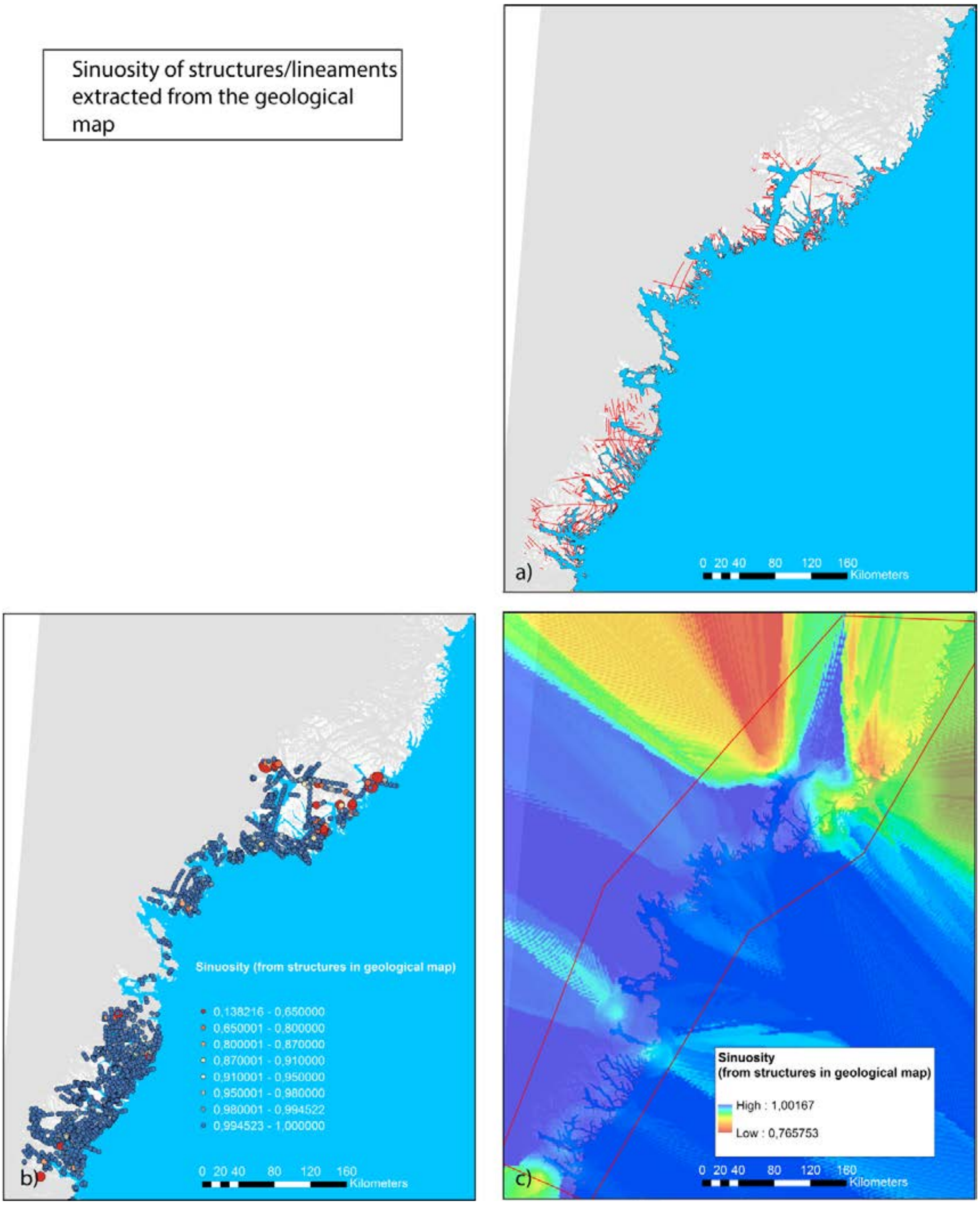

Figure 19. *Major bends of structures.* ***A.*** *Structures and lineaments (red lines) are extracted from the 1:500 000 geological map.* ***B.*** *To determine the bending of these lineaments on a rather fine spatial resolution, they are first fragmented into sub-structures by using a 5 x 5 km raster. Then the sinuosity, the ratio of the curvilinear length (along the curve) and the Euclidean distance (straight line) between the end points of the curve, is determined for these sub-structures. Dots are located at the mid points of the considered sub-structures and their size and color shows their sinuosity.* ***C.*** *Interpolation of the data in B by using kriging (interpolation parameters are described in section "Step 2: Used datasets, processing and resulting evidential maps"). The red line encompasses the area that is used in probability calculations. The interpolated grid is used for the criteria/proxy element T3.*

Geochemistry data

SEGMENT Stream sediment data (T3a to T3i)

A regional sampling for stream sediment geochemistry was carried out in 2009 and 2010 in South-East Greenland during the SEGMENT project (Stensgaard *et al.* 2010; Kolb *et al.* 2016). The data have been made publicly available via the online 'Greenland Mineral Resource Portal' (www.greenmin.gl). In this study, the stream sediment data from (Au, As, W, Mo, Sb, Cs and Bi) and the ratio Mg/Ni are used to create evidential maps (T3a, T3b, T3c, T3d, T3e, T3f, T3g and T3i; see Table 5) which can provide indications for the physical and chemical scrubber.

To distribute the geochemistry point data information across the complete area of interest, for all relevant elements (Au, As, W, Mo, Sb, Cs and Bi) and the Ni/Mg ratio, interpolations were performed with the kriging method (see Figs. 20–27).

Kriging is a commonly used interpolation method for receiving maps from stream sediment data (e.g. Spadoni *et al.*, 2003, Oyarzun *et al.*, 2007). However, it has to be kept in mind that stream sediment concentrations are complex composite products of erosion and weathering and represent the source catchment area of the stream sediment drainage network.

Because the topography is strong in most regions of Southeast Greenland and, hence, catchment areas are highly variable and weathering, erosion and mass movement processes may be complicated, the sample values and their locations are not necessarily good representatives of the local, real bedrock geology. These uncertainties have to be kept in mind, when interpolated maps from stream sediments are used as evidential maps.

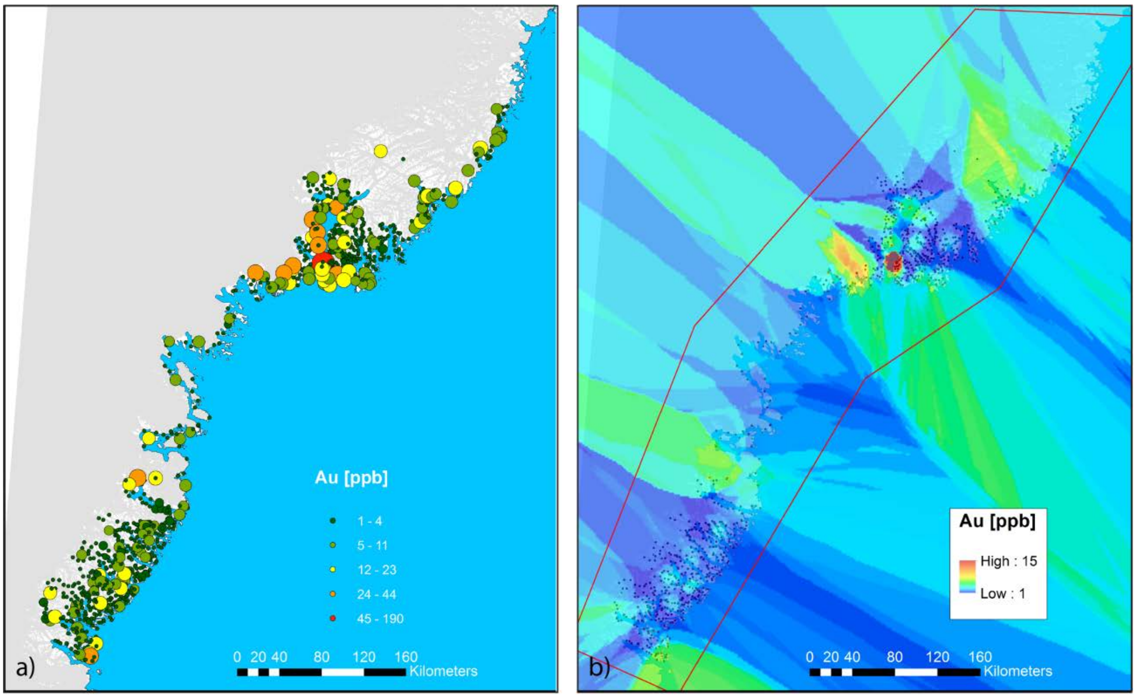

Figure 20. ***A.*** *Gold (Au) concentrations in regional stream sediment geochemistry samples.* ***B.*** *Interpolation of the data in A by using kriging (interpolation parameters are described in section ”Step 2: Used datasets, processing and resulting evidential maps”). The red line outlines the area used in probability calculations. The interpolated grid is used for the criteria/proxy element T3a.*

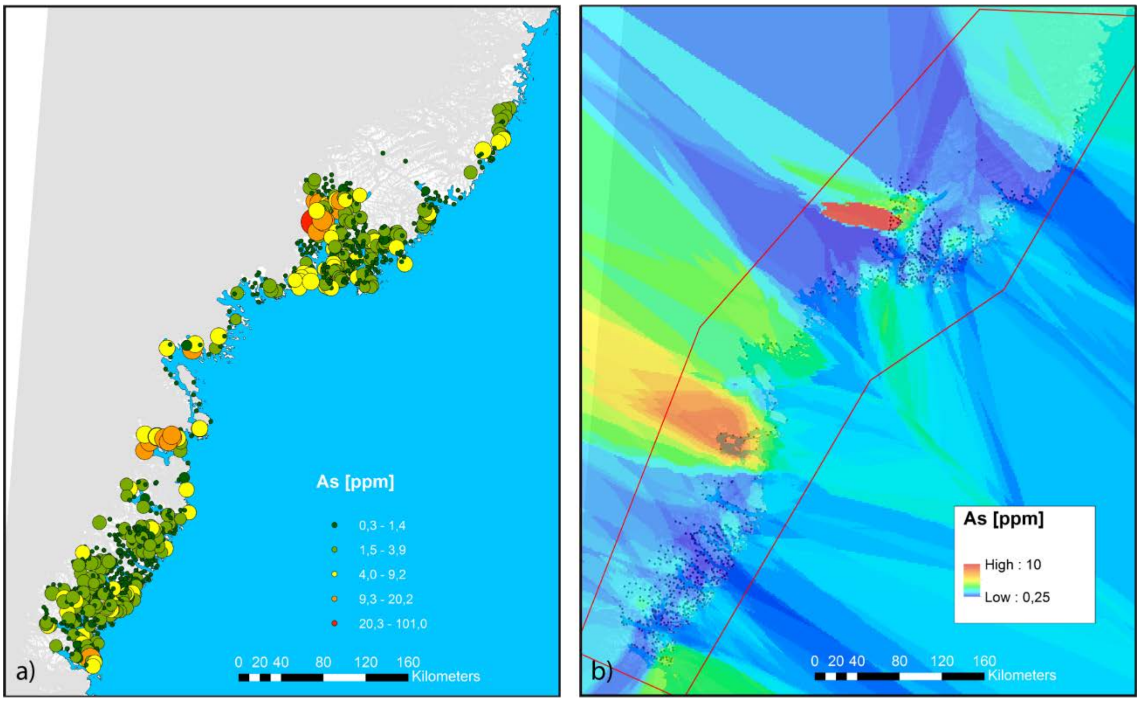

Figure 21. ***A.*** *Arsenic (As) concentrations in regional stream sediment geochemistry samples.* ***B.*** *Interpolation of the data in A by using kriging (interpolation parameters are described in section ”Step 2: Used datasets, processing and resulting evidential maps”). The red line encompasses the area used in probability calculations. The interpolated grid is used for the criteria/proxy element T3b.*

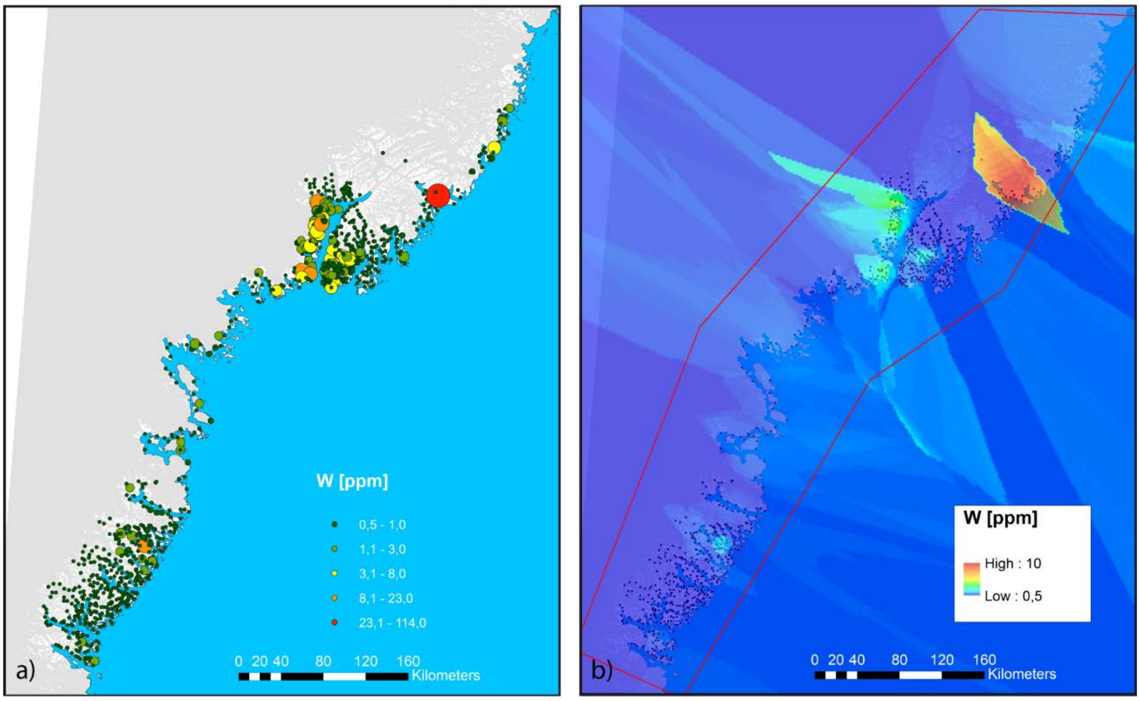

Figure 22. ***A.*** *Tungsten (W) concentrations in regional stream sediment geochemistry samples.* ***B.*** *Interpolation of the data in A by using kriging (interpolation parameters are described in section "Step 2: Used datasets, processing and resulting evidential maps"). The red line encompasses the area used in probability calculations. The interpolated grid is used for the criteria/proxy element T3c.*

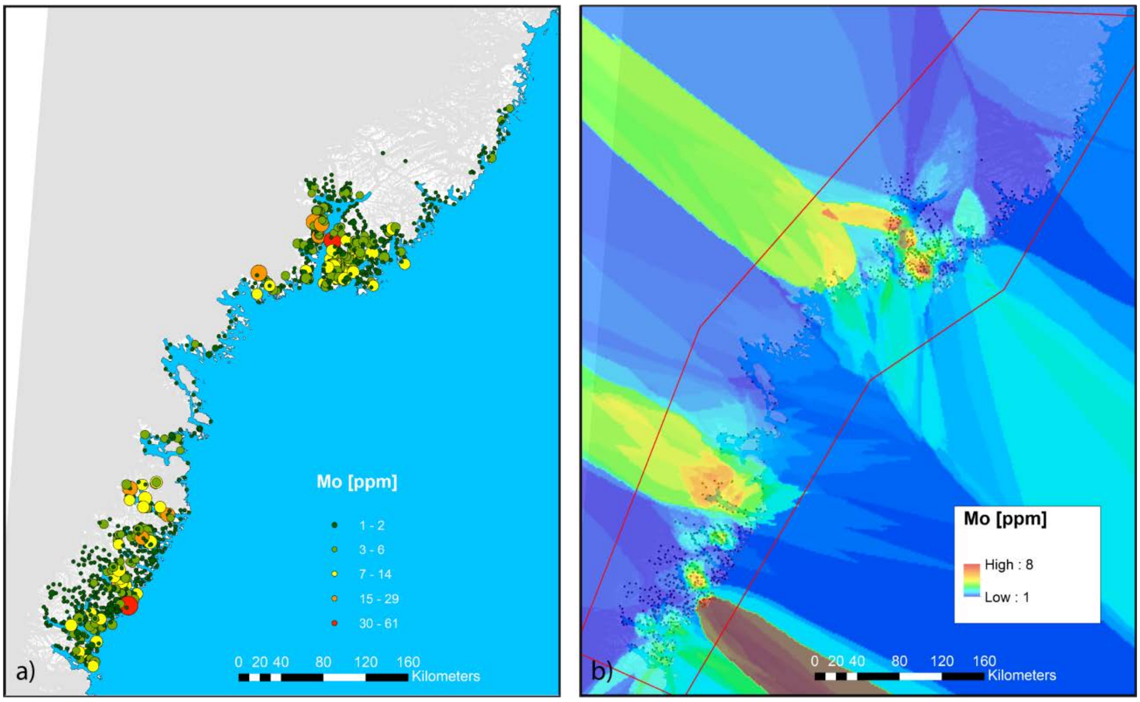

Figure 23. ***A.*** *Molybdenum (Mo) concentrations in regional stream sediment geochemistry samples.* ***B.*** *Interpolation of the data in A by using kriging (interpolation parameters are described in section "Step 2: Used datasets, processing and resulting evidential maps"). The red line encompasses the area used in probability calculations. The interpolated grid is used for the criteria/proxy element T3d.*

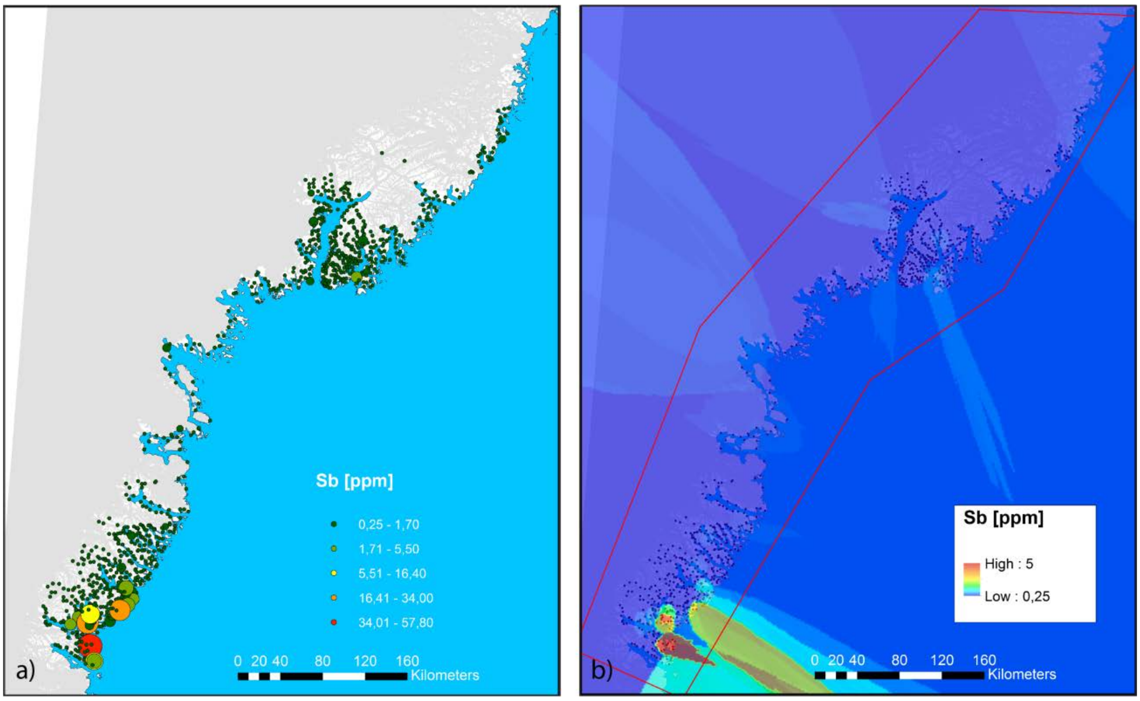

Figure 24. ***A.*** *Antimony (Sb) concentrations in regional stream sediment geochemistry samples.* ***B.*** *Interpolation of the data in A by using kriging (interpolation parameters are described in section "Step 2: Used datasets, processing and resulting evidential maps"). The red line encompasses the area used in probability calculations. The interpolated grid is used for the criteria/proxy element T3e.*

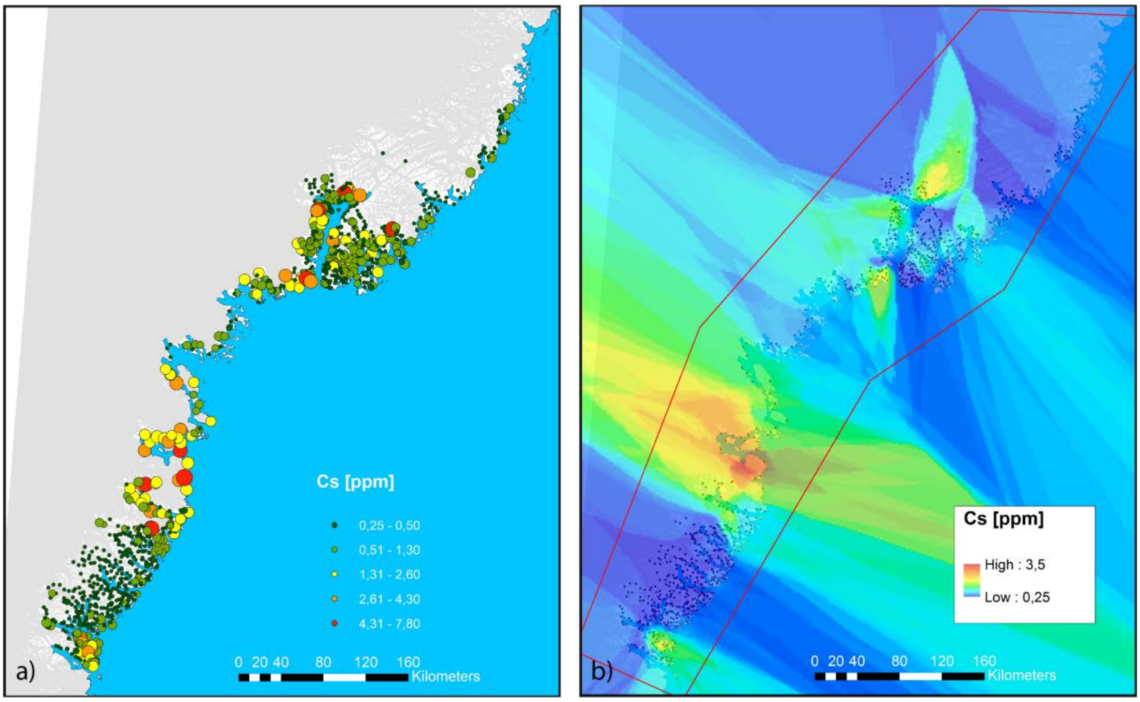

Figure 25. ***A.*** *Cesium (Cs) concentrations in regional stream sediment geochemistry samples.* ***B.*** *Interpolation of the data in A by using kriging (interpolation parameters are described in section "Step 2: Used datasets, processing and resulting evidential maps"). The red line encompasses the area used in probability calculations. The interpolated grid is used for the criteria/proxy element T3f.*

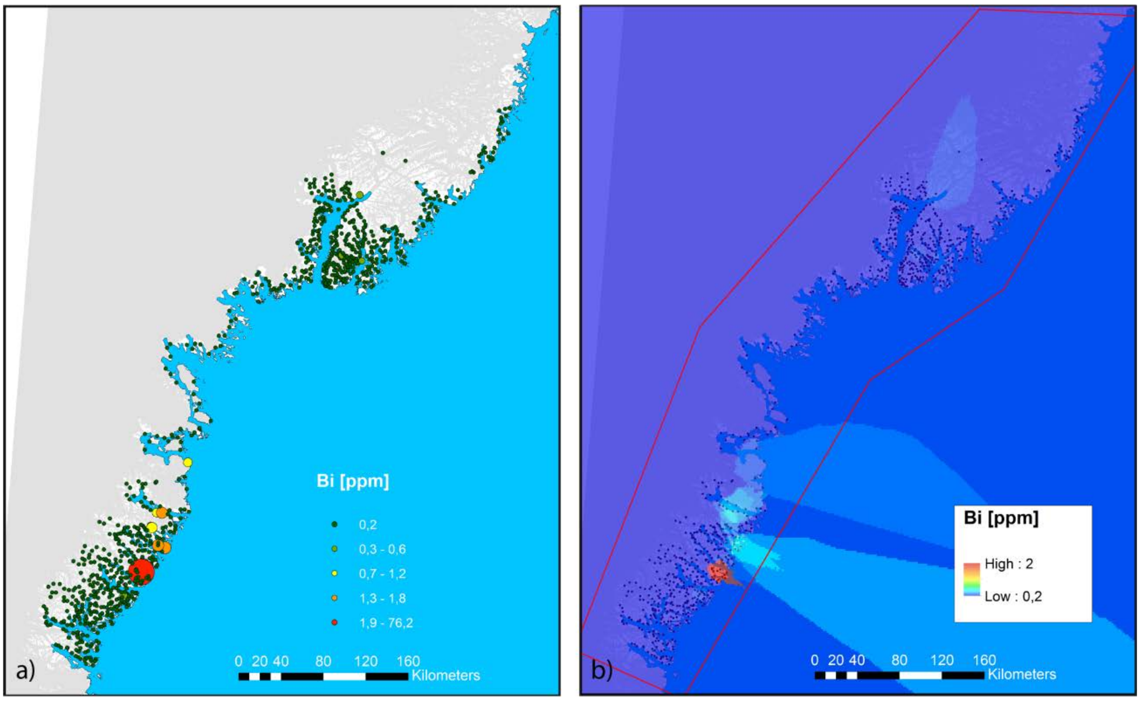

Figure 26. ***A.*** *Bismuth (Bi) concentrations in regional stream sediment geochemistry samples.* ***B.*** *Interpolation of the data in A by using kriging (interpolation parameters are described in section ”Step 2: Used datasets, processing and resulting evidential maps”). The red line encompasses the area used in probability calculations. The interpolated grid is used for the criteria/proxy element T3g.*

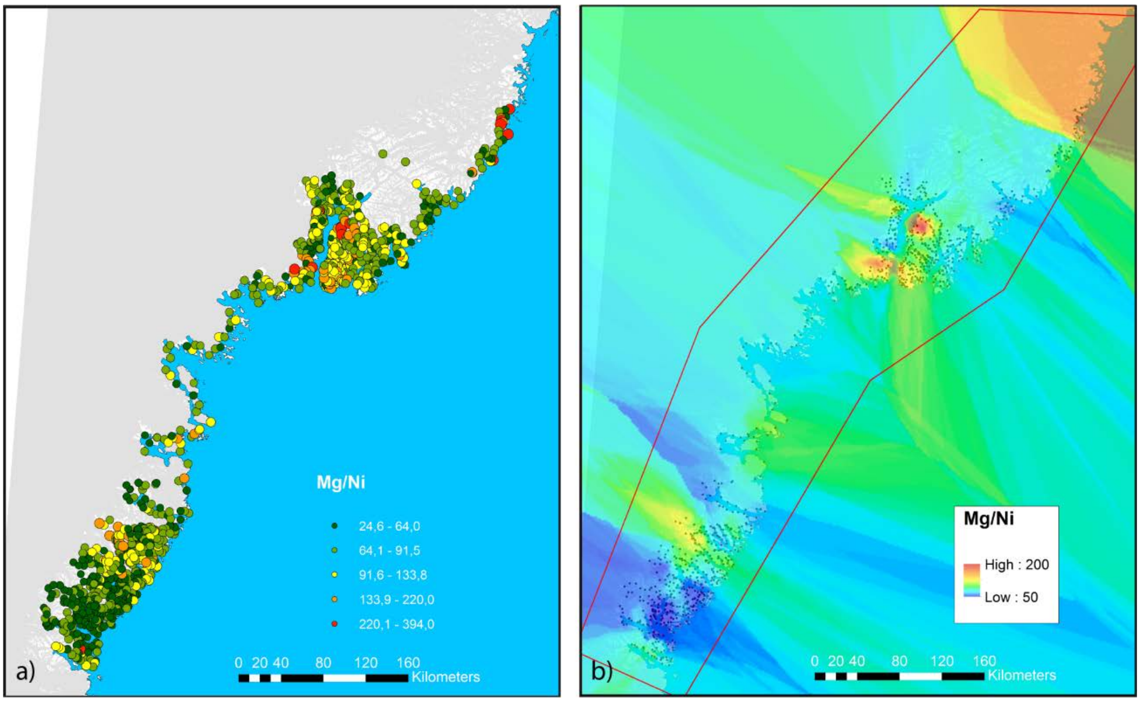

Figure 27. ***A.*** *Ratio of magnesium over nickel (Mg/Ni) in regional stream sediment geochemistry samples.* ***B.*** *Interpolation of the data in A by using kriging (interpolation parameters are described in section ”Step 2: Used datasets, processing and resulting evidential maps”). The red line encompasses the area used in probability calculations. The interpolated grid is used for the criteria/proxy element T3h.*

Remote Sensing

The Advanced Spaceborne Thermal Emission and Reflection Radiometer (ASTER) instrument was launched in 1999 on board the Terra satellite. The multispectral satellite system comprises three optical imaging subsystems acquiring fourteen spectral bands operating in the visible near infrared (VNIR), shortwave infrared (SWIR) and thermal infrared (TIR) channels, having spatial resolutions of 15 m, 30 m and 90 m, respectively. ASTER has a ground swath width of 60 km and a revisit time of 16 days. Because the TIR channels (band numbers 10 to 14, see

Table 7) cover spectral ranges associated with absorption features of different minerals/rocks (Fig. 28), they can help to distinguish rock composition within a scene (e.g. Corrie *et al.* 2010).

GEUS bought a number of ASTER scenes from Greenland including the complete area of interest in Southeast Greenland. The processing applied to receive “reflectance” products from the raw data follows much the procedure used for the Australian ASTER geoscience maps from the Western Australian Centre of Excellence for 3D Mineral Mapping (C3DMM 2012). This involves correction for instrument, illumination, atmospheric and geometric effects. In additions, procedures applied to blank out areas covered by ice and water. These “reflectance” maps of the different bands are then used to calculate the spectral indices (see Fig. 29a to Fig. 31a).

To determine evidential maps that also cover parts of the area of interest, ice-covered or located offshore, kriging was first applied as an interpolation procedure on maps of selected spectral indices. In a second run, interpolations were repeated with natural neighbor gridding to obtain second versions of evidential maps that provide very precise representations of the real values in areas of high data coverage (ice-free onshore area). Because the raster maps have a very dense sampling, there are computational problems in performing the interpolation with these large amounts of data; we down-sampled the input data sets before the interpolation was carried out so that only 10% of the data are used. Maps of the spectral indices after kriging interpolation and natural neighbor interpolation are shown in Figs 29b to 31b and Figs 108a and 110a, respectively.

We consider here the following three spectral indices that are indicative for carbonate rock, silica bearing rocks and mafic rocks.

Table 7. *Spectral ranges and spatial resolution of the ASTER bands in the thermal infrared (TIR).*

Band number	Spectral range (μm)	Centre λ (μm)	Spatial resolution (m)
10	8.125 – 8.475	8.3	90
11	8.475 – 8.825	8.65	
12	8.925 – 9.275	9.1	
13	10.25 – 10.95	10.6	
14	10.95 – 11.65	11.3	

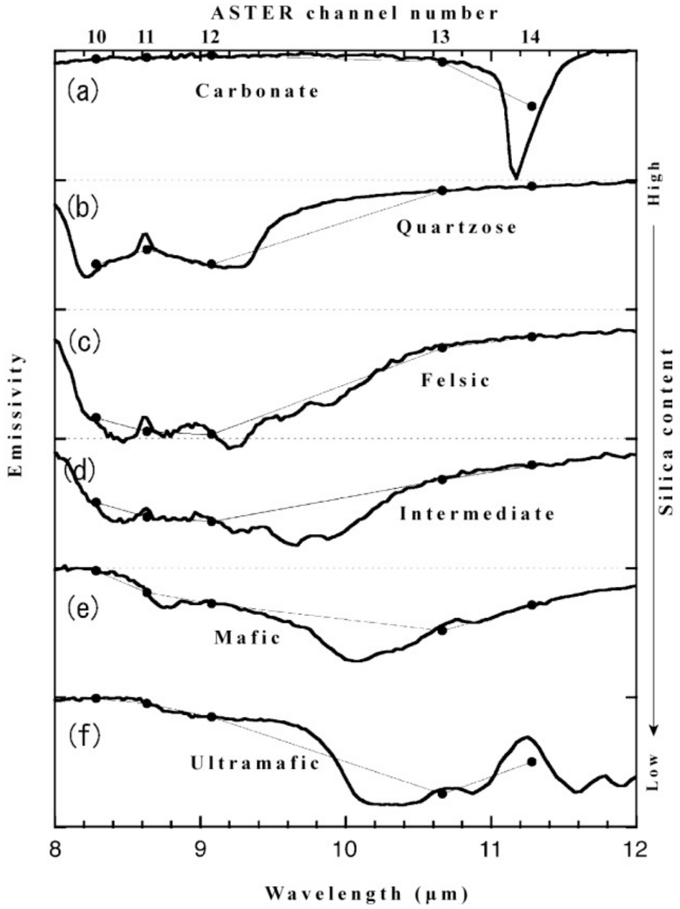

Figure 28. *Spectral properties for different rock types and the locations of the different ASTER data (Figure taken from Corrie et al.2010).*

Mafic mineral index (T2a)

The spectral properties of silicate minerals and rocks in the thermal infrared generally change with the content of chemical SiO_2 in that the emissivity minimum is moved toward lower frequencies with increasing wavelengths. This means felsic rock types and ultramafic rock types (e.g. peridotite) show higher emissivity at longer wavelengths (i.e. band 13) and shorter wavelengths (i.e. band 12), respectively, (see Fig. 28b-f) and a Mafic Index (MI) is, hence, defined as:

$MI = Band_{12}/Band_{13}$

We emphasize that the quartz does not have to be available in a pure form to have this impact onto the Mafic Index (MI) and in this way the resulting information differs from the one obtained from the Quartz Index (QI). The resulting evidential map of the mafic mineral index from the ASTER data and the gridded evidential map are shown in Figure 29.

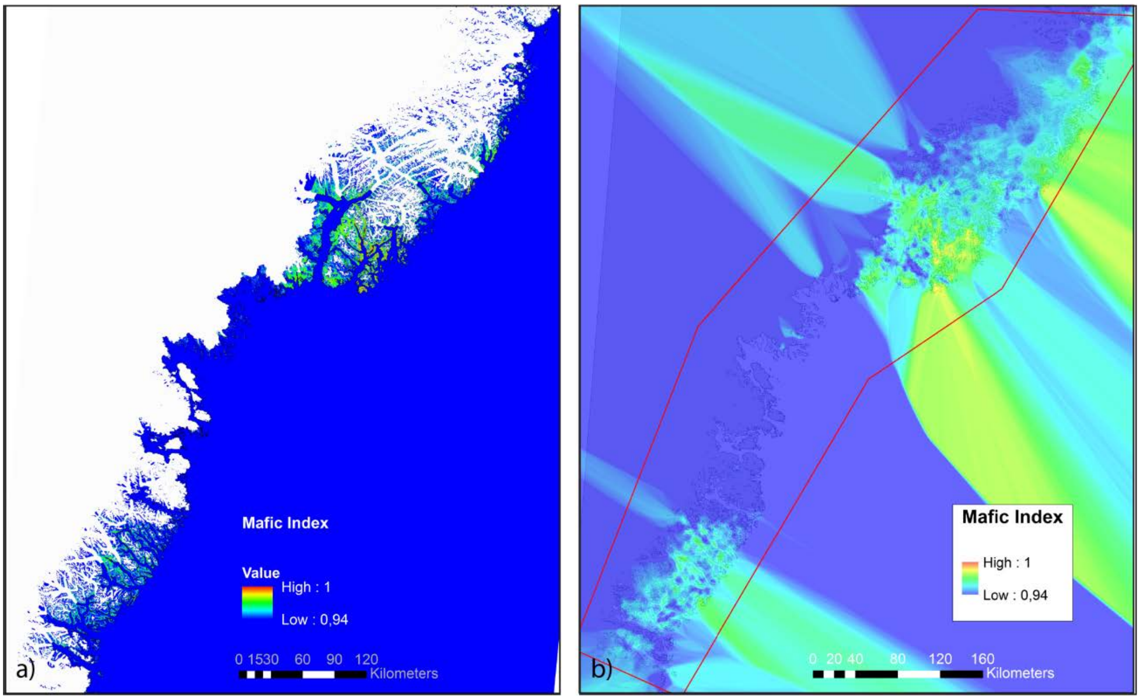

Figure 29. ***A.*** *Mafic mineral index (MI) determined from the "Advanced Spaceborne Thermal Emission and Reflectance Radiometer" (ASTER) launched on the Terra satellite.* ***B****. Interpolation of the MI data by using kriging (interpolation parameters are described in section "Step 2: Used datasets, processing and resulting evidential maps"). Due to computational limitations, it was required to reduce the number of data by 90% before performing the interpolation. The red line outlines the area used in probability calculations. The interpolated grid is used for the criteria/proxy element T2a.*

Carbonate mineral index (T2b)

Carbonate minerals calcite and dolomite have an unique spectral absorption feature in band 14 (see Fig. 28a) and based on the ratio of the digital numbers (DN) of bands 13 and 14, the Carbonate Index is defined as:

$CI = Band_{13}/Band_{14}$

This means high values are expected in a pixel, if the content of calcite and/or dolomite is high; however, the index is not sensitive to other carbonate rocks. The resulting evidential map of the carbonate mineral index from the ASTER data and the gridded evidential map are shown in Figure 30.

Quartz mineral index (T2c)

Pure silica (SiO_2) bearing rocks as quartzite have specific absorption features around the bands 10 and 12 and the Quartz Index is defined as:

$QI = (Band_{11} \times Band_{11})/(Band_{14} \times Band_{14})$

It is common that the emissivity is higher for band 11 than for the bands 10 and 12 for quartzite and other siliceous rocks (see Fig. 28b), (but not for potassium feldspar and gypsum). The resulting evidential map of the carbonate mineral index from the ASTER data and the gridded evidential map are shown in Figure 31.

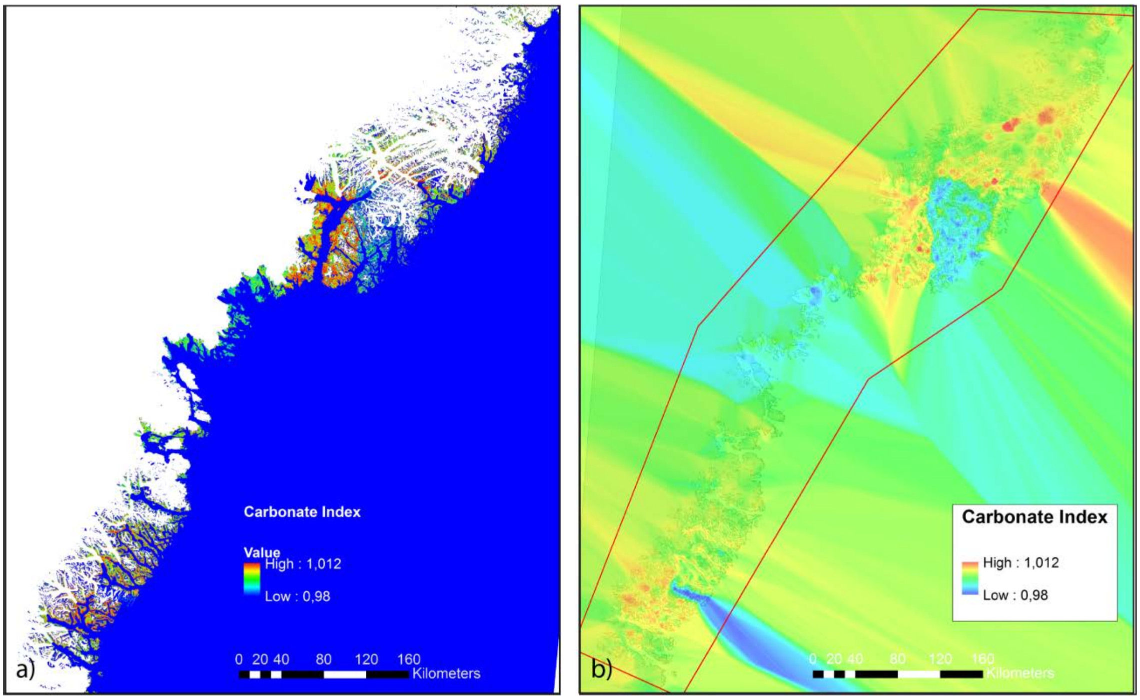

Figure 30. ***A.*** *Carbonate mineral index (CI) determined from the "Advanced Spaceborne Thermal Emission and Reflectance Radiometer" (ASTER) launched on the Terra satellite.* ***B****. Interpolation of the MI data by using kriging (interpolation parameters are described in section "Step 2: Used datasets, processing and resulting evidential maps"). Due to computational limitations, it was required to reduce the number of data by 90% before performing the interpolation. The red line outlines the area used in probability calculations. The interpolated grid is used for the criteria/proxy element T2b.*

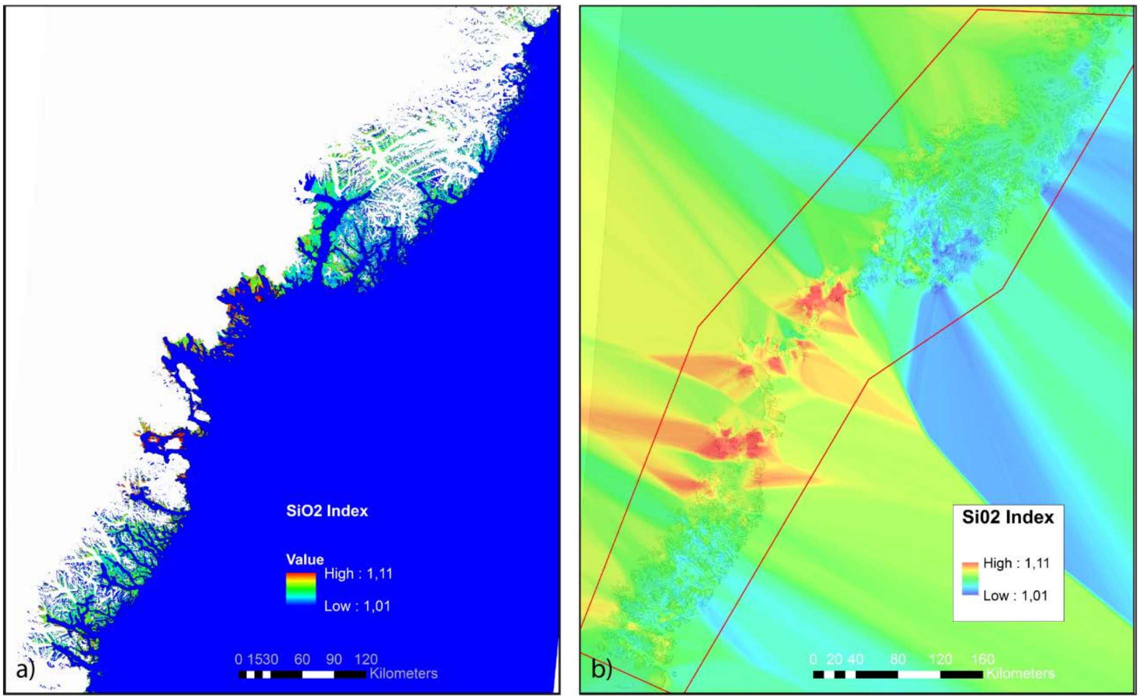

Figure 31. ***A.*** *Quartz mineral index (QI) determined from the "Advanced Spaceborne Thermal Emission and Reflectance Radiometer" (ASTER) launched on the Terra satellite.* ***B****. Interpolation of the MI data by using kriging (interpolation parameters are described in section "Step 2: Used datasets, processing and resulting evidential maps"). Due to computational limitations, it was required to reduce the number of data by 90% before performing the interpolation. The red line outlines the area used in probability calculations. The interpolated grid is used for the criteria/proxy element T2c.*

Geophysical data

Aeromagnetic and gravity data was used and processed in order to produce evidential maps for certain proxies. Velocity distribution from full-waveform tomography, earthquake distribution and information from magnetotelluric profiles was also assessed in order to evaluate their usefulness (see Appendix C). However, all these datasets was because of low resolution and uncertainties decided not to be used.

Aeromagnetic data - AEROMAG

Airborne magnetic surveys from fixed-wing aircrafts with dense line spacing and GPS positioning has been acquired for large part of Greenland under the AEROMAG program (Rasmussen *et al.* 2013).

In 2012 and 2013 two magnetic surveys were carried out for GEUS and the Government of Greenland along the East Coast from Greenland as a continuation of the AEROMAG surveys (Rasmussen 2013; Rasmussen *et al*. 2013; Riisager and Rasmussen 2013). The two surveys cover the remote coastal area of East Greenland from Cap Cort Adelaer (61°45´N) in the South and the area around Kap Gustav Holm to the North (67°30´N) (see Fig. 32).

The surveys were carried out by flying along a gently draped surface 300 m above the ground. Separation of the survey lines was 500 m,oriented approximately orthogonal to the coast line in an ENE-WSW direction and in a NE-SW direction for the 2012 and 2013 survey, respectively.

Figure 32. *Shaded total magnetic intensity plots (inclination and declination of light source is 45°) from the regional airborne surveys of the AEROMAG project in East Greenland. a) and b) show the northern and southern part these surveys, respectively. A downward continuation of 100 m and a reduced-to pole transform have been applied to the displayed data.*

Detection of lineaments from regional airborne magnetic data (Pb1, P2, T1, T2)

AEROMAG data were used to map second order lineaments (used for the targeting elements P1b, P2, T1 and T2).

For lineament detection standard, processed magnetic data from these two surveys (and the eastern part of the AEROMAG survey 1995 that covers the southern tip of Greenland; Stemp *et al.* 1997) are merged into one grid with a 100 x 100 m point spacing using the "GridKnit" tool from GEOSOFT. The resulting total magnetic intensity (TMI) grid is used as a starting point for the procedure described below.

Procedure

Many different strategies are proposed in the literature to enhance lineaments and to detect edges in airborne magnetic data. For edge detection, e.g. Wijns *et al.* (2005) use the total horizontal derivative of the tilt angle and the total horizontal derivative normalized by the analytic signal, respectively. (We calculated the horizontal derivative of the tilt angle. However, we do not show the results of these tests here because the images are (despite of low pass filtering) quite noisy and provide therefore rather little new information for our purpose). Cooper and Cowan (2008) edge detection method is based on ratios of windowed standard deviations of field derivatives. Zhang *et al.* (2006) proposed a lineament detection strategy that is based on Radon transform. Holden *et al.* (2008) presented a fully automated scheme to visualize and extract secondary fault zone patterns from airborne magnetic data. Like this study, they developed their scheme to identify fault zones for evaluating potential gold.

We considered the advanced processing flow from Holden *et al.* (2008) as particularly suited for our purpose and decided to apply their method on the AEROMAG data from East Greenland. However, first tests showed that this fully automated scheme does not successfully work in the presence of deep-cutting fjords causing large variations in the topography. Such topography variations create 1) either elongated negative magnetic trends (due to larger distances of sensor from the magnetic sources) obscuring the magnetic anomalies caused by susceptibility variations in the shallow surface, or 2) strong variations of the magnetic field (caused by a combination of shallow magnetic sources and rapid changes of the topography) resulting in artificially determined lineaments.

We investigated therefore how their procedures can be adjusted such that secondary fault zones can be reliably determined under such conditions. In addition, we looked for other alternative procedures to visualize and extract such lineaments. Finally, we ended up with two workflows that can be applied on the TMI images. One of the schemes is largely automated, while the other one requires some hand editing at the final stage, when lineaments are selected.

In the following, these procedures are briefly described. Processing is performed with standard tools from GEOSOFT MONTAJ and therefore we explain some of the settings in this software, we have chosen during the workflow. We emphasize that these workflows are considered as a starting point to develop more advanced and reliable strategies for fracture detection in other regions of Greenland with similarly topography.

First workflow:

The first work flow is very similar to the one described in Holden *et al.* (2008) and most of the processing routines are part of the "CET_Grid_Analysis.omn" GEOSOFT package. The resulting lineaments are used in the targeting element P2. The workflow involves the following steps:

1) **Downward continuation of 100 m for the total intensity map.**
The downward continuation is performed to get shallow high frequency anomalies associated with fault zones enhanced and sharpened. The shift should be smaller than the minimum ground clearance to avoid artifacts from near-surface magnetic sources.

2) **Reduction-to-pole transformation**.
Some of the following processing steps assume that the anomaly variations associated with fault zones are mostly symmetric. For this reason, the reduced-to-pole and not the original TMI data are considered for the following processing (see Fig. 32).

3) **Spatial 2-D high-pass filter** (cut-off frequency of 1/(300 m)).
This slightly improves the resolutions of the following procedures by reducing the level of stochastic noise. To avoid artifacts from the frequency filtering, it is recommended to extrapolate the grid before filtering with the GEOSOFT routine GRDFILL.GX. After filtering the extrapolated area is removed again by using a polygon of the survey area.

4) **Texture analysis** (using the entropy as a measure; Holden *et al.* 2008). This method uses the local neighborhood of each pixel/image location to evaluate the image entropy, which is determined by the spread pattern of grayscale pixel intensities of the neighborhood. The motivation for this step is to identify regions that are characterized by a local high complexity in the magnetic field. Shallow steeply dipping fault zones are characterized by such a complexity and have strong positive values in the texture analysis image. Another advantage of this procedure is that the impact of the amplitude level is reduced (Holden et al. 2008) such that also faults having weak anomaly amplitudes are significantly enhanced.

   In the GEOSOFT package, we chose the “Entropy” option and tested different filter lengths for the different windows that range from 5 to 15 cells (see Fig. 33 and Fig. 34). Although fewer cells result into noisier images, they provide a spatially more accurate detection and we decided therefore to use small windows of 5 x 5 cells. It is important to choose large number of bins (standard settings of 512 seems to be too small and we used 2048 in our procedure) such that the images have enough dynamic range for the following symmetry filtering.

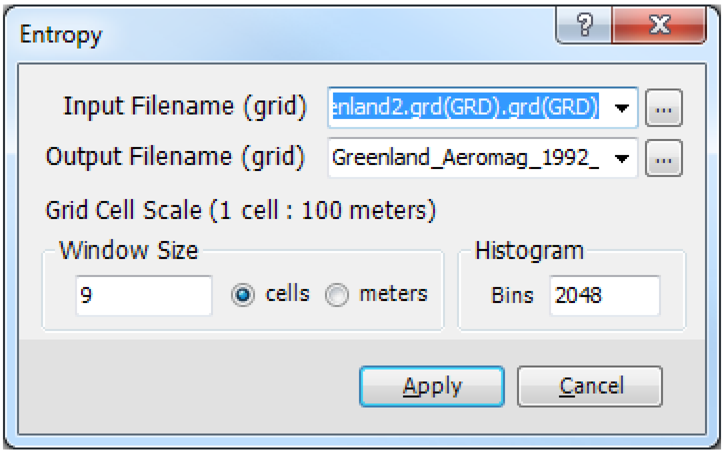
Entropy
Input Filename (grid) enland2.grd(GRD).grd(GRD)
Output Filename (grid) Greenland_Aeromag_1992_
Grid Cell Scale (1 cell : 100 meters)
Window Size
9 ● cells ○ meters
Histogram
Bins 2048

Figure 33. *Typical settings used for the texture analysis.*

It should be noted, that if the resulting texture imaging maps (see e.g. elongated low-value anomalies in Fig. 34) is considered can it be observed that the bottom of the deep-cutting fjords and valleys are characterized by low complexity, resulting in small entropy values, whereas large topography often curvatures mainly at the crests of the mountains are characterized by high values. The reasons for the low values at the fjord and valley bottoms are 1) that the anomalies are broadened due to the higher flight altitude and 2) that the topography along the bottom typically is locally flat. This means that faults that run along the fjords are not detected by assuming high texture analysis values for faults. The reason for high values along the crests is that the undulations of the topography are responsible for variations of the shallow susceptibility distribution. Because such topography variations and faults are both characterized by high texture values, it is more difficult to completely distinguish them in an automated scheme. Therefore some additional processing steps are applied at the end of the scheme accounting for this problem (see point 5-7); but even then the scheme is far from optimum and some visual inspection and hand editing is still required at the end to distinguish artifacts from real faults.

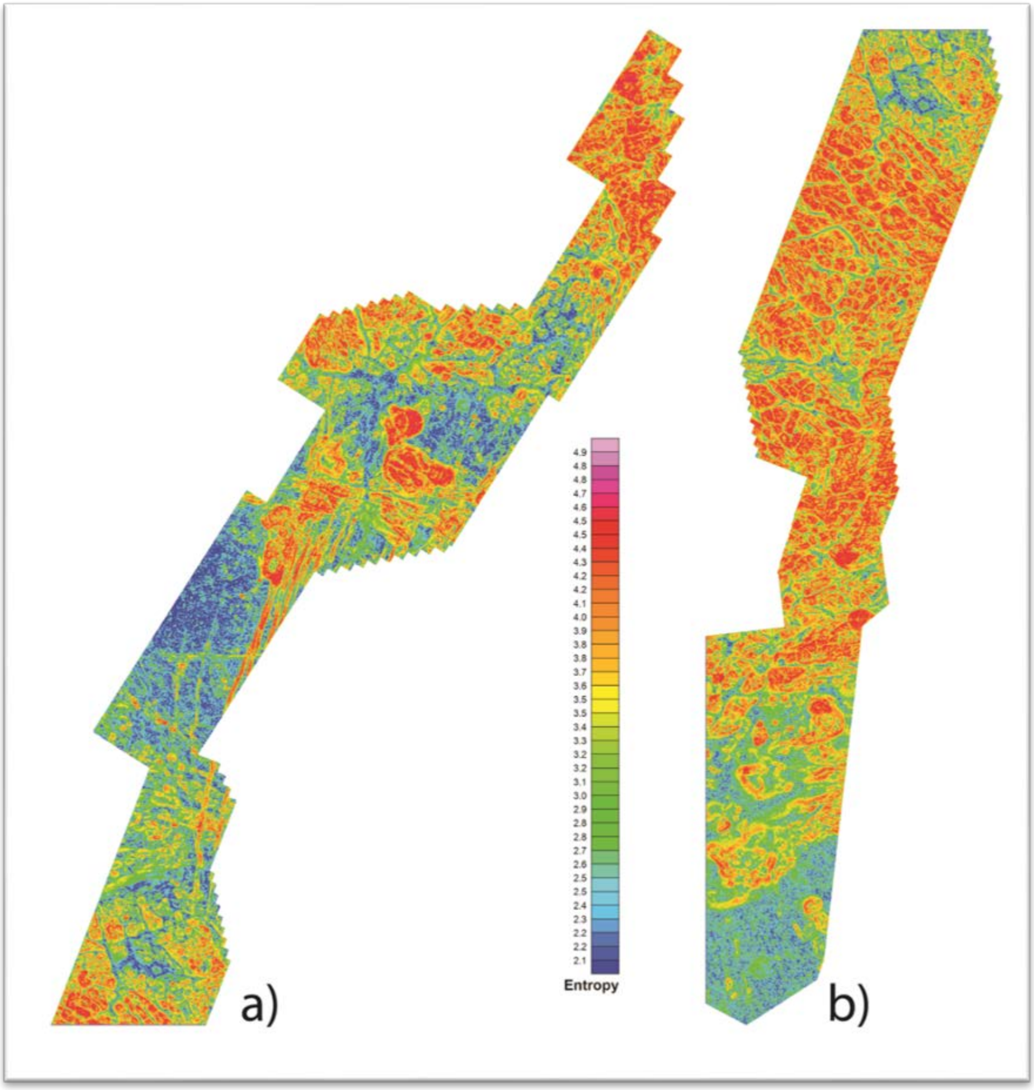

Figure 34. *Texture analysis (entropy option) is applied to the reduced-to the pole images shown in Figure 32. Window size of the applied filter is 5x5 cells and in total, 2048 histogram levels are used.*

5) **Applying the phase symmetry filter as described in Holden et al. (2008).** This filter, based on a wavelet transform technique in the Fourier domain, enhances symmetrical features having specific (narrow) widths.

In GEOSFOFT we used in the tool “Phase symmetry (ridges/valleys)” a minimum wavelength of 4 cells for the wavelet (see Fig. 35). The maximum wavelength is determined by the width of the anomalies that should be highlighted. In our case widths of the anomalies are in the range of 500 m to 2000 m and the maximum wavelength considered is 12.8 km. To reduce the noise level a “value of robustness” has to be chosen. Slightly dependent on the data (and type of applied processing), values in the range from 1 to 5 seems to be adequate for these surveys.

First the “Positive” option for the polarity is chosen to detect faults (and other lineaments) that appear as high amplitude features in the texture analysis image (as long as the topography does not change). Results (see Fig. 36) indicate that lineaments are reliably detected, if the topography effect is minor. However, if the topography undulations are larger also areas with large rapid topographic changes are emphasized that might cover the effects of lower amplitude faults. This indicates that the procedure does not work perfectly in a fully automated manner in the presence of topography.

In addition, faults that are eroded and coincide with fjords/valleys are not detected, because they have low values in the texture analysis image. To emphasize these. we chose the “Negative” option instead (see Fig. 37).

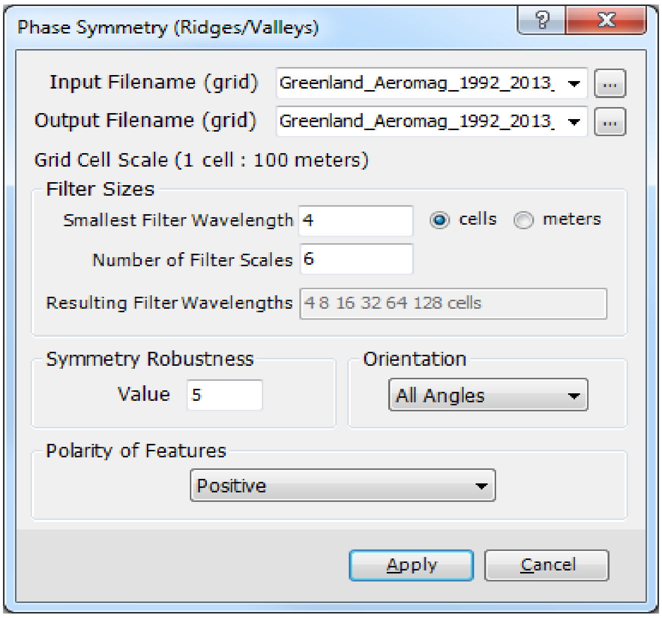

Phase Symmetry (Ridges/Valleys)

Input Filename (grid) Greenland_Aeromag_1992_2013_

Output Filename (grid) Greenland_Aeromag_1992_2013_

Grid Cell Scale (1 cell : 100 meters)

Filter Sizes

Smallest Filter Wavelength 4 ● cells ○ meters

Number of Filter Scales 6

Resulting Filter Wavelengths 4 8 16 32 64 128 cells

Symmetry Robustness

Value 5

Orientation

All Angles

Polarity of Features

Positive

Figure 35. *Typical settings used for the phase symmetry filtering. The level of “Symmetry Robustness” varies a bit for the different surveys. For the “Polarity of Features” both the “Positive” and “Negative” option is used. Holden et al. (2008) explains the meanings of the different settings in detail.*

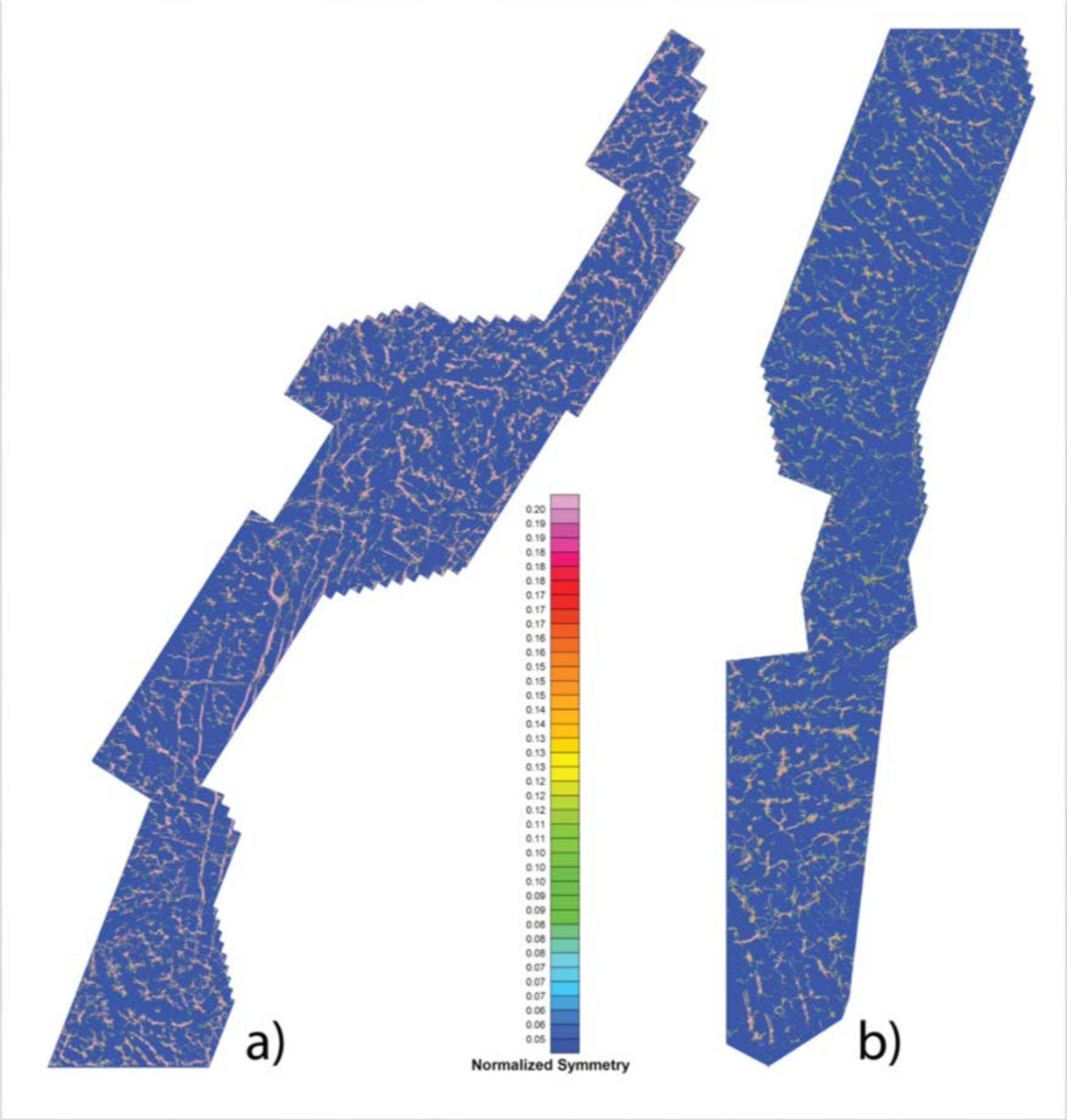

Figure 36. *Results from the phase symmetry filtering of the texture analysis image (see Fig. 34). Highlighted features have a positive polarity.*

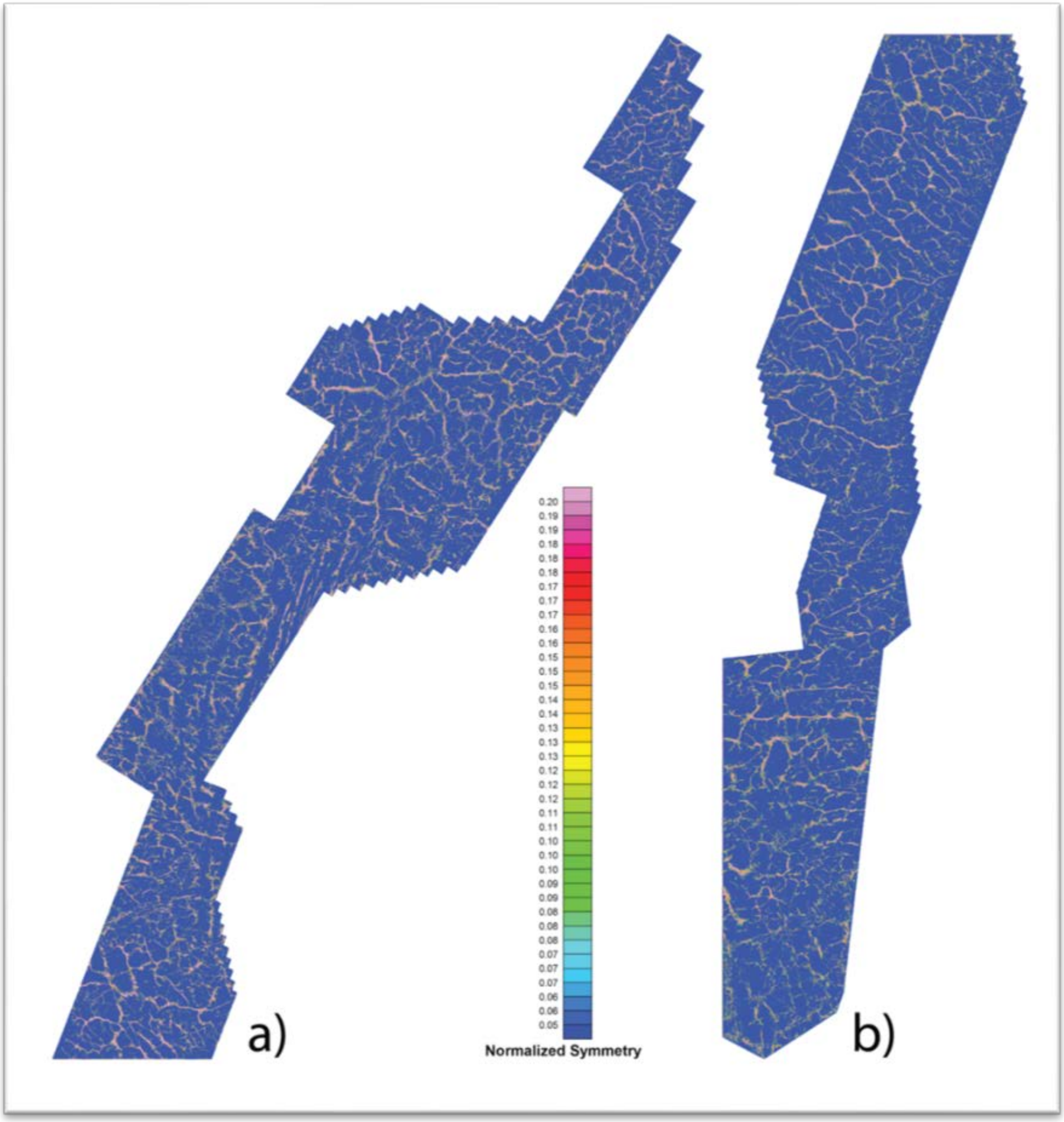

Figure 37. *Results from the phase symmetry filtering of the texture analysis image (see Fig. 34). Highlighted features have a negative polarity.*

6) **Applying a topological skeleton process.**
On the images obtained from the symmetry filter, we perform in the next step a topological skeleton process. “Topological skeleton” is a digital imaging process that narrows features having some widths to some thin lines (e.g. Jain 1989). This allows us to associate potential fracture and faults as narrow features in the following mineral prospective mapping.

Because both images from the symmetry filters, where “positive” and “negative” polarities are assumed, contain information about lineaments and fault zones under specific conditions (see point 5), we apply the skeleton procedure on both of them. As input for the skeleton process, binary data are required. Therefore, we first apply the tool “Amplitude Thresholding” that includes an amplitude threshold in conjunction with a non-maximal suppression (NMS) filter (see Fig. 38; as parameters we choose an amplitude threshold of 0.01 and an “output ridge width” of 10 cells) and that outputs binary values of 1 and 0 depending on if the considered pixel is associated with the ridge of an lineament or not. Next, the morphological thinning operation (skeleton) is applied to features in these binary images (see Fig. 39). To ignore very small features, all resulting lines containing less than 25 pixels are removed within the process (see option in Fig. 39. The final images after the skeleton process are shown in the Figs 40 and 41 (using a “positive” and “negative” polarity for the phase symmetry filter, respectively).

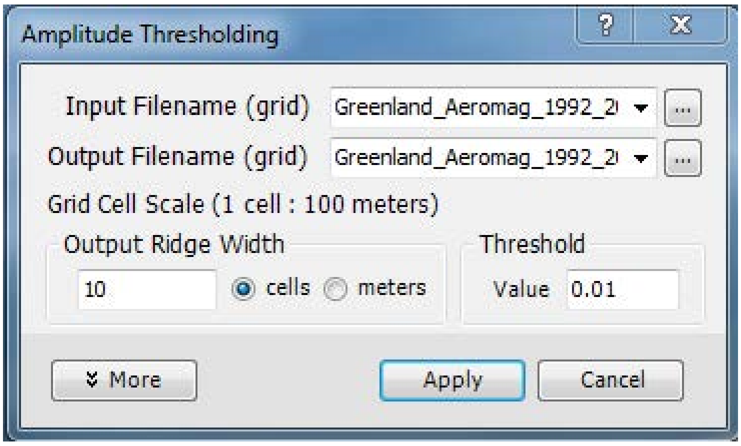
Amplitude Thresholding

Input Filename (grid) Greenland_Aeromag_1992_2

Output Filename (grid) Greenland_Aeromag_1992_2

Grid Cell Scale (1 cell : 100 meters)

Output Ridge Width

10 ● cells ○ meters

Threshold

Value 0.01

Figure 38. *Settings of the process that transform amplitude values in the symmetry filtered data to binary values (0 and 1). The process is controlled by an amplitude threshold. In parallel, a non-maxima suppression (NMR) filter is applied to preserve only local maximum values of linear features. The output of this process is the input for the skeleton process (see Fig. 39).*

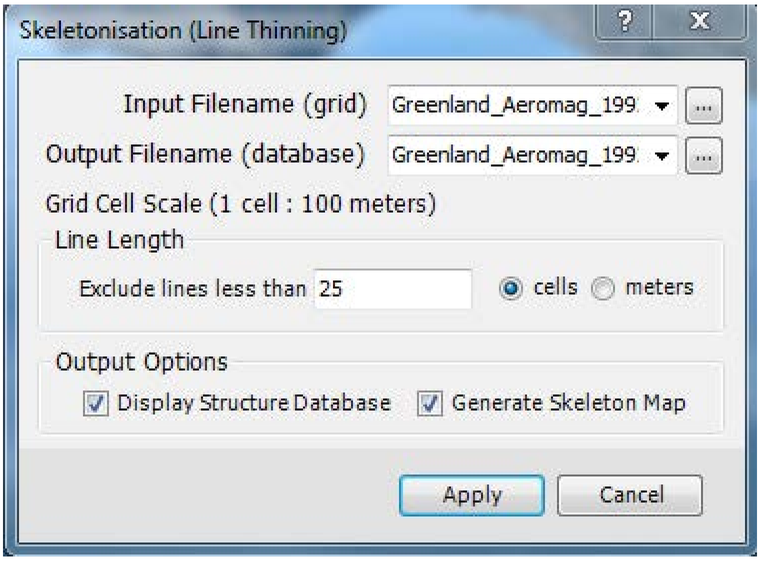
Skeletonisation (Line Thinning)

Input Filename (grid) Greenland_Aeromag_199

Output Filename (database) Greenland_Aeromag_199

Grid Cell Scale (1 cell : 100 meters)

Line Length

Exclude lines less than 25 ● cells ○ meters

Output Options

☑ Display Structure Database ☑ Generate Skeleton Map

Figure 39. *Settings of the morphological skeleton process for line thinning. (To ignore very small structures, all features having less than 25 cells are removed during this process.)*

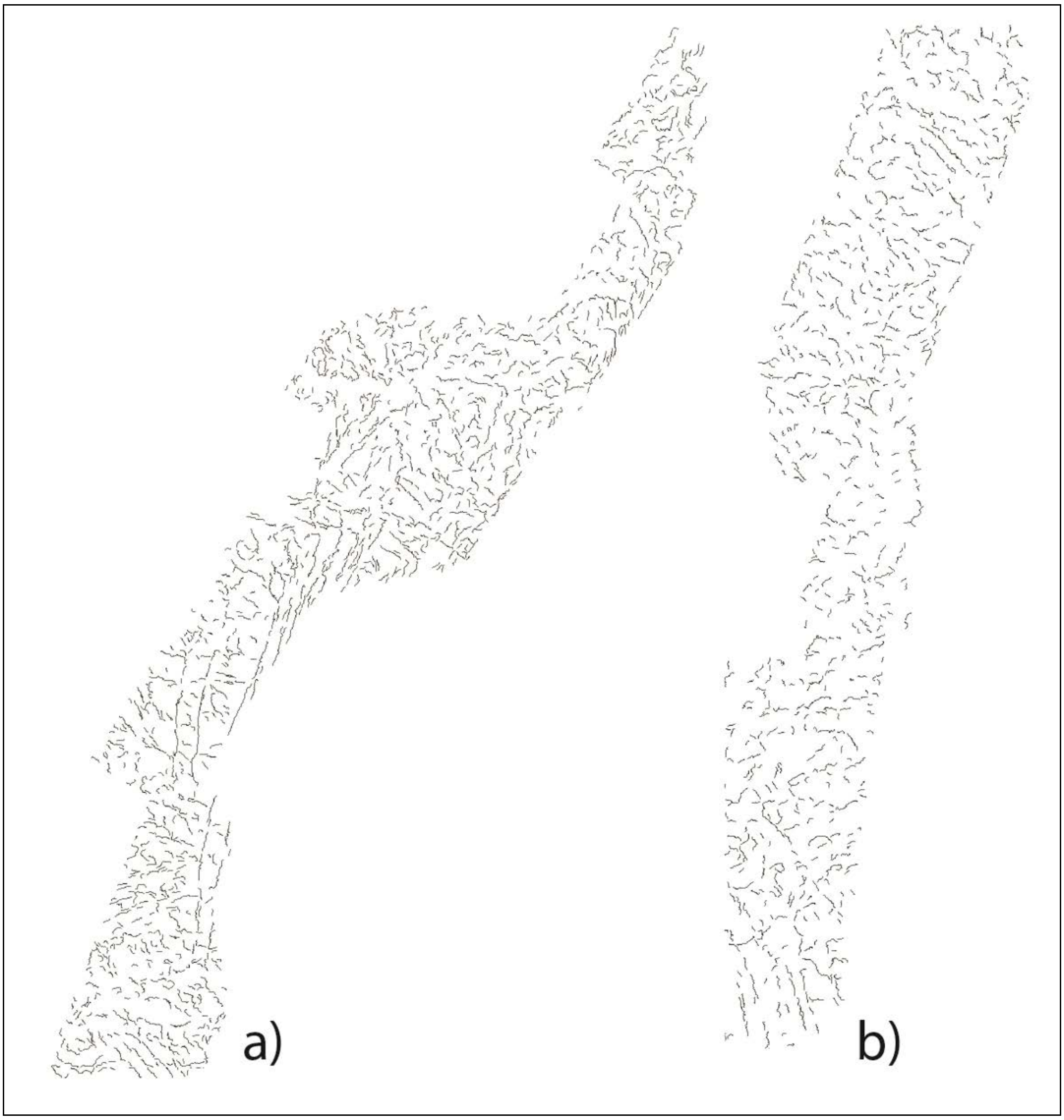

Figure 40. *Skeleton process applied on the symmetry filtered data shown in Figure 36 (detected features have a positive polarity). Lines extending over less than 25 cells are removed.*

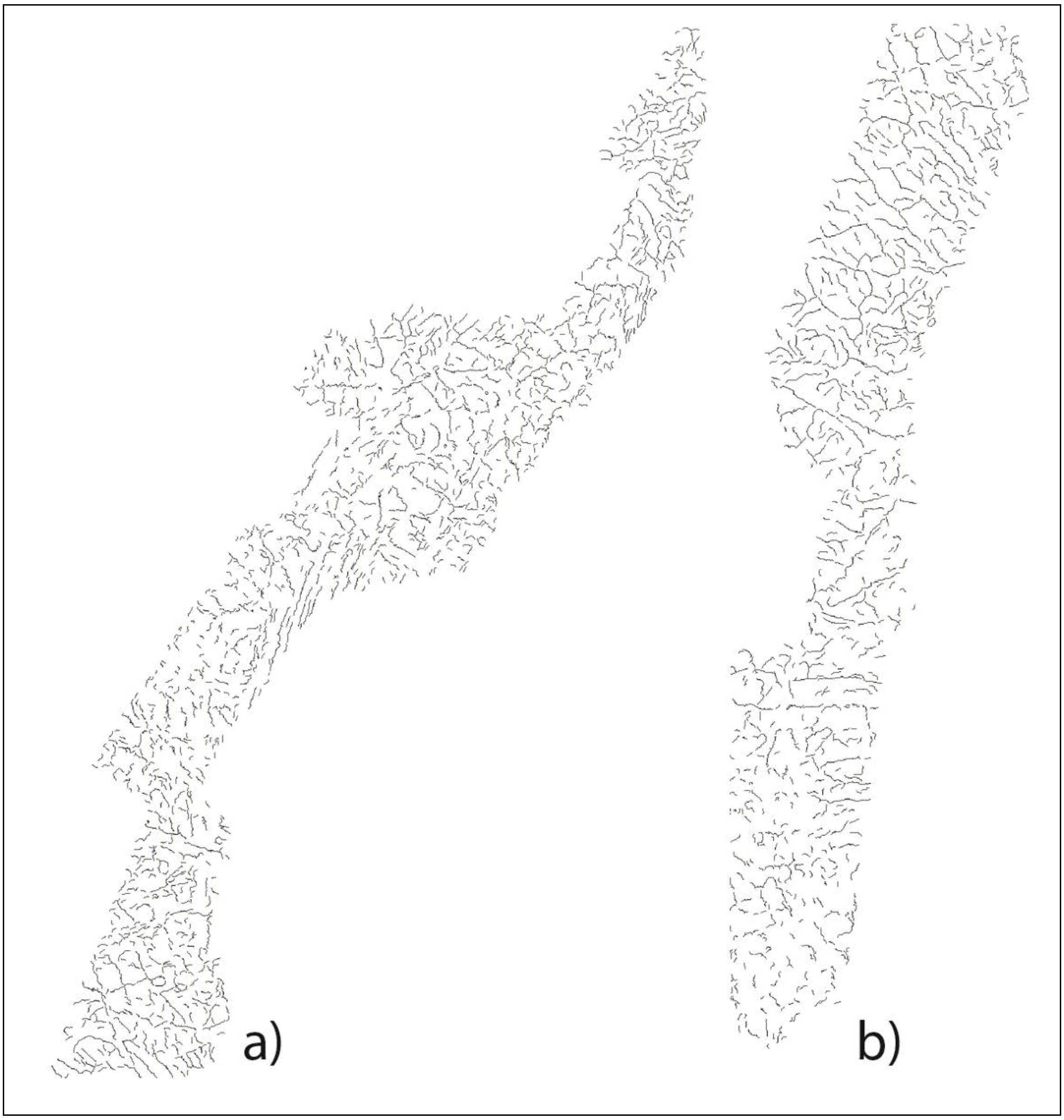

Figure 41. *Skeleton process applied on the symmetry filtered data shown in Figure 37 (detected features have a negative polarity). Lines extending over less than 25 cells are removed.*

7) Removing detected lines associated with strong topographic variations.

After applying the symmetry filter that highlight features with positive polarity and the subsequent skeleton process (see Fig. 40), some of the resulting lines are associated with undulations in topography and not with real lineaments. To remove these features, we extracted the ground clearance of the AEROMAG surveys (see Fig. 42) and determined the curvature from it (see Fig. 43). Afterwards, we removed lineaments obtained after the skeleton process at locations, where the curvature had larger absolute values than 0.2. Finally, we cleaned the image from remaining smaller segments (see Fig. 44).

The lineaments shown in Figure 41 (features having negative polarity after texture analysis) and Figure 44 (features having negative polarity after texture analysis) are used as the input for determining the evidential map for P2. To determine this evidential map the distances from the lineaments are calculated (see Fig. 49b, c) and afterwards these two maps are combined in a fuzzy logic process (see Appendix B).

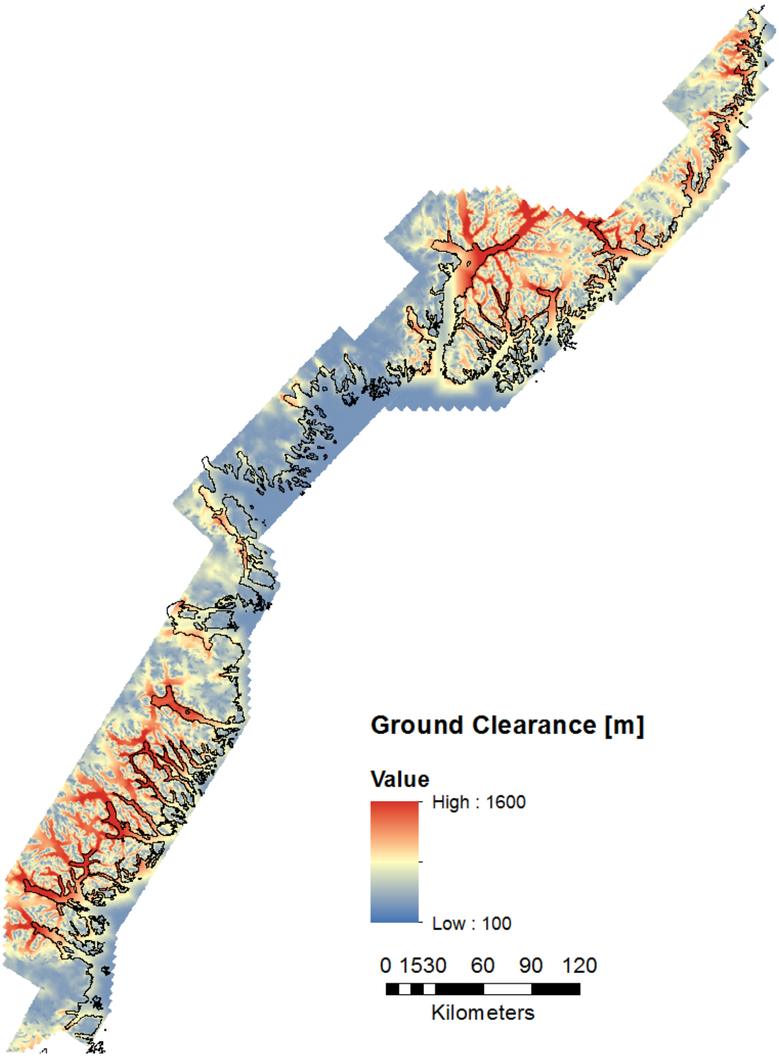

Figure 42. *Ground clearance (vertical distance from the ground to the magnetic sensor) for the AEROMAG surveys from 2012 and 2013.*

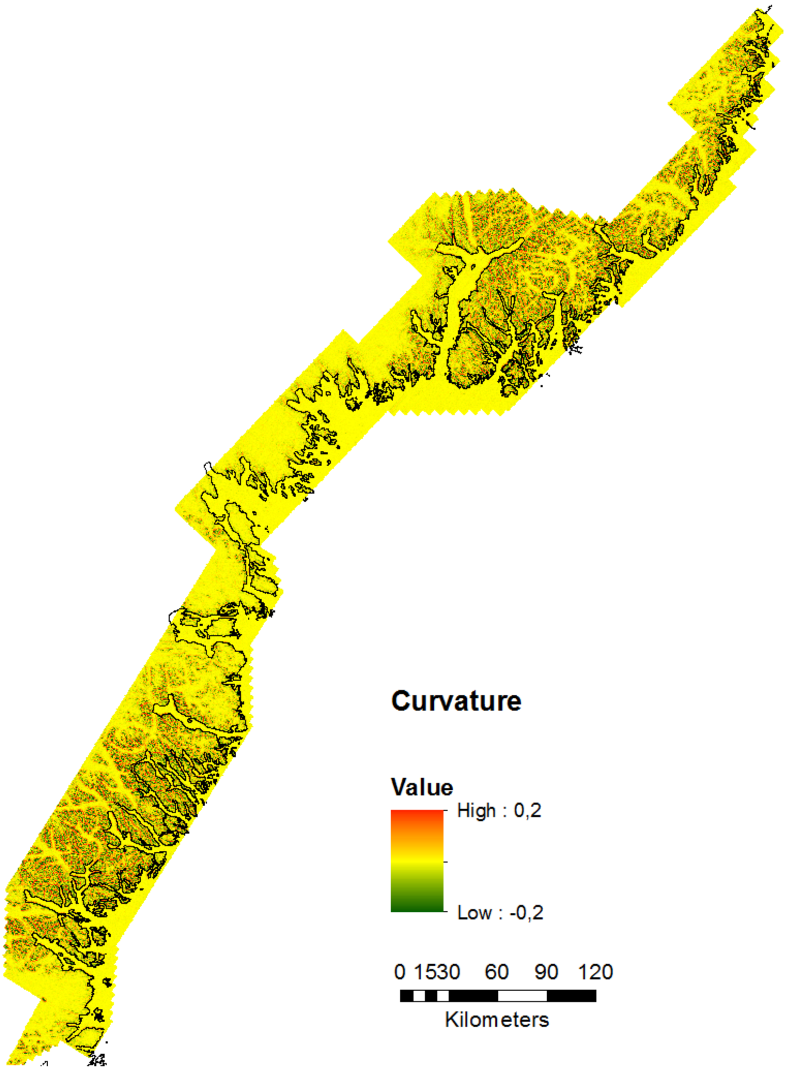

Figure 43. *Curvature that is determined from the ground clearance data (see Fig. 42).To smooth the measure, a 2-D Savitzky-Golay filter (Schafer 2011) is applied afterwards.*

Figure 44. *Because the topography of the survey area (ground clearance of the flights) artificially introduces features in Figure 40, features are removed in areas, where the curvature of the ground clearance (Fig. 43) has high magnitudes.*

Second workflow:

The second workflow is used to facilitate manual picking of lineaments used for the evidential maps P1b, T1 and T2. In this workflow, the “Dynamic range compression” filter (see e.g. Kovesi 2012) is applied to visualize week fault zones and other narrow lineaments. To enhance such feature already before filtering we choose as filter input not the TMI, but a down-continued vertical derivative of the magnetic field.

1) **Perform a downward continuation of 100 m for the total intensity map** (as in the first workflow).
2) **Apply a reduced-to-pole transformation** (as in the first workflow).

3) **Apply a spatial 2-D high-pass filter** (cut-off frequency of 1/(300 m))
This step is required because the downward continuation and the following application of the vertical derivative boost up high-frequency stochastic noise. (If this step is performed in GEOSOFT, the borders of the survey area should be tapered before frequency filtering to avoid filtering artifacts. This can be achieved by extrapolating the borders of the surveys before filtering. After filtering, the extrapolated area is removed again.)

4) **Determine the first vertical derivative**
Already this “standard” processing provides images that allow an appropriate manual picking of lineaments if grey-scale colors and shading options are used (see Fig. 45).

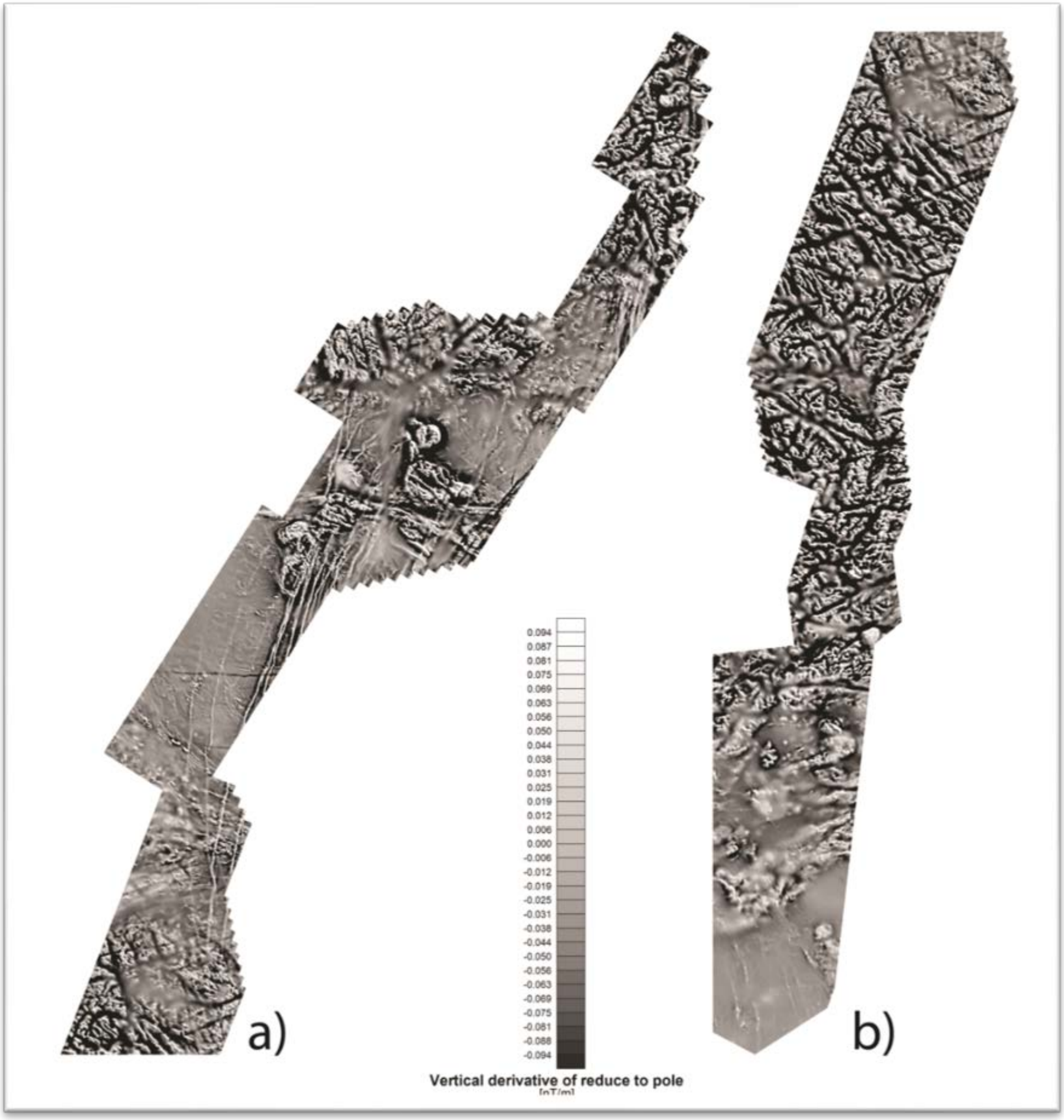

Figure 45. *Vertical gradient of the reduced-to-pole image shown in Figure 32. (Color shading is applied to this plot; declination and inclination of the light source is 45°).*

5) **Apply a dynamic range compression**

The Phase Preserving Dynamic Range Compression filter emphasizes subtle features without distorting them. This means that anomaly changes in the signal are purely a function of their amplitudes, which means that the phase information is preserved. It operates as follows: First, a high-pass filter is applied to the data, which controls the desired frequency range for the following analysis. The 2-D analytic signal of the data is then computed to obtain local phase and amplitude at each point in the image. To balance the amplitudes their logarithm is taken and finally the signal is reconstructed using the original phase values and the modified amplitude values.

In GEOSOFT we choose four "resulting filter wavelengths" starting from 10 cells (corresponding to 1 km) up to 2520 cells (corresponding to 252 km) (see Fig. 46). We observed that the image that has a cut-off frequency of 63 cells (corresponding to 6.3 km) enhances adequately thin lineaments (see Fig. 47).

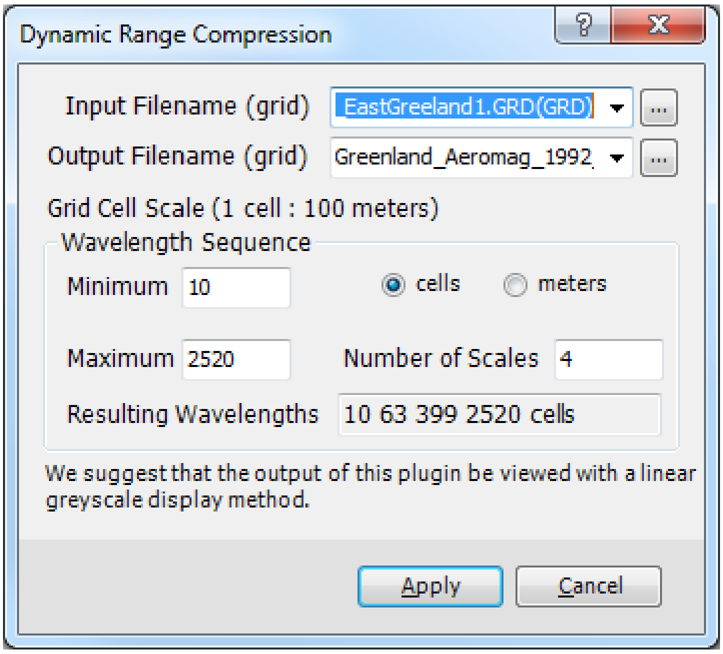

Dynamic Range Compression

Input Filename (grid): EastGreeland1.GRD(GRD)

Output Filename (grid): Greenland_Aeromag_1992

Grid Cell Scale (1 cell : 100 meters)

Wavelength Sequence

Minimum: 10

● cells ○ meters

Maximum: 2520

Number of Scales: 4

Resulting Wavelengths: 10 63 399 2520 cells

We suggest that the output of this plugin be viewed with a linear greyscale display method.

Figure 46. *Typical settings used for the "Dynamic Range Compression". In the resulting image with a spatial cut-off frequency of 1/(39.9 km) secondary faults and other lineaments are significantly enhanced. The different settings are explained in Kovesi (2012).*

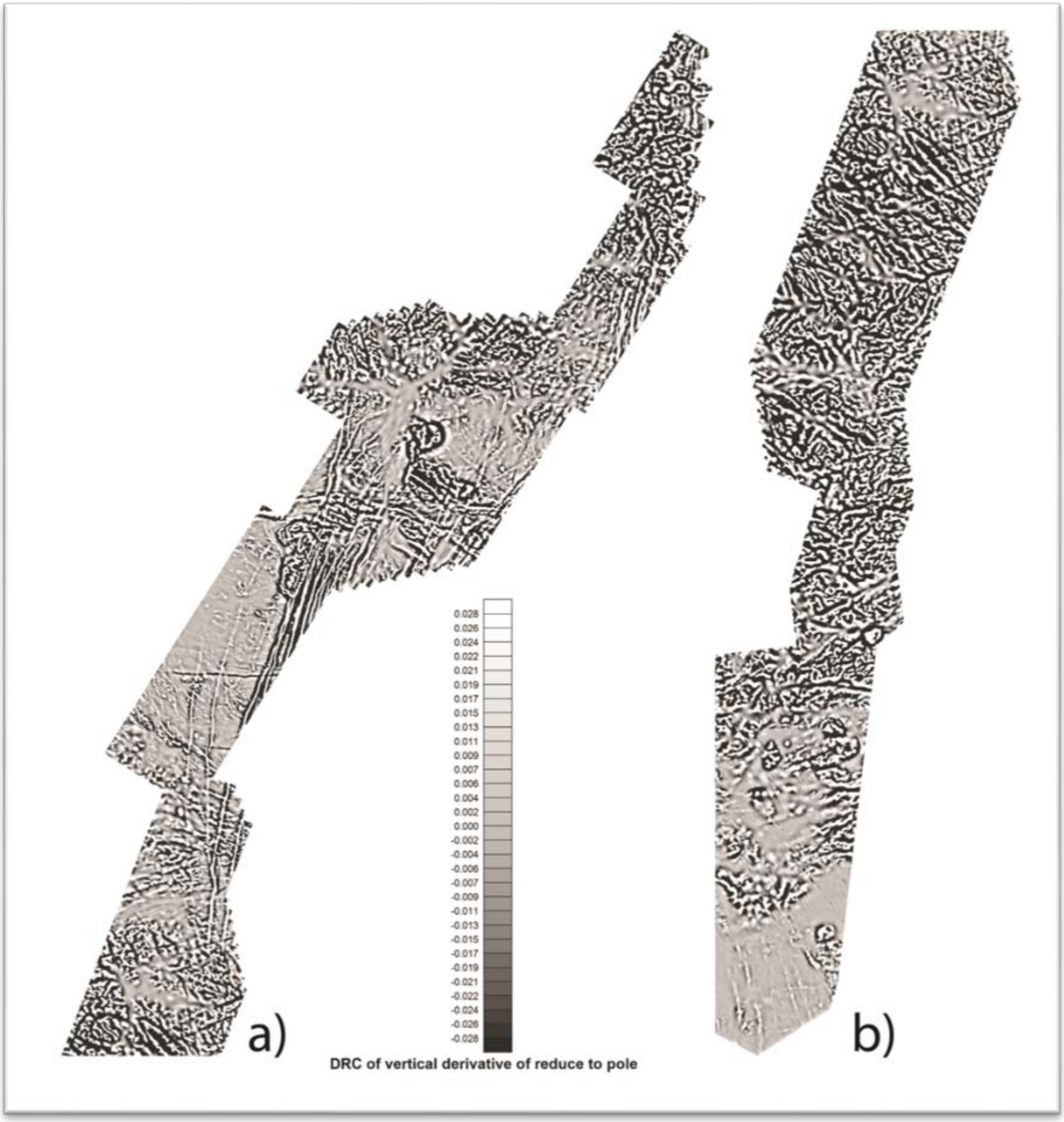

Figure 47. *Dynamic range compression (Kovesi 2012) is applied on the vertical derivative shown in Figure 10. The displayed image has a spatial cut-off frequency of 1/(6.3 km).*

Determination and interpretation of lineaments (P1b, T1, T2)
Potential secondary fault zones are extracted (see Fig. 48) by considering several of the maps (see Figs 34, 36, 37, 45 and 47) obtained from the two workflows. Elongated magnetic lineaments that correlate both with and without topography variations are considered as potential fault zones.

We do not distinguish between them, because valley and fjords often form along the weakened rock mass of fault zones. However, based on geological pre-knowledge, it is possible to separate tertiary dikes that strike predominately north-southerly direction and are related to the continental breakup from other lineaments.

The identified lineaments (see yellow lines in Fig. 48) were used in the following ways for the different targeting elements:

- To determine the evidential map of P1b (related to the targeting element of second order shear zones as active pathways), we calculated the minimum distance (see Fig. 49a) from the identified lineaments in Figure 48 (yellow lines).
- To determine the evidential map of T1 (associated with the targeting element of structural intersections for the physical traps/throttle), the minimum distances from the intersections points of these lineaments were calculated (Fig. 50).
- To obtain the evidential map of T2 (associated with the intersections of these lineaments with interfaces of geological units and used for evaluating the physical throttle), these intersections are first counted in cells of a 5 x 5km raster (see Fig. 17a, b). Afterwards kriging interpolation is used to extent estimates of these counts in areas not accessible for geological mapping (ice covered areas, fjord and nearby coastal regions) (Fig. 17c). (See also section “Intersection of structures with interfaces between rock units” at page 49).

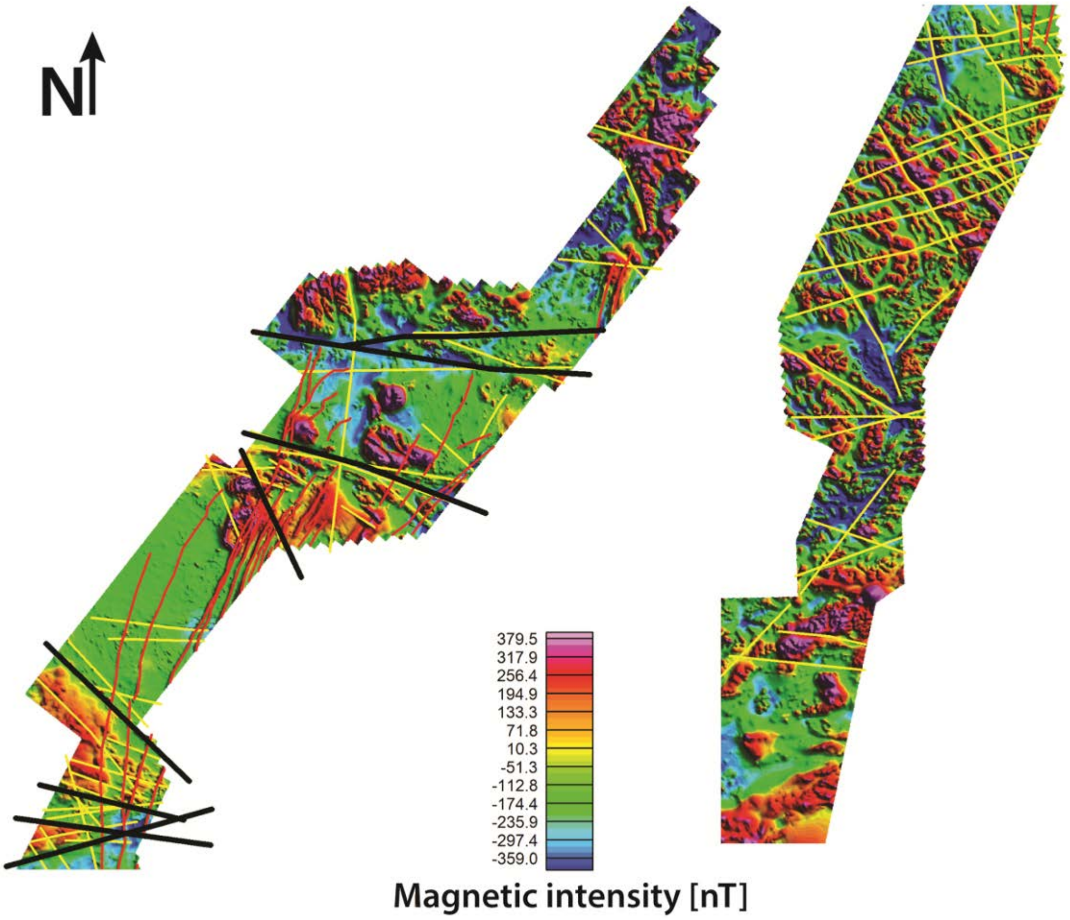

Figure 48. *Lineaments determined from the AEROMAG data. Thick black lines indicate broader elongated anomalies having low wavenumber and considered to be related to regional trends. Yellow and red lines show narrow elongated anomalies. The re-marked anomalies are associated with tertiary dikes, and the yellow marked anomalies probably originate from other types of shallow features, like secondary fault zones.*

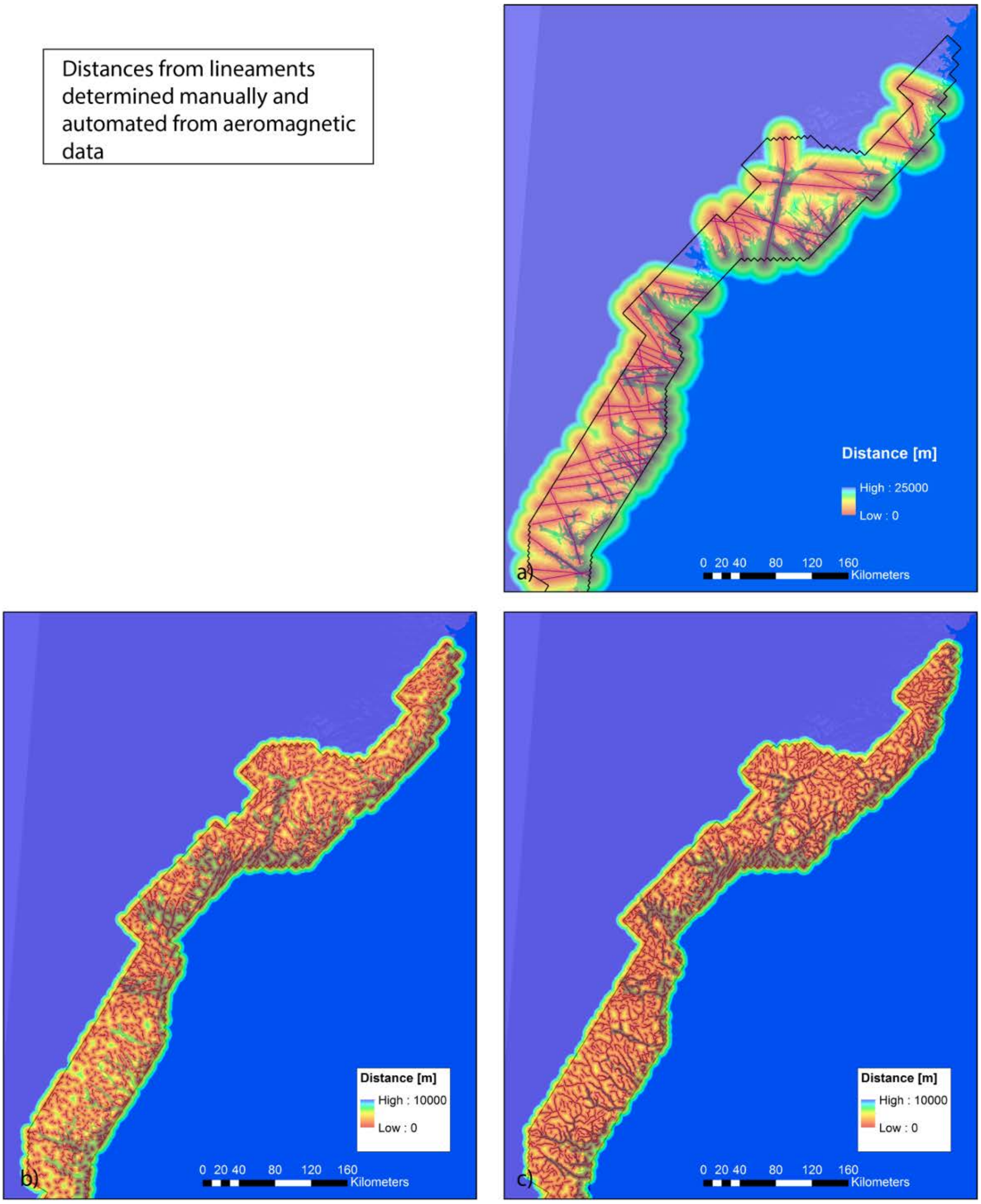

Figure 49. *Distances from lineaments determined from the AEROMAG data sets. In* ***A.*** *the manually determined features are used (see yellow lines in Figure 48) associated with e.g. secondary fault zones. In* ***B.*** *and* ***C.,*** *features are used calculated with the automated scheme involving texture analysis, symmetry filtering and morphological skeleton process (see section "Detection of lineaments from regional airborne magnetic data (Pb1, P2, T1, T2)"). For the features* ***B.*** *and* ***C.,*** *phase symmetry filters are employed that detect elongated anomalies with positive and negative polarities, respectively. (Because topography variations introduce artificially determined features, features are not considered in B at locations, where the curvature of the ground clearance has high magnitudes (see Fig. 43). The distance maps are used for the criteria/proxy elements P1b (using the manual detected features in A) and P2 (using the automated detected features in B and C).*

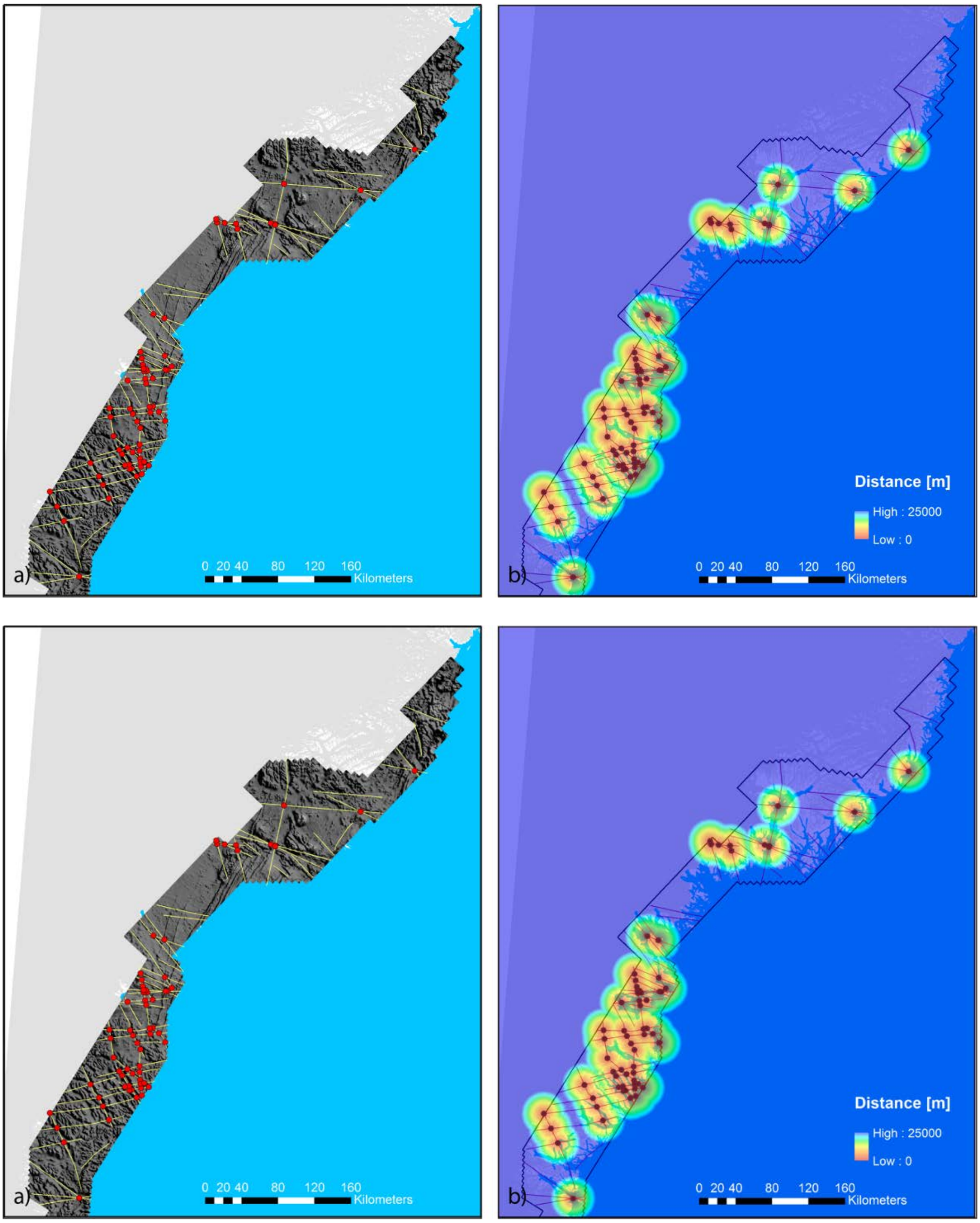

Figure 50. *Distances from structural intersections.* ***A.*** *The intersections (red dots) of lineaments (yellows) are shown that are manually determined from the AEROMAG data sets (the greyscale image shows the TMI of these magnetic data).* ***B.*** *Minimum distances from these intersections are presented as a colored image. The distance map is used for the criteria/proxy element T1.*

Circum-Artic magnetic and gravity data

The areas of AEROMAG surveys from South-East Greenland are rather narrow (widths of ~40 - 70 km in an E-W direction) and therefore they are not well suited to identify deep-seated, regional structures typically associated with low spatial wavenumbers in the magnetic maps. In recent years a few of compilations of magnetic and gravity data from the complete Arctic region are made (e.g. Verhoef *et al.* 1996; Kenyon *et al*. 2008; Gaina *et al.* 2011), and they can be very helpful in identifying some of these regional trends not detectable by the AEROMAG data. In particular, they allow some tracing of trends across the inland ice, inaccessible for any kind of field reconnaissance.

Because the most recent compilations performed within the development of the NAG-TEC atlas are not released for public use yet, we use here instead the Circum-Arctic magnetic and gravity maps (CAMP-M and CAMP-G) made by Gaina *et al.* (2011).

Magnetic data from the CAMP-M compilation (Gaina *et al.* (2011) combines different air-borne and ship-borne data for short-wavelength (< 400 km), but uses satellite-derived magnetic anomalies for the long wavelengths. In the area we consider (onshore South Greenland and offshore Southeast Greenland), the CAMP-M uses mainly airborne data from the former Verhoef *et al.* (1996) compilation and from the earlier AEROMAG surveys performed in West Greenland from 1992 to 2001 (Rasmussen *et al.* 2013) and from the GICAS survey by GEUS. The grid generated after merging the airborne data were upward continued to 1 km above the ground, high-pass filtered and finally combined with the low frequencies from satellite data. Grid spacing of the final compilation is 2 x 2 km.

Gravity data from the CAMP-G compilation (Gaina *et al.* (2011) is a combination of Free Air anomaly (for oceanic areas) and Bouguer anomaly (for land areas), having a grid size of 10 x 10 km. For many parts of the onshore regions, they applied a Bouguer correction to the grid from the former ArcGP compilation (Kenyon et al. 2008) available as Free Air anomalies. To perform the Bouguer correction on the ice shield, ice-thickness estimates from the National Snow and Ice Data Center (http://nsidc.org/data/dems/index.html) are used.

Detection of first-order trends from CAMP magnetic and gravity data (S1b, S1c)

The obtained deep-seated 1st-order lineaments from the regional gravity and magnetic data are used for the determination of the evidential maps S1b and S1c, respectively. These evidential maps are used to identify areas possibly having the required mantle source.

Trends from CAMP magnetic data

Because of the combination of data sets of varying quality (e.g. some data were collected in the 80-ties before GPS was available for precise positing) and different acquisition parameters (e.g. different line spacing and flight heights), the resolution and reliability of the CAMP-M compilation is varying spatially. This makes the identification of magnetic trends challenging, because they can be difficult to trace over large distances. For this reason, identification of trends is not based on a single parameter, but a number of different quantities (see Fig. 51) are considered to identify and pick them.

We are of the opinion that the workflows used for lineament detection in the AEROMAG data are very helpful in this context and therefore we exposed the regional data to the same workflows. However, parameters in the workflow were changed in a way that lineaments with larger wavelength associated with deep-seated fault zones are pronounced in the processing.

Main trends we obtained are shown in Figure 51. Some of the trends are rather significant in all maps, but others are only reliably detectable in some of the maps. In addition, orientations and locations obtained from the different images may differ to some extent. Such uncertainties have to be kept in mind if these regional features are correlated and compared with much more precisely located lineaments from the AEROMAG data set at the interpretation stage.

To determine the evidential map S1c, the distances from these main trends are calculated (see Fig. 53a).

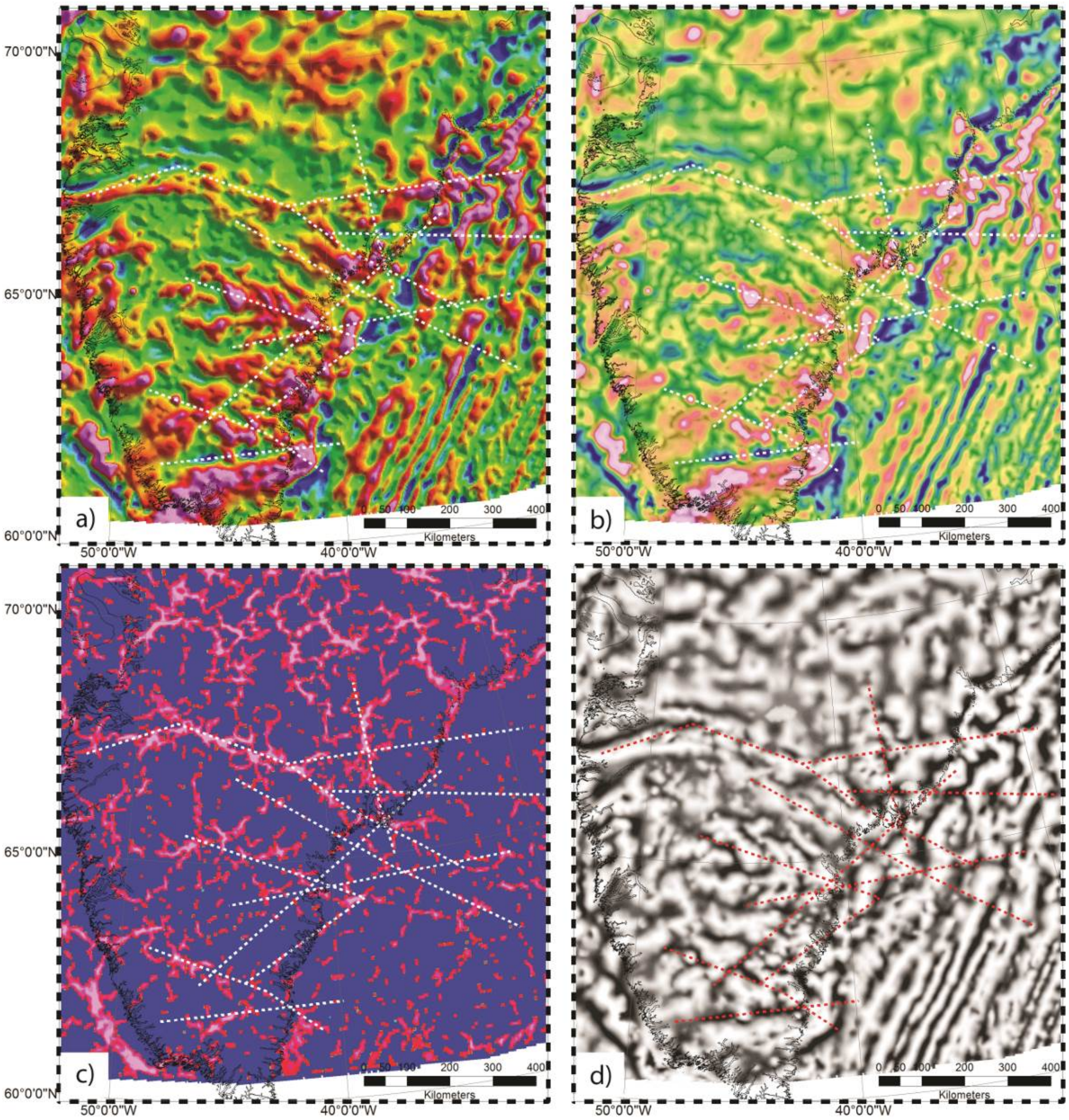

Figure 51. *Different maps determined from the magnetic field compilation CAMP-M (Gaina et al. 2011) and used to extract the main magnetic trends (see dashed lines in all figures; trends located apart from the area of interest are not picked). The different maps show: a) Color shaded map from total magnetic intensity. b) Colored map of the total magnetic intensity overlain by a transparent greyscale image of the tilt derivative. c) Map of the phase symmetry (see Holden et al. 2008) after applying the first workflow described in the section about the AEROMAG processing. In this case, a window of 5x5 cells was used in the entropy texture analysis and the wavelets of the symmetry filter had wavelengths from 8 to 128 km-. d) Map after applying a dynamic range compression (see workflow 2 and Kovesi 2012) to the magnetic field data; here, a cut-off frequency of 64 (1/km) is used for the high-pass filter. Note that magnetic fields used to generate these images have been reduced to the pole.*

Trends from CAMP gravity data

As is the case for the regional magnetic data, also the CAMP-G gravity data suffer from variations in data coverage and quality. As for the magnetic data, we therefore decided to determine the main trends again on basis of a combination of different maps, and we tested similar workflows as presented for the magnetic.

A particular problem arises from the combination of Bouguer and Free Air at the transfer zone. Therefore, it is rarely possible to resolve lineaments that run along the continental margin because such trends are obscured by a large, strong positive anomaly at the continental shelf (see Fig. 52a). This problem cannot be solved by using other compilations, because also pure Free Air or Bouguer corrected data show strong variations in the continental shelf region. Therefore, without discarding any physical reason for these trends, we ignore all trends in the gravity maps that run mostly parallel to the shoreline (i.e. do not pick them as lineaments for this study).

We observed that it is more difficult than it was for the regional magnetic data, reliably to identify regional trends. The trends, which seem to be reliable, are presented in Fig. 52. The NW-SE trend (named A in Fig. 52c) is most uncertain, and one may argue that it can be traced only over a rather short distance and may be associated with an alignment of intrusions in the Tasiilaq region.

To determine the evidential map S1b, the distances from these main trends are calculated (see Fig. 53b).

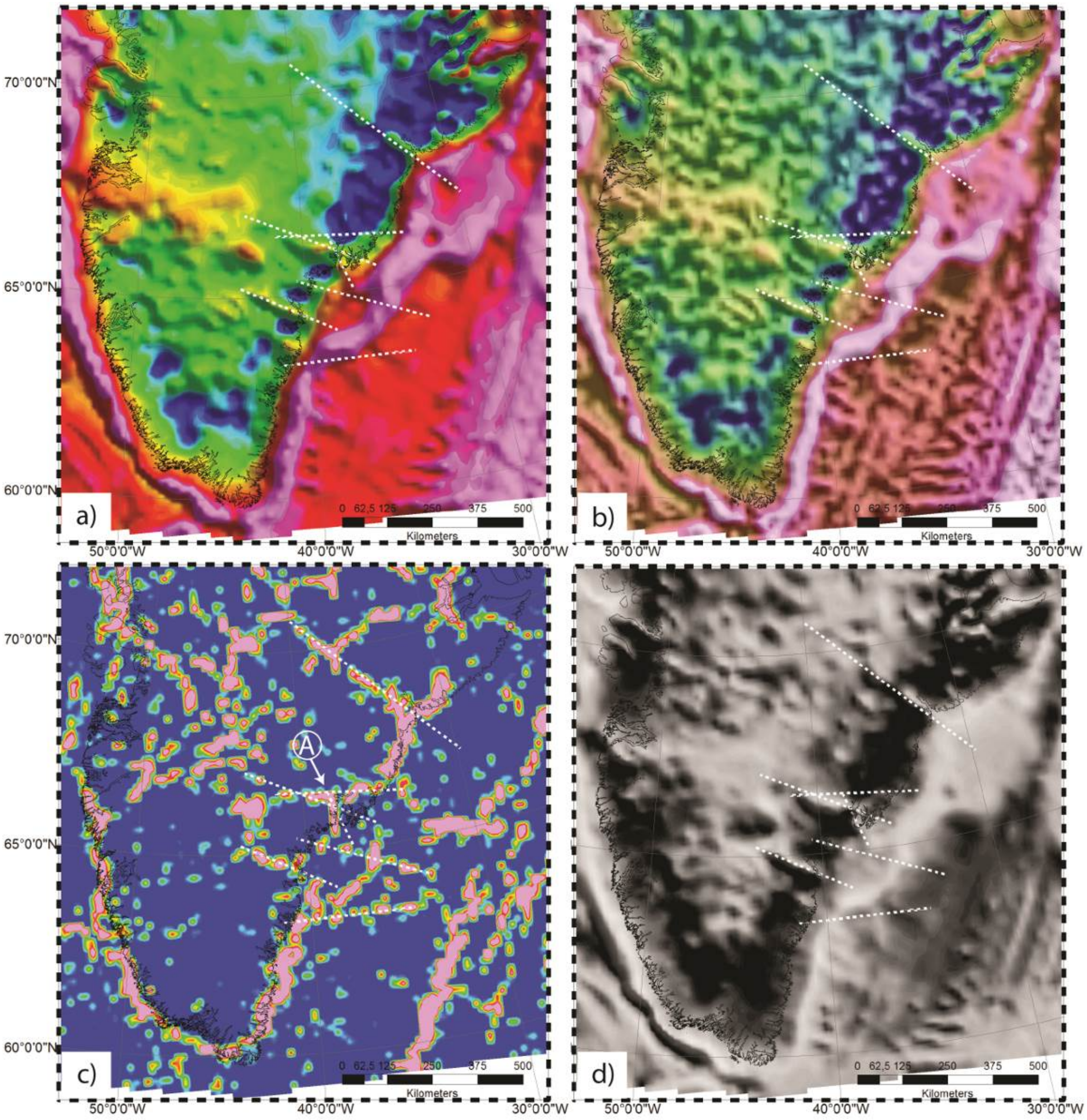

Figure 52. *Different maps that are determined from the gravity field compilation CAMP-G (Gaina et al. 2011) and used to extract the main trends in the gravitational attraction (see dashed lines in all figures; trends located apart from the area of interest are not picked). The different maps show: a) Color shaded map from combined Bouguer and Free Air anomaly. b) Colored map of the same anomaly that overlain by a transparent greyscale image of the tilt derivative. c) Map of the phase symmetry (Holden et al. 2008) after applying a similar workflow as the ones described in the section about the AEROMAG processing. In this case, 1) a dynamic range compression (see workflow 2 and Kovesi 2012) was performed with a cut-off frequency of 1/5000 km, 2) afterwards the entropy (window size 3x3 cells) was calculated in the texture analysis (see workflow 1), and 3) finally the symmetry filter was applied (using wavelets with wavelength of 30 to 480 km). d) Map after applying a dynamic range compression onto the gravity anomaly; here, a cut-off frequency of 170 (1/km) is used for the high-pass filter.*

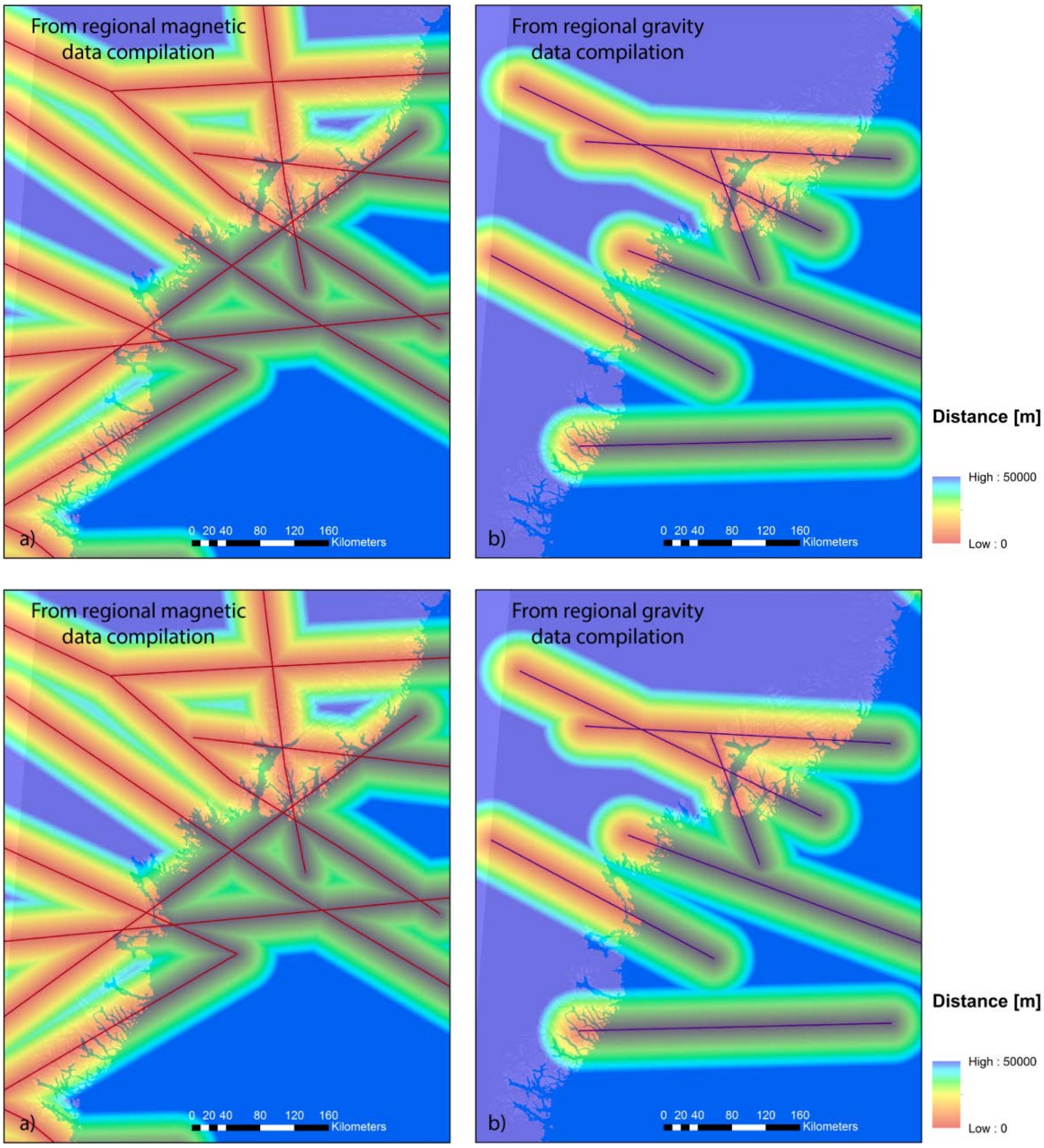

Figure 53. *Distances from lineaments that are determined from magnetic field compilation (**A.**) CAMP-M and the gravity field compilation (**B.**) (See Figs 51 and 52). The distance maps are used for the criteria/proxy elements S1c (from magnetic) and S1b (from gravity).*

Evidential maps not considered in the next steps

The following maps were evaluated after processing and judged not to be suitable for further use in this study.

T3 – Major bends of structures: The evidential map produced to mimic bends on structural components like faults, shear zones, etc. is very much affected by topographical effects creating uncertain or artificial bends of the structures. Moreover, areas with very sparse information on structures, e.g. the southwestern-most part of the study area and, even more pronounced, the north-eastern and northern parts of the study area, are showing broad artificial signatures. In the gridding process associated with the production of the evidential map, these areas are wrongly mapped out as being characterised by structures with a high degree of bending. This is caused by the presence of structures lying just outside the affected areas.

Step 3: Fuzzification of evidential maps

In the current work, the evidential maps are transformed by a fuzzy membership function (see also the section ‘Step 3: Fuzzification’ on page 35).

The fuzzification process

The evidential maps are transformed using the Fuzzy Membership tool in ArcGIS Spatial Analyst. The description of the fuzzy membership functions below is partly based on the description provided by ArcGIS v. 10.3 manual.

In the fuzzification process, the ideal definition for membership to the set is defined. Each value of the phenomenon, which is reflected in the evidential maps, most central to the core of the definition of the set will be assigned as 1. Those values that definitely are not part of the set, are assigned a 0. The values that fall between the two extremes fall in the transitional zone of the set, the boundary. As the values move away from the ideal or the centre of the set, they are assigned a decreasing value on a continuous scale from 1 to 0. As the assigned values decrease, the original phenomenon value has less possibility of being a member of that set.

The fuzzification process characterizes the imprecision of classes for phenomena that do not have sharply defined boundaries. Fuzzification converts the original values of the phenomenon to the possibility that they belong to a defined set. The assignment of the membership values is based on expert knowledge; the operator of the process (the geologists – the expert) is determining the membership values. The membership function is tuned to reflect the experts’ opinion on the membership for specific values of the phenomenon. The defined set can consist of being suitable or within a favorable distance or having the possibility of finding a specified mineral (Fig. 55). The original values of the phenomenon are reclassified on this membership continuum through predefined fuzzy membership functions or through any other reclassification techniques.

Two parameters are essential in the definition of the functions; the spread parameter and the midpoint. In principle, the skewedness of the membership function can be controlled by tuning these parameters. In the current work the fuzzy membership functions ‘Small’ and ‘Large’ are used – the expression of the functions are given here:

Function:	Expression:	Description:
Large	$\mu(x) = \frac{1}{1 + \frac{x - f_1}{f_2}}$ $where\ user\ input\ f_1\ is\ the\ spread\ and\ f_2\ is\ the\ midpoint$ $where\ user\ input\ f_1\ is\ the\ spread\ and\ f_2\ is\ the\ midpoint$	Sigmoid shape where large inputs have large membership
Small	$\mu(x) = \frac{1}{1 + \frac{x f_1}{f_2}}$ $where\ user\ input\ f_1\ is\ the\ spread\ and\ f_2\ is\ the\ midpoint$ $where\ user\ input\ f_1\ is\ the\ spread\ and\ f_2\ is\ the\ midpoint$	Sigmoid shape where small inputs have large membership

The *spread* determines how rapidly the fuzzy membership values decrease from 1 to 0. The larger the value is, the steeper the fuzzification around the so-called midpoint is (see here below for explanation). Formulated in another way, as the spread gets smaller, the fuzzy memberships approach 0 more slowly. The selection of the appropriate spread value is a subjective process dependent on the range of the input (also called crisp) values. For the functions FuzzyGaussian and FuzzyNear, the default value of 0.1 is a good starting point. Typically, the values vary within the ranges of [0.01–1] or [0.001-1], respectively. For Small and Large, the default value of 5 is a good starting point where, typically, the values vary between 1 and 10. For example of different spread see Figure 54.

The *midpoint* assigns the value of the input data wherewere the fuzzy membership function is set to be 0.5 (Figs 54 and 55). Any fuzzy membership value greater than 0.5, implies that the original phenomenon value may be a member of the set. As the fuzzification values go below 0.5, it is less likely that the original phenomenon's value is a member of the set; the values may not be part of the set. Depending on the fuzzy membership function, the midpoint is somewhat comparable to what is referred the cross over point for the fuzzy function (Fig. 55).

The fuzzy membership functions used to transform the evidential maps in the current work are summarized in Table 8. The used fuzzy membership functions were visualized with a MatLab software application. This together with visual trial-and-error exercise and inspection in ArcGIS was used to determine the most appropriate fuzzy membership parameters for the evidential maps. The resulting fuzzified evidential maps and a plot of their corresponding membership function can be seen in Figure 78 to 103 (using kriging) and Figure 104 to 110 (using natural neighbour interpolation).

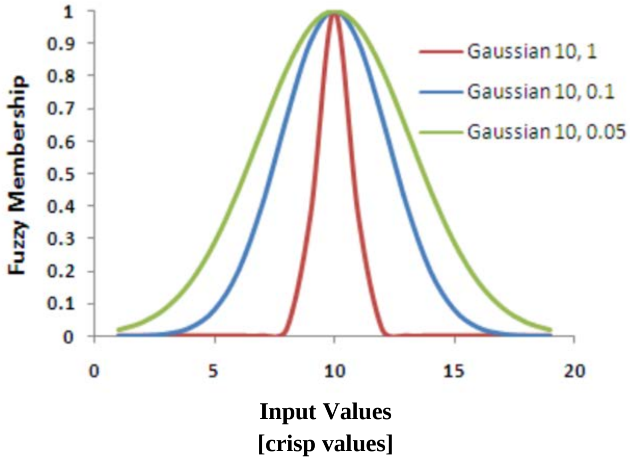

Figure 54. *FuzzyGaussian membership functions with different spread parameters values. The midpoint value is set at 10. Figure from ArcGIS v. 10.3 manual.*

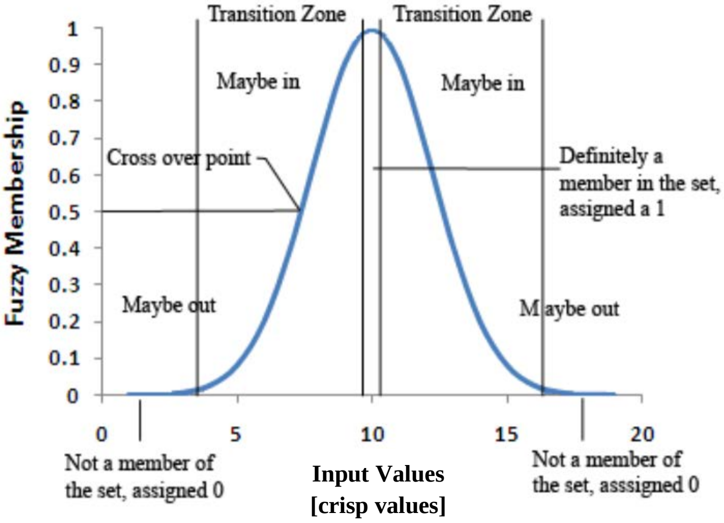

Figure 55. *Fuzzy membership function diagram. Cross over point corresponds to an assigned midpoint at which the fuzzy membership value is 0.5; everything above a membership of 0.5 can be thought of ‘maybe in’ whereas everything below can be thought of as ‘maybe out’. A membership value of 1 (or very near 1) is definitely ’in’ (in other words; highly evident for the phenomena mimicked by the data) whereas 0 (or very nearby 0) is definitely ‘out’. The width of the transition zone depends on the phenomenon being modeled, what is known about the phenomenon, the definition of the set, and the accuracy of the measurement. Changing the parameters of the fuzzification function can define the characteristics of the transition zone. Figure from ArcGIS v. 10.3 manual.*

Table 8. *Summary of fuzzy membership functions used to transform evidential maps. The spread parameter and midpoint are explained in the text.*

Fuzzy Membership function	Description	Transformed evidential maps	Spread parameter	Midpoint	Lowest membership score	Min. in evidential map input data	Max in evidential map input data
Small	Defines a fuzzy membership function with the smaller input values having membership closer to 1.	T1	8	3000	0.0012	0	141424
		Pb1	8	3000	0.000005	0	79329
		T1a	2	1500	0.0003	0	82640
		T1b	2	1500	0.000048	0	215914
		T1c	2	1500	0.0000084	0	516160
		S2	2	10000	0.000083	0	104762
		S1b	5	20000	0.0025	0	65744
		S1c	5	20000	0.00004	0	151186
		P2comb	8	1000	$2.82e^{-10}$	0	19176
		P2pos	8	2000	0.00000003	0	17240
		P2neg	8	2000	0.00000001	0	19176

(Table 8 continued)

Fuzzy Membership function	Description	Transformed evidential maps	Spread parameter	Midpoint	Lowest membership score	Min. in evidential map input data	Max in evidential map input data
Large	This function is used to indicate that large values of the input raster have high membership in the fuzzy set.	P4	5	6	0.000001	0	12.44
		T1e	3	2.5	0.06	1	4.88
		T2	5	1.25	0.000001	0.01	2.52
		T2a	100	0.94	0.00002	0.84	0.99
		T2b	100	1.0	0.09	0.97	1.02
		T2c	100	1.1	0.0002	1.00	1.19
		T4	5	2	0.01	0.00019	9.15
		T3a	5	8	0.00003	1	40.74
		T3b	5	7	0.000001	0.25	14.43
		T3c	5	3	0.00013	0.5	12.02
		T3d	5	4.5	0.0005	1	8.17
		T3e	5	2	0.00003	0.25	5.99
		T3f	5	0.8	0.0029	0.25	3.49
		T3g	5	0.25	0.25	0.2	6.56
		T3i	5	100	0.01	40.57	206.51

Step 4. Integration of datasets

The fuzzy integration process

Set-theoretic operations can, similar to classical or Boolean set theory, be applied on fuzzy sets. The purpose of the applied operators is to integrate the different fuzzy membership functions and hereby get a portrait in the form of a single integrative map that reflects the relationship between all sets of evidential maps chosen to reflect a conceptualised model of, in this case, a mineral system for orogenic type of gold. The resulting integrative map is here referred to as prospectivity map.

Several operations are available and commonly used in ArcGIS™ and spatial data analysis. The five operators most commonly used in mineral exploration-related datasets are: Fuzzy AND, Fuzzy OR, Fuzzy algebraic product, Fuzzy algebraic sum and Fuzzy Gamma operator. An *et al* (1991), Bonham-Carter (1994) and Carranza & Hale (2001) have described these in further details. In this work is only the Fuzzy AND and the Fuzzy OR operators used. The Fuzzy Overlay tool in the ArcGIS™ extension Spatial Analyst was used for the integration of evidential maps into a single prospectivity map.

The equation of the Fuzzy AND (FA) and the Fuzzy OR (FO) is:

Fuzzy AND $\mu_{FA} = MIN(\mu_1, \mu_2, \dots, \mu_n)\ \mu_{FA} = MIN(\mu_1, \mu_2, \dots, \mu_n)$

and

Fuzzy OR $\mu_{FO} = MAX(\mu_1, \mu_2, \dots, \mu_n)\mu_{FO} = MAX(\mu_1, \mu_2, \dots, \mu_n)$

Where, for the Fuzzy ARE, the $\mu_{FA}\mu_{FA}$ is the output fuzzy score and $(\mu_1, \mu_2, \dots, \mu_n)(\mu_1, \mu_2, \dots, \mu_n)$ are, respectively, the input fuzzy evidential scores at location in fuzzified evidential map 1, fuzzyfied evidential map 2, …, fuzzified evidential map n. The $MINMIN$ is the arithmetic function that selects the smallest value among a number of input values. The output of the FA operator is subsequently controlled by the lowest fuzzy score at every location. This means, that if one fuzzified evidential map at a location has a score 0 in one evidential map, the resulting output will be zero even though other maps have higher values. The FA is consequently useful for combining complementary sets of evidence, meaning that the pieces of evidence to be combined via the FA operator are deemed all to be necessary to support the proposition of mineral prospectivity at every location (above description modified after Carrenza, 2009).

For the Fuzzy OR, the $\mu_{FO}\mu_{FO}$ is the output fuzzy score and $(\mu_1, \mu_2, \dots, \mu_n)(\mu_1, \mu_2, \dots, \mu_n)$ are, respectively, the input fuzzy evidential scores at location in fuzzified evidential map 1, fuzzyfied evidential map 2, …, fuzzified evidential map n. The $MAXMAX$ is the arithmetic function that selects the highesth value among a number of input values. The output of the FO operator is subsequently controlled by the highest fuzzy score at every location. This means, that if one fuzzified evidential map at a location is 1, even though in at least one of the other fuzzified evidential maps combined with this map by the use of the FO operator has a score of 0 at the same location, the resulting output fuzzy score at this location is still 1 Consequently, the FO operator is well-suited for combining supplementary sets of evidence, meaning that at least one of the pieces of evidence to be combined via this operator is deemed necessary to support the proposition of mineral prospectivity at every location (above description modified after Carrenza, 2009).

In the current work a score of exactly zero in the fuzzified evidential maps has been set to a very low score value. This is done as the study region is much underexplored and only sparsely covered with data at low resolution. Consequently, to make sure that areas at which the fuzzy score in one evidential dataset, which could be caused by the underexplored and poor data resolution, still is reflected by other datasets with higher fuzzy score, a score of zero is set to a low score above zero (see 'Lowest membership value' in Table 8).

The fuzzified evidential maps for the different mineral system components ('Source', 'Pathways', 'Physical Trap' and 'Chemical Trap') combined by fuzzy operators are referred to as **'fuzzified intermediate maps'**. The final combination of these fuzzified intermediate maps area here called **'prospectivity maps'**.

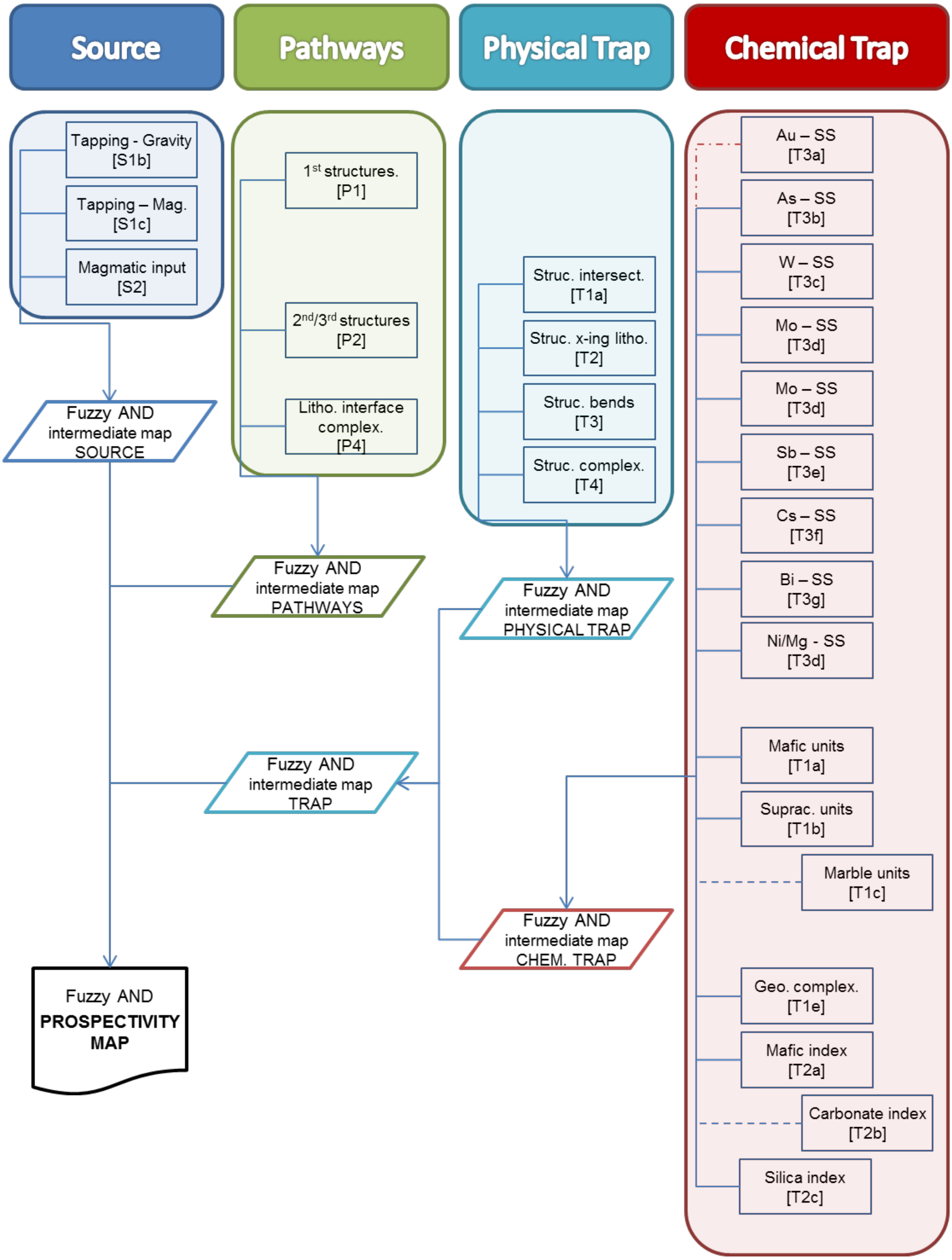

Figure 56. *Inference network used for combining the fuzzified evidential maps into a prospectivity map. The red and blue stippled lines for 'Au-SS', 'Marble units' and 'Carbonate index' indicated evidential maps are discussed in the text.*

Resulting fuzzified, intermediate maps and prospectivity maps

The inference network used to define the integration procedure can be seen in Figure 56. It summarises the exploration model for the mineral system of orogenic type gold and the available evidential data. The integration is done stepwise: In a first step, intermediate maps for the different mineral system components are built from the evidential maps and in the second step these intermediate maps are combined to create final prospectivity maps. To test the influence of different combinations of evidential datasets and the reliability of some of the evidential maps (see Table 9) the process was repeated and a number of different prospectivity maps were produced.

Table 9. *The different combination of fuzzified intermediate maps representing source (O1), pathways (O2), physical trap (O3) and chemical trap (O4) to determine final perspective maps (named "ProspecX"). Red boxes highlight intermediate maps, in which the combination of evidential maps has been changed from one to the next run.*

Source	Pathways	Physical Trap	Geochemical Trap	Resulting prospectivity map
All* - O1a	All* - O2a	All* - O3a	All* - O4a	**ProspecA** (Fig. 64)
All** - O1b	All** - O2b	All** - O3b	All** - O4b	**ProspecB** (Fig. 65)
All**	All**	All**	All** - O4c - excluding Au SS	**ProspecC** [not shown]
All**	All**	All**	All** - O4d - excluding Au and As SS	**ProspecD** [not shown]
All**	All**	All**	All** - O4e - excluding Au SS - excluding 'Geol. Marble units' - excluding 'Carbonate Index'	**ProspecE** [not shown]
All**	All** - O2c - excluding automatically detected faults	All**	All** - O4c - excluding Au SS	**ProspecF** (Fig. 66)
All**	All** - 02b	All**	All** - O4f - excluding all SS	**ProspecG** (Fig. 67)
All**	All**	All**	All* - O4g - excluding "mafic index" - excluding "Geol. Mafic units"	**ProspecH** (Fig. 68)

All*: Kriging is used for all evidential maps that involve gridding.
All**: The evidential maps for P4, T2, T4, T1e, T2a, T2b, T2c are done by natural neighbour interpolation gridding; Kriging is employed for all other evidential maps that involve gridding.

Prospectivity map ‘ProspecA’

In the first produced prospectivity map (‘ProspecA’; see Table 9 and Fig. 64), all evidential maps (except for T3 that will not be considered in any of the prospectivity maps) were used and all gridded maps were generated by kriging. The intermediate maps of ‘ProspecA’ are shown in Figure 57. Using the kriging method enables an evaluation of areas with low or no data coverage (e.g. areas without samples or areas covered by fjords or ice). This helps extrapolating patterns and hereby generates an understanding of the overall regional prospectivity. However, kriging is not a precise interpolation method for dense data coverage, e.g. the evidential datasets for mineral indices from satellite data.

Prospectivity map ‘ProspecB’

Consequently, a second prospectivity map (‘ProspecB’; see Table 9 and Fig. 65) were produced in which gridded evidential maps with dense data coverage are generated by natural neighbour gridding (proxy code P4, T2, T4, T1e, T2a, T2b, T2c). All other gridded evidential maps, e.g. stream sediment geochemistry, are still done by kriging. The intermediate maps of ‘ProspecB’ are shown in Figure **58**. The resulting prospectivity map ‘ProspecB’ are a better representation of true data values in areas with high coverage.

To test the reliability and the influence of different evidential maps in the fuzzy inference network, the process was repeatedly run excluding a number of different evidential maps.

Prospectivity map ‘ProspecC’

In the first test, prospectivity map ‘ProspecC’ (see Table 9), the evidential map of gold in the stream sediment geochemistry was excluded from the intermediate map for the mineral system component ‘Chemical Trap’. Because the changes of the resulting prospectivity map ‘ProspecC’ are minor compared to ‘ProspecB’, we only show here the changes of the corresponding intermediate map of the ‘Chemical Trap’ (Fig. 59). The reason for excluding the gold from the fuzzy inference network system is to validate the system’s independence of gold in stream sediment geochemistry.

Prospectivity map ‘ProspecD’

In the next test both stream sediment geochemistry for arsenic and gold were excluded from the inference network, and the prospectivity map ‘ProspecD’ was generated (see Table 9). Arsenic is regarded as one of the stronger pathfinder elements for gold mineralisation, which is why we would like to test the dependency of this evidential map, and if the resulting prospectivity is robust with respect to the remaining targeting elements. As for the ‘ProspectC’, the changes in the intermediate ‘Geochemical Trap’ map (Fig. 60), and hence also to the resulting ‘ProspecD’ map, are only minor when excluding arsenic from the stream sediment geochemistry.

Prospectivity map 'ProspecE'

To test the significance of marble (extracted from the 1:500 000 geological map; Stensgaard *et al.* 2016) and carbonate mineral index (from processed remote sensing data), both are excluded in the inference network for prospectivity map 'ProspecE'. The resulting intermediate map for 'Geochemical Trap' (Fig. 61) show only minor changes.

Prospectivity map 'ProspecF'

Because of the impact of the topography on the automatically picked lineaments and to test the dependency of these relatively uncertain measures, a test was carried out by excluding the evidential map for the second- and third-order structures (see Table 9) derived from the automatically picked lineaments from the aeromagnetic data (proxy code P2). Although, changes in the intermediate map for 'Pathways' (Fig. 61) are significant it can be seen in the following discussion that the resulting prospectivity map ('ProspecF'; Fig. 66) provides similar prediction curves (i.e. validation results, see Fig. 74) as maps from the previous tests.

Prospectivity map 'ProspecG'

The stream sediment geochemistry evidential maps (proxy T3a to T3i) dominate very much the intermediate map for 'Geochemical Trap' due to their large number compare to the remaining evidential maps. In addition, it should be tested how much impact the high variability amongst stream sediment geochemistry evidential maps has onto the prospectivity map ('ProspecG) and whether it controls its overall quality. The resulting intermediate map for 'Geochemical Trap' (see Table 9 and Fig. 62) shows that there are significant changes by excluding all stream sediment geochemistry evidential maps. But again, the changes in the prediction capabilities from 'ProspecG' (Fig. 67) to the other prospectivity maps (i.e. validation results, see Fig. 74) are only small.

Prospectivity map 'ProspecH'

From an inspection of the different evidential maps and the resulting prospectivity, it appears that the distribution of features related to mafic rocks, especially as arising from the mafic mineral index, may dominate the prospectivity results. One area that seems to be especially influenced by the mafic mineral index is situated in the region between Timmiarmiut and Skjoldungen. This region is not characterised by any observations of gold mineralisation and neither the stream does sediment geochemistry support a gold potential. Consequently, a test excluding the evidential maps of the mafic mineral index (proxy code T2a) from processed remote sensing data and the distribution of mapped out mafic rock units (proxy code T1b) were performed (see Table 9). The resulting intermediate map for 'Geochemical Trap' (Fig. 63) show significant changes. Not only the area between Timmiarmiut and Skjoldungen is affected but also other regions are influenced (e.g. around Tasiilaq). However, the overall prediction rate is improved (see Fig. 74). This means that the results have to be viewed and explained according to all evidential maps and geological validation. The resulting prospectivity map 'ProspecH' is shown in Figure 68.

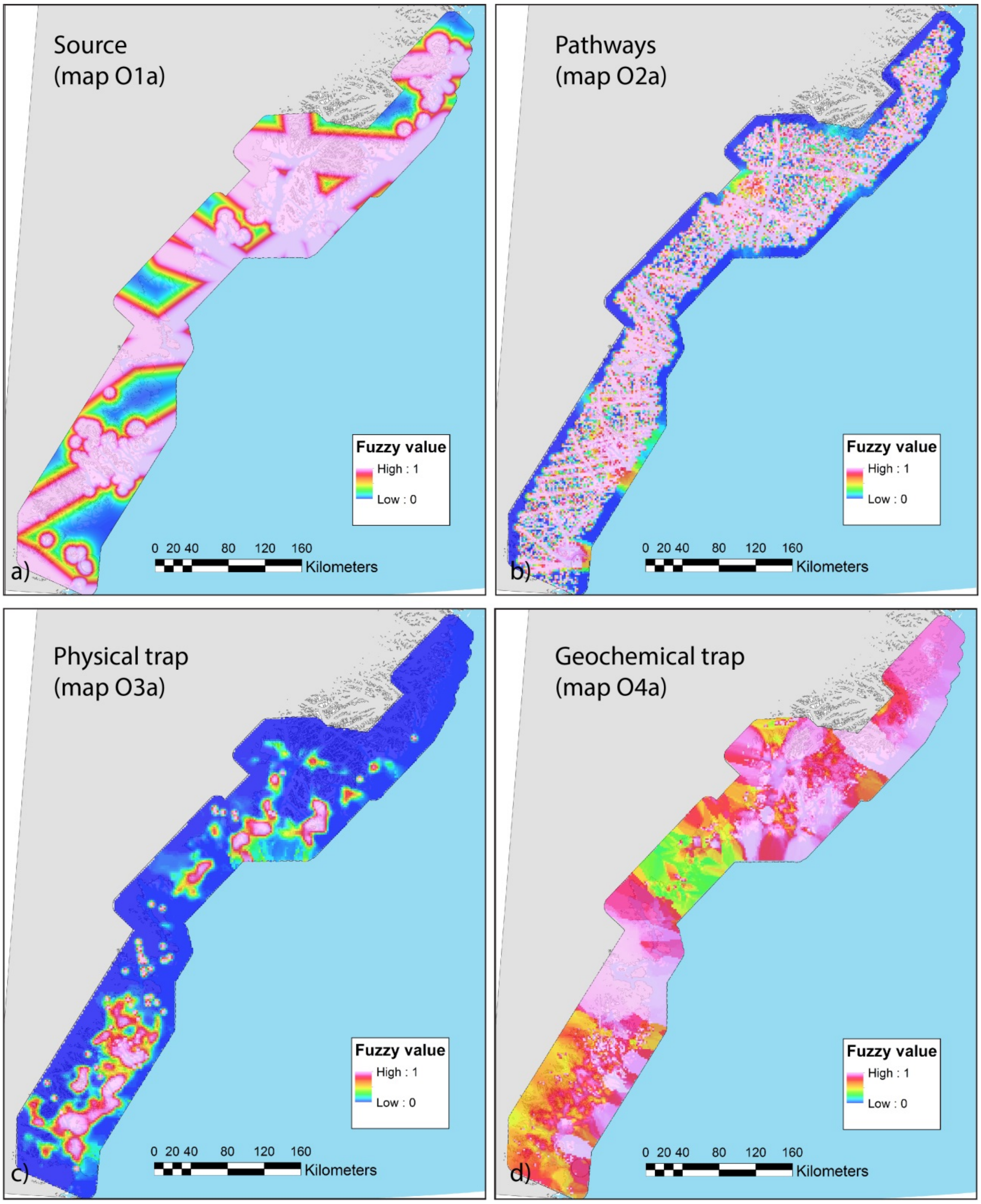

Figure 57. *Fuzzified intermediate maps describing* ***A*** *the source,* ***B*** *the pathways,* ***C*** *the physical trap and* ***D*** *the chemical trap. Kriging is used as interpolation method for all involved evidential maps that are obtained by gridding of data. The final prospectivity map that is obtained from these intermediate maps is “ProspecA” (Fig. 63).*

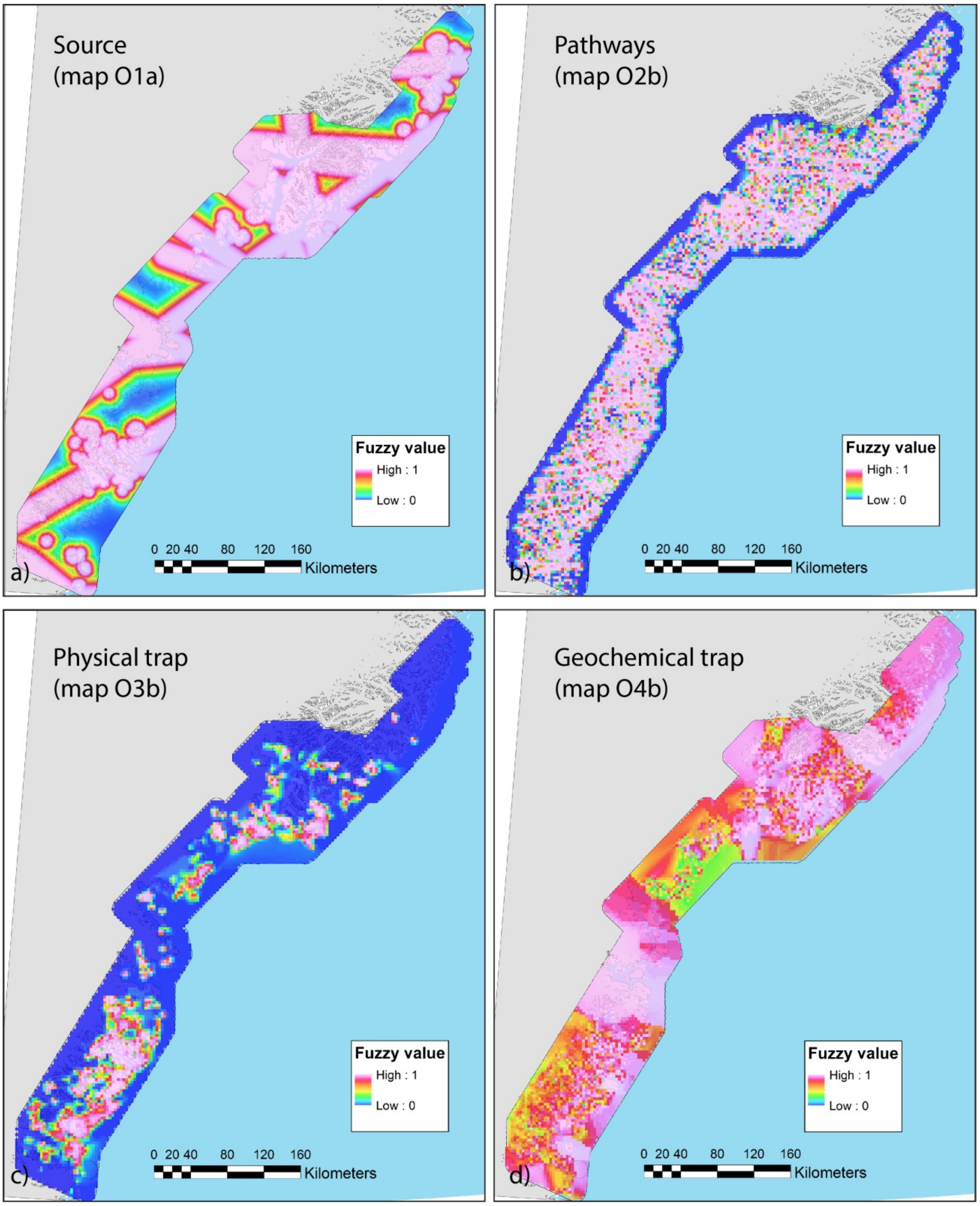

Figure 58. *Fuzzified intermediate maps describing A the source, B the pathways, C the physical trap and D the chemical trap. For the considered evidential maps P4 T2, T4, T1e, T2a, T2b, natural neighbor interpolation is used for gridding of data, but for other evidential maps used to build these intermediate maps kriging is performed. The final prospectivity map that is obtained from these intermediate maps is “ProspecB” (Fig. 65).*

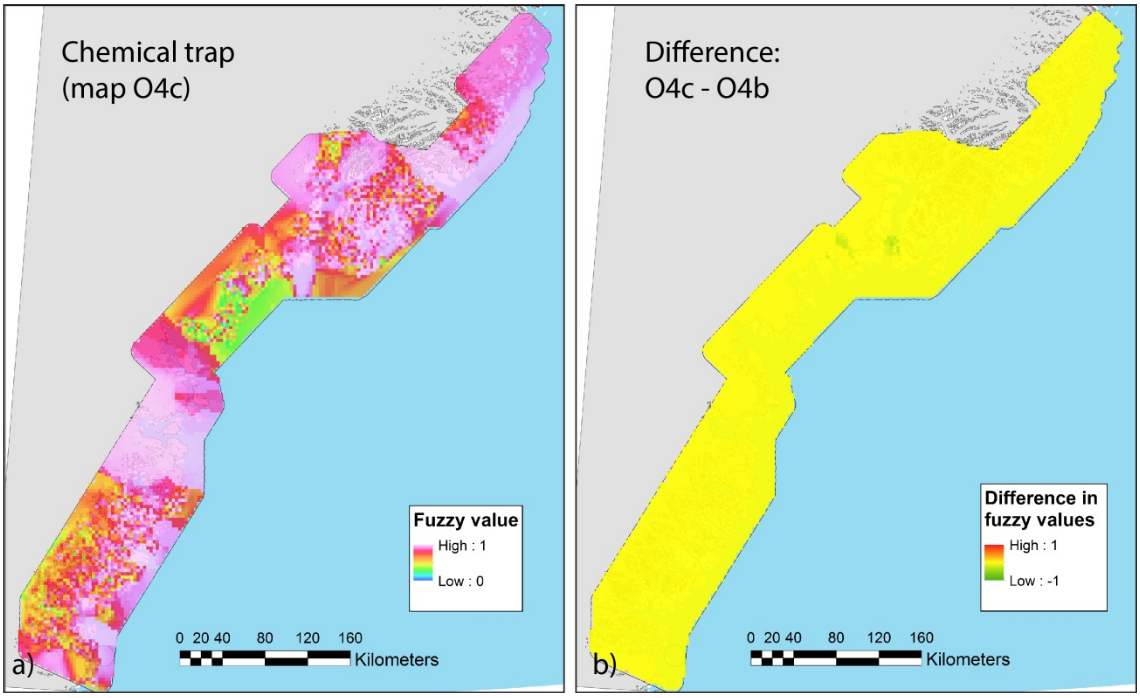

Figure 59. ***A*** *Fuzzified intermediate map O4c of the chemical trap that is used to create the prospectivity map "ProspecC". In contrast to the "ProspecB", evidential map T3a that is associated with the Au-concentrations from the stream sediments (Fig. 89 in Appendix A) is not considered in the calculation of the map of the chemical trap. In* ***B*** *the difference of the corresponding intermediate maps O4c and O4b of the chemical trap is shown, where the evidential map of Au-concentrations are not considered and are considered, respectively. Note that the changes in the resulting fuzzified intermediate map are very minor.*

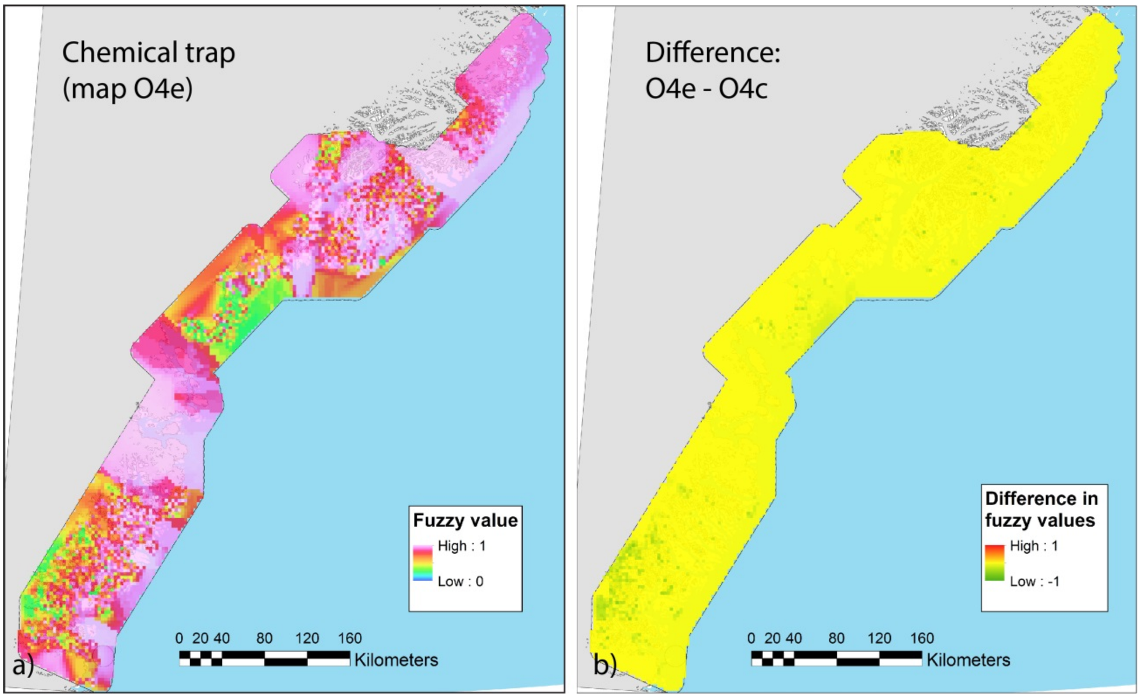

Figure 60. ***A*** *Fuzzified intermediate map O4e of the chemical trap that is used to create the prospectivity map "ProspecE". In contrast to the "ProspecC", the evidential maps T2b and T1c received from the carbonate index of the multispectral ASTER satellite data (Fig. 102 in Appendix B) and from the marble rock units extracted from the digital geological map (Fig. 99 in Appendix A) are not used. In* ***B*** *the difference of the corresponding intermediate maps O4e and O4c of the chemical trap are shown, where these two evidential maps are not considered and are considered, respectively. Note that the changes in the resulting fuzzified intermediate map are relatively minor.*

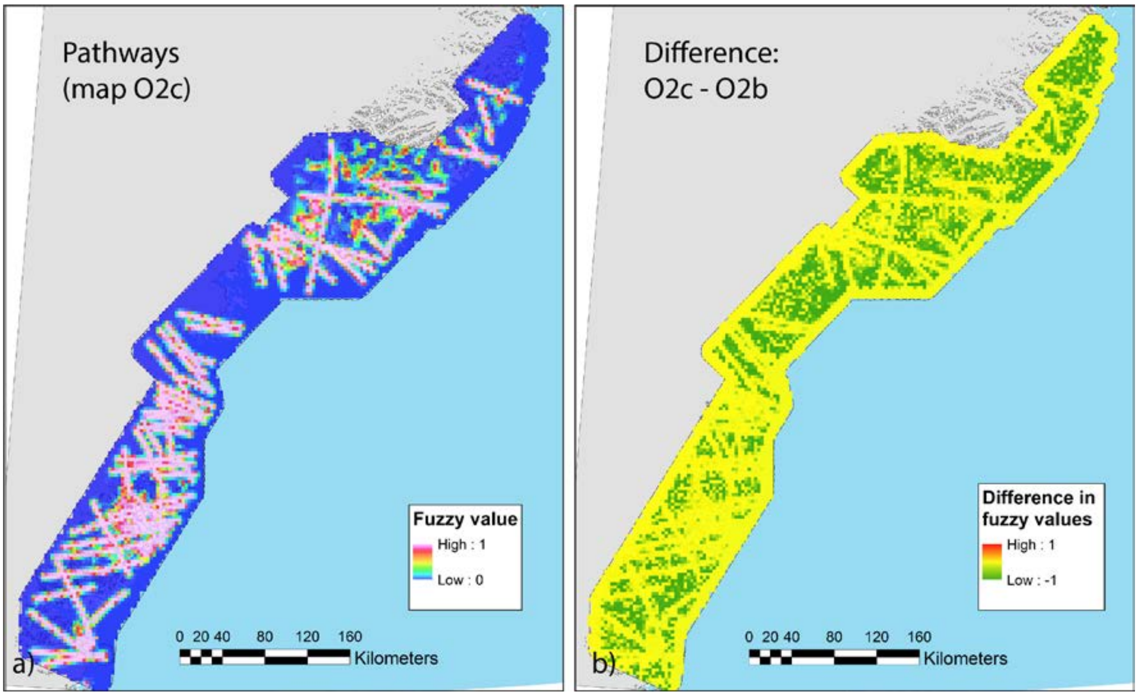

Figure 61. ***A*** *Fuzzified intermediate map O2c of the pathways that is used to create the prospectivity map "ProspecF". In contrast to the "ProspecC", the evidential map P2 received from the automated picked lineaments in the aeromagnetic data (in Appendix A) is not used. In* ***B*** *the difference of the corresponding intermediate maps O2e and O2b of the pathways is shown, where the evidential map associated with the automated picked lineaments is not considered and is considered, respectively.*

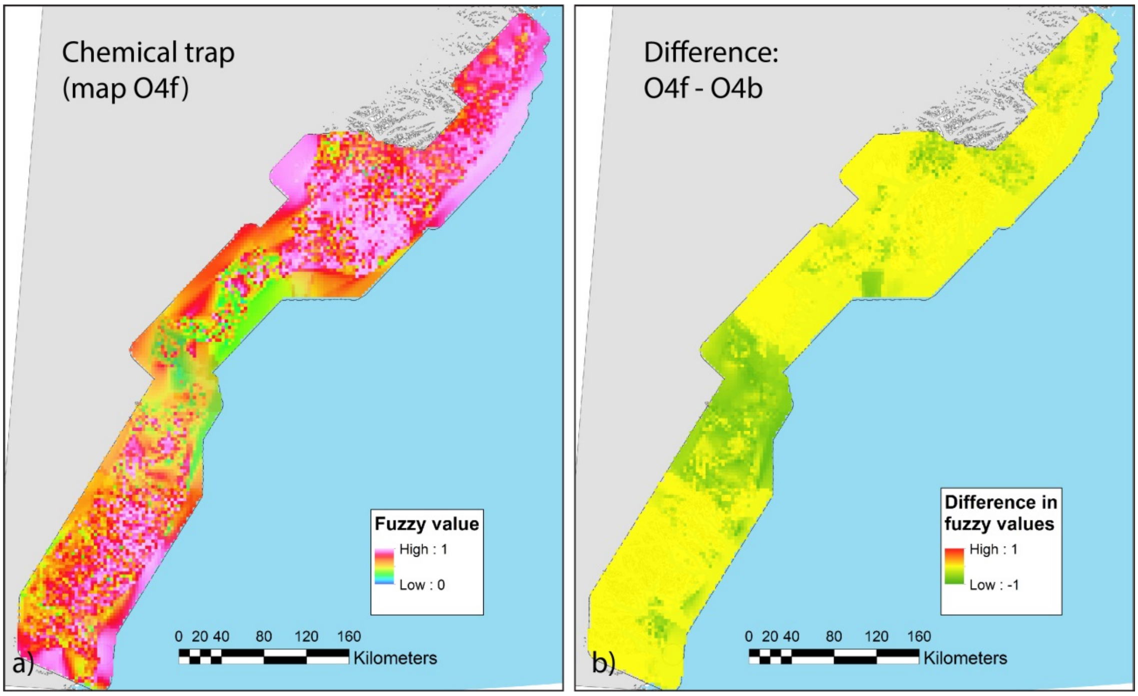

Figure 62. ***A*** *Fuzzified intermediate map O4f of the chemical trap that is used to create the prospectivity map "ProspecG". In contrast to the "ProspecB", the evidential maps of all stream sediment data are removed (Figs 89 to 96 in Appendix A). In* ***B*** *the difference of the corresponding intermediate maps O4f and O4b are shown, where evidential maps from stream sediment geochemistry are not considered and are considered, respectively.*

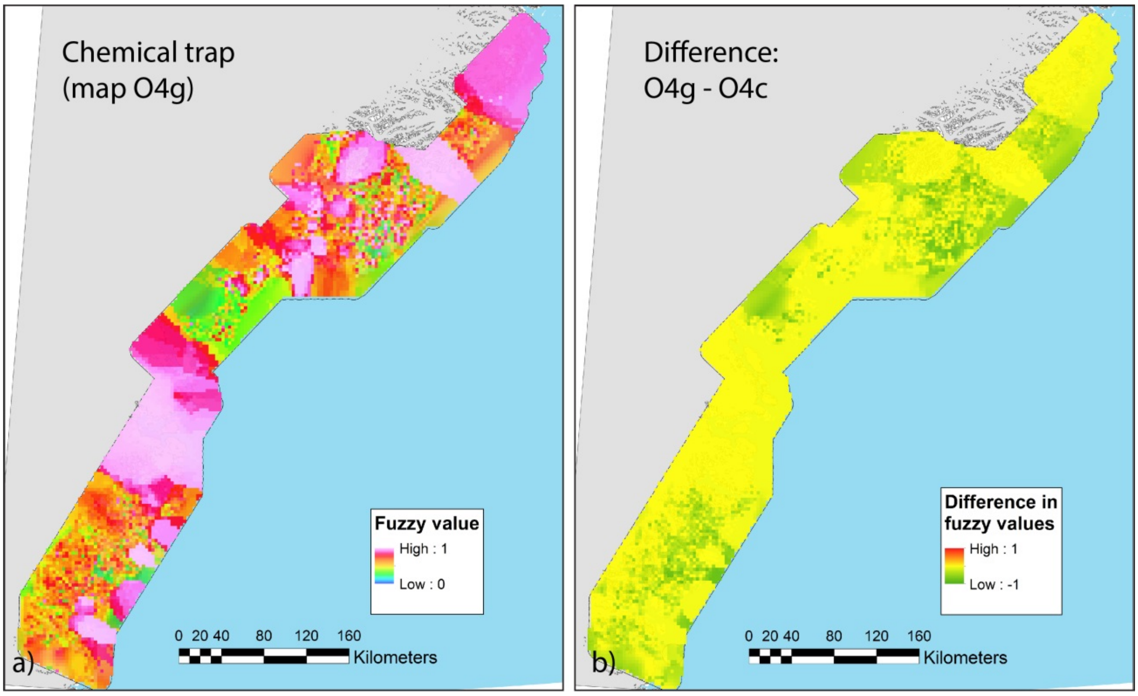

Figure 63. ***A*** *Fuzzified intermediate map O4g of the chemical trap that is used to create the prospectivity map "ProspecH". In contrast to the "ProspecC", the evidential maps of mafic geological units and the mafic mineral index from remote sensing are removed (see Fig. 97 in Appendix A and Fig. 108 in Appendix B). In* ***B*** *the difference of the corresponding intermediate maps O4g and O4c where evidential maps from the two proxies of mafics are not considered and are considered, respectively.*

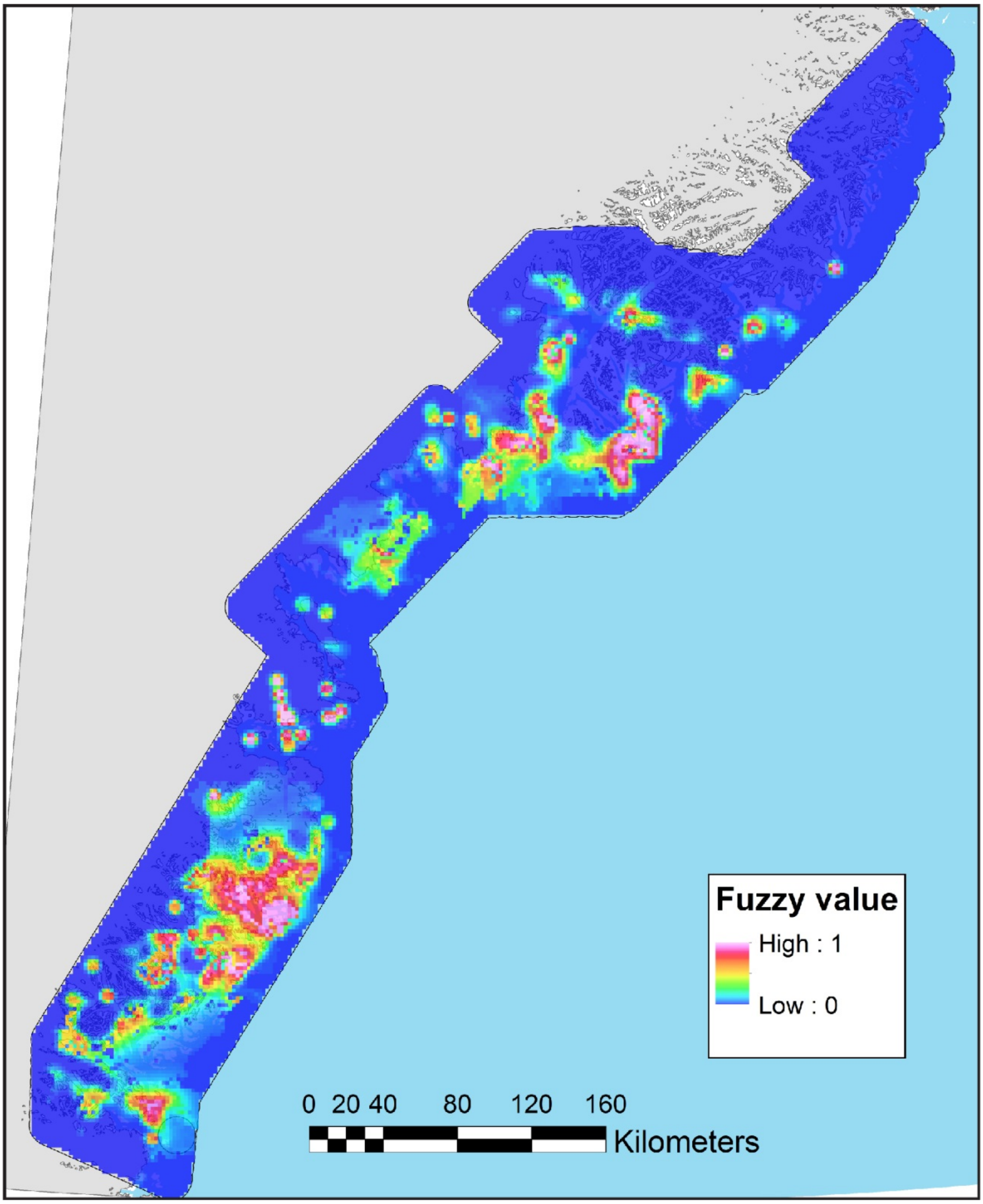

Figure 64. *Fuzzified prospectivity map "ProspecA" received by a combination of the intermediate maps O1a, O2a, O3a and O4a (see Fig. 57). All involved evidential maps that are obtained by gridding of data are generated with kriging (interpolation).*

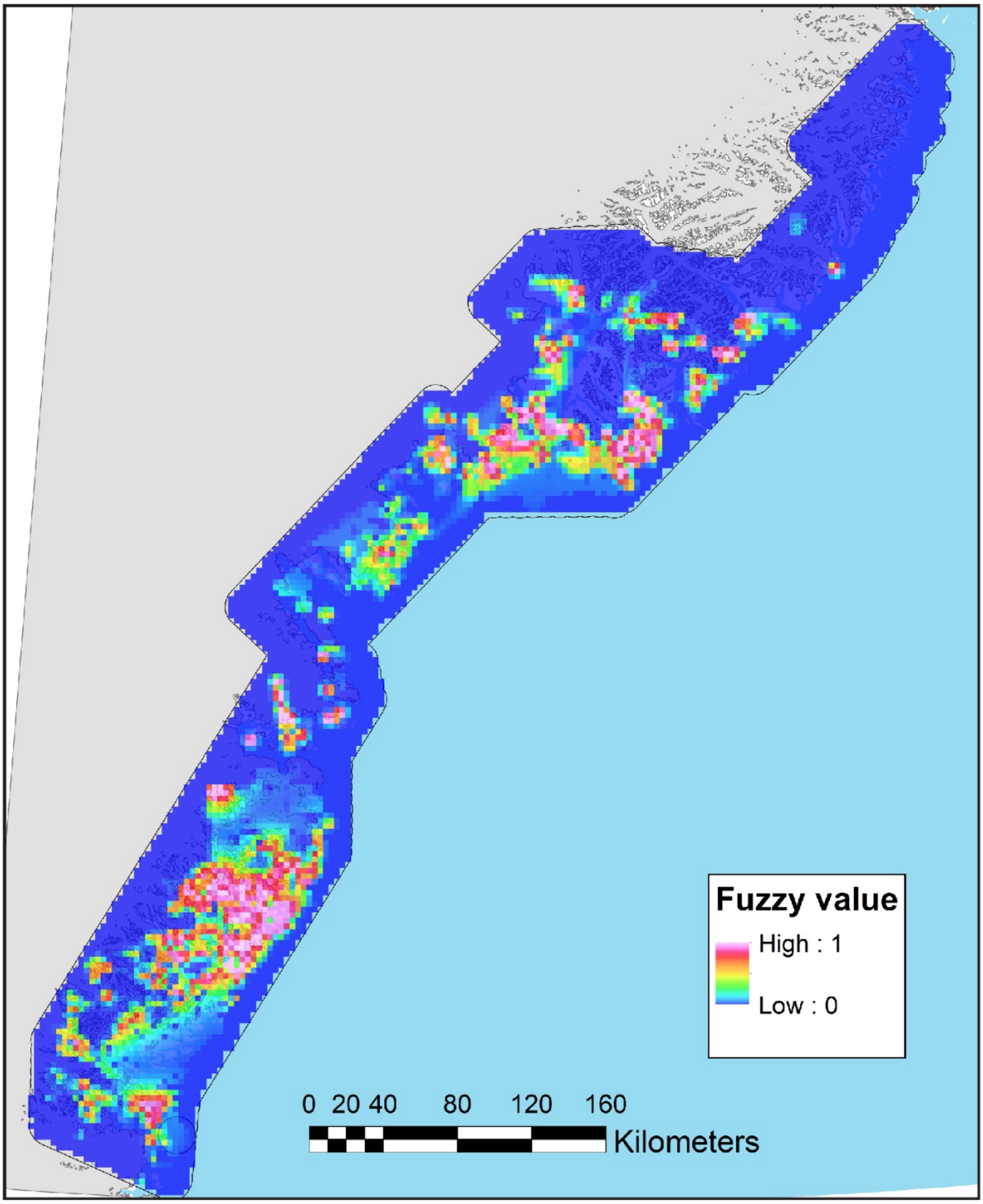

Figure 65. *Fuzzified prospectivity map "ProspecB" received by a combination of the intermediate maps O1a, O2b, O3b and O4b (see Fig. 58). The grids of the involved evidential maps P4, T2, T4, T1e, T2a, T2b and T2c are generated with natural neighbor interpolation, but grids from other evidential maps are created by using kriging (interpolation).*

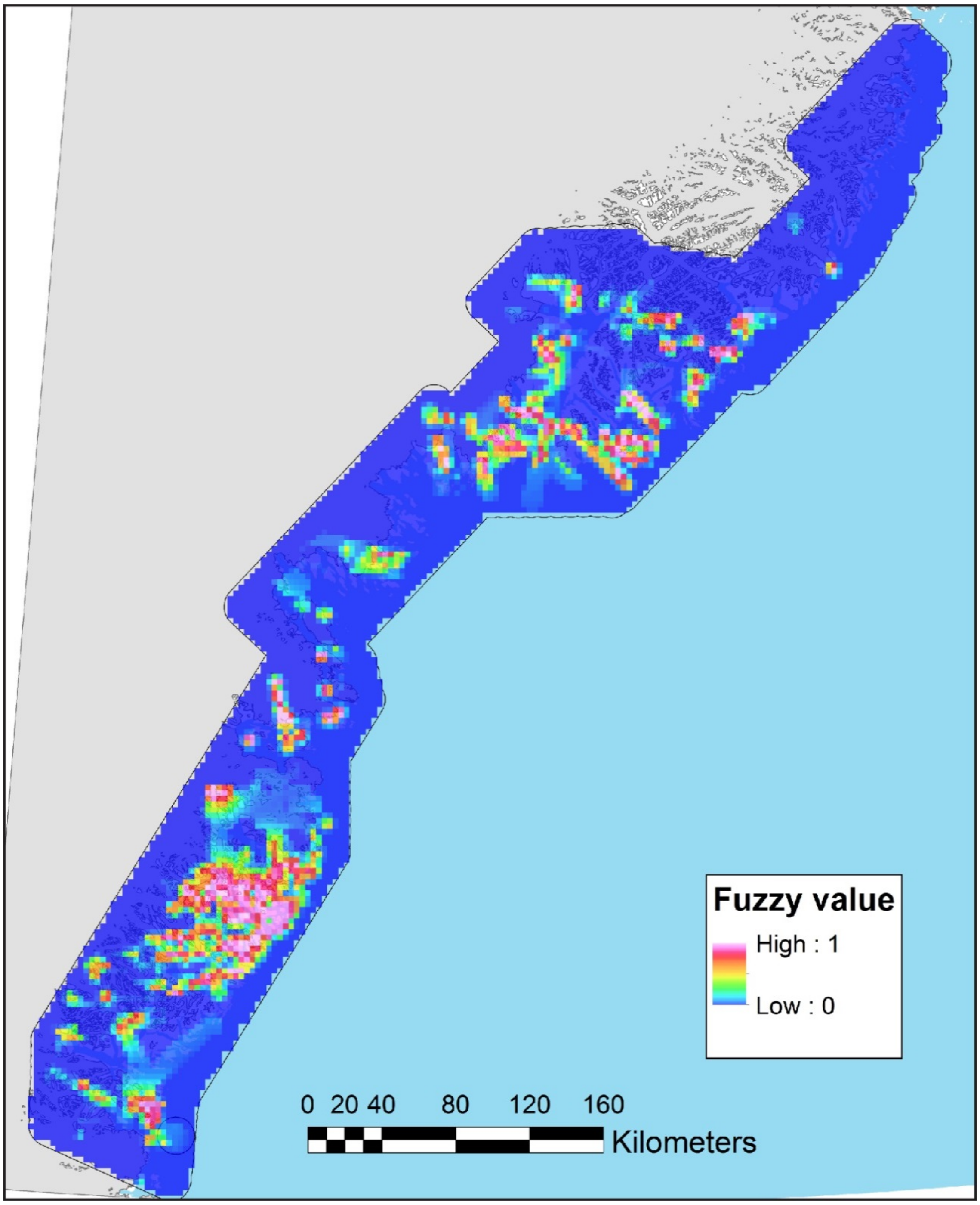

Figure 66. *Fuzzified prospectivity map "ProspecF" received by a combination of the intermediate maps O1a, O2c, O3b and O4c.In the intermediate map O2c for the pathways (*Fig. 61*), the evidential map (P2) that is associated with the automated picked lineaments from the aeromagnetic data is not considered.*

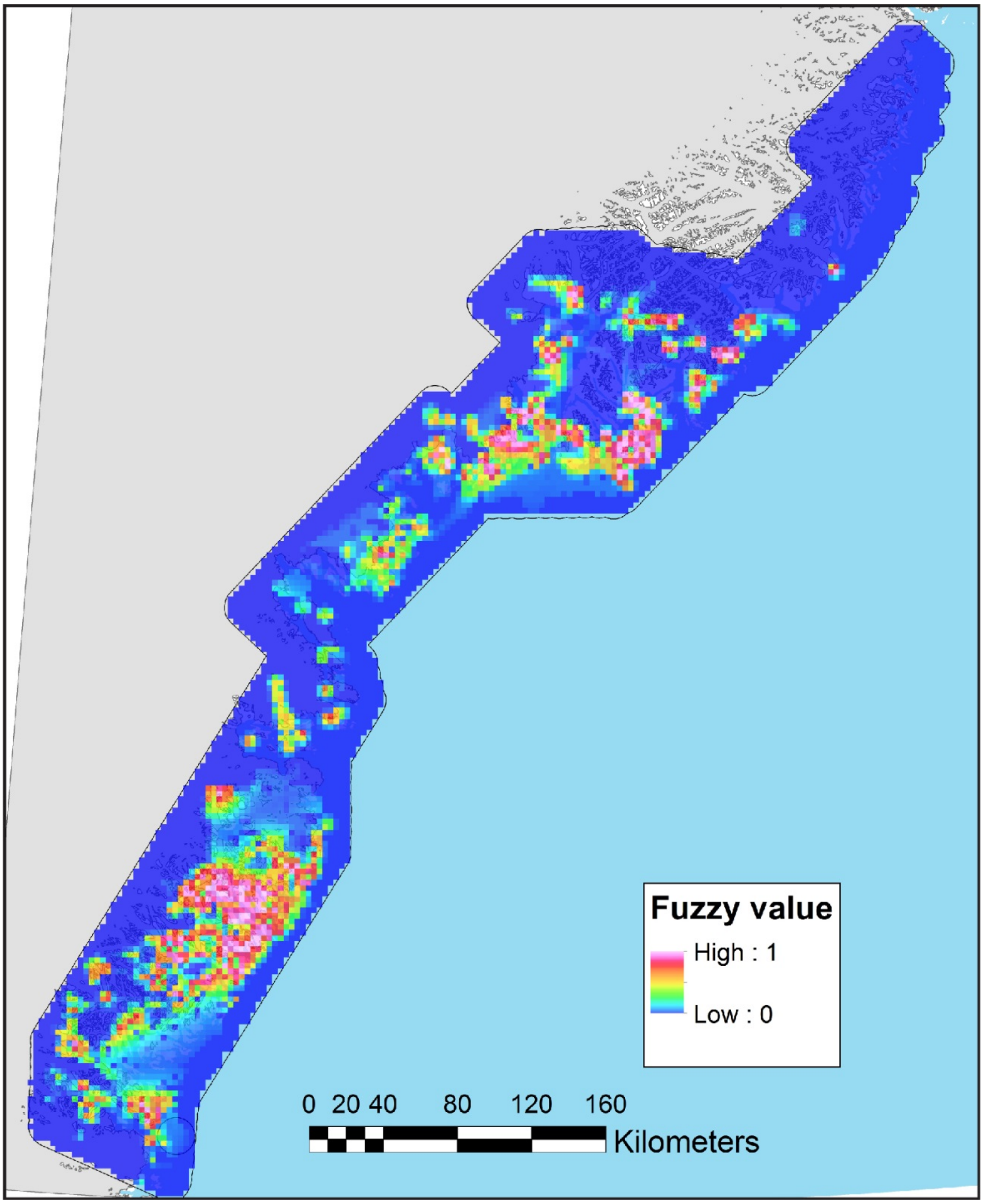

Figure 67. *Fuzzified prospectivity map ”ProspecG” received by a combination of the intermediate maps O1a, O2b, O3b and O4f). In the intermediate map O4f (Fig. 62) for the geochemical trap, the evidential maps associated with stream sediment geochemistry are not considered.*

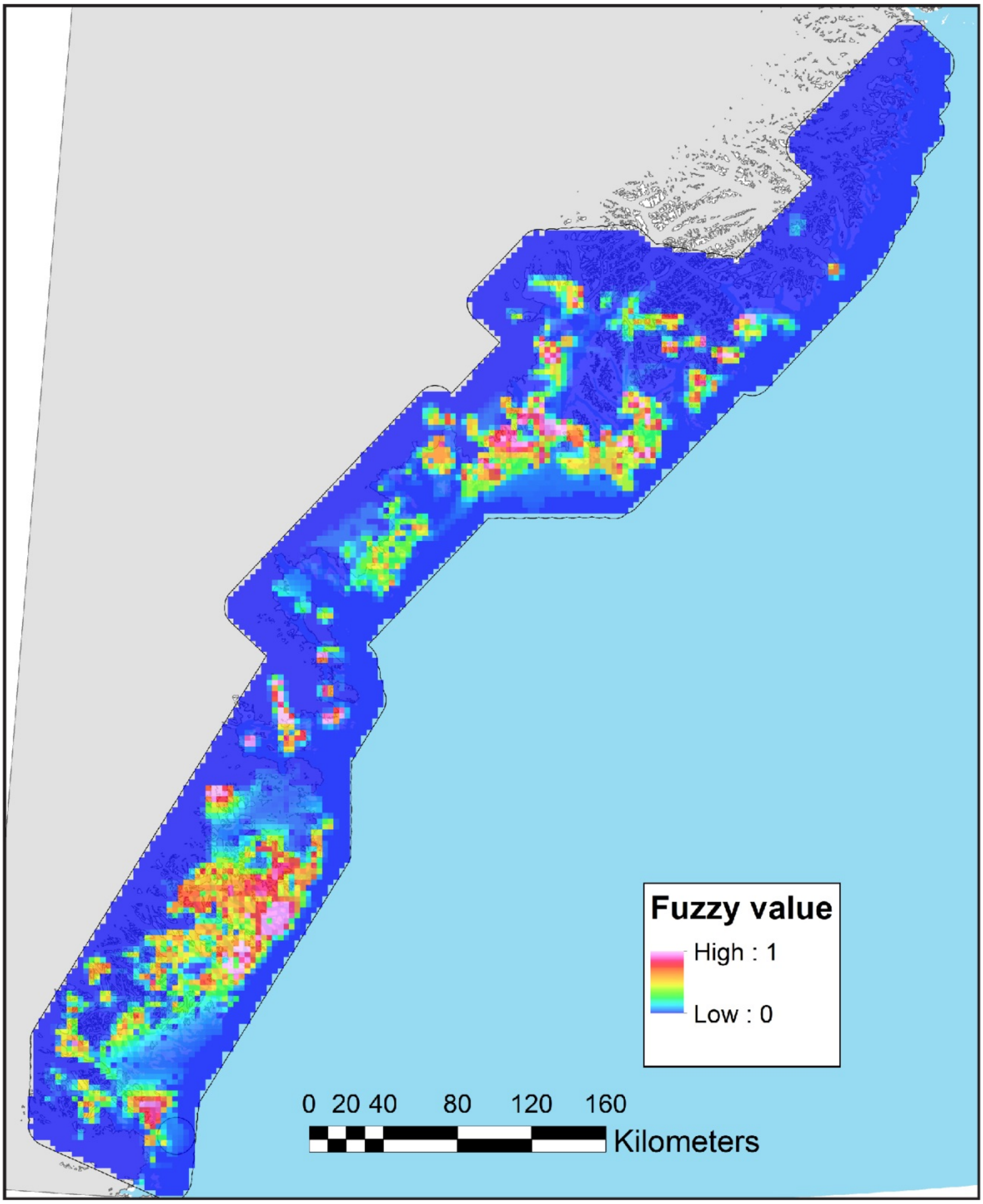

Figure 68. *Fuzzified prospectivity map "ProspecH" received by a combination of the intermediate maps O1a, O2b, O3b and O4g). In the intermediate map O4g (Fig. 63) for the geochemical trap, the evidential maps associated with mafic rock units and mafic mineral index are not considered.*

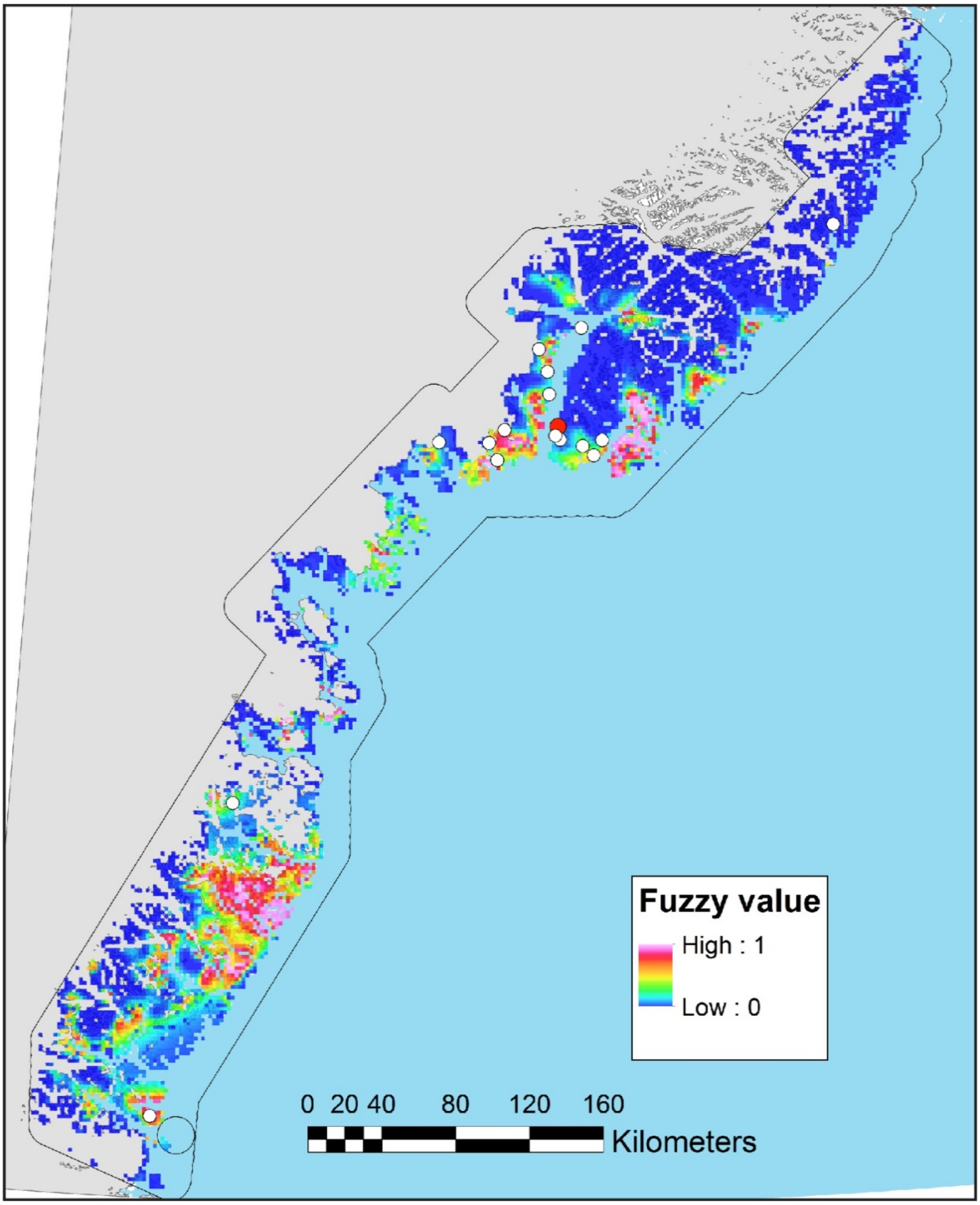

Figure 69. *Fuzzified prospectivity map "ProspecA" (as in Fig. 64) with only pixels from the non-ice-covered onshore area shown. The white dots indicate locations of stream sediments, where the Au-concentration is > 20 ppb and the red dot highlights the location with the largest gold concentration of 190 ppb.*

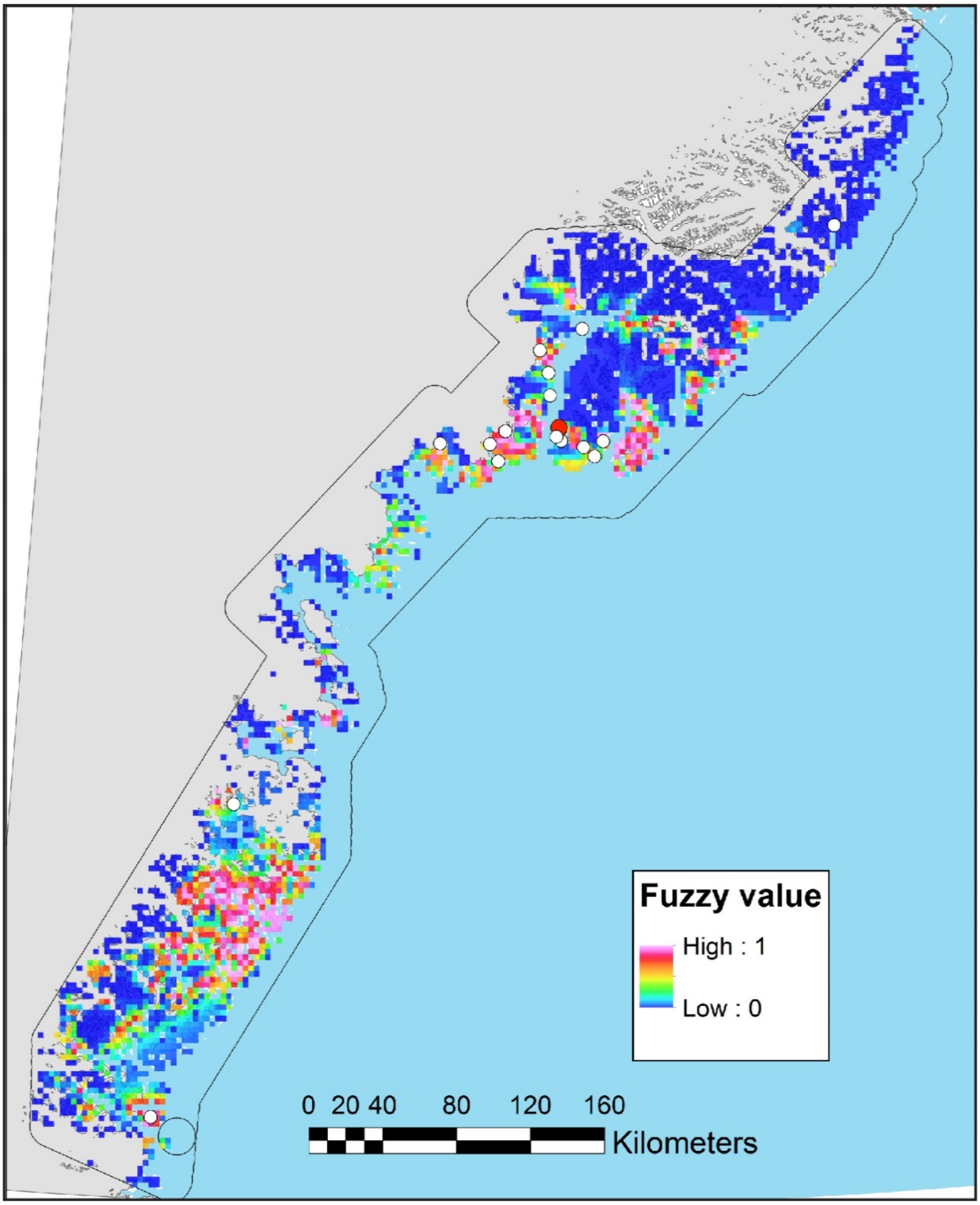

Figure 70. *Fuzzified prospectivity map "ProspecB" (as in Fig. 65) with only pixels from the non-ice-covered onshore area are shown. The white dots indicate locations of stream sediments, where the Au-concentration is > 20 ppb and the red dot highlights the location with the largest gold concentration of 190 ppb.*

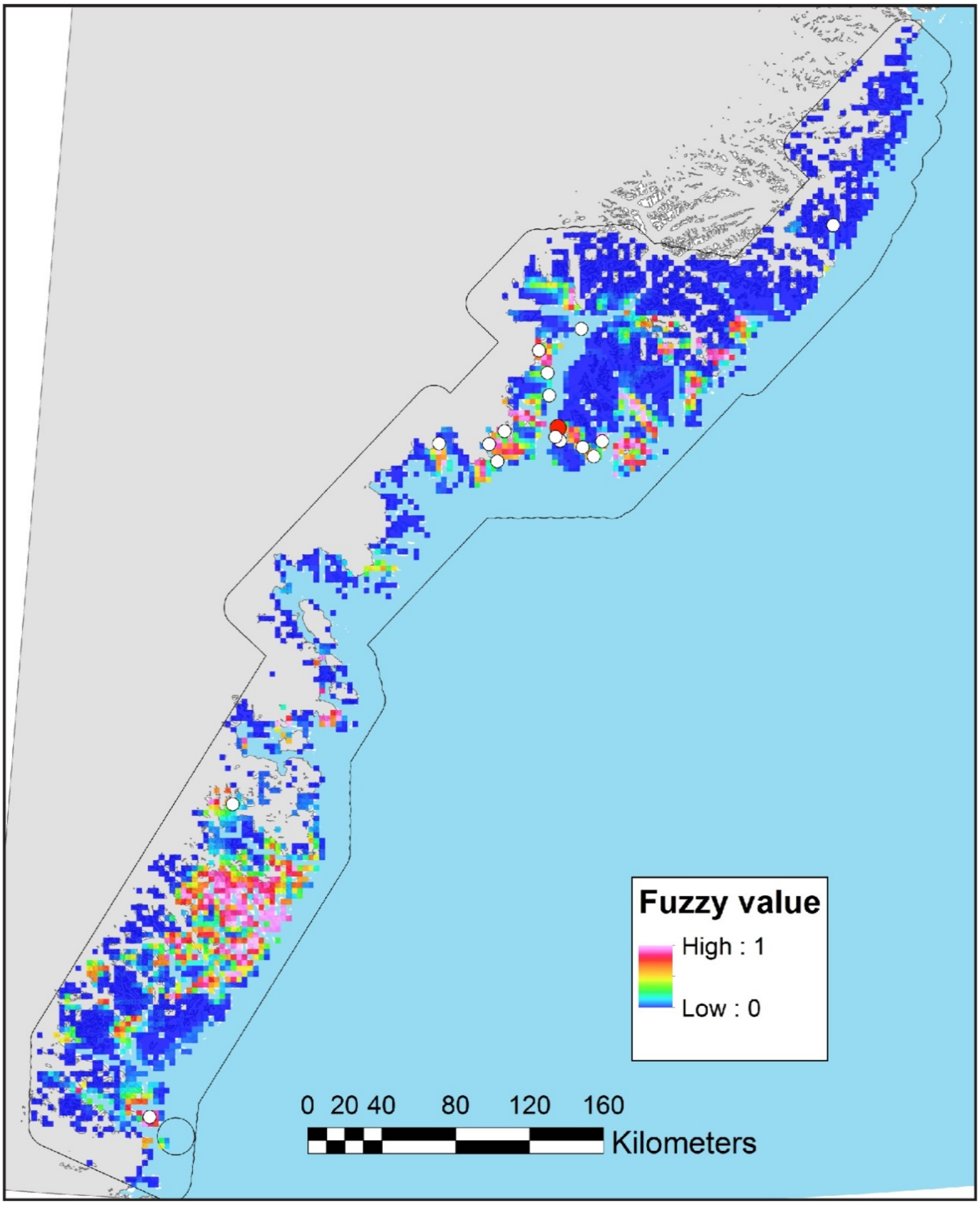

Figure 71. *Fuzzified prospectivity map "ProspecF" (as in Fig. 66) with only pixels from the non-ice-covered onshore area are shown. The white dots indicate locations of stream sediments, where the Au-concentration is > 20 ppb and the red dot highlights the location with the largest gold concentration of 190 ppb.*

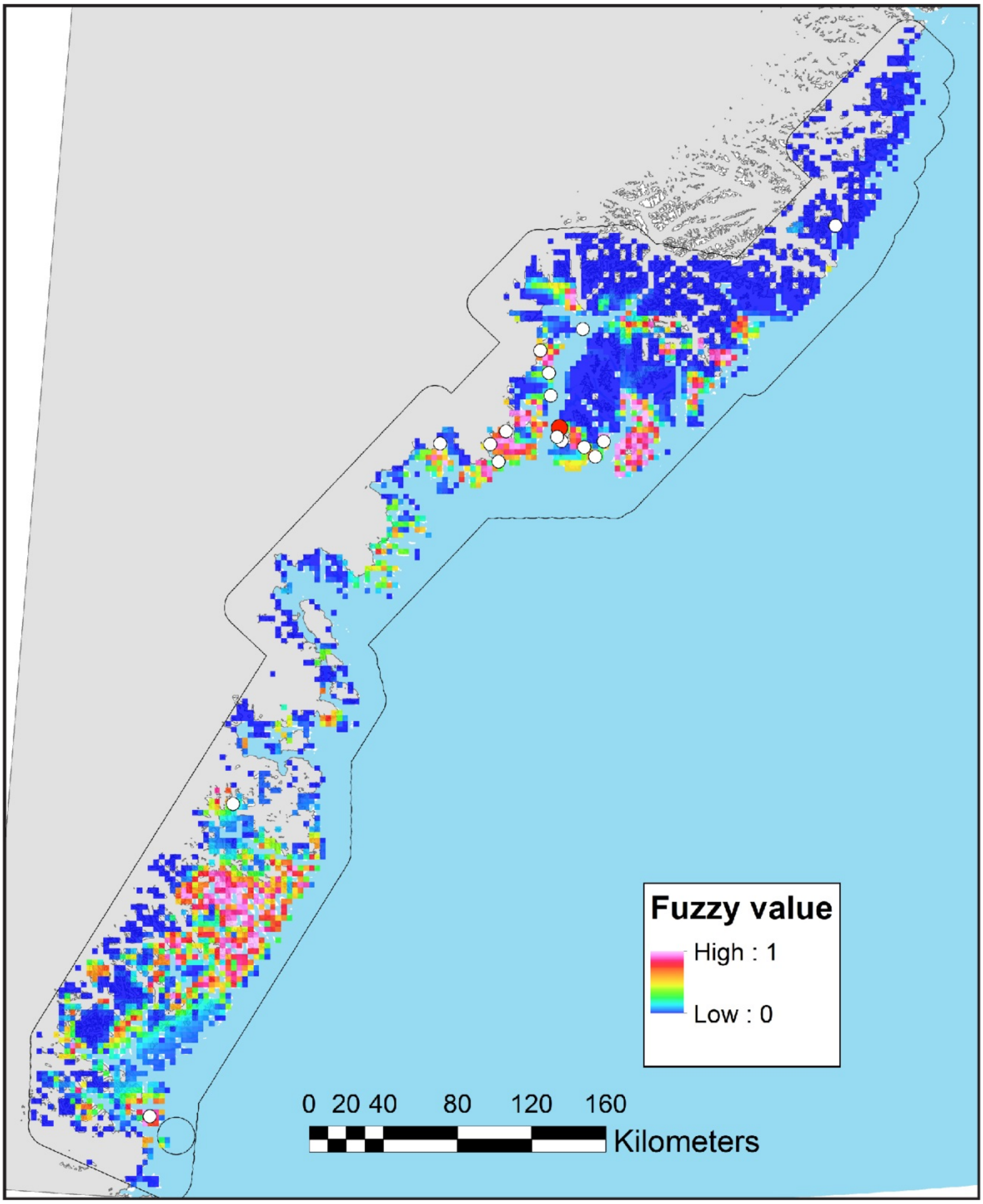

Figure 72. *Fuzzified prospectivity map "ProspecG" (as in Fig. 67) with only pixels from the non-ice-covered onshore area are shown. The white dots indicate locations of stream sediments, where the Au-concentration is > 20 ppb and the red dot highlights the location with the largest gold concentra-tion of 190 ppb.*

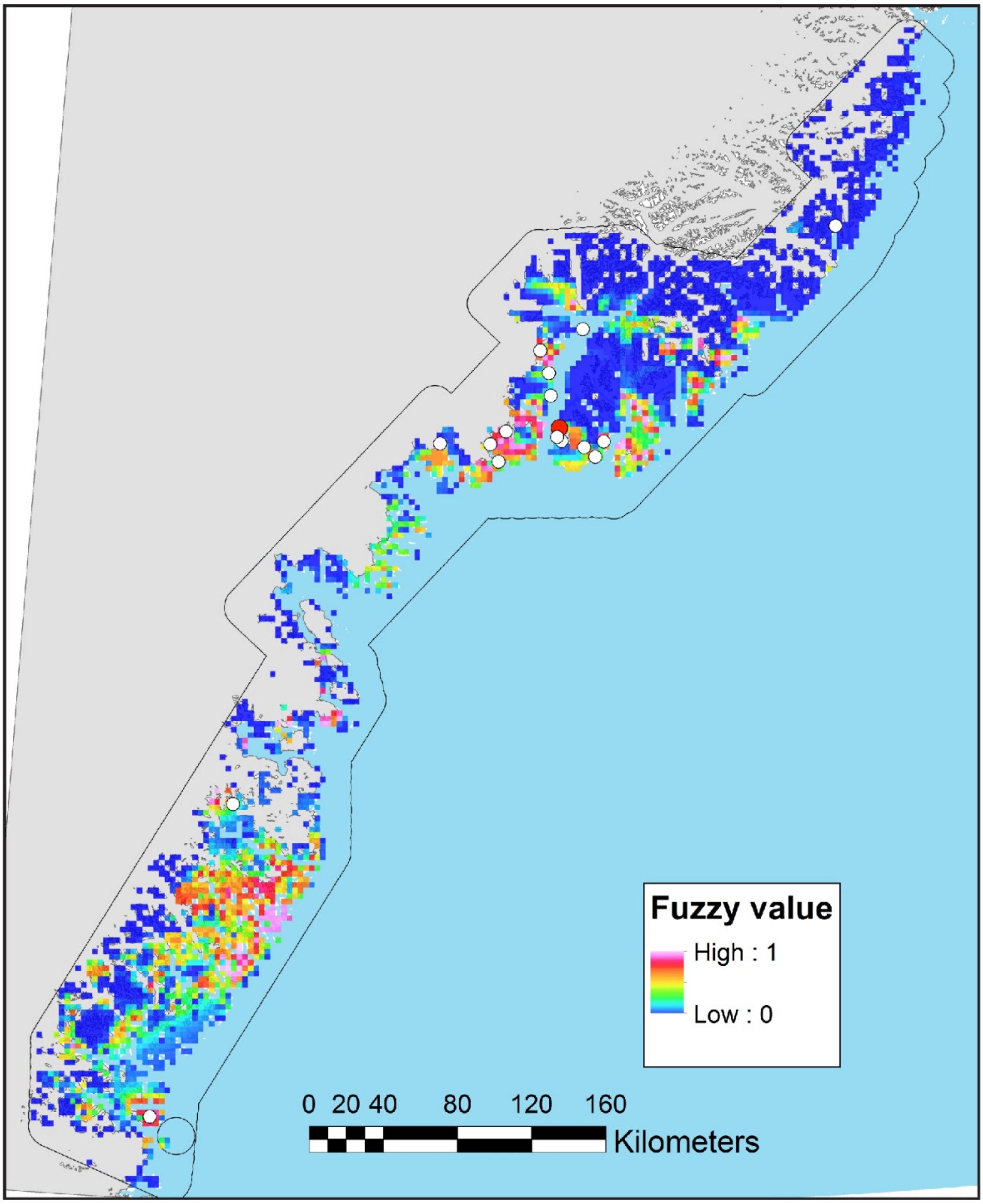

Figure 73. *Fuzzified prospectivity map "ProspecH" (as in Fig. 68) with only pixels from the non-ice-covered onshore area are shown. The white dots indicate locations of stream sediments, where the Au-concentration is > 20 ppb and the red dot highlights the location with the largest gold concentration of 190 ppb.*

Discussion

In the following sections, a validation of the prospectivity analysis is carried out and discussed, some of the uncertainties associated with the methodology and the current study in South-East Greenland are briefly touched, and finally the main results of the mapping prospectivity for orogenic gold is summarised.

Validation

To evaluate to what extent the received prospectivity maps are reliable, and also how stable they are referring to the used information and associated prediction capabilities, typically prediction-rate curves are calculated.

In typical prediction-rate curves, the cumulative proportion of the study areas with decreasing fuzzy score in the prospectivity map are plotted against the cumulative proportion of the total number of (found) deposits of the considered commodity found in the same selected areal. Usually this would have been done by calculating the the cumulative proportion of the study areas and the number of deposits are given in percentage relative to the total area under investigation and the total number of deposits, respectively).

However, because there are no identified deposits in this area, we decided to use the gold (Au) concentrations from the stream sediment geochemistry in this evaluation instead. As the lower limit for a significant gold concentration, we choose 20 ppb and all samples having concentrations above this threshold are considered in the calculation of the prediction rate curve as "deposit"(see Fig. 74). Using this threshold, 17 of 996 stream sediment samples are selected.

The gold-bearing samples (with more than 1 ppm Au reported from the region are all from the public hunt for mineral program, Ujarassiorit. As the sample location and origin of these samples are related with a high amount of uncertainty, it was decided not to make use of thee samples for the validation.

Using stream sediment samples in the prediction-rate curve introduces a number of inaccuracies and it can be assumed that the prediction curve using “real” deposits would provide prediction-rate curves that shows a better rating (i.e. a larger number of deposits are located within the proportion of the investigated area having a large fuzzy score): Firstly, all the locations, where the stream sediment is taken, do typically not coincide with locations where the corresponding Au was eroded from the rock and it is not clear where in the catchment area the actual source (or sources) are located. Secondly, there is not a clear and unique functional that link concentrations of Au occurrences and stream sediment samples.

For the calculation of the prediction-rate curve, we considered only the ice-free accessible land area (see Figs. 69 to 73); because this is the part that a) is accessible for taking stream sediments and b) the area that is realistically relevant for potential exploration.

We calculated predication-rate curves for all prospectivity maps ‘ProspecA’ to ‘ProspecH’. The first inspection shows (see Fig. 74) that except for the ‘ProspecB’ map, the different curves have a similar shape and behavior and we can conclude that the differences between them are relatively minor. All these curves have a steep slope for the first 30% of the accumulated areas and more than 80% of stream sediments with high concentrations are located in these areas. This can be considered as a very satisfying results and indicate that the established mineral system is adequately set up; in particular if one considers that use of stream sediments in prediction-rate curves introduces a rather large error source.

We will now look closely on the individual prospectivity maps to evaluate their results in more details:

- It is obvious that the ‘ProspecB’ is the only map showing a significantly worse prediction than the others (see red line in Fig. 74). All involved gridded evidential maps are obtained by using kriging as interpolation method. As already mentioned before (see section ‘Step 2: Used datasets, processing and resulting evidential maps’ on page 37), kriging is not known as a method providing the most precise estimates in areas densely and uniformly covered with data points. Obviously, the other resulting prospectivity maps, where some of the involved evidential maps are generated with natural neighbor gridding, can be considered more reliable for prospection.

- In the “ProspeC” and “ProspecD” prospectivity maps, evidential maps associated with the Au –concentrations and Au and As –concentrations from stream sediments are excluded, respectively (see section ‘Resulting fuzzified, intermediate maps and prospectivity maps’ on page 102) . Compared to the original prospectivity map “ProspecB”, where all evidential maps are used, changes are very minor. However, the “Au deposit” prediction associated with the prediction curve is slightly better if Au and As concentrations are included (Fig. 74; compare blue line (ProspecB) and green line (ProspecD)). In particular, for a small percentage of the accumulated area (<10%) more stream sediments with high Au concentration are present in the ‘ProspecB’ map. This is not a surprise because including evidential maps with direct Au measurements (even if they are only stream sediment samples) should improve the overall prospectivity map. On the other hand, the changes in the prediction are insignificant (changes are limited to few areas and changes are below 0.2 in the fuzzy score) indicating that the proposed mineral system with the used interference network is reliably working without directly having Au in evidential maps involved.

- In the prospectivity map “ProspecE”, information from the carbonate index and from the marble rock units are taken out from the interference network. The “Au deposit” prediction is slightly reduced if the evidential maps associated with carbonate rocks are not considered, and particularly for a small percentage of the accumulated area (<10%) more stream sediment samples with high Au concentrations are gathered (Fig. 74; compare blue line (“ProspecB’”) and black continuous line (ProspecE)). As for the stream sediments, this suggest that adding information from carbonate rocks generally improve the prediction; however, improvements are not significant and excluding (or vice versa including) this information is not essential for the prediction capabilities of the fuzzy inference network and, hence, not for the mineral system in the present study.

- In the prospectivity map “ProspecF”, the evidential map associated with the automatic determined lineaments from the regional aeromagnetic is not considered. Although there are large changes in the corresponding intermediate map of the “Pathways”, the changes of the prospectivity map are relatively small (compare

Figs 68 and 67). Considering the prediction rate-curves of the prospectivity maps with and without the automatic determined lineaments (compare blue colored line associated with "ProspecB" and magenta colored line associated with "ProspecF" in Fig. 74), it is observed that the prediction of Au occurrences worsen slightly if the evidential map associated with the automatically determined lineaments is taken out of the calculation. This is to some extent a surprising result, because the automatic lineament detection was to a large extent affected by topography-related artifacts and one may argue that these artifacts could reduce the reliability of the evidential map.

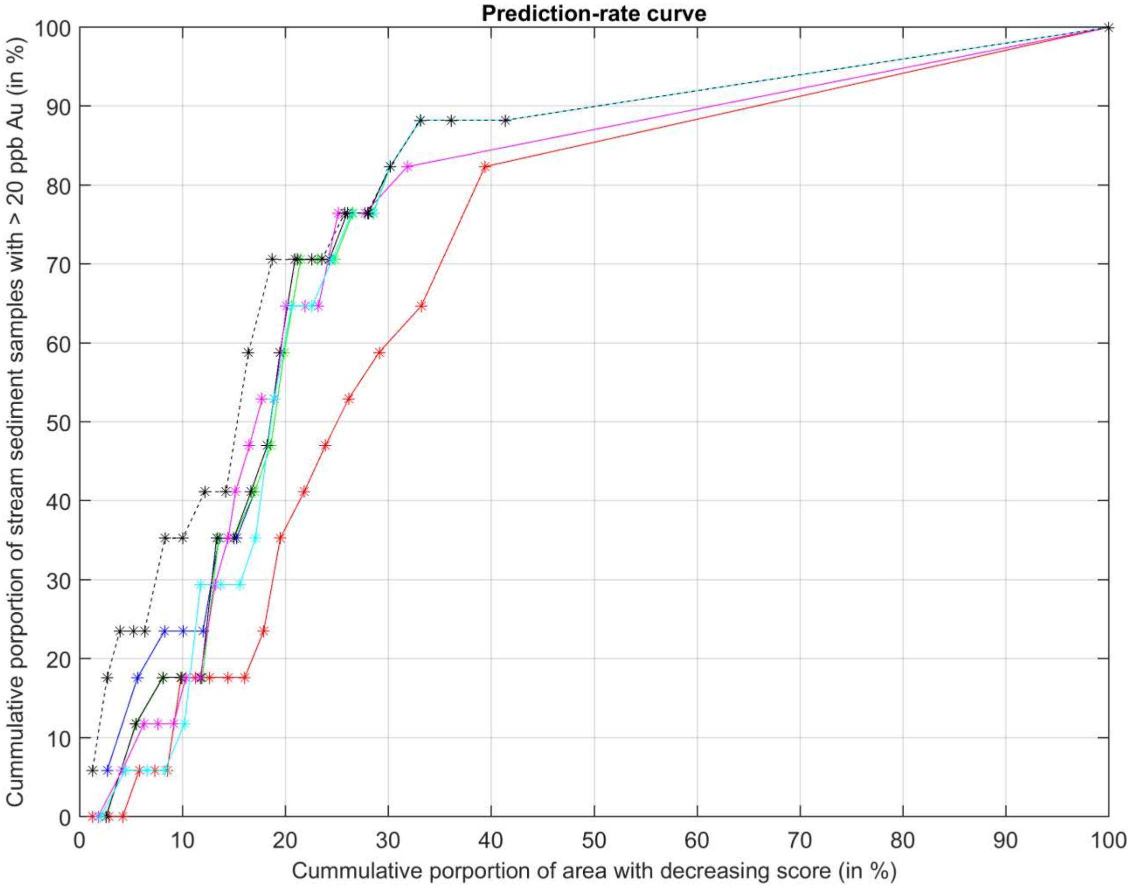

Figure 74. *Prediction curves for the different prospectivity maps (ProspecA = red line; ProspecB = blue line; ProspecD = green line; ProspecE = black line; ProspecF = magenta line; ProspecG = cyan; ProspecH = black dashed).The x-axis represents the cumulative proportion of the area with decreasing scores. Only pixels of the prospectivity maps from the onshore regions (see Figs 69 to 73) are considered in these calculations. The y-axis shows the cumulative proportion of stream sediments samples having > 40 ppb Au content.*

- In the prospectivity map "ProspecG" all evidential maps from stream sediments are excluded from the interference network. Although about half of the evidential maps are removed from the intermediate map associated with the "Chemical Trap", the final prospectivity map is surprisingly little affected (compare Fig. 69 and Fig. 67). Also, the prediction of Au occurrences is only slightly reduced if the stream sediment information are completely ignored (Fig. 71; compare blue line ("ProspecB") and cyan line ("ProspecG")), which means that adding them have a smaller (positive) effect onto the overall mineral system. This demonstrates that the overall mineral system seems to be rather robust, even if major parts of information are not incorporated. (In this context also the question arises, if all the remaining stream sediment element concentrations apart from Au and As may have a measurable influence on the overall mineral system; this has not been systematically tested, but this simple test gives at least some hints that some of them may not needed or does have not a positive effect in improving the prediction of potential gold occurrences.)

- In prospectivity map "ProspecH", all evidential maps related to mafic rocks (mafic index determined from multispectral ASTER data and mafic rock units extracted from the digital geological map) are not considered in the calculation. Changes in the intermediate map of the "Chemical Trap" are rather significant (see Fig. 63), leading to some interesting changes in the final prospectivity map. Comparing "ProspecB" (Fig. 70) and "ProspecH" (Fig. 73), where these evidential maps are respectively included and excluded, , it is observed that the Skjoldungen area has a lower fuzzy score after exclusion of information associated with mafic rocks. Another important observation is that the prediction of Au occurrences improves after taking out the evidential maps related to mafic rocks (compare the blue line with the dashed black line in the prediction rate-curve; see Fig. 74). This behavior is different from the other prospectivity maps "ProspecC" to "ProspecG", where a reduction of information leads to decreased prediction ability. It seems that information from mafic rocks worsen results in the mineral system for orogenic gold - at least for this area. An alternative explanation may be that this indicates that the high fuzzy score (in the other prospectivity maps) in the Skjoldungen area is an overestimation of the true gold potential of this specific region.

Uncertainties

Prospectivity mapping is considered as a very powerful tool for targeting of areas high resource potential (see e.g. Bonham-Carter 1994; Carranza 2009). Integration of data can largely reduce the size of areas assessed as relevant for selecting targets for future research and exploration. Furthermore, prospectivity mapping provides valuable insight into the data and their capacity for reflecting certain geological processes and can successfully be used to address future data acquisition programs. A reduction of area would be not possible by a separate consideration of data. However, there are several uncertainties and limitations in mineral system approaches in general and fuzzy prospectivity mapping in particular and many assumptions are made or are inherent in these procedures (e.g. Wyborn *et al.* 1994; Carranza 2009; McCuaig *et al.*, 2010; Joly *et al.* 2015), when:

a) mineral system components (in this study 'Source', 'Pathway', 'Chemical Trap', 'Physical Trap') are defined to establish the specific mineral system for the commodity under consideration (in this study 'orogenic gold'),

b) mineral system components are translated to the constituent processes and, hence, to targeting elements reflecting the geology (in this study processes and targeting elements for orogenic gold type mineralisation),

c) target criteria or proxies are assigned to the target elements (in this study e.g. anomalies in magnetic data are associated with faults of different order), and

d) different maps from the target criteria/proxies are (mathematically) combined and integrated in an interference network to obtain the resulting prospectivity maps.

A number of these uncertainties are listed below and discussed in relation to the system used here to evaluate the orogenic gold potential in Southeast Greenland:

1) Resolution of mapable criteria in datasets is often limited.

   For example, we use potential field data to identify faults. These types of geophysical methods are known to sometimes result in some spatial inaccuracies. This is particularly true for the data compilations CAMP-M and CAMP-G which are based to a large extent on satellite data and "older" airborne data, have a coarse gridding and have been up-ward continued. In addition, manual (and even automated) picking of these features is not always precise. This means that the identified locations of faults have uncertainties that have to be considered in the corresponding membership functions.

2) An even more critical issue is that some features associated with a targeting element may not be adequately mapped (or even not be identified) by the used criteria/proxy elements.

   In our case, it is for example possible that a major fault (relevant for the "Source" mineral system component) is not identified, because it does not show a significant anomaly pattern in the magnetic and the gravity field data. This can happen, if a fault is e.g. shallowly dipping or if rocks have verylow magnetic susceptibility. Also, the lack of geological elements (e.g. structures or geological units) in the digital geologic map due to limited geological mapping in areas difficult to access, can result in similar problems in the components "Pathways" and "Physical Trap". These unmapped or otherwise missing features in the evidential maps can be very critical in the used fuzzy logic, because a FuzzyAND operator is employed to combine the intermediate maps and, hence, low fuzzy score in one of the mineral components (e.g. a potential prospective area has an erroneously low score in the "Source" intermediate map because of an unidentified 1st order fault zone) would also result in a low score in the final prospectivity map.

3) Another challenge is to balance the impacts of the different evidential maps for a mineral system component.

   This is a non-trivial task; on the one hand it is desirable from a mathematical viewpoint that the different evidential maps should somehow be "equally/similar" weighted such that the outcome of the corresponding intermediate map is not completely dominated by only one evidential map (For example, one of the stream sediment evidential maps have everywhere a high score due to the relatively high abundance of the associated element; this evidential map causes then also everywhere high fuzzy scores in the resulting intermediate map for the "chemical trap" and, hence, dominates the final output very much). On the other hand, evidential maps are "representatives" of real physical, chemical or other types of earth processes and the membership functions to use should be chosen so that the values of the original evidential map are proper represented by their fuzzy scores (e.g. it is indeed possible that one of the stream sediment elements show a clearly higher relative abundance and that the resulting intermediate “Chemical Trap” map is then dominated by only one of the evidential maps). To find a compromise between these two extremes, requires fundamental and quantitative knowledge about how the different targeting elements are linked to the corresponding mineral components. Because this requires both long-term experience with fuzzy prospectivity systems and a complete understanding of the different physical and chemical processes, this is beyond the scope of this study.

We followed the strategy that most of the evidential maps are equally weighted relatively to each other (using the FuzzyOr operator) as long as we do not have a clear quantitative understanding of their exact impact. Exceptions from this procedure are the maps based on distances from fractures and lineaments mapped from magnetic and gravity data.

4) Optimising of fuzzy membership functions.

This uncertainty is mentioned at the previous point. It is challenging to find a representative and more or less correct membership function, (assuming that it exists and can be described by a continuous function (!)), linking an original evidential map with its fuzzified version. Imagine the case that the stream sediment samples are mixed constituents eroded from different places of a catchment area in a mountainous area. It will then be likely that there is a correlation of e.g. Au concentrations in stream sediments with the potential for gold occurrences in an area, but this can most likely not be described by a simple function. The fact that the stream sediment concentrations have to be gridded by applying an interpolation to create adequate evidential maps may make it even more difficult.

5) Challenges related to South-East Greenland and the available data.

Finally, there are a number of problems specific for our area of investigation. Firstly, the strong topography in Southwest Greenland is responsible for inaccuracies and distortions in a number of evidential maps. In particular, evidential maps that are based on automatically picked features from aeromagnetic data (see section 'Detection of lineaments from regional airborne magnetic data (Pb1, P2, T1, t2) on page 65) or on the bending of structures extracted from the digital elevation map (see section ‘Major bends of structures (T3)’ on page 53), have to be considered very carefully or should even be excluded from the interference network. Additional research is required to find novel processing strategies to make these evidential maps more reliable. Secondly, large areas are either covered by ice or sea-water, resulting in data sampling which is not homogenous for all datasets not based on geophysics. The lack of data coverage leads to some inaccuracies in the resulting evidential maps. The distribution of inaccuracies varies with the type of applied interpolation method (e.g. kriging or natural neighbour gridding), but is generally lower in areas with none or sparse data coverage.

Results of the prospectivity

The final resulting prospectivity maps for South-East Greenland (Figs 64 to 73) were constructed by the use of evidential maps (proxies), which are believed to reflect certain processes of the components that constitute a mineral system for orogenic gold mineralisation.

The top 85% most prospective cells of the final prospectivity map (here referring to the prospectivity map "ProspecB"; Fig. 65 and Fig. 70) are highlighted in Figure 75.

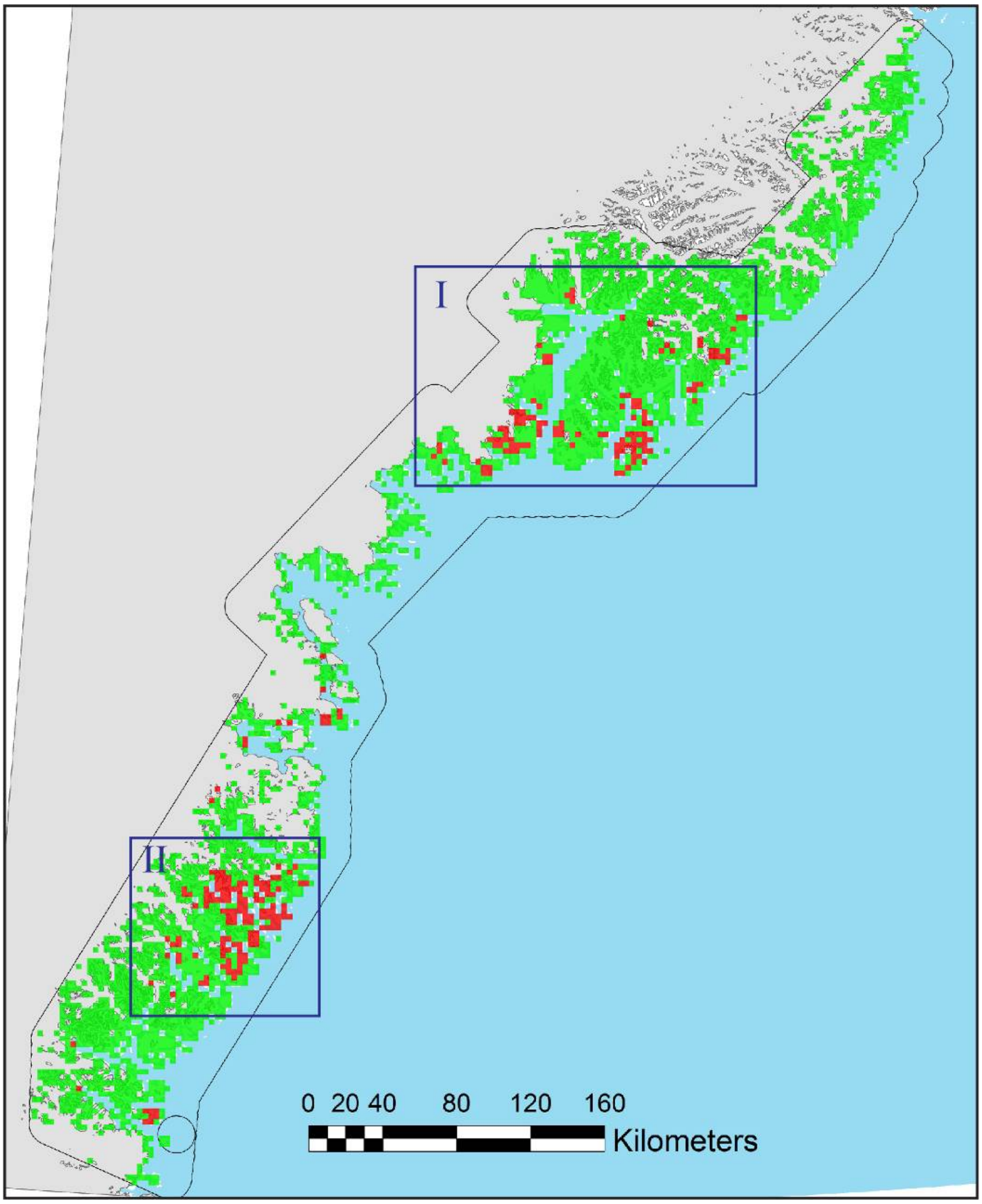

Figure 75. *Red and green areas correspond to ice-free onshore areas where the fuzzy score of the prospectivity map "ProspecB" (Fig. 70) is larger and smaller 0.85, respectively. Each pixel cell is 3 × 3 km. The framed areas I and II are discussed in the text.*

High prospective areas are in the following termed ‘tracts’. Two larger areas within the study region stand out from the final prospectivity analysis as being highly prospective for gold (Fig. 75); these are named the ‘Graah Fjord tract’ and the ‘Tasiilaq tract’.

The geological settings of these tracts, including a brief summary of the positive indications as well as the indications that downgrade the prospectivity, are presented in the following sections. Many of the downgrading indications belongs to evidence that not necessarily are represented in the evidential maps included in this study. For example is the overall geotectonic settings not considered, neither is the metamorphic conditions considered.

Graah Fjord tract

The southern-most one, here named the ‘Graah Fjord tract’ (II in Fig. 77), corresponds to an area situated between Kassortoq and Graah Fjord in the Skjoldungen region within the central part of the Thrym Complex and the Skoldungen Alkaline Province.

Especially a NW-SE oriented corridor along the northern part of the island Skjoldungen and Graah Fjord is characterised by high prospectivity. This corridor also hosts most of the metamorphosed mafic, ultramafic and sedimentary rocks that occur as dismembered slivers and belts within mafic granulites and orthogneiss (Kolb *et al.* 2016). The Graah Fjord area, especially the area in the inner part at Lommen, is the host of some of the more notable nickel-copper sulphide mineralisation in the Thrym Complex within metamorphosed mafic-ultramafic bands and lenses in orthogneiss (Kolb *et al.* 2016). The rocks within the tract have been metamorphosed at granulite facies peak conditions. Subsequently, they underwent variably degrees of retrogression in amphibolite facies. Greenschist facies overprint related to post-collisional relaxation of the stress field at c. 2680-2650 Ma associated with orogeny-normal extension is localised to metre-scale shear zones that are especially pronounced in this corridor along the Graah Fjord and peninsula Langenæs.

No known gold mineralisation have been encountered within the tract nor does the stream sediment geochemistry point any potential for gold. However, quartz vein systems in some of the smaller shear zone within the tracts with associated hydrothermal alteration in the form of weak biotite-pyrrhotite-pyrite alteration have been found. Even though the WNW-ESE trending axis of the majorities of the intrusions of the Skjoldungen Alkaline Province (SAP) may represent a tapping of magmas derived from melting of a metasomatised subcontinental mantle lithosphere (hydrous melting of a mantle wedge source, which have been metasomatized by hydrous fluids from a subducting oceanic slab (Blichert-Toft *et al.* 1995)) it is uncertain whether or not this also generated gold-bearing fluids, especially considering the deep level crustal section and relative dry high granulite facies conditions that are present. Also, it is difficult to evaluate how possible fluid migrated through the crust. The Thrym complex lacks major shear zone systems or structural breaks, and no regional-scale alteration is observed. Finally, the presence of reactive rocks and variability in lithological units are very restricted and only confined to narrow belts or slivers intercalated in granulites and orthogneisses.

One of the main causes for the high prospectivity for orogenic gold within the Graah Fjord tract is the contribution from the evidential maps of the proxies ‘mafic units’ and ‘mafic mineral index’ (proxy code T1a and T2a, respectively). The prospectivity map ‘ProspecH’ in Figure 73 excludes these maps from the fuzzy inference network. Comparing ‘ProspecB’ with ‘ProspecH’ (see Fig. 70 and Fig. 73), it is clear that the Graah Fjord tract is lower in prospectivity responses for the latter. This is also observed by the validation curves, where the overall capability to detect areas characterised by gold in stream sediment geochemistry actually gets higher, when excluding the ‘mafic units’ and ‘mafic mineral index’. The high number of mafic units and the high response from the mafic mineral index derived in the Skjoldungen region, including the Graah Fjord tract, is a reflection of the mafic granulites that are making up a large portion of the basement rocks in this area as well as the narrow belts of mafic and ultramafic rocks hosting the deep-crustal formed nickel-copper mineralisation in this area. These rocks are not believed to be more prosperous for orogenic gold type mineralisation and will therefore, if included in the prospectivity mapping, generate a unreliable response.

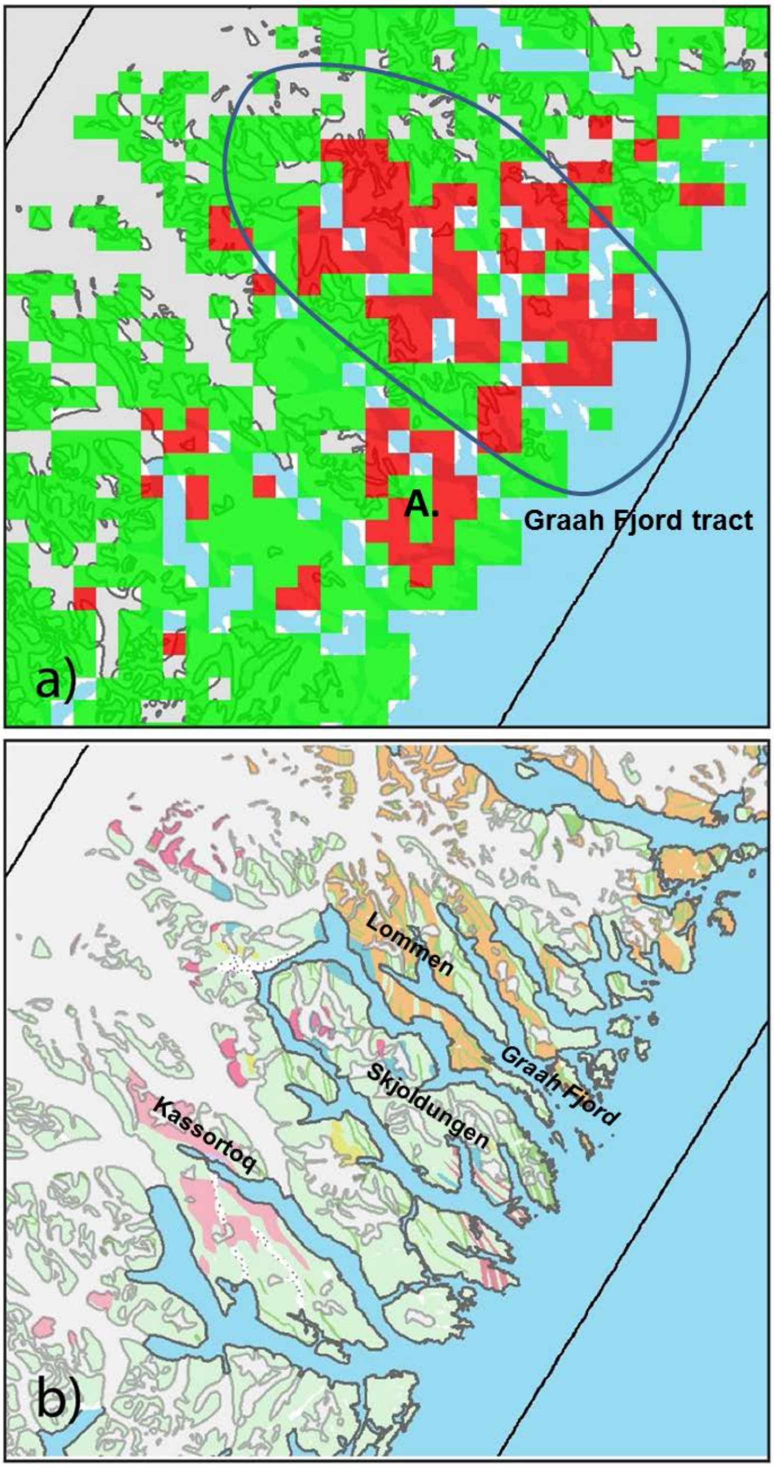

Figure 76. *Central part of the North Atlantic Craton in South-East Greenland centered on the island Skjoldungen.* ***A.*** *Red and green areas correspond to ice-free onshore areas where the fuzzy score of the prospectivity map “ProspecB” (Fig. 70) is larger and smaller 0.85, respectively. Each pixel cell is 3 × 3 km.* ***B.*** *Geological map for the area around Graah Fjord (Stensgaard et al. 2016; refer to this publication for a legend).*

Tasiilaq Tract

The northernmost, larger tract corresponds to a WNW-ESE oriented corridor situated on both sides of the Ammassalik Intrusive Complex (AIC). This tract is here named ‘Tasiilaq tract’.

The Tasiilaq tract is underlain by the southernmost part of the Kuummiut Terrane and the northernmost part of the Isortoq Terrane. Sandwiched between these terranes is the AIC, which, however, is not picked as prospective for orogenic gold by the prospectivity analysis. One or several deep mantle tapping structures in the form of major structural suture zone(-s?) related to the subduction have been suggested to be present in the tract; one straddling the northern boundary of the AIC (Fig. 4; see Kolb 2014; Kolb et al. 2016) another one have previously been suggested to be located north of Isortoq (Chadwick & Vasudev, 1986). Nutman *et al.* (2008) furthermore suggest that another fault zone straddle the southern boundary of the AIC. These structures provide favourable pathways and are also picked up in the evidential maps and the resulting prospectivity analysis.

The Kuummuit Terrane is characterized by Meso- to Neoarchean orthogneiss with narrow belts and slivers of ultramafic rocks and mafic rocks retrogressed from the eclogite facies (Nutman *et al.* 2008; Kolb 2014; Kolb *et al.* 2016).From a lithological point, the Palaeoproterozoic <2200-2100 Ma Kuummiut unit amphibolite facies metamorphosed mafic, ultramafic, paragneiss, marbles and psammitic and pelitic graphitic-schist rock units within the Kuummuit Terrane (Kolb 2014) pose a, in places diverse and variable, reactive host rock for gold-bearing fluids. This diversity is also picked up by the evidential maps and reflected in the prospectivity mapping. However, these rock units occur within narrow belts and slivers interleaved with the Archaean rocks in thin-skinned thrust sheets that were refolded (Nutman *et al.* 2008; Kolb 2014; Kolb *et al.* 2016). At least four deformation stages are recognised in the Kuummiut Terrane (Nutman *et al.* 2008; Kolb 2014). The eclogite facies mineral assemblages have been found to be unstable during decompression at high-pressure amphibolite facies conditions (Müller *et al.* 2016). This was followed by retrograde decompression between 1870 Ma and 1820 Ma during thrust imbrication in an ENE-WSW compressional stress field (Kolb 2014). Later structures in the form of folds, reverse-oblique-slip and normal shear zones from during NE-SE compression at amphibolite facies conditions.

The amphibolite facies doubly folded belts of predominately amphibolite with ultramafic lenses and very minor sedimentary rocks of the <1910 Ma Kap Tycho Brahe unis south of the AIC within the northernmost part of the Isortoq Terrane pose another favourable reactive and lithological diverse setting for a gold bearing system. The meta-sedimentary rocks are interpreted as flysch deposits sourced from the erosion of a developing volcanic-arc and a bimodal nature of the meta-volcanc rocks suggest a volcanic arc setting (Kolb 2014). Again, the favourable rock succession is picked up by the prospectivity mapping. The northernmost part of the Isortoq Terrane is structurally more simple than the Kuummuit Terrane, and record peak-metamorphism contemporaneous with NW-SE compression and nappe transport to the southeast in this terrane (Nutman *et al.* 2008; Kolb 2014).

Several quartz veins and associated alteration systems have been located within the Kuummiut Terrane (see Baden 2016; Søgaard-Jensen 2016); however, of these only one site, at Auppaluttoq (Fig. 77), which is located in a restricted prospective area north of the Tasiilaq tract, is found to carry notable amounts of gold (see the section ‘Gold – previous investigations’ on page 20). No quartz vein systems have been described from the Isortoq Terrane; however, this may be because no focused investigations have been carried out for such mineralisation in this terrane.

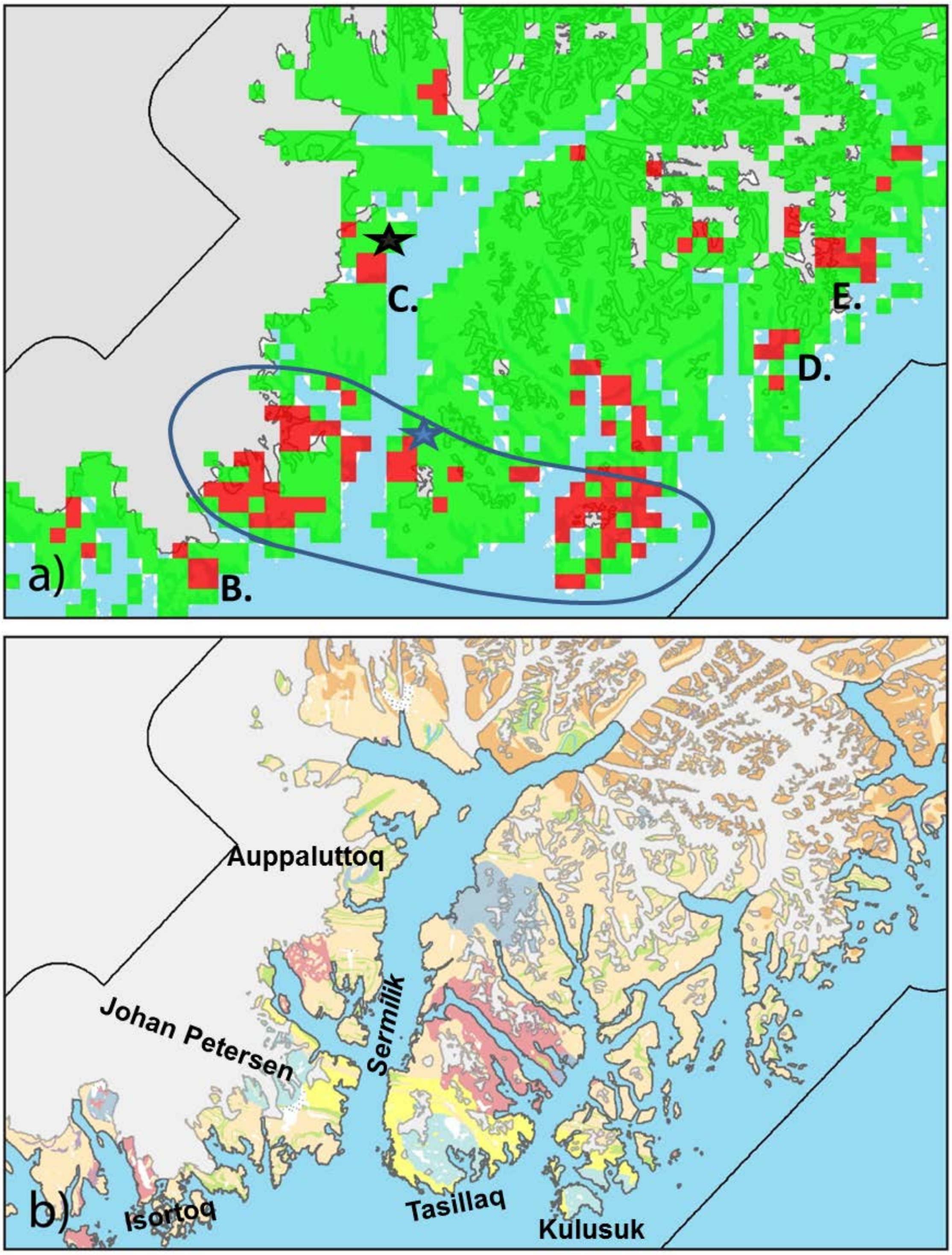

Figure 77. *The Tasiilaq area in South-East Greenland. A. Red and green areas correspond to ice-free onshore areas where the fuzzy score of the prospectivity map “ProspecB” (Fig. 70) is larger and smaller 0.85, respectively. Each pixel cell is 3 × 3 km. B. Geological map for the area around Graah Fjord (Stensgaard et al. 2016; refer to this publication for a legend).*

One of the more pronounced prospective areas within the tract is located south and north of the Johan Petersen Fjord (formally Hoobs) Intrusive Centre of the AIC (Kolb *et al.* 2016). Another pronounced area occurs north of the Kulusuk Intrusive Centre of the AIC (Kolb *et al.* 2016). Both areas contain a wide sequence of supracrustal rocks of the Kuummiut unit that has been contact metamorphosed by the AIC. The Tasiilaq Centre of the AIC (Kolb *et al.* 2016) is only characterised by a couple of 3 × 3 km pixels prospective for orogenic gold; all are located northeast of the centre with the most pronounced area towards the Sermilik fjord. This latter area is also where the site were the highest gold in stream sediment geochemistry was encountered (190 ppb Au).

Collisional belts, as the Nagssugtoqidian orogen, are traditionally though to be less prospective than accretionary belts; more prospective are orogenic belts with new crust (arcs, back arcs and accretionary wedges). Also, the high metamorphic facies conditions, especially the eclogite facies nature of the Kuummiut Terrane, also downgrade the prospectivity for gold.

Other tracts

Some of the smaller areas (smaller tracts) with high prospectivity for orogenic gold according to the prospectivity analysis are marked in Figure 76 and Figure 77

Tract A - Kong Skjold Halvø, Skjoldungen

Tract A is located south of the Graah Fjord area (Fig. 76) with the south-eastern part of Kong Skjold Halv Ø. The area is characterised by several narrow belts of mafic granulite, minor paragneiss, meta-peridotite and amphibolites. Several smaller shear zones are also present in the tract.

Tract B – Kitak, north of Isortoq, east of Tasiilaq

Tract B is located north of Isortoq at Kitak (Fig. 77). This area is characterised by a pronounced succession of amphibolite and minor meta-sedimentary rocks in a large antiform. Several thrust zones and shear zones are present in the area (see Fig. 5; Chadwick & Vasudev 1989; Kolb et al. 2016; Stensgaard et al 2016). Shear zones-related mylonites are concordant with foliation in the southern limb of the antiform. Chadwick & Vasudev (1989) indicate this as being a large crustal (suture?) structure.

Tract C – Auppaluttoq, northwest of inner Sermilik

Tract C is located at Auppaluttoq (Fig. 77) in the inner part of the fjord Sermilik. This is also in the vicinity of the location, where a sample with 11.1 ppm Au won the 1st prize in the public hunt for mineral program, Ujarassiorit. Please refer to section 'Gold – previous investigations' on page 20 for further description of the area.

Tract D – Sermiligaaq

Tract D is located just east of the settlement Sermiligaaq in an area with several belts of supracrustal rock units. Several samples from the Ujarssioirit program from the neighbouring area of Qianarteq (see Fig. 6) have been handed in with elevated gold content.

Tract E – Depotfjord
Tract E is located at Depotfjord (Fig. 77 and Fig. 5) in an area also hosting the graphite occurrence named Kangikajik (similar to the graphite occurrence at Auppaluttoq; (see section 'Graphite mineralisation' on page 18), which also is the area hosting the gold mineralisation).

Technical Aspects and Outlook

At many different stages of the mineral prospectivity mapping procedure, the process can be improved and refined in the future.

1) First of all, it is important to improve the quality of used input data either by adapting additional processing routines or by adding new and higher-resolution data types:

   - The topography can significantly distort the automated lineament detection procedure and reduce the reliability of the resulting evidential map used for identify faults as "Pathways". Therefore, it is important to look for novel processing techniques that can reduce the terrain effects in the magnetic field data (e.g. Pedersen et al. 2014). The idea is to apply such a filter to the original magnetic field data and afterward apply an automated processing flow for extracting lineaments to the filtered data (as presented in section: "Detection of lineaments from regional airborne magnetic data (Pb1, P2, T1, t2)").

   - Use of accurate topography information can aid lineament and fracture detection. At the beginning of this project, the digital elevation model from the ASTER satellite data was considered as an option to incorporate such information. However, these elevation data are affected by artifacts and the data quality was too inferior to be of practically use. New DEM models based on both satellite data (e.g. the ArticDEM generated from data of the "Worldview" satellites; see http://www.pgc.umn.edu/arcticdem; or the TanDEM-X received from the SAR missions; see https://directory.eoportal.org/web/eoportal/satellite-missions/t/tandem-x) and on compilations of aerial photographs (Korsgaard et al. 2015) have recently or will soon be recently released. Such data with higher resolution (and hopefully higher quality) offers the option to map superficial faults from DEMs. Also, high resolution radar data may be very useful.

   - Hyperspectral data having higher spatial and spectral resolution (e.g. van der Meer et al. 2012) compared to the ASTER data used here can provide significantly more precise knowledge about the different rock types and the mineralogical composition. Incorporating hyperspectral data in the future can improve the accuracy of many evidential maps and adapt measures better to the mineralogy specifically required for a mineral system.

   - For the orogenic gold model, particularly the accuracy of the evidence from the "chemical trap" can be improved.

2) The type of interpolation method used to create gridded maps of evidential maps has a significant impact on the quality of the rating of the final prospectivity map (as also seen in this study). In this study, a rather coarse grid of 3 x 3 km is chosen and for a more focused targeting of occurrences a finer gridding should be attempted. In this case, the

choice of the gridding routine plays an even larger role and it is worthwhile to investigate the optimal interpolation strategy for different types of data in the future.

3) The choice of an optimum membership function is important for obtaining adequate prospectivity maps, but it is a challenging task to find an adequate, continuous function that appropriately describes the relation of the targeting elements and its proxy on the one hand, and the fuzzified membership functions describing its impact in the mineral system on the other hand. This is particularly difficult, if such relations are complex and not well understood. In a system where many evidential maps are involved, manual trial-and-error tests (i. e. a membership function is modified and afterwards it is checked how the corresponding prospectivity map and its prediction-rate curves have been changed) can become time-consuming and involved. To solve this problem, an option could be to find optimal membership functions for all evidential maps at the same time by describing the membership functions by a few parameters and using global optimization schemes (e.g. Monte-Carlo inversions, particle swarm inversion, generic algorithms, etc.) and consider the prediction rate curves as the penalty function (typically called objective function) that has to be optimized. To involve a-priori knowledge in this process, parameter ranges are constrained according to geological and other information. Nowadays, computer resources are more and more capable for the handling of necessary sizes of data, and this open the door for optimizing at least the “mathematical” aspects of complex mineral systems.

4) In this study, only the fuzzy OR and the fuzzy AND operators are used for determining the intermediate maps by combining the evidential maps and for determining the prospectivity maps by combining the intermediate maps, respectively. It can be questioned if these are optimal operators for all combinations, because it assumes that all individual targeting elements contribute to the associated mineral system component in a similar manner and that the relevance of the different mineral system components is the same when trying to achieve a relevant prospectivity map. Other operators are available (e.g. PRODUCT and SUM) and there are other ways to combine operators in a plausible manner. Following the idea in point 3), it can also be investigated in a global optimization scheme, how the combination of logic operators in an interference network can be optimized obtaining the best outcome for a specific mineral system (and region).

Conclusion

A prospectivity analysis for orogenic gold was carried out in South-East Greenland through a mineral system approach combined using integration of evidential data by a fuzzy logic methodology.

Based on the mineral system for orogenic gold and the prospectivity generated through fuzzy logic, two larger tracts and a number of smaller tracts were outlined as having a high prospectivity for gold. The prospectivity mapping was validated and found to be reliable and robust. Especially the Tasiilaq Tract but also the smaller tracts in the Palaeoproterozoic part of the region, at Kitak, Auppaluttoq and Depotfjord,require more detailed follow-up either in the form of further and more detailed data analysis or in the form of targeted follow-up and detailed targeted geochemical sampling programs in the field.

However, it could be argued, that the geological settings and conditions in South-East Greenland does not pose the most promising environments for the existence of orogenic gold.

Deep mantle tapping features, in the form of a mantle tapping intrusive province in the Archaean North Atlantic Craton (NAC), and major linear structural (and/or possible subduction-related suture) zones in the central part of the Palaeoproterozoic Nagssugtoqidian Orogen of South-East Greenland is present. Furthermore, diverse and reactive metavolcanic and meta-sedimentary rocks are present; especially in the orogenic parts of South-East Greenland. However, these are restricted in size and dismembered. The cratonic parts of the study area are dominated by mafic granulites and orthogneisses with thin belts of mafic and ultramafic sequences that was formed at deeper levels of the crust and lesser prosperous for gold. Also, the present day exposed lower crustal section is believed to be less prospective for gold than upper crustal levels. Also, the high metamorphic granulite conditions in the Thrym Complex of the NAC as well as the high metamorphic conditions encountered in the terranes of the Palaeoproterozoic orogenic parts of the study area, in particular the ecologite conditions encountered in the Kuummiut Terrane, lowers the prospectivity based on the geological settings and conditions. Nevertheless, the presence of stream sediment geochemistry anomalies as well as numerous gold-bearing samples from the public hunt for mineral program Ujarassiorit in the Paleoproterozoic orogenic parts justified a prospectivity mapping to evaluate the possibilities for a gold mineralising system to be present in the region.

The mineral system and fuzzy inference network here established for the evidential maps (data reflecting processes in the mineral system) can easily be tuned, tested and changed according to new knowledge, and new or modified evidential maps can be produced for the interpretational process.

References

An, P., Moon, W.M & Rencz, A. 1991: Application of fuzzy set theory to integrated mineral exploration. Canadian Journal of Exploration Geophysics **27**, p. 1–11.

Andersen, T., Austrheim, H. and Bridgwater, D., 1989: P-T and fluid evolution of the Angmagssalik "charnockite" complex, SE Greenland. In: D. Bridgwater (Editor), Fluid Movements, Element Transport and the Composition of the Deep Crust. NATO Advanced Study Institute, Mathematical and Physical Sciences, Kluwer, Dordrecht, pp. 71-94.

Andrews, J.R., Bridgwater, D., Gulson, B. & Watterson, J. 1971: Reconnaissance mapping of south-east Greenland between 62°30'N and 60°30'N. Rapport Grønlands Geologiske Undersøgelse **35**, p. 32-38.

Andrews, J.R., Bridgwater, D., Gormsen, K., Gulson, B., Keto, L. & Watterson, J. 1973: The Precambrian of South-East Greenland. In: Park,R.G. & Tarney,J. (ed.) The Early Precambrian of Scotland and related rocks of Greenland, 143-156.: Newcastle (Staffs): Geology Department University Keele.

Baden, K., 2016: Palaeoproterozoic hydrothermal graphite-sulfide ± gold mineralization from the Tasiilaq area, South-East Greenland, Geological Survey of Denmark and Greenland Report, Copenhagen. [based on: Baden, K.2013: Palaeoproterozoic hydrothermal graphite-sulfide ± gold mineralization from the Tasiilaq area, South-East Greenland. Master Thesis, University of Copenhagen, Denmark. 18/09/13, supervisor Jochen Kolb & Tod E. Waight, 53 pp.

Bagas, L., Næraa, T., Kolb, J., Reno, B.L. and Fiorentini, M.L., 2013: Partial melting of the Archaean Thrym Complex of southeastern Greenland. Lithos, **160-161**, p. 164–182.

Bagas, L., Kolb, J., Fiorentini, M.L., Thébaud, N., Owen, J., Rennick, S. and Stensgaard, B.M., 2016: On the processes that formed Archaean Ni-Cu sulfide mineralisation inthe deep continental crust, Thrym Complex, southeastern Greenland. Precambrian Research, **277**, p. 68–86.

Bartels, A. 2015: The mid-Proterozoic Gardar Province, South Greenland: geology and rare-earth element potential - Greenland and Nunavut Geoscience Workshop 2014, Nuuk, Greenland. In: Thorsøe, K., Mate, D.J. & Poulsen, M.D. (eds): Summary of Activities 2014, 184. Canada-Nunavut Geoscience Office

Bierlein, F.P., Groves, D.I., Goldfarb, R.J. & Dubé, B. 2006: Lithospheric controls on the formation of provinces hosting giant orogenic gold deposits. Mineralium Deposita, **40**, p. 874–886.

Blichert-Toft, J., Rosing, M.T., Lesher, C.E. & Chauvel, C. 1995: Geochemical constraints on the origin of the late Archean Skjoldungen alkaline igneous province, SE Greenland. Journal of Petrology 3**6/2**, p. 515–561.

Bonham-Carter, G.F. 1994: Geographic Information Systems for Geoscientists –Modelling with GIS. Computer Methods in the Geosciences **13**. Pergamon Press, New York.

Bridgwater, D., Davies, F.B., Gill, R.C.O., Gorman, B.E., Henriksen, N. and Watterson, J., 1977: Field mapping in the Nagssugtoqidian of South-East Greenland. Grønlands Geologisk Undersøgelse, Rapport **85**, p. 74–83.

Bridgwater, D. and Myers, J.S., 1979: Outline of the Nagssugtoqidian mobile belt of East Greenland. Grønlands Geologisk Undersøgelse (GGU), Rapport **89**, p. 9–18.

Bridgwater, D., Austrheim, H., Hansen, B.T., Mengel, F., Pedersen, S. & Winter, J. 1990: The Proterozoic Nagssugtoqidian mobile belt of southeast Greenland: a link between the eastern Canadian and Baltic shields. Geoscience Canada **17**, p. 305-310.

Brooks, C.K. and Stenstrop, G., 1989: The Ivnartivaq complex, Sermilik, Ammassalik. In: F. Kalsbeek (Editor), Geology of the Ammassalik region, South-East Greenland. Grønlands Geologiske Undersøgelse (GGU), Rapport **146**, p. 87–91.

C3DMM 2012: Satellite ASTER Geoscience Product Notes for Australia. Version 1, August 2012 – CSIRO ePublish No. EP-30-07-12-44.

Carranza, E.J.M. 2009: Geochemical Anomaly and Mineral Prospectivity Mapping in GIS. Handbook of Exploration and Environmental Geochemistry, 11, Elsevier, Amsterdam, 351 pp.

Carranza, E.J.M. & Hale, M. 2001: Geologically-nostrained fuzzy mapping of gold mineralization potential, Baguio district, Philippines. Natural Resource Research **10/2**, pp. 125–136.

Chadwick, B. and Vasudev, V.N., 1989: Some observations on the structure of the early Proterozoic, Ammassalik mobile belt in the Ammassalik region, South-East Greenland. In: F. Kalsbeek (Editor), Geology of the Ammassalik region, South-East Greenland. Grønlands Geologiske Undersøgelse (GGU), Rapport 146, p. 29–40.

Chadwick, B., Dawes, P.R., Escher, J.C., Friend, C.R.L., Hall, R.P., Kalsbeek, F., Nielsen, T.F.D., Nutman, A.P., Soper, N.J. & Vasudev, V.N. 1989: The Proterozoic mobile belt in the Ammassalik region, South-East Greenland (Ammassalik mobile belt): an introduction and re-appraisal. Rapport Grønlands Geologiske Undersøgelse **146**, p. 5–12.

Cooper, G.R.J. & Cowan, D.R. 2008: Edge enhancement of potential-field data using normalized statistics. Geophysics **73**, H1–H4.

Corrie, R.K., Nimomiya, Y. & Aitchison, J.C. 2010: Applying Advanced Spaceborne Thermal Emission and Reflection Radiometer (ASTER) spectral indices for geological mapping and mineral identification on the Tibetian Plateau. International Archives of the Photogrammetry, Remote Sensing and Spatial Information Science, 39, p. 464–469.

Cox, S.F. 1999: Deformational controls on the dynamics of fluid flow in mesothermal gold systems. In: McCaffrey KJW, Lonergan L, Wilkinson JJ (eds), Fractures, fluid flow and mineralisation. Geol Soc Lond Spec Publ 155, p. 123–140.

Cox, S.F., Knackstedt, M.A. & Braun, J. 2001: Principles of structural control on permeability and fluid flow in hydrothermal systems.Society of Economic Geology Review, 14, p. 1–24.

Dawes, P.R., 1989a: The Grusgraven locality: border relationships between Precambrian supracrustal rocks and orthogneisses, Kangikajik, South-East Greenland. In: F. Kalsbeek (Editor), Geology of the Ammassalik region, South-East Greenland. Grønlands Geologiske Undersøgelse (GGU), Rapport **146**, p. 23–28.

Dawes, P.R., Soper, N.J., Escher, J.C. and Hall, R.P., 1989b: The northern boundary of the Proterozoic (Nagssugtoqidian) mobile belt of South-East Greenland. In: F. Kalsbeek (Editor), Geology of the Ammassalik region, South-East Greenland. Grønlands Geologiske Undersøgelse (GGU), Rapport **146**, pp. 54–65.

Dubrule, O, 2003: Geostatistics for Seismic Data Integration in Earth Models. 2003: Distinguished Instructor Short Course from the EAGE **6**.

Escher, J.C., 1990: Skjoldungen 62°30’–67°00’N; 35°50’–43°15’W. Geological map of Greenland 1:500 000 (Geologisk kort over Grønland), Sheet 14. Geological Survey of Denmark and Greenland, Copenhagen.

Escher, J.C. & Nielsen, T.F.D. 1983: Archaean gneisses and supracrustal rocks of the Tingmiarmiut region, South-East Greenland. Rapport Grønlands Geologiske Undersøgelse **115**, p. 79–82.

Ford, A., Miller, J. M. & Mol, A.G. 2016: A comparative analysis of Weights of Evidence, Evidential Belief Functions, and Fuzzy Logic for mineral potential mapping using Incomplete data at the scale of investigation. Natural Resources Research, **25/1**, p. 19–33.

Gaina, C., Werner, S.C., Saltus, R., Maus, S. and the CAMP-GM GROUP. 2011: Circum-Arctic mapping project: new magnetic and gravity anomaly maps of the Arctic. In: Spencer, A. M., Embry, A. F., Gautier, D. L., Stoupakova, A. V. & Sørensen, K. (eds) Arctic Petroleum Geology. Geological Society, London, Memoirs **35**, p. 39–48.

Garde, A.A., Grocott, J. & McCaffrey, K.J.W. 1999: New insights on the north-eastern part of the Ketilidian orogen in South-East Greenland. Geology of Greenland Survey Bulletin **183**, p. 23–33.

Goldfarb, R.J., Groves, D.I. & Gardoll, S. 2001a: Orogenic gold and geologic time: A global synthesis. Ore Geology Reviews **18/1-2**, p. 1–75.

Goldfarb, R.J., Baker, T., Dubé, B., Groves, D.I., Hart, C.J.R. & Gosselin, P. 2001b: Distribution, Character, and Genesis of Gold Deposits in Metamorphic Terranes, Economic Geology 100th Anniversary Volume, p. 407-450.

Grøtner, B.D., 2014: Sulphide mineralisation in the Tasiilaq Intrusion, Ammassalik, South-East Greenland, Copenhagen University, Copenhagen, 30 pp.

Hall, R.P., Chadwick, B., Escher, J.C. and Vasudev, V.N., 1989: Supracrustal rocks in the Ammassalik region, South-East Greenland. In: F. Kalsbeek (Editor), Geology of the Ammassalik region, South-East Greenland. Grønlands Geologiske Undersøgelse (GGU), Rapport **146**, p. 17–22.

Harris, J.R. & Sanborn-Barrie, M. 2006: Mineral potential mapping: examples from the Red Lake Greenstone Belt, Northwest Ontario. In: J.R. Harris (Ed.), GIS for the Earth Sciences, Geological Association of Canada Special Publication **44**, Geological Association of Canada, St. John's, p. 1–21.

Hansen, B.T. and Kalsbeek, F., 1989: Precise age for the Ammassalik Intrusive Complex. In: F. Kalsbeek (Editor), Geology of the Ammassalik region, South-East Greenland. Grønlands Geologiske Undersøgelse (GGU), Rapport **146**,, pp. 46-47.

Holden, E-J., Dentith, E-J. & Kovesi, P. 2008: Towards the automated analysis of regional aeromagnetic data to identify regions prospective for gold deposits. Computer & Geosciences, 34, p. 1505–1513.

Hodgson, C.J. 1989: The structure of shear-related, vein type gold deposits: a review. Ore Geology Review **4**, p. 231–273.

Hodgson, C.J. 1993: Mesothermal lode-gold deposits. In: Kirkham RV, Sinclair WD, Thorpe RI, Duke JM (eds) Mineral deposit modelling, geological association of Canada special paper **40**, p. 635–678.

Jain, A. K. 1989: Fundamentals of Digital Image Processing. Prentice-Hall, Inc.

Joly, A., Porwal, A.,McCuaig, T.C. 2012: Exploration targeting for orogenic gold deposits in the Granites–Tanami Orogen: mineral system analysis, targeting model and prospectivity analysis. Ore Geology Review **48**, p. 349–383.

Joly, A., Dentith, M.V., Porwal, A., Spaggiari, C.V., Tyler, I.M. & McCuaig, T.C. 2013: An integrated geological and geophysical study of the west Arunta Orogen and its mineral prospectivity. Geological Survey of Western Australia, Report **113**, 89 pp.

Joly, A., Porwal, A., McCuaig, T.C., Chuddasama, B., Dentith, M.C. & Aitken, A.R.A. 2015: Mineral systems approach applied to GIS-based 2D-prospectivity modelling of geological regions: Insights from Western Australia. Ore Geology Reviews **71**, p. 673–702.

Kalsbeek, F., Austrheim, H., Bridgwater, D., Hansen, B.T., Pedersen, S. and Taylor, P., 1993: Geochronology of Archaean and Proterozoic events in the Ammassalik area, South-East Greenland, and comparisons with the Lewisian of Scotland and the Nagssugtoqidian of West Greenland. Precambrian Research, **62**, p. 239–270.

Kenyon, S., Forsberg, S.R. & Coakley, B. 2008: New Gravity Field for the Arctic. EOS, **89**, p. 1–2.

Kerrich, R. & Fyfe, W.S. 1981: The gold carbonate association: source of CO2 and CO2-fixation reactions in Archaean lode deposits. Chemical Geology, **33**, pp. 265–293.

Klausen, M.B. and Kokfelt, T.F., 2014: Field report from the 2011 field season on the Skjoldungen Alkaline Province, South-East Greenland. Geological Survey of Denmark and Greenland Report, **2014/81**: 85 pp.

Kolb, J., 2014: Structure of the Palaeoproterozoic Nagssugtoqidian Orogen, South-East Greenland: model for the tectonic evolution. Precambrian Research, **255**, p. 809–822.

Kolb, J., Thrane, K. & Bagas, L. 2013: Field relationship of high-grade Neo- to Mesoarchaean rocks of South-East Greenland: Tectonometamorphic and magmatic evolution. Gondwana Research **23**, p. 471–492.

Kolb, J., Stensgaard, B.M. & Kokfelt, T.F. (eds.) 2016: Geology and Mineral Potential of South-East Greenland. Danmarks og Grønlands Geologiske Undersøgelse Rapport **2016/38**, 157 pp. + memory stick.

Korsgaard, N.J., Nuth, C., Khan, S.A., Kjeldsen, K.K., Bjørk, A.A., Schomaker, A.& Kjær, K.H. 2016: Digital elevation model and orthophotographs of Greenland based on aerial photographs from 1978–1987, Scientific Data, **3**, p. 1-15.

Kovesi, P. 2012: Phase preserving tone mapping of non-photographic high dynamic range images. Proceedings of the Australian Pattern Recognition Society Conference on Digital Image Computing Techniques and Applications (DICTA 2012). Fremantle. 2012.

Knox-Robinson C.M. 2000: Vectorical fuzzy logic: a novel technique for enhance mineral prospectivity mapping with reference to the orogenic gold mineralisation potential of the Kalgoorlie Terrance, Western Australia. Australian Journal of Earth Sciences **47/5**, p. 929–942.

Luo, X. and Dimitrakopoulos, R. 2003: Data-driven fuzzy analysis in quantitative mineral resource assessment. Computers and Geosciences, **29**, p. 3–13.

Lie, A. 1997: Reconnaissance scale geochemical exploration and compilation of regional data from the Ammassalik area, South-East Greenland. Nunaoil A/S (Exploration Licence 15/96). 22 pp. + 32 enclosed thematic maps, 1 disc (in archives of Geological Survey of Denmark and Greenland, GEUS Report File GRF **21520**).

Lie, A., 1998: Nickel, Gold and PGE-Discoveries on the Ammassalik Island, South East Greenland, and Results of the VLF-EM Test Survey, NunaMinerals A/S, 43 pp., 8 appendices. (in archives of Geological Survey of Denmark and Greenland, GEUS Report File GRF **21690**).

McCuaig, T.C., Beresford, S., Hronsky, J.M.A., 2010: Translating themineral systems approach into an effective exploration targeting system. Ore Geol. Rev. 38 (3), p.128–138.

Müller, S., Dziggel, A. & Kolb, J. 2016: Metamorphic evolution of relict eclogite-facies rocks in the Nagssugtoqidian Orogen, Southeast Greenland, North Atlantic Craton Conference, NAC+ 2016, Edinburgh, 26 pp.

Myers, J.S. 1984: The Nagssugtoqidian mobile belt of Greenland. In: A. Kröner and R. Greiling (Editors), Precambrian Tectonics Illustrated. Schweitzerbart, Stuttgart, p. 237-250.

Myers, J.S. 1987: The East Greenland Nagssugtoqidian mobile belt compared with the Lewisian complex. In: R.G. Park and J. Tarney (Editors), Evolution of the Lewisian and comparable Precambrian high-grade terranes. Special Publication of the Geological Society of London, London, p. 235-246.

Myers, J.S., Austrheim, H., Gill, R.C.O., Gorman, B.E. and Rex, D.C. 1979: Field work on the Nagssugtoqidian boundary north of Angmagssalik and Tertiary igneous rocks of Kialineq and Kap Gustav Holm, East Greenland. Rapport Grønlands geologisk Undersøgelse, **95,** p. 82-85.

Nielsen, T.F.D. & Rosing, M.T. 1990: The Archaean Skjoldungen alkaline province, South-East Greenland. Rapport Grønlands Geologiske Undersøgelse **148**, p. 93–100.

Nutman, A.P. & Friend, C.R.L. 1989: Reconnaissance P, T studies of the Proterozoic crustal evolution of the Ammassalik area, South-East Greenland. In: F. Kalsbeek (Editor), Geology of the Ammassalik region, South-East Greenland. Grønlands Geologiske Undersøgelse (GGU), Rapport **146**, p. 48–53.

Nutman, A.P., Kalsbeek, F. and Friend, C.R.L. 2008: The Nagssugtoqidian Orogen in South-East Greenland: evidence for Palaeoproterozoic collision and plate assembly. American Journal of Science, **308,** p. 529-–572.

Nykänen, V., Groves, D.I., Ojala, V.J., Eilu P. & Gardoll, S.J. 2008: Reconnaissance-scale conceptual fuzzy-logic prospectivity modelling for iron oxide copper – gold deposits in the northern Fennoscandian Shield, Finland. Australian Journal of Earth Sciences **55**, p. 25–38.

Nykänen, V. & Salmirinne, H. 2007: Prospectivity analysis of gold using regional geophysical and geochemical data from the Central Lapland Greenstone Belt, Finland. Geological Survey of Finland, Special Paper **44**, p. 251–269.

Owen, J. 2011: Characterisation of the nickel sulphide mineralisation between Graah Fjord and Bernstorff Isfjord, South-East Greenland, thesis, University of Western Australia.

Oyarzun, R., Oyarzun, J., Lillo, J., Maturana, H.& Higueras, P. 2007: Mineral deposits and Cu–Zn–As dispersion–contaminationin stream sediments from the semiarid Coquimbo Region, Chile. Environmental Geology **53**, p. 283–294.

Pedersen, L.B., Bastani, M. & Kamm, J. 2014: Gravity gradient and magnetic terrain effects for airborne applications — A practical fast Fourier transform technique, Geophysics, vol. **80**, p. 119-126.

Petersen. J. & Thomsen, L.L. 2014: Results in South-East Greenland from Ujarassiorit-program In: Stensgaard, B.M. (ed.) 2014: South-East Greenland Mineral Endowment Task (SEGMENT): 2014 Workshop Abstract Volume and Status Primo-2014. Danmarks og Grønlands Geologiske Undersøgelse Rapport **2014/79**. GEUS, p. 65-66.

Phillips G.N. & Powell R. 2009: Formation of gold deposits: Review and evaluation of the continuum model: Earth-Science Reviews, v. **94**, p. 1–21.

Phillips G.N. & Powell R. 2010: Formation of gold deposits: A metamorphic devolatilization model: Journal of Metamorphic Geology, **28**, p. 689–718.

Powell R., Will T.M. & Phillips G.N. 1991: Metamorphism in Archaean greenstone belts: Calculated fluid compositions and implications for gold mineralisation: Journal of Metamorphic Geology, **9**, p. 141–150.

Porwal, A., Carranza, E.J.M., Hale, M. 2003: Knowledge-driven and data-driven fuzzy models for predictive mineral potential mapping. Natural Resources Research **12/1**, p. 1–25.

Rasmussen, T.M., Thorning, L., Riisager, P.& Tukiainen, T. 2013: Airborne geophysical data from Greenland. Geology and Ore, Exploration and Mining in Greenland **22**, 12 pp.

Rasmussen, T.M. 2013: Airborne geophysical surveys in Greenland. Exploration and Mining in Greenland. Fact Sheet No.**27**, 2 pp.

Riisager, P.& Rasmussen, T.M. 2013: Aeromagnetic survey in south-eastern Greenland: Project Aeromag 2013. Geological Survey of Denmark and Greenland Bulletin **31**, p. 63–67.

Robert, F., Brommecker, R., Bourne, B. T., Dobak, P. J., McEwan, C.J., Rowe, R. R. and Zhou, X. 2007: Models and Exploration Methods for Major Gold Deposit Types. In "Proceedings of Exploration 07: Fifth Decennial International Conference on Mineral Exploration" edited by B. Milkereit, 2007, p. 691-711.

Rosa, D. and Ulrich, T., 2015: A quartz-wolframite-molybdenite vein and scheelite in amphibolite horizons from Thrudvang peninsula, Skjoldungen, SE Greenland. Geological Survey of Denmark and Greenland Bulletin, **33**: p. 49-52.

Rosing-Schow, N., Bagas, L., Kolb, J., Balić-Žunić, T., Korte, C. and Fiorentini, M.L. (in review): Hydrothermal flake graphite mineralisation in Palaeoproterozoic rocks of South-East Greenland. Mineralium Deposita.

Sambridge, M., Braun, J.& McQueen, H. 1995: Geophysical parametrization and interpolation of irregular data using natural neighbours. Geophysical Journal International, **122**, p. 837–857.

Silva, E.C.E.. Silva, A.M., Toledo, C.L.B. Mol, A.G., Otterman, D.W. & de Souza, S.R.C. 2012: Mineral Potential Mapping for Orogenic Gold Deposits in the Rio Maria Granite Greenstone Terrane, Southeastern Pará State, Brazil. Economic Geology, **107**, p. 1387–1402.

Schafer, R.W. 2011: What is a Savitzky-Golay Filter? IEEE Signal Processing Magazine, July 2011, p. 111–117.

Schaeffer, A.S. & S. Lebedev, S. 2013: Global shear speed structure of the upper mantle and transition zone. Geophysical Journal International, **194**, p. 417–449.

Spadoni, M., Cavarretta, G. & Patera, A. 2003: Cartographic techniques for mapping the geochemical data of stream sediments: the "Sample Catchment Basin" approach. Environmental Geology **45**, p. 593–599.

Stemp, R.W., Thorning, L. & Poulsen, L.H. 1997: Airborne Geophysical Projects in Greenland. In: “Proceedings of Exploration 97: Fourth Decennial International Conference on Mineral Exploration” edited by A.G. Gubins, p. 869–872.

Steenfelt, A. 2000: Geochemical signatures of gold provinces in South Greenland. Applied Earth Science IMM Transactions section B **109/1**, p. 14–22.

Stensgaard, B. & Steenfelt, A. 2007: Geological and statistical validation of a gold-prediction model based on low-density surface geochemistry and other geoscientific data, Nuuk region, West Greenland. *In* "Proceedings of Exploration 07: Fifth Decennial International Conference on Mineral Exploration" edited by B. Milkereit, 2007, p. 979-983.

Stensgaard, B.M., Steenfelt, A. & Rasmussen, T.M. 2005: Gold potential of the Nuuk region based on multi-parameter spatial modeling. Progress 2005. Danmarks og Grønlands Geologiske Undersøgelse Rapport **2006/27**, 207 pp.

Stensgaard, B.M., Kolb, J., Nielsen, T.F.D., Olsen, S.D., Pilbeam, L., Lieber, D. & Clausen, A. 2010: The mineral resource assessment project, South-East Greenland: year one. Geological Survey of Denmark and Greenland Bulletin **20**, pp. 59–62.

Stensgaard, B.M , Kolb, J., Kokfelt, T .F . & Klausen, M .B. 2016: Digital revised 1:500 000 geologic al map of South-East Greenland 62°00’N – 67°00’N and 33°00’W – 44°00’W. Geologic al Survey of Denmark and Greenland (GEUS).

Søgaard-Jensen, C. 2016: Petrographic and geochemical characterization of hydrothermally altered metamorphic rocks from the Tasiilaq area, Southeast Greenland. Collobarative project with GEUS. Project Report, University of Copenhagen. 22/08/2016, supervisor Jochen Kolb & Tod Waight, 109 pp.

Tomkins A.G. 2010: Windows of metamorphic sulfur liberation in the crust: Implications for gold deposit genesis. Geochimica et Cosmochimica Acta, **74**, p. 3246–3259.

van Gool, J.A.M., Connelly, J.N., Marker, M. & Mengel, F.C. 2002: The Nagssugtoqidian Orogen of West Greenland: tectonic evolution and regional correlations from a West Greenland perspective. Canadian Journal of Earth Sciences **39/5**, p. 665–686.

van der Meer, F. D., van der Werff, H.M.A., van Ruitenbeek, F.J. A., Hecker, C. A., Bakker, W. H., Noomen, M. F., van der Meijde, M., Carranza, E. J. M., de Smeth, J. B., Woldai, T.

2012: Multi- and hyperspectral geologic remote sensing: A review. International Journal of Applied Earth Observation and Geoinformation. Vol. **14**, 112-128.

Verhoef, J., Roest, W. R., Macnab, R.& Arkani, H. J. 1996: Magnetic Anomalies of the Arctic and North Atlantic Oceans and Adjacent Areas, CD Compilation. Geological Survey of Canada, Ottawa.

Wilson C.J.L., Schaubs P. & Leader L.D. 2013: Mineral precipitation in the quartz reefs of the Bendigo gold deposit, Victoria, Australia: Economic Geology and the Bulletin of the Society of Economic Geologists, **108**, p. 259–278.

Wyborn, L.A.I., Heinrich, C.A., Jaques, A.L., 1994: Australian Proterozoic mineral systems: essential ingredients and mappable criteria [abs.]. In: Hallenstein, P.C. (Ed.), Australian Mining Looks North — the Challenges and Choices: Australian Institute of Mining and Metallurgy Publication Series, **5**, p. 109–115.

Wijns, C., Perez, C. & Kowalczyk, P. 2005: Theta map: Edge detection in magnetic data. Geophysics **70**, L39–L43.

Wright, A.E., Tarney, J., Palmer, K.F., Moorlock, B.S.P. and Skinner, A.C., 1973: The geology of the Angmagssalik area, East Greenland and possible relationships with the Lewisian of Scotland. In: R.G. Park and J. Tarney (Editors), The Early Precambrian of Scotland and related rocks of Greenland. University of Keele, Keele, p. 157–177.

Zadeh L A. 1965: Fuzzy sets. Information and Control, **8**, p. 338-53

Zhang, L., Wu, J., Hao, T. & Wang, J. 2006: Automatic lineament extraction from potential-field images using the Radon transform and gradient calculation **71**, p. J31–J40.

Appendix A:
Fuzzified evidential maps

In this Appendix figures from fuzzified evidential maps from all targeting elements are shown that are used in the following for determining the prospectivity maps. We emphasize that in this Appendix only versions of evidential maps are shown, when either kriging interpolation is applied on the data or the evidential map is based on distances from some structures, lineaments or rock units. Versions of the evidential maps, where natural neighbor gridding is involved, are shown in the following Appendix B:
Fuzzified evidential maps obtained by using natural neighbor interpolation.

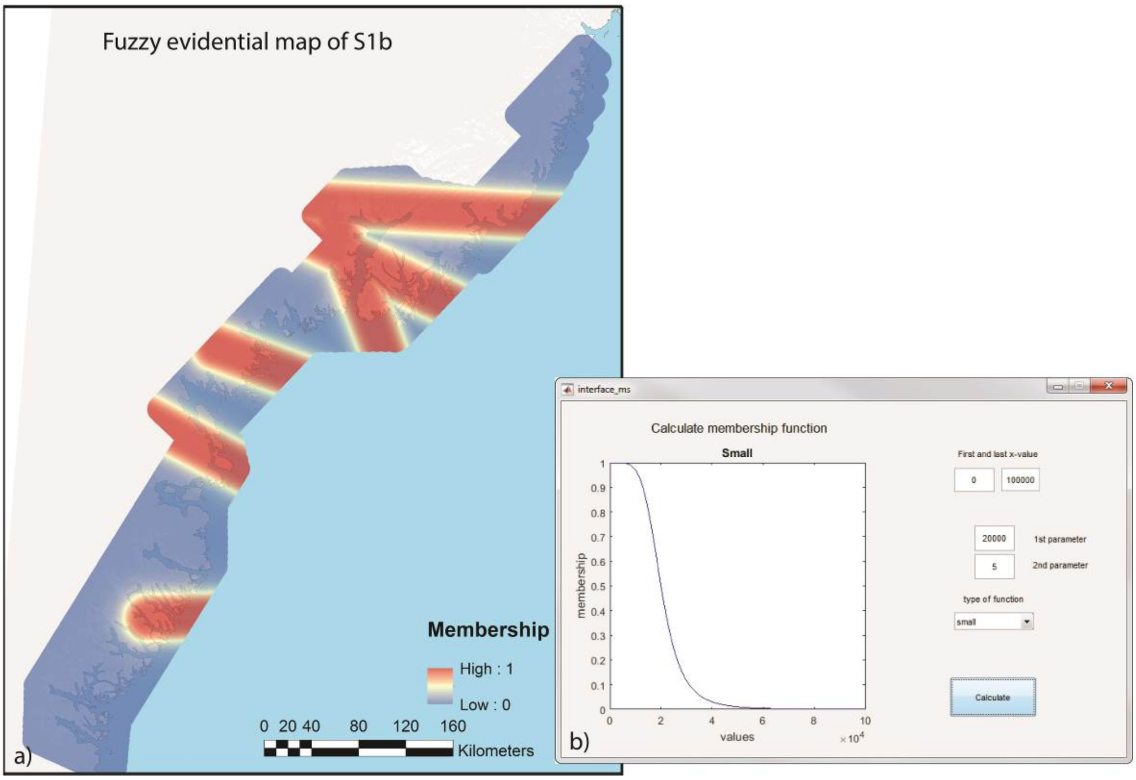

First and last x-value: 0 100000

1st parameter: 20000

2nd parameter: 5

type of function: small

Figure 78. ***A*** *Fuzzy evidential map for the target criterion/proxy S1b that is used later on for the calculation of the prospectivity maps. "Deep seated structures" is the associated targeting element that it is represented by the distances from lineaments in regional gravity data (target criterion/proxy "tapping gravity"). In* ***B*** *the membership function is shown that is used for the fuzzification of these distances (input data are shown in Fig. 53b). (The used functional "small" is described in the main text on page 92).*

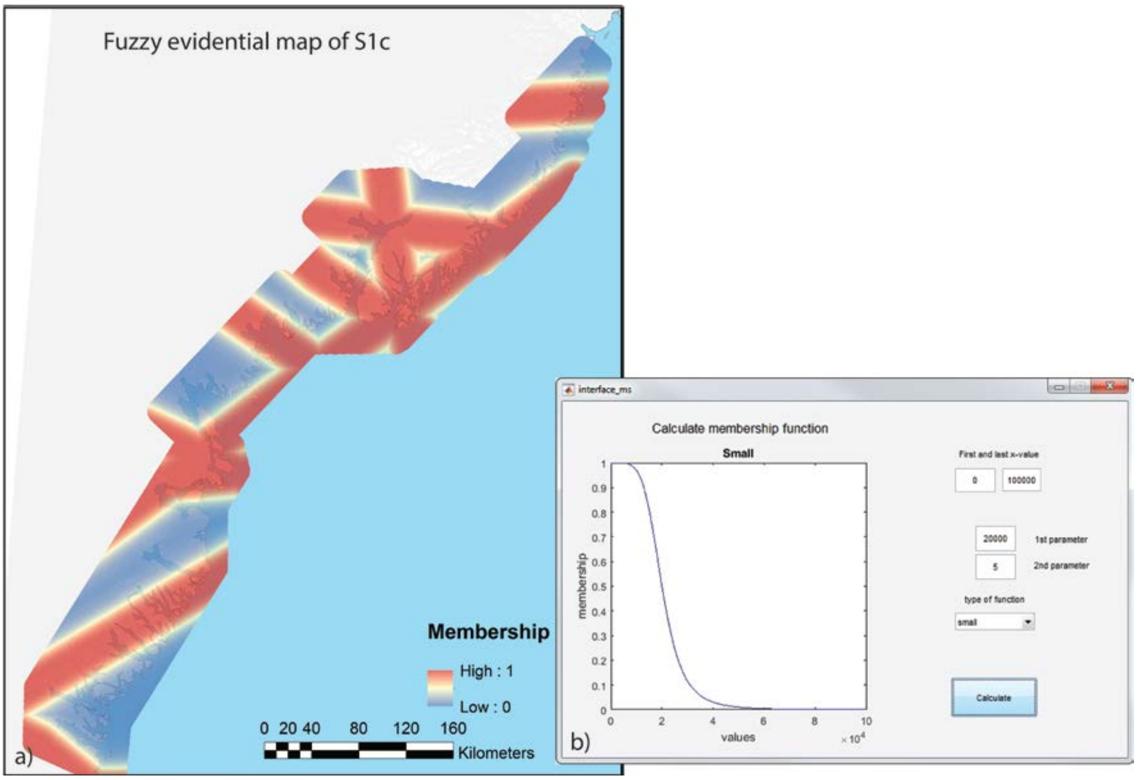

First and last x-value: 0 100000

1st parameter: 20000

2nd parameter: 5

type of function: small

Figure 79. ***A*** *Fuzzy evidential map for the target criterion/proxy S1c that is used later on for the calculation of the prospectivity maps. “Deep seated structures” is the associated targeting element that it is represented by the distances from lineaments in regional magnetic data (target criterion/proxy “tapping magnetic”). In* ***B*** *the membership function is shown that is used for the fuzzification of these distances (input data are shown in Fig. 53a). (The used functional “small” is described in the main text on page 92).*

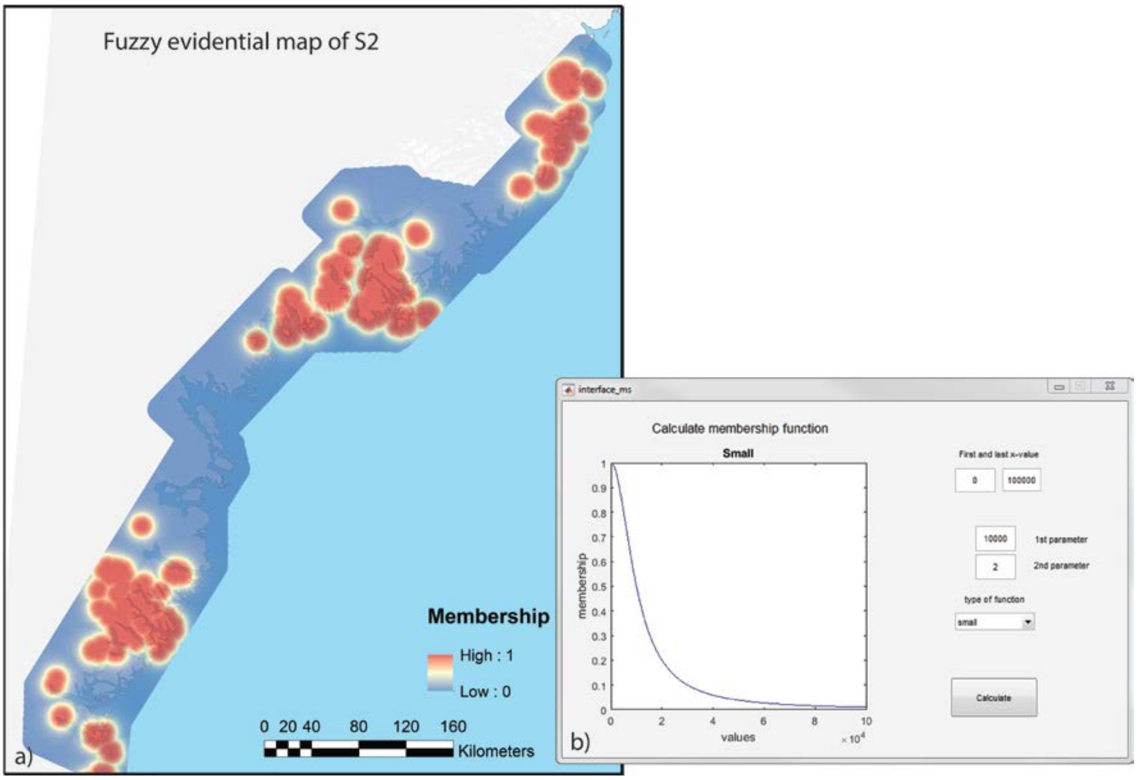

First and last x-value: 0 100000

1st parameter: 10000

2nd parameter: 2

type of function: small

Figure 80. ***A*** *Fuzzy evidential map for the target criterion/proxy S2 that is used later on for the calculation of the prospectivity maps. "Intrusions regarded as the access to the source area" (targeting element) is represented by distances from mapped intrusions (target criterion/proxy "magmatic input"). In* ***B*** *the membership function is shown that is used for the fuzzification of these distances (input data are shown in Fig. 14b). (The used functional "small" is described in the main text on page 92).*

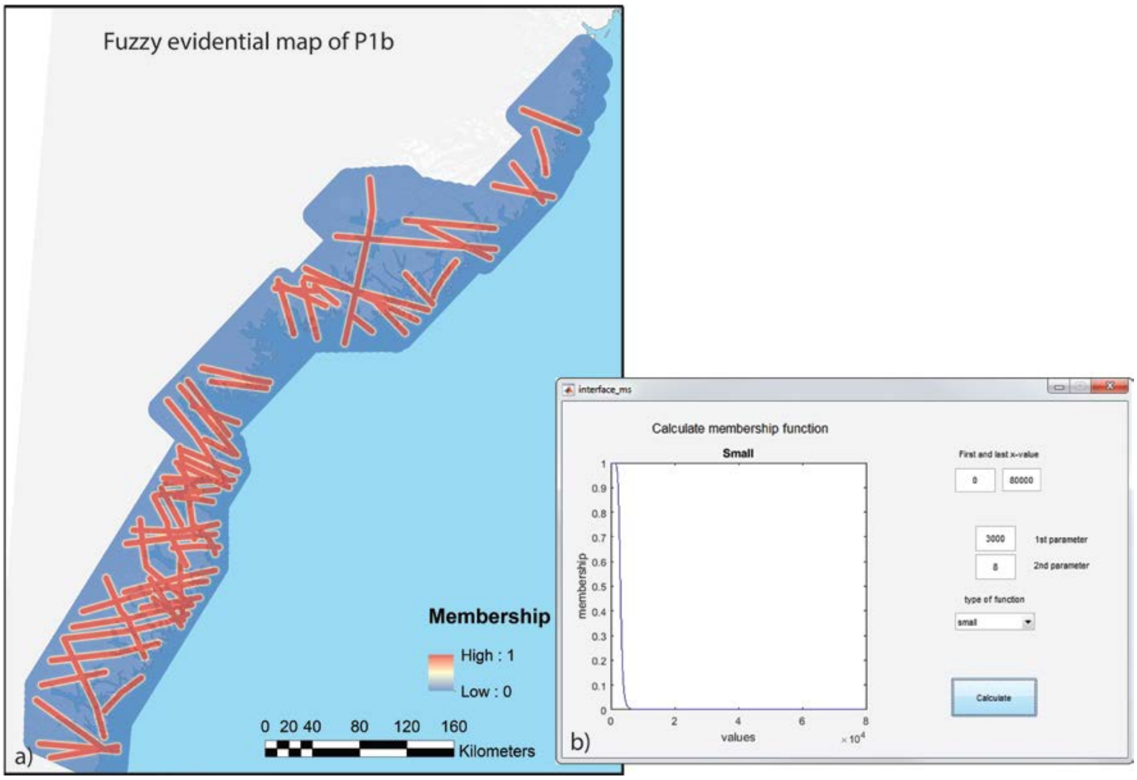

First and last x-value: 0 80000

1st parameter: 3000

2nd parameter: 8

type of function: small

Figure 81. ***A*** *Fuzzy evidential map for the target criterion/proxy P1b that is used later on for the calculation of the prospectivity maps. “First order shear and fault zones regarded as pathways for mineralizing fluids” (targeting element) is represented by distances from lineaments that are manually determined from the aeromagnetic data (target criterion/proxy “1st order structures”). In* ***B*** *the membership function is shown that is used for the fuzzification of these distances (input data are shown in Fig. 49a). (The used functional “small” is described in the main text on page 92).*

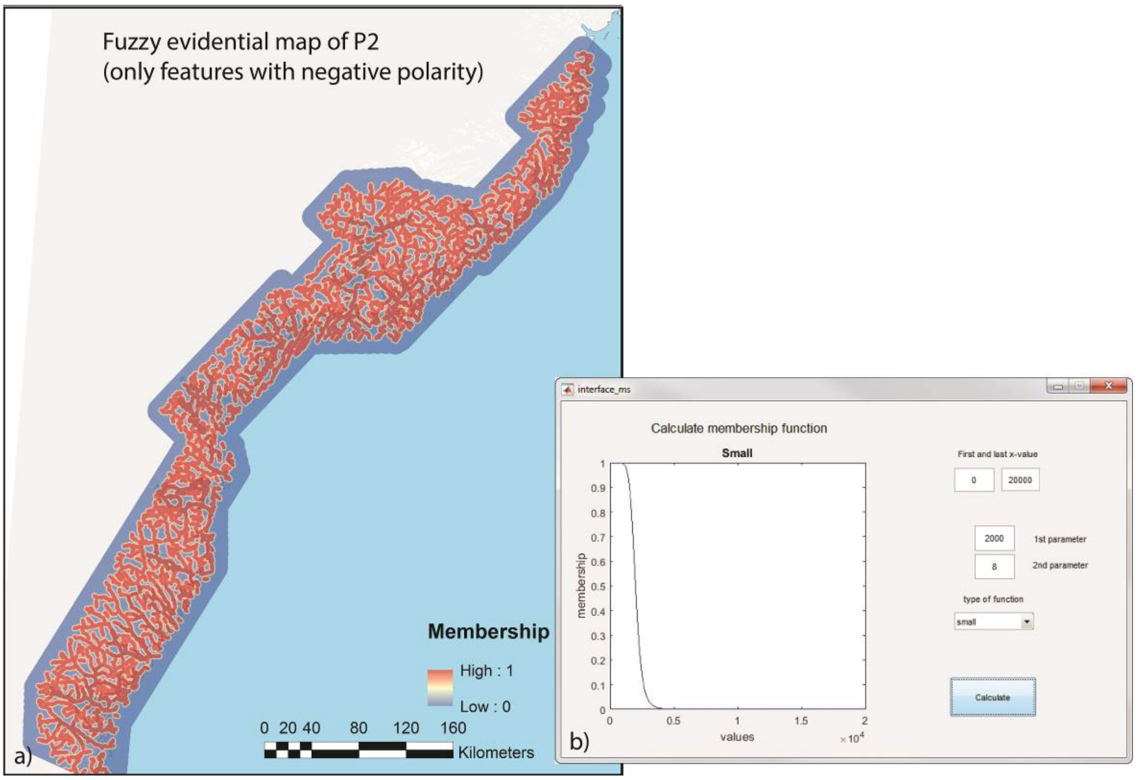

First and last x-value: 0, 20000

1st parameter: 2000

2nd parameter: 8

type of function: small

Figure 82. ***A*** *Fuzzy evidential map for the target criterion/proxy P2 that is used later on for the calculation of the prospectivity maps. "Second and third order shear and fault zones regarded as pathways for mineralizing fluids" (targeting element) is represented by distances from lineaments that are automatically determined from the aeromagnetic data (target criterion/proxy "2nd/3rd order structures"). Because strong topography in the target area biases the automated detection, two complementary processing flows are applied, in which different settings are used in the "symmetry filtering" (elongated magnetic anomalies with either positive or negative polarities after texture analysis are detected) to identify all features associated with lineaments. In this figure only features derived from the first flow (identifying features having negative polarities) are shown, but the remaining features from the second flow (identifying features having positive polarities) are shown in Figure 83. In* ***B*** *the membership function is shown that is used for the fuzzification of the distances (input data are shown in Fig. 49c). (The used functional "small" is described in the main text on page 92).*

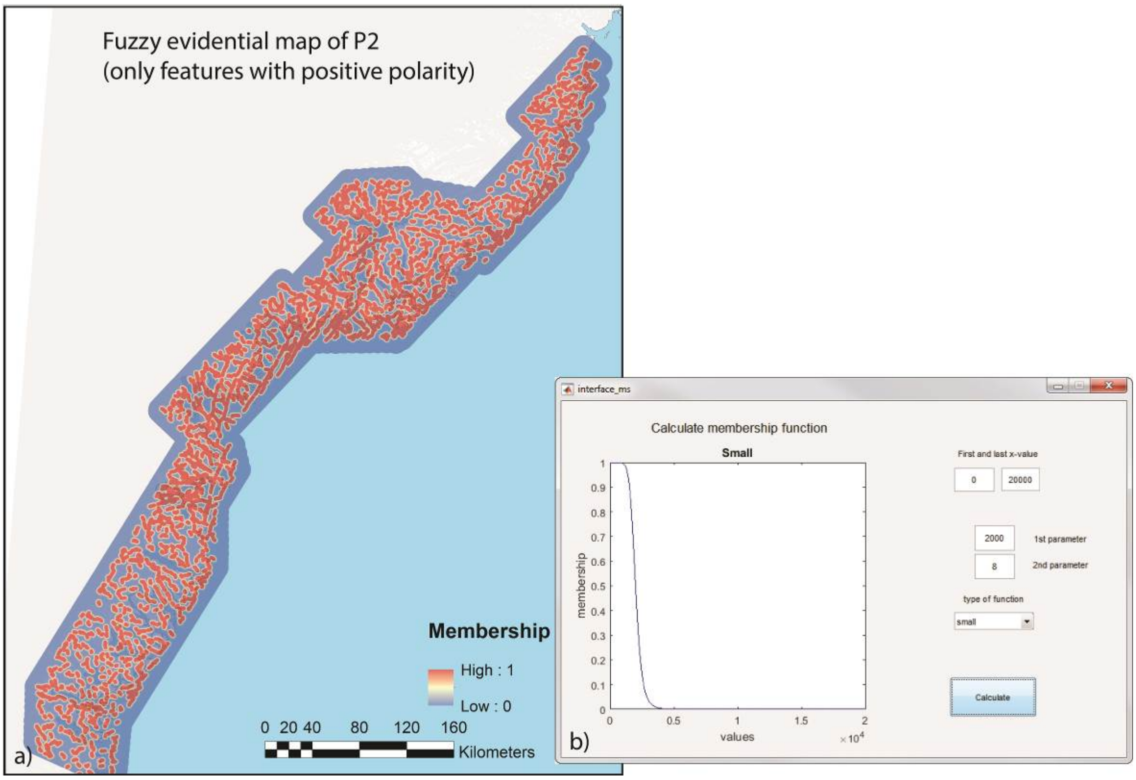

First and last x-value: 0 20000

1st parameter: 2000

2nd parameter: 8

type of function: small

Figure 83. ***A*** *Fuzzy evidential map for the target criterion/proxy P2 that is used later on for the calculation of the prospectivity maps. “Second and third order shear and fault zones regarded as pathways for mineralizing fluids” (targeting element) is represented by distances from lineaments that are automatically determined from the aeromagnetic data (target criterion/proxy “$2^{nd}/3^{rd}$ order structures”). Because strong topography in the target area biases the automated detection (see section ”Detection of lineaments from regional airborne magnetic data (Pb1, P2, T1, t2)”), two complementary processing flows are applied, in which different settings are used in the “symmetry filtering” (elongated magnetic anomalies with either positive or negative polarities after texture analysis are detected) to identify all features associated with lineaments. In this figure only features derived from the second flow (identifying features having positive polarities) are shown, but the remaining features from the first flow (identifying features having negative polarities) are presented in Figure 82. In* ***B*** *the membership function is shown that is used for the fuzzification of the distances (map of input data is plotted in Fig. 49b). (The used functional “small” is described in the main text on page 92).*

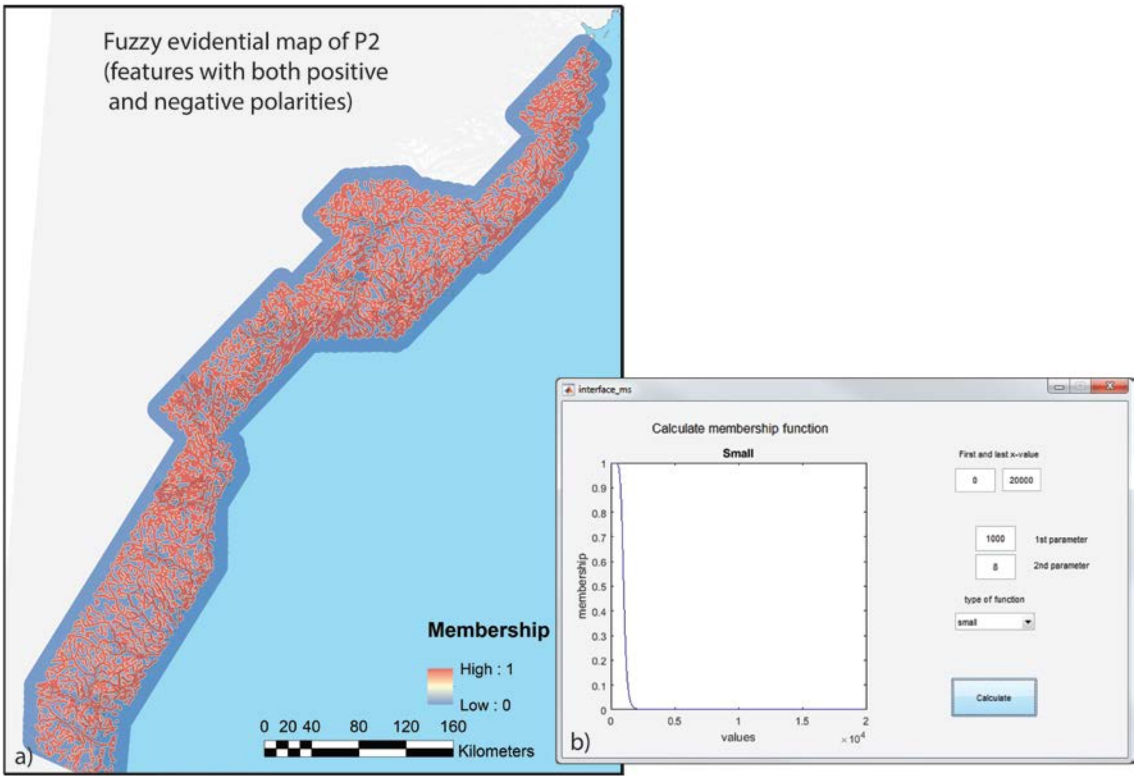

First and last x-value: 0 20000

1st parameter: 1000

2nd parameter: 8

type of function: small

Figure 84. ***A*** *Fuzzy evidential map for the target criterion/proxy P2 that is used later on for the calculation of the prospectivity maps. Here, features from both processing flows are combined, whose fuzzy evidential maps are shown in the Figure 82 and Figure 83. This means all automatically detected lineaments from both flows are used in the distance calculation. In* ***B*** *the membership function is shown that is used for the fuzzification of the distances. (The used functional “small” is described in the main text on page 92).*

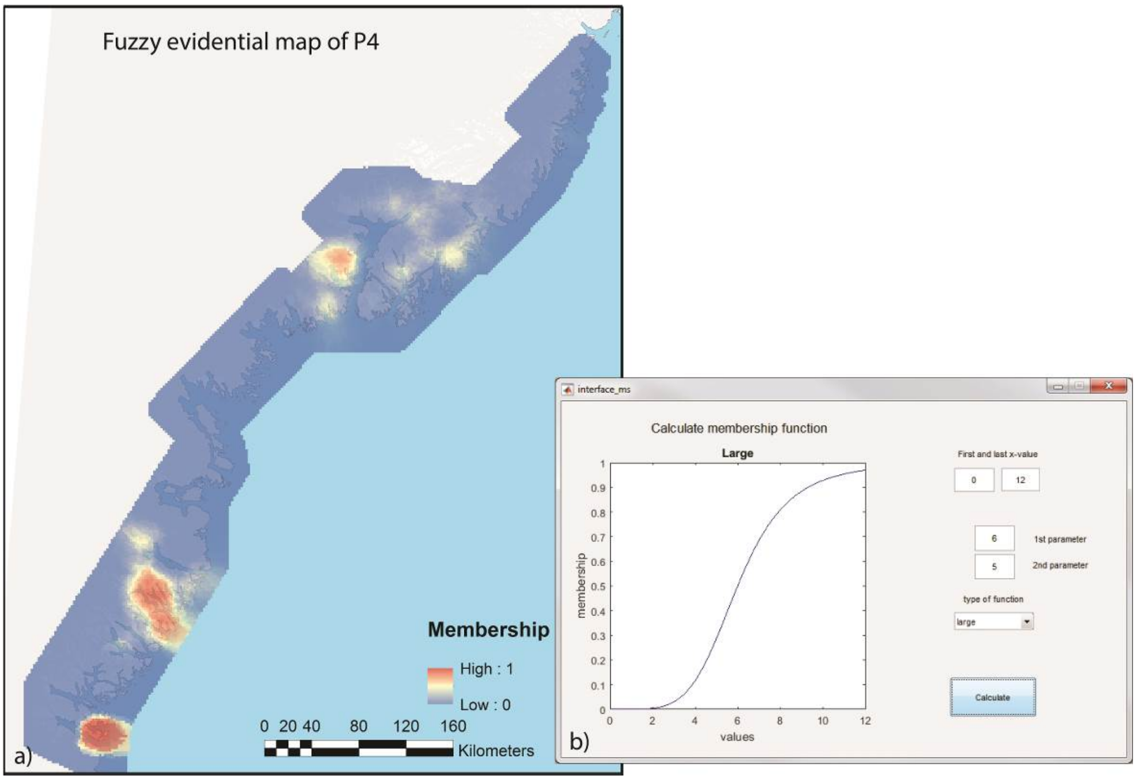

First and last x-value: 0 12
6 1st parameter
5 2nd parameter
type of function: large

Figure 85. ***A*** *Fuzzy evidential map for the target criterion/proxy P4 that is used later on for the calculation of the prospectivity maps. "Lithological interfaces regarded as pathways for mineralizing fluids" (targeting element) is represented by the density of interfaces from geological units (target criterion/proxy "Lithological units interface complexity").In* ***B*** *the membership function is shown that is used for the fuzzification of the map describing the density of interfaces (the input evidential map is obtained by applying a kriging interpolation to the density values and is shown in Fig. 16c). (The used functional "large" is described in the main text on page 92).*

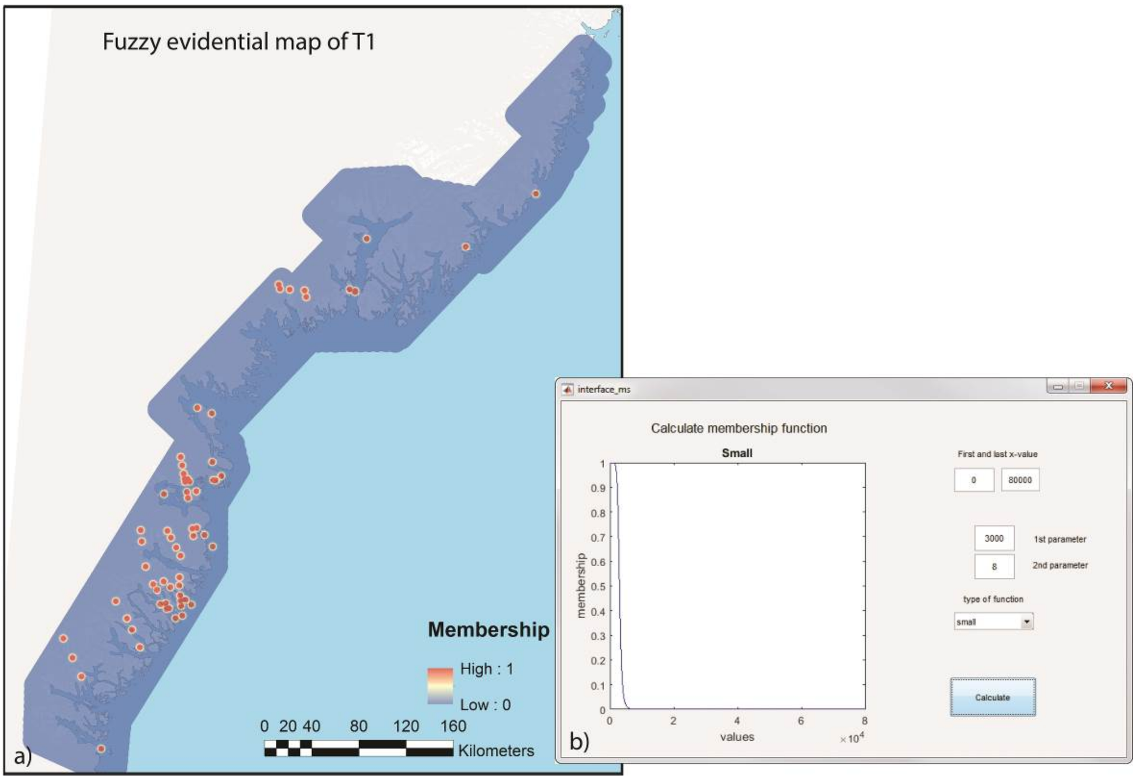

First and last x-value: 0 80000

1st parameter: 3000

2nd parameter: 8

type of function: small

Figure 86. ***A*** *Fuzzy evidential map for the target criterion/proxy T1 that is used later on for the calculation of the prospectivity maps. “Structural intersection” (targeting element) is represented by distances from intersections of lineaments that are manually determined from the aeromagnetic data (target criterion/proxy “structural intersection”).In* ***B*** *the membership function is shown that is used for the fuzzification of these distances (input data are shown in Fig. 50b). (The used functional “small” is described in the main text on page 92).*

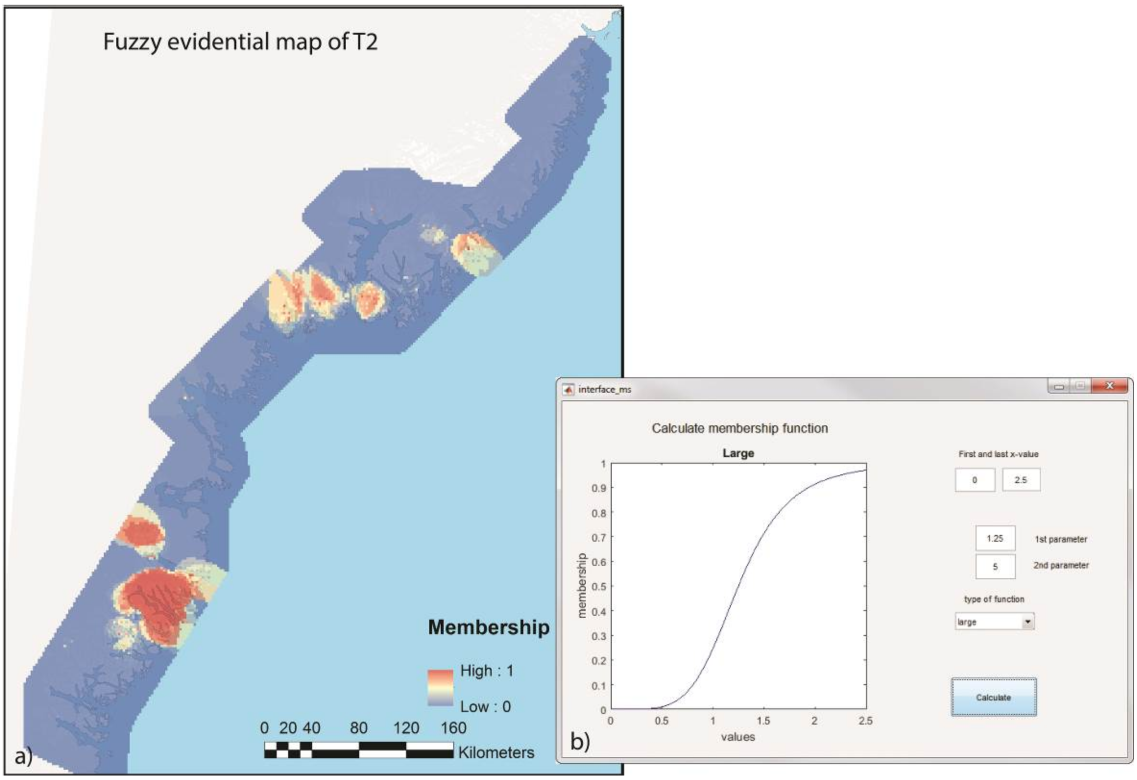

First and last x-value: 0 2.5

1st parameter: 1.25

2nd parameter: 5

type of function: large

Figure 87. ***A*** *Fuzzy evidential map for the target criterion/proxy T2 that is used later on for the calculation of the prospectivity maps. "Structure intersection with lithostratigraphy interfaces" (targeting element) is represented by the density of intersections between lineaments (manually determined from aeromagnetic data) and interfaces from geological units (target criterion/proxy "Structures crossing lithologies").In* ***B*** *the membership function is shown that is used for the fuzzification of the map representing the density of intersections (the input evidential map is obtained by applying a kriging interpolation to the density values and is shown in Fig. 18c). (The used functional "large" is described in the main text on page 92).*

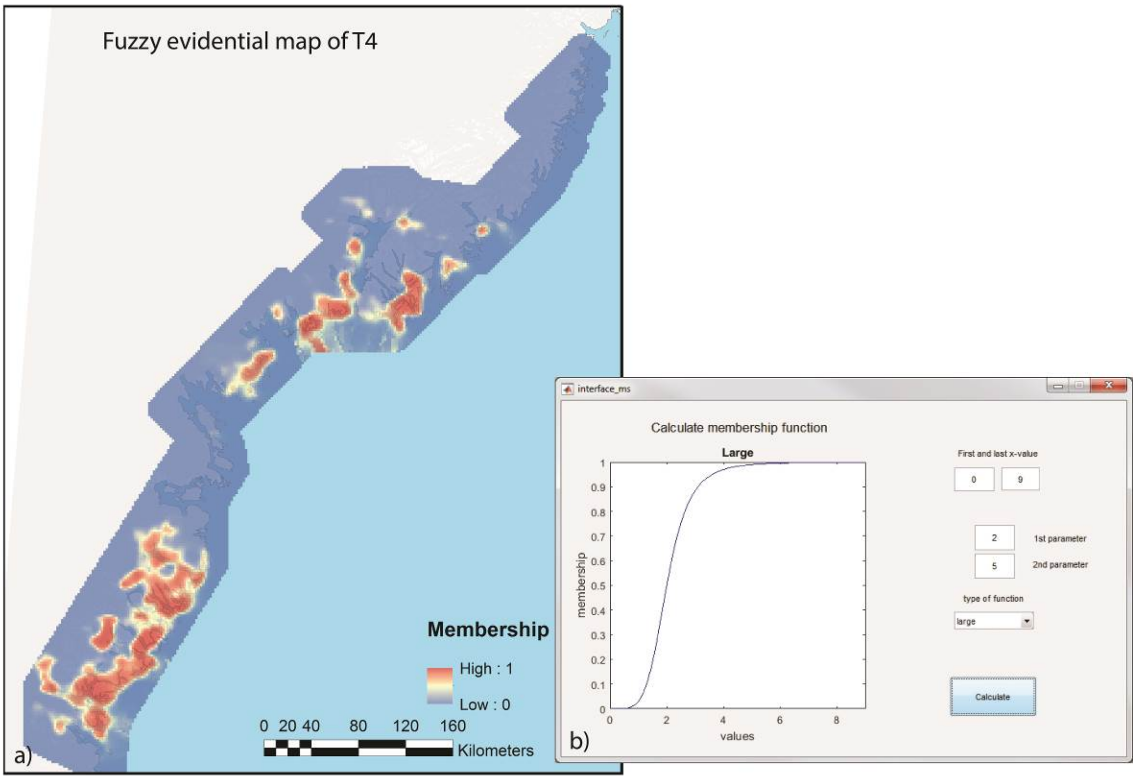

First and last x-value: 0 9

1st parameter: 2

2nd parameter: 5

type of function: large

Figure 88. ***A*** *Fuzzy evidential map for the target criterion/proxy T4 that is used later on for the calculation of the prospectivity maps. "Structural complexity" (targeting element) is represented by the density of structures (extracted from the digital geological map; target criterion/proxy "Structural complexity").In* ***B*** *the membership function is shown that is used for the fuzzification of the map associated with the density of structures (the input evidential map is obtained by applying a kriging interpolation to the density values and is shown in Fig. 18c). (The used functional "large" is described in the main text on page 92).*

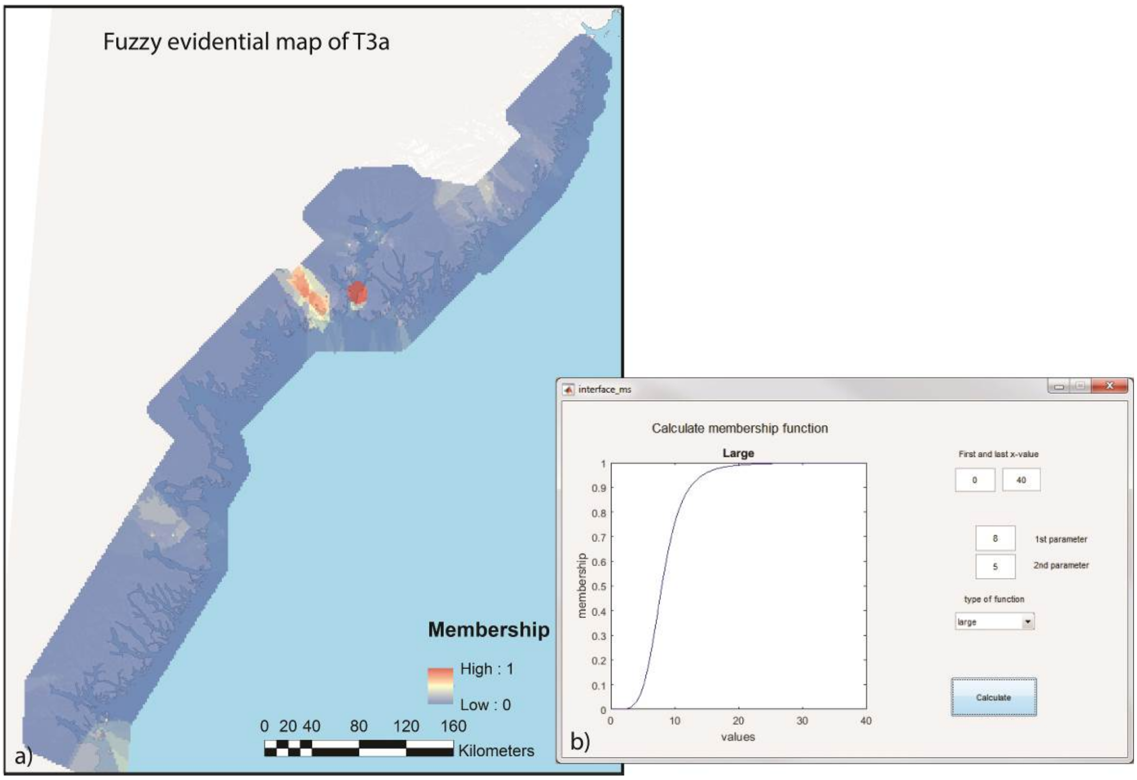

First and last x-value: 0 40

1st parameter: 8

2nd parameter: 5

type of function: large

Figure 89. ***A*** *Fuzzy evidential map for the target criterion/proxy T3a that is used later on for the calculation of the prospectivity maps. "Geochemical anomalies of Au" (targeting element) is represented by distribution of Au in stream sediments (target criterion/proxy "Au -SS").In* ***B*** *the membership function is shown that is used for the fuzzification of the map associated with the distribution of Au concentrations (the input evidential map is obtained by applying a kriging interpolation of stream sediment concentrations and is shown in Fig. 20b). (The used functional "large" is described in the main text on page 92).*

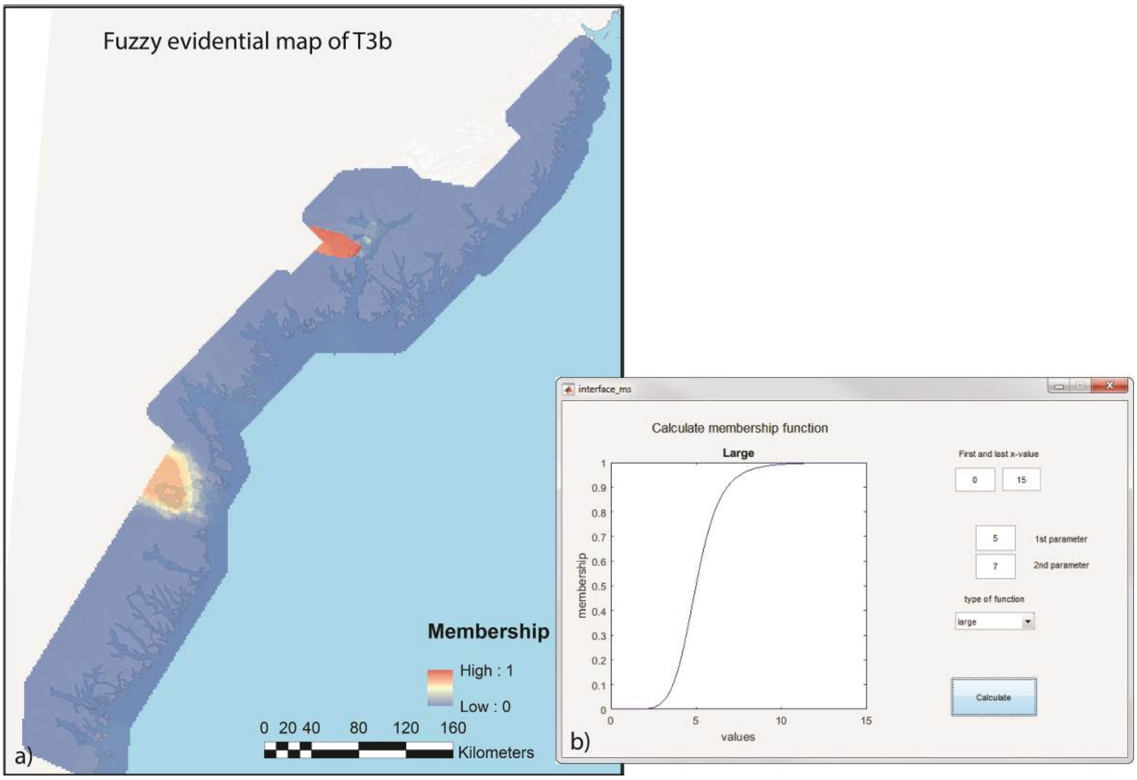

First and last x-value: 0, 15

1st parameter: 5

2nd parameter: 7

type of function: large

Figure 90. ***A*** *Fuzzy evidential map for the target criterion/proxy T3b that is used later on for the calculation of the prospectivity maps. "Geochemical anomalies of As" (targeting element) is represented by distribution of As in stream sediments (target criterion/proxy "As -SS").In* ***B*** *the membership function is shown that is used for the fuzzification of the map associated with the distribution of As concentrations (the input evidential map is obtained by applying a kriging interpolation of stream sediment concentrations and is shown in Fig. 21b). (The used functional "large" is described in the main text on page 92).*

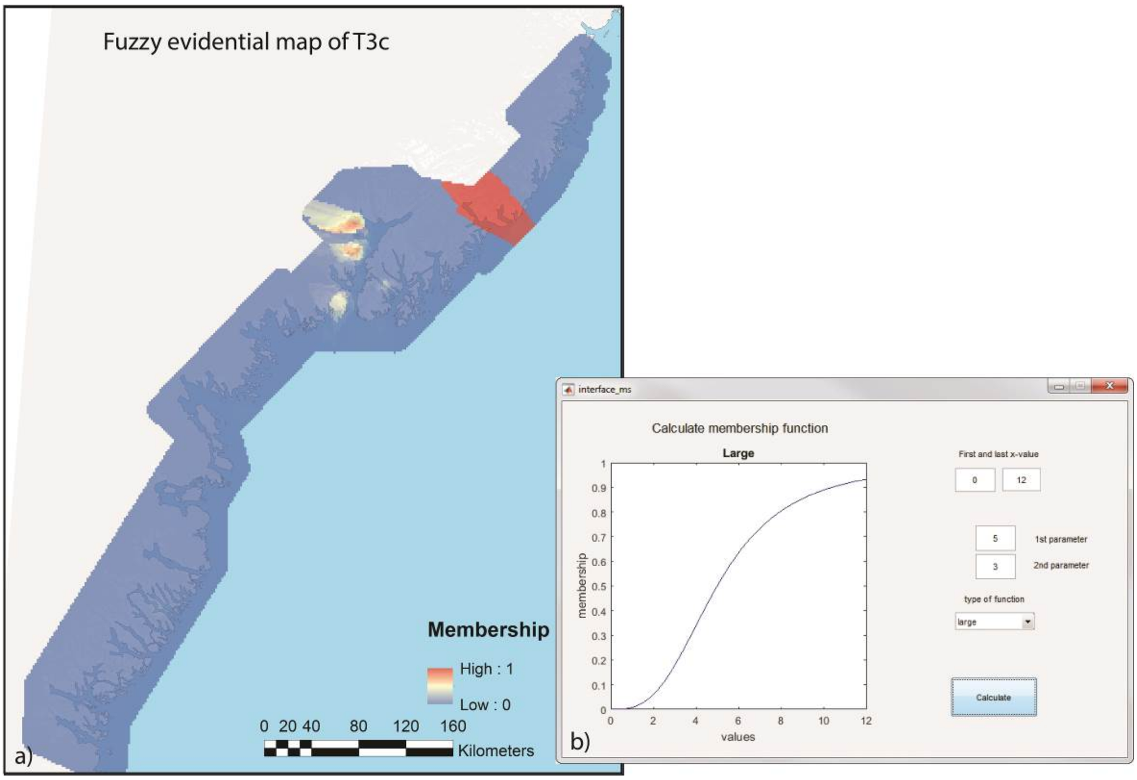

First and last x-value: 0 12

1st parameter: 5

2nd parameter: 3

type of function: large

Figure 91. ***A*** *Fuzzy evidential map for the target criterion/proxy T3c that is used later on for the calculation of the prospectivity maps. “Geochemical anomalies of W” (targeting element) is represented by distribution of W in stream sediments (target criterion/proxy “W -SS”).In* ***B*** *the membership function is shown that is used for the fuzzification of the map associated with the distribution of W concentrations (the input evidential map is obtained by applying a kriging interpolation of stream sediment concentrations and is shown in Fig. 22b). (The used functional “large” is described in the main text on page 92).*

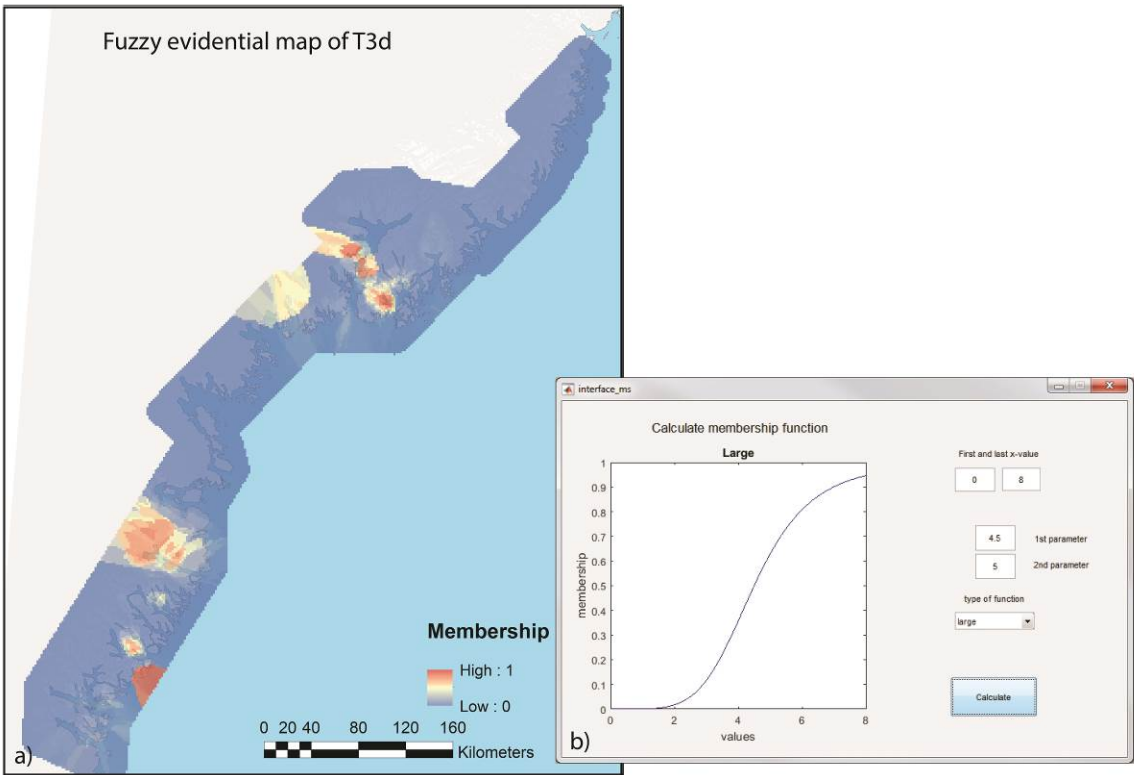

First and last x-value
0 8
4.5 1st parameter
5 2nd parameter
type of function
large

Figure 92. ***A*** *Fuzzy evidential map for the target criterion/proxy T3d that is used later on for the calculation of the prospectivity maps. "Geochemical anomalies of Mo" (targeting element) is represented by distribution of Mo in stream sediments (target criterion/proxy "Mo -SS").In* ***B*** *the membership function is shown that is used for the fuzzification of the map associated with the distribution of Mo concentrations (the input evidential map is obtained by applying a kriging interpolation of stream sediment concentrations and is shown in Fig. 23b).(The used functional "large" is described in the main text on page 92).*

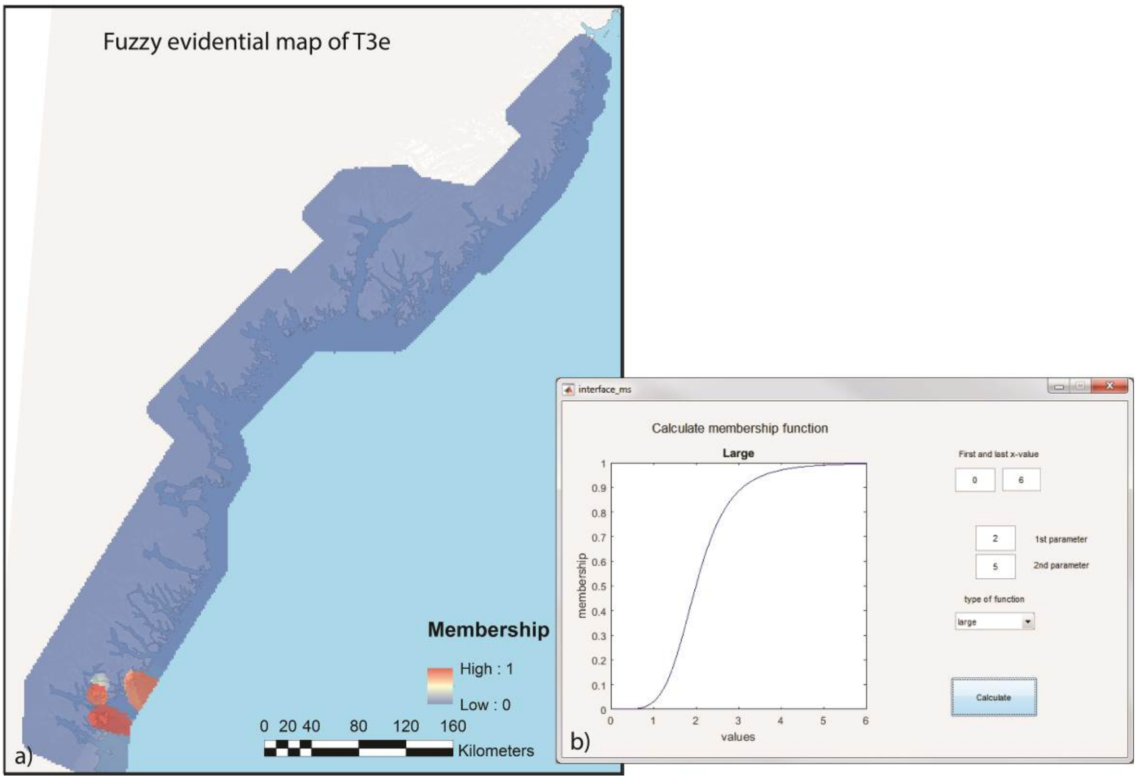

First and last x-value: 0, 6

1st parameter: 2

2nd parameter: 5

type of function: large

Figure 93. ***A*** *Fuzzy evidential map for the target criterion/proxy T3e that is used later on for the calculation of the prospectivity maps. “Geochemical anomalies of Sb” (targeting element) is represented by distribution of Sb in stream sediments (target criterion/proxy “Sb -SS”).In* ***B*** *the membership function is shown that is used for the fuzzification of the map associated with the distribution of Sb concentrations (the input evidential map is obtained by applying a kriging interpolation of stream sediment concentrations and is shown in Fig. 24b).(The used functional “large” is described in the main text on page 92).*

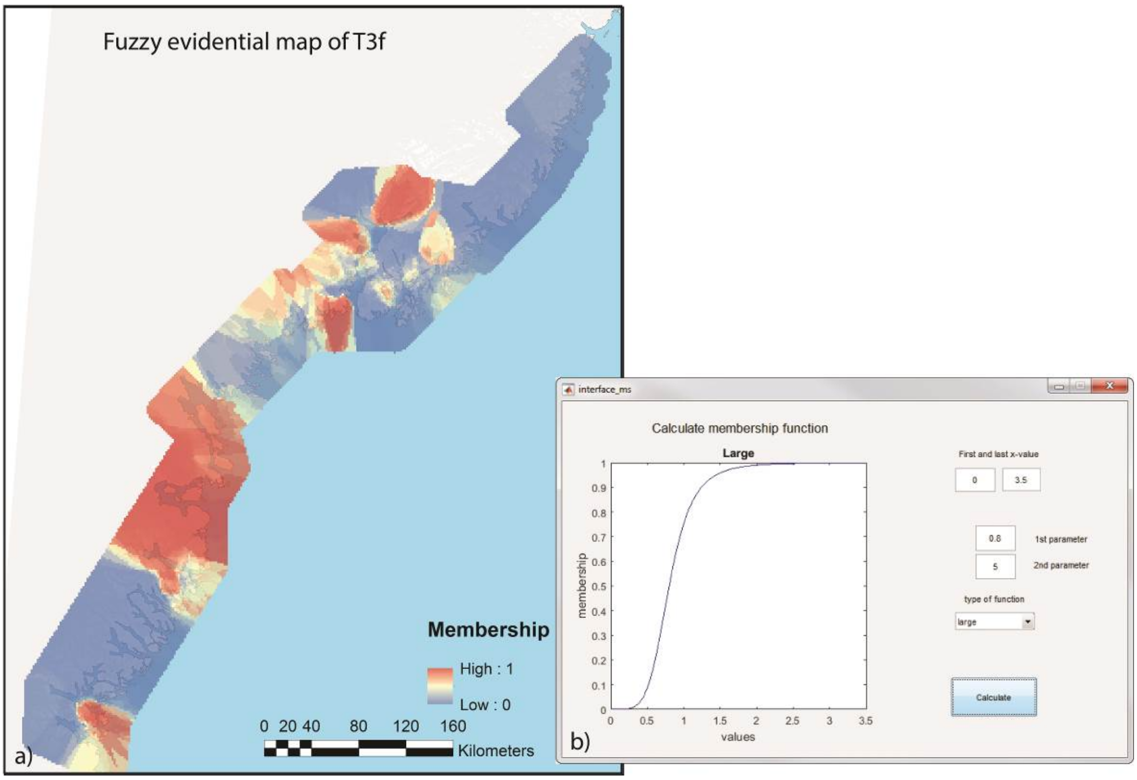

First and last x-value: 0 3.5

1st parameter: 0.8

2nd parameter: 5

type of function: large

Figure 94. ***A*** *Fuzzy evidential map for the target criterion/proxy T3f that is used later on for the calculation of the prospectivity maps. “Geochemical anomalies of Cs” (targeting element) is represented by distribution of Cs in stream sediments (target criterion/proxy “Cs -SS”).In* ***B*** *the membership function is shown that is used for the fuzzification of the map associated with the distribution of Cs concentrations (the input evidential map is obtained by applying a kriging interpolation of stream sediment concentrations and is shown in Fig. 25b).(The used functional “large” is described in the main text on page 92).*

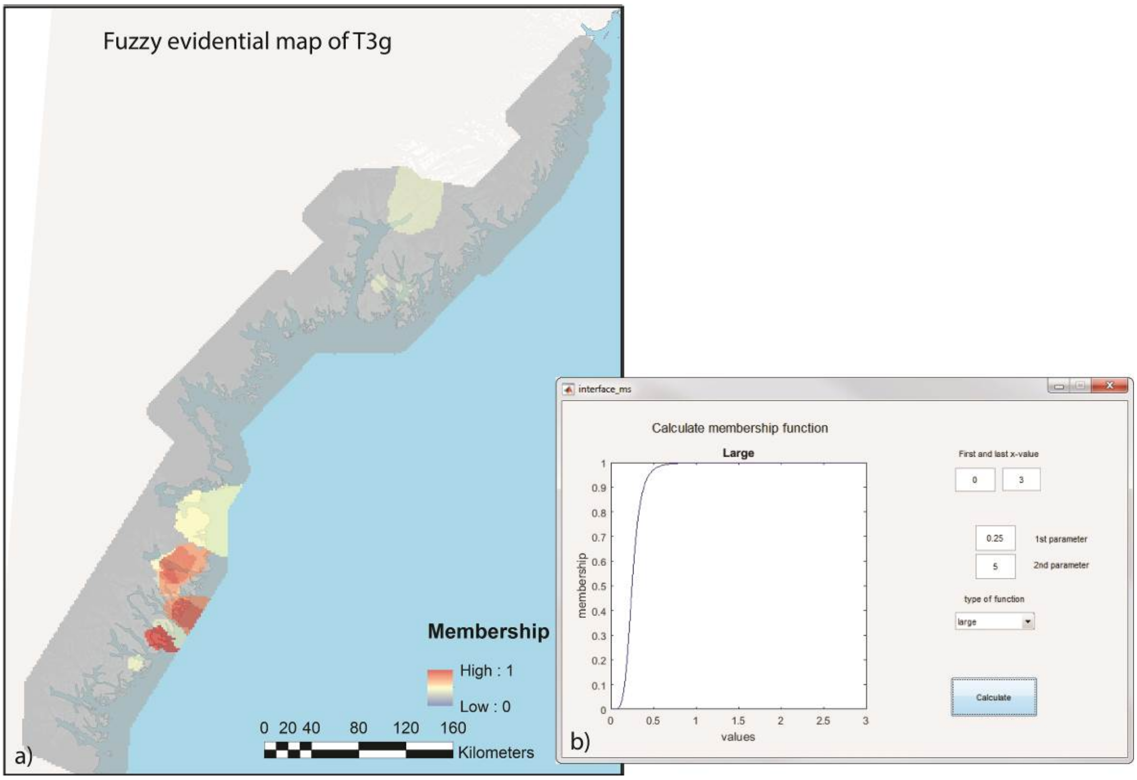

First and last x-value: 0 3

1st parameter: 0.25

2nd parameter: 5

type of function: large

Figure 95. ***A*** *Fuzzy evidential map for the target criterion/proxy T3g that is used later on for the calculation of the prospectivity maps. “Geochemical anomalies of Bi” (targeting element) is represented by distribution of Bi in stream sediments (target criterion/proxy “Bi -SS”).In* ***B*** *the membership function is shown that is used for the fuzzification of the map associated with the distribution of Bi concentrations (the input evidential map is obtained by applying a kriging interpolation of stream sediment concentrations and is shown in Fig. 26b).(The used functional “large” is described in the main text on page 92).*

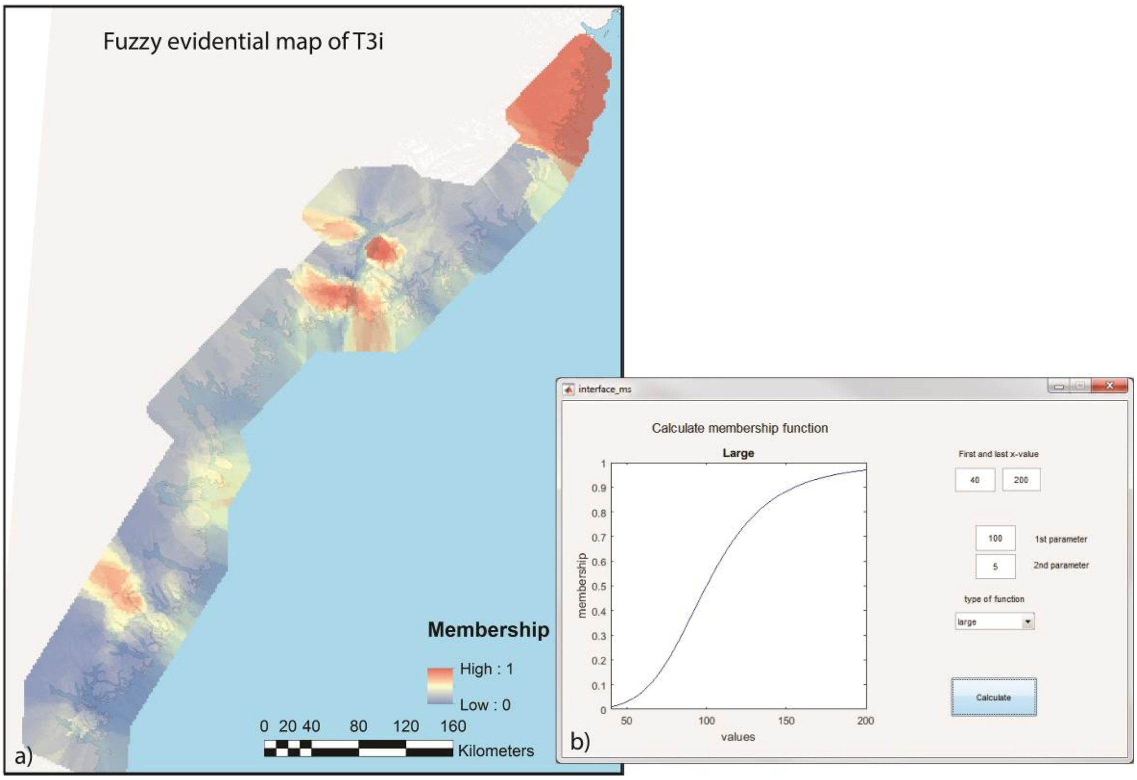

First and last x-value: 40 200

1st parameter: 100

2nd parameter: 5

type of function: large

Figure 96. ***A*** *Fuzzy evidential map for the target criterion/proxy T3i that is used later on for the calculation of the prospectivity maps. "Geochemical anomalies of Bi" (targeting element) is represented by distribution of Ni/Mg ratio in stream sediments (target criterion/proxy "Ni/Mg-SS").In* ***B*** *the membership function is shown that is used for the fuzzification of the map associated with the distribution of these relative concentrations (the input evidential map is obtained by applying a kriging interpolation of stream sediment data and is shown in Fig. 27b).(The used functional "large" is described in the main text on page 92).*

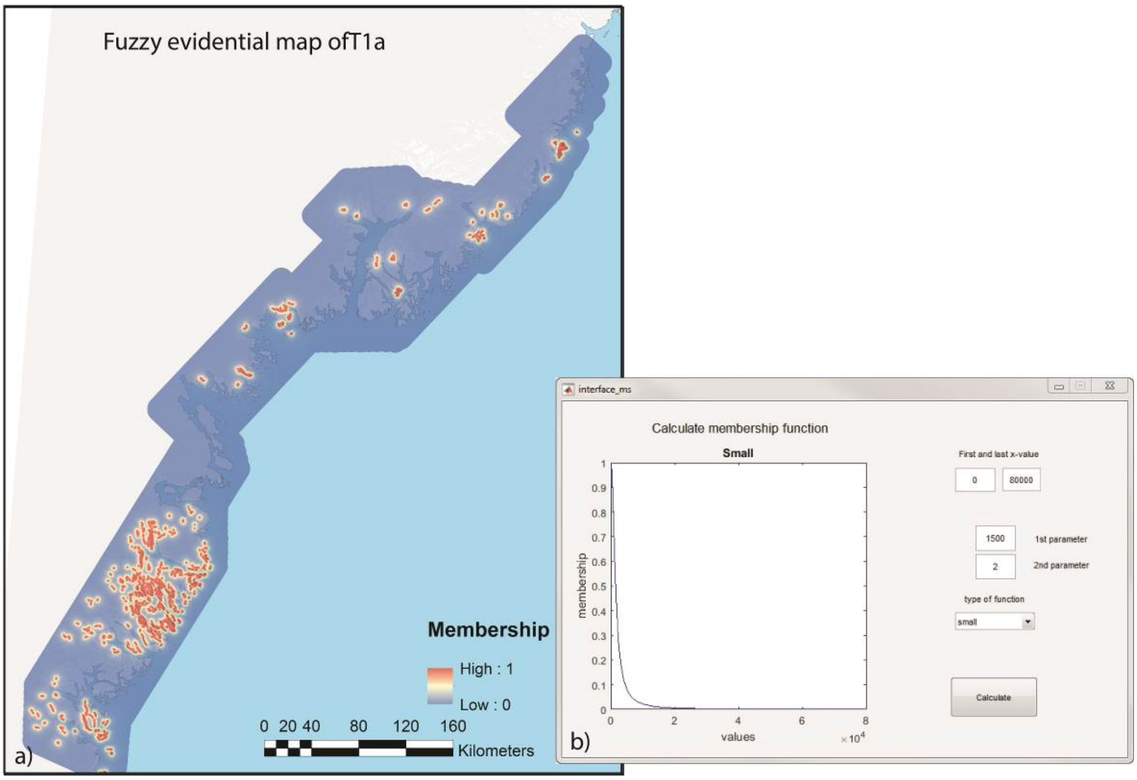

First and last x-value: 0 80000

1500 1st parameter

2 2nd parameter

type of function: small

Figure 97. ***A*** *Fuzzy evidential map for the target criterion/proxy T1a that is used later on for the calculation of the prospectivity maps. "Chemical favorable host rock for mineralization" (targeting element) is represented by distances from mafic rock units as they are present in the digital geological map (target criterion/proxy "mafic units").In* ***B*** *the membership function is shown that is used for the fuzzification of these distances (input data are shown in Fig. 13a). (The used functional "small" is described in the main text on page 92).*

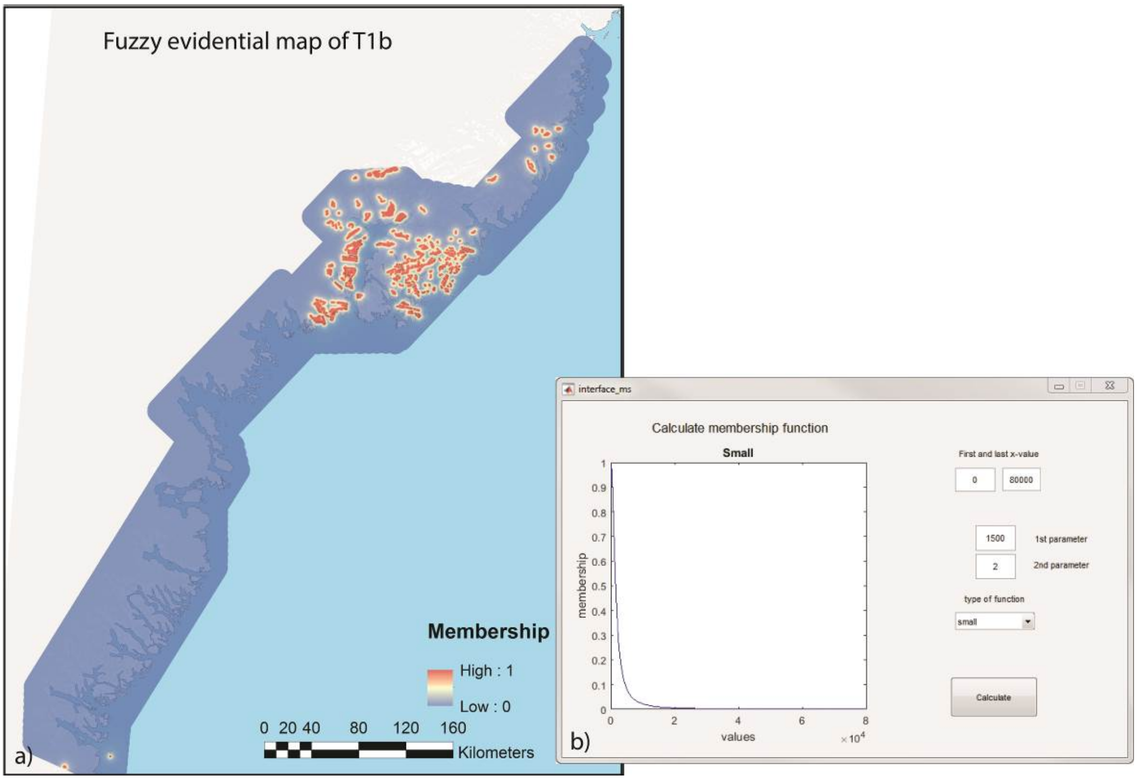

First and last x-value: 0 80000

1st parameter: 1500

2nd parameter: 2

type of function: small

Figure 98. ***A*** *Fuzzy evidential map for the target criterion/proxy T1b that is used later on for the calculation of the prospectivity maps. “Chemical favorable host rock for mineralization” (targeting element) is represented by distances from supracrustal rock units as they are present in the digital geological map (target criterion/proxy “supracrustal units”).In* ***B*** *the membership function is shown that is used for the fuzzification of these distances (input data are shown in Fig. 13b). (The used functional “small” is described in the main text on page 92).*

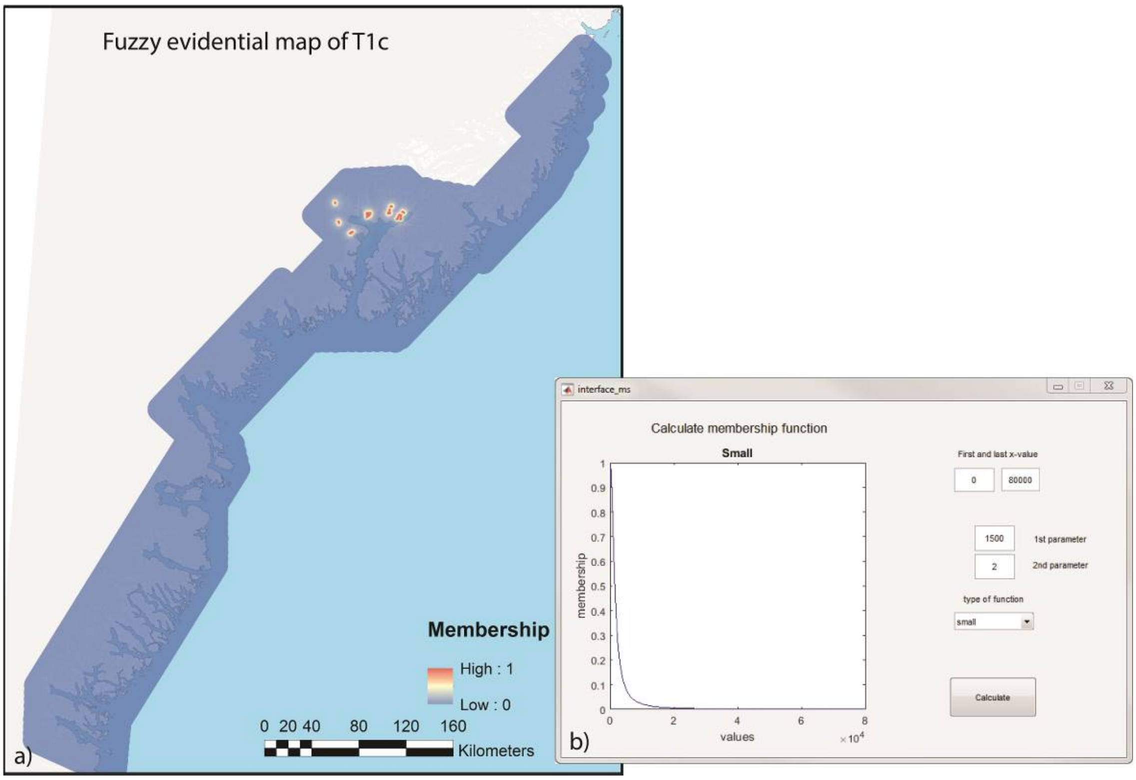

First and last x-value: 0 80000

1st parameter: 1500

2nd parameter: 2

type of function: small

Figure 99. ***A*** *Fuzzy evidential map for the target criterion/proxy T1c that is used later on for the calculation of the prospectivity maps. "Chemical favorable host rock for mineralization" (targeting element) is represented by distances from marble rock units as they are present in the digital geological map (target criterion/proxy "marble units").In* ***B*** *the membership function is shown that is used for the fuzzification of these distances (input data are shown in Fig. 13c). (The used functional "small" is described in the main text on page 92).*

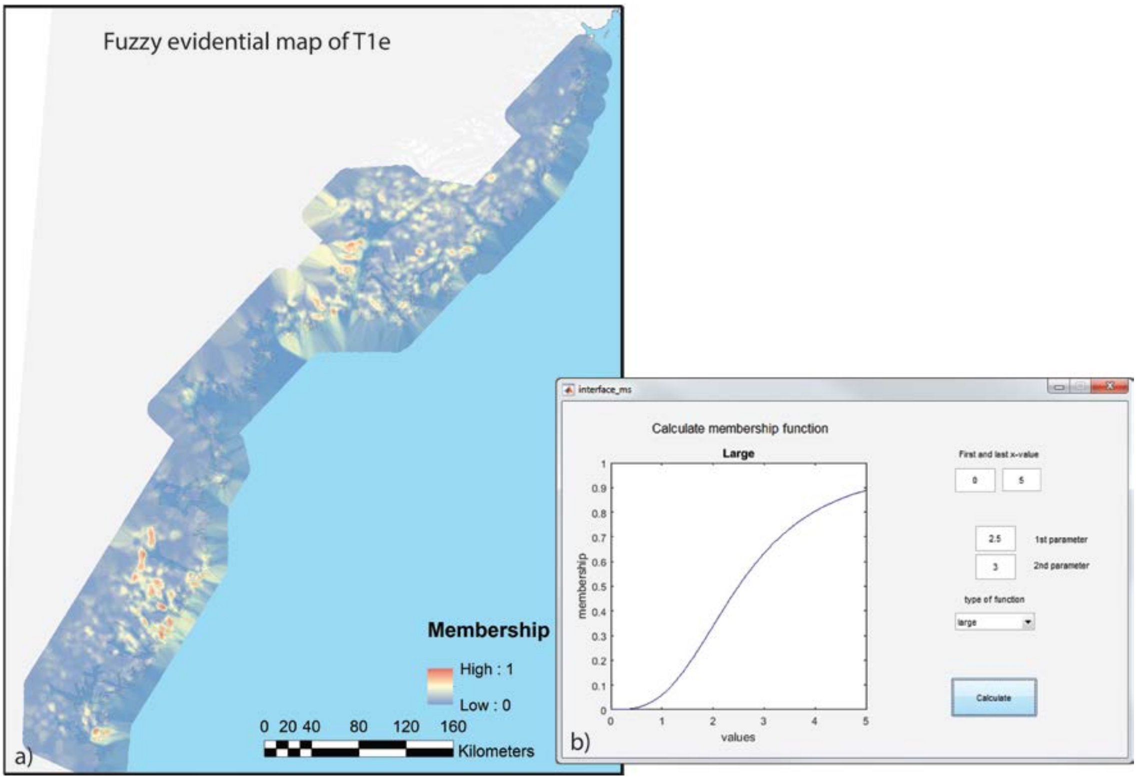

First and last x-value: 0 5

2.5 1st parameter

3 2nd parameter

type of function: large

Figure 100. ***A*** *Fuzzy evidential map for the target criterion/proxy T1e that is used later on for the calculation of the prospectivity maps. “Chemical favorable host rock for mineralization” (targeting element) is represented by the density of geological layers (extracted from the digital geological map; target criterion/proxy “Geological complexity”). In* ***B*** *the membership function is shown that is used for the fuzzification of the map associated with the density of geological layers (the input evidential map is obtained by applying a kriging interpolation to the density values and is shown in Fig. 15b). (The used functional “large” is described in the main text on page 92).*

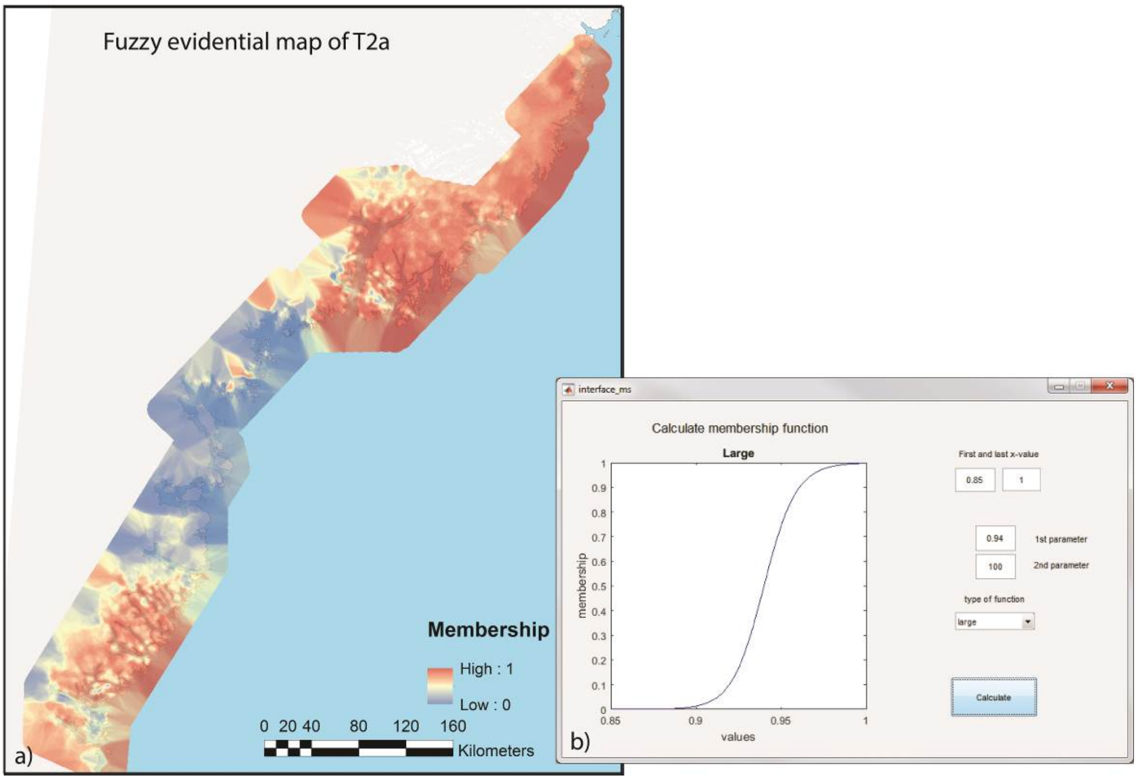

Calculate membership function

First and last x-value: 0.85 1

1st parameter: 0.94

2nd parameter: 100

type of function: large

Figure 101. ***A*** *Fuzzy evidential map for the target criterion/proxy T2a that is used later on for the calculation of the prospectivity maps. “Favorable host rock for mineralization” (targeting element) is represented by the mafic index determined from multispectral ASTER satellite data (target criterion/proxy “Mafic index”). In* ***B*** *the membership function is shown that is used for the fuzzification of the map associated with the mafic index (the input evidential map is obtained by applying a kriging interpolation to the pixels data from the satellite data and is shown in Fig. 29b). (The used functional “large” is described in the main text on page 92).*

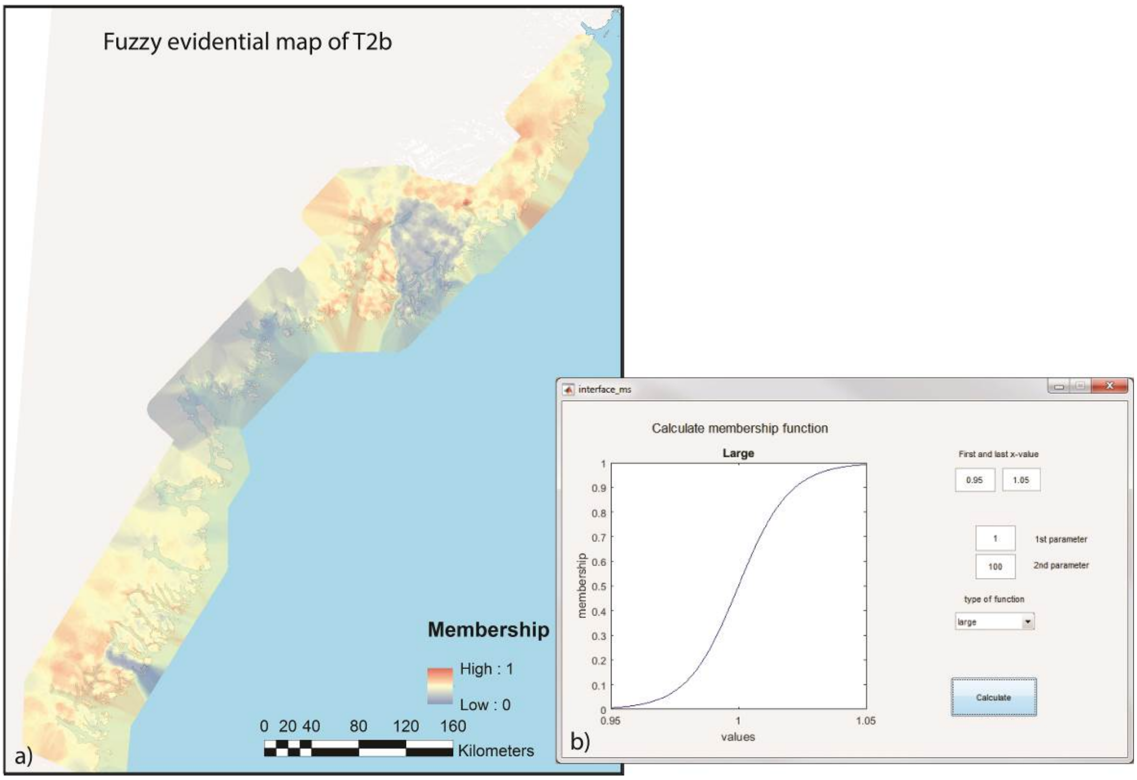

First and last x-value: 0.95 1.05

1st parameter: 1

2nd parameter: 100

type of function: large

Figure 102. ***A*** *Fuzzy evidential map for the target criterion/proxy T2b that is used later on for the calculation of the prospectivity maps. "Favorable host rock for mineralization" (targeting element) is represented by the carbonate index determined from multispectral ASTER satellite data (target criterion/proxy "Carbonate index"). In* ***B*** *the membership function is shown that is used for the fuzzification of the map associated with the mafic index (the input evidential map is obtained by applying a kriging interpolation to the pixels data from the satellite data and is shown in Fig. 30b). (The used functional "large" is described in the main text on page 92).*

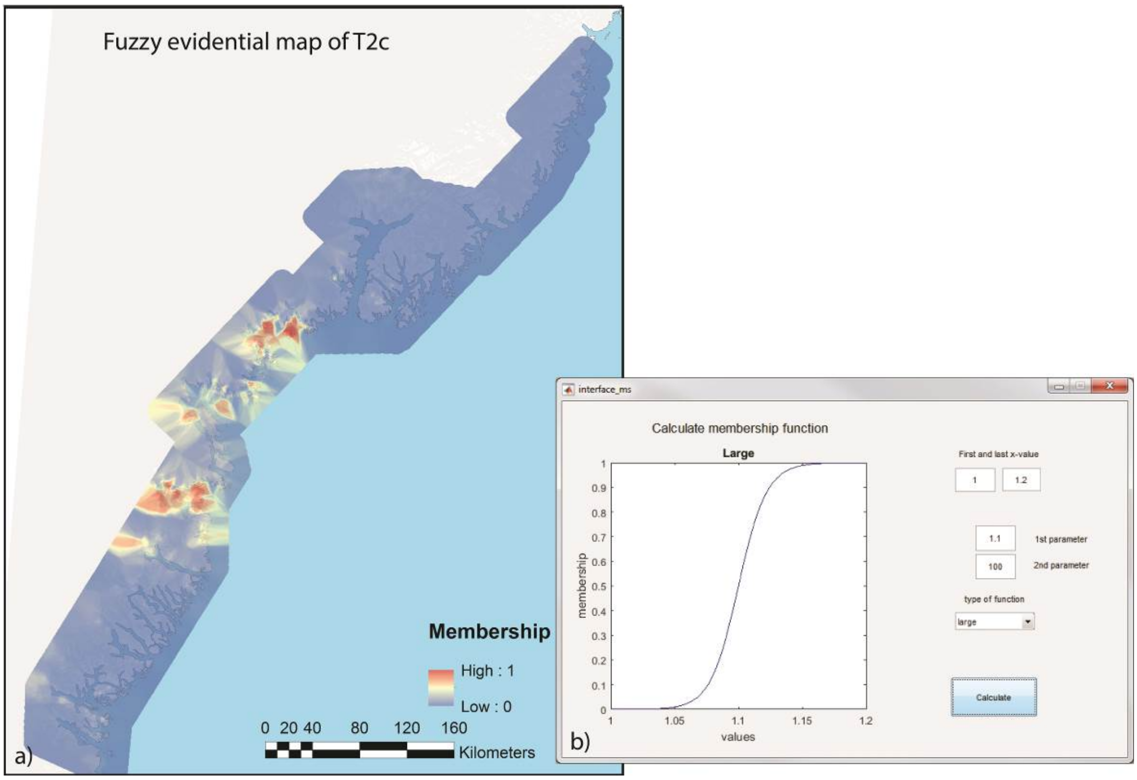

First and last x-value: 1 1.2

1.1 1st parameter

100 2nd parameter

type of function: large

Figure 103. ***A*** *Fuzzy evidential map for the target criterion/proxy T2c that is used later on for the calculation of the prospectivity maps. “Favorable host rock for mineralization” (targeting element) is represented by the SiO2 index determined from multispectral ASTER satellite data (target criterion/proxy “Silica index”). In* ***B*** *the membership function is shown that is used for the fuzzification of the map associated with the mafic index (the input evidential map is obtained by applying a kriging interpolation to the pixels data from the satellite data and is shown in Fig. 31b). (The used functional “large” is described in the main text on page 92).*

Appendix B:
Fuzzified evidential maps obtained by using natural neighbor interpolation

This Appendix shows versions of evidential maps (before and after fuzzification) that are generated with natural neighbour gridding. Fuzzified evidential maps based on kriging interpolation are presented in the previous Appendix A:
Fuzzified evidential maps.

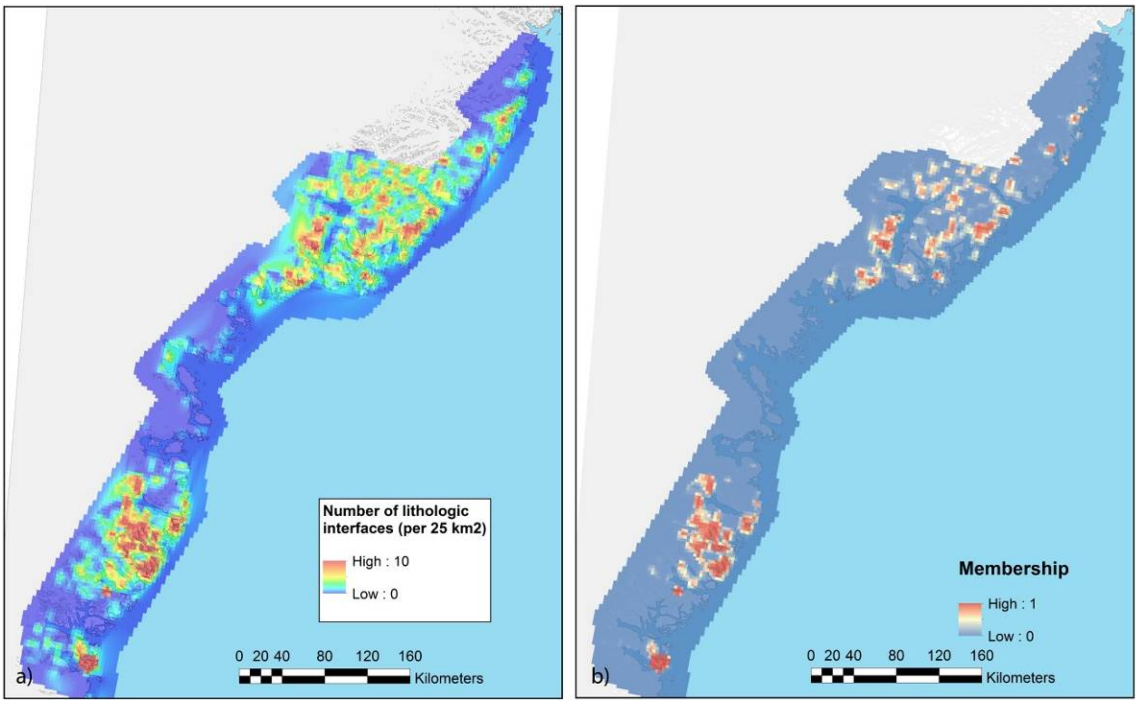

Figure 104. *As an alternative to kriging, natural neighbor interpolation is applied on the numbers of lithologic interfaces on a 5 x 5 km grid (see Fig. 16b) that is associated with the criterion/proxy element P4 and the target element "Lithological units interface complexity".* ***A*** *shows the grid obtained from the natural neighbor interpolation and* ***B*** *shows the fuzzy evidential map that is determined from A by employing the same fuzzy membership function (see Fig. 85b) as used before for corresponding map obtained by kriging.*

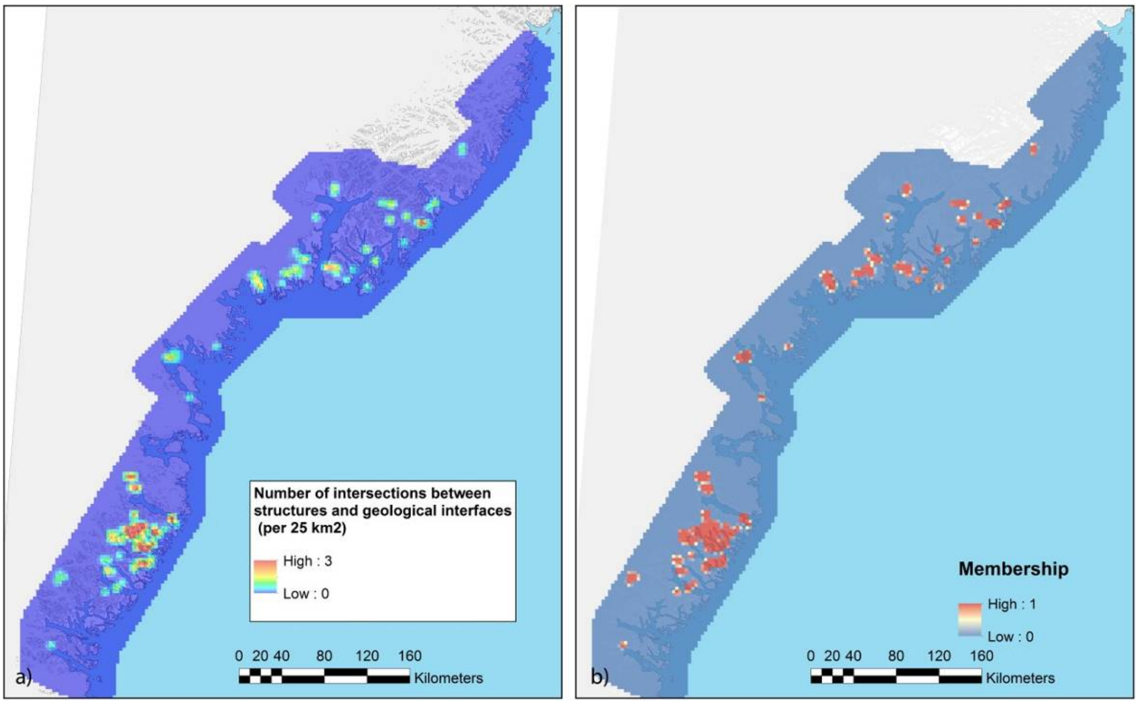

Figure 105. *As an alternative to kriging, natural neighbor interpolation is applied on the numbers of intersections between structures and geological interfaces on a 5 x 5 km grid (see Fig. 17b) that is associated with the criterion/proxy element T2 and the target element "Structural crossing lithologies".* ***A*** *shows the grid obtained from the natural neighbor interpolation and* ***B*** *shows the fuzzy evidential map that is determined from A by employing the same fuzzy membership function (see Fig. 87b) as used before for corresponding map obtained by kriging.*

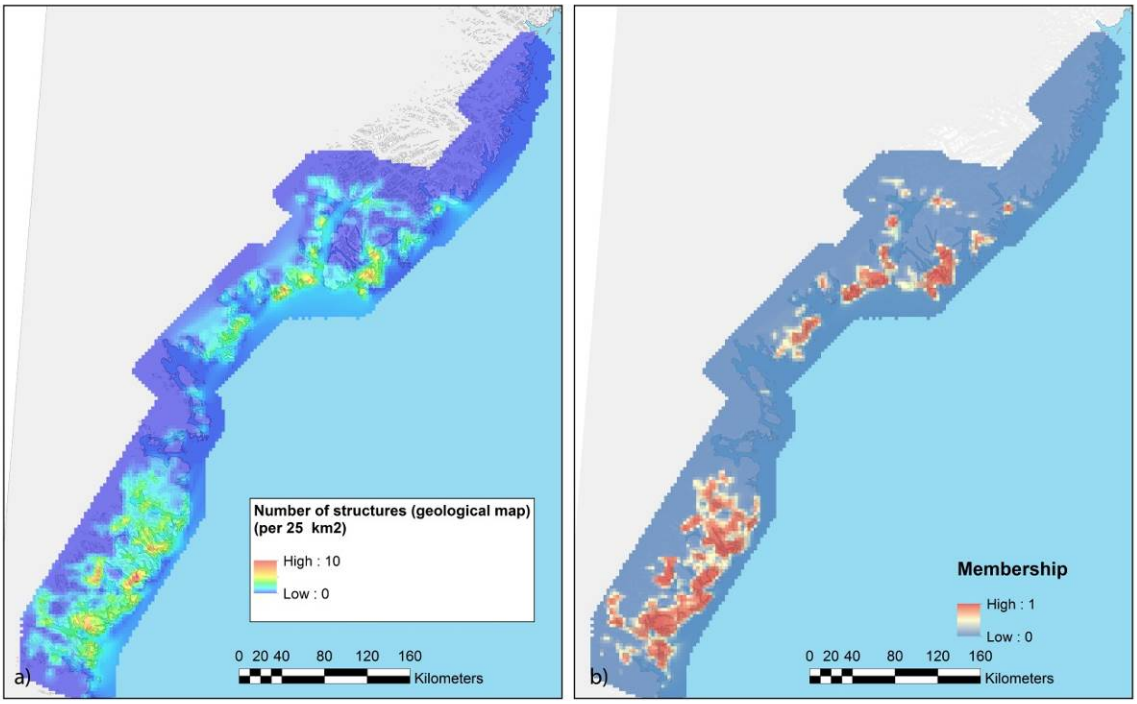

Figure 106. *As an alternative to kriging, natural neighbor interpolation is applied on the numbers of structures on a 5 x 5 km grid (see Fig. 18b) that is associated with the criterion/proxy element T4 and the target element "Structural complexity". **A** shows the grid obtained from the natural neighbor interpolation and **B** shows the fuzzy evidential map that is determined from A by employing the same fuzzy membership function (see Fig. 88b) as used before for corresponding map obtained by kriging.*

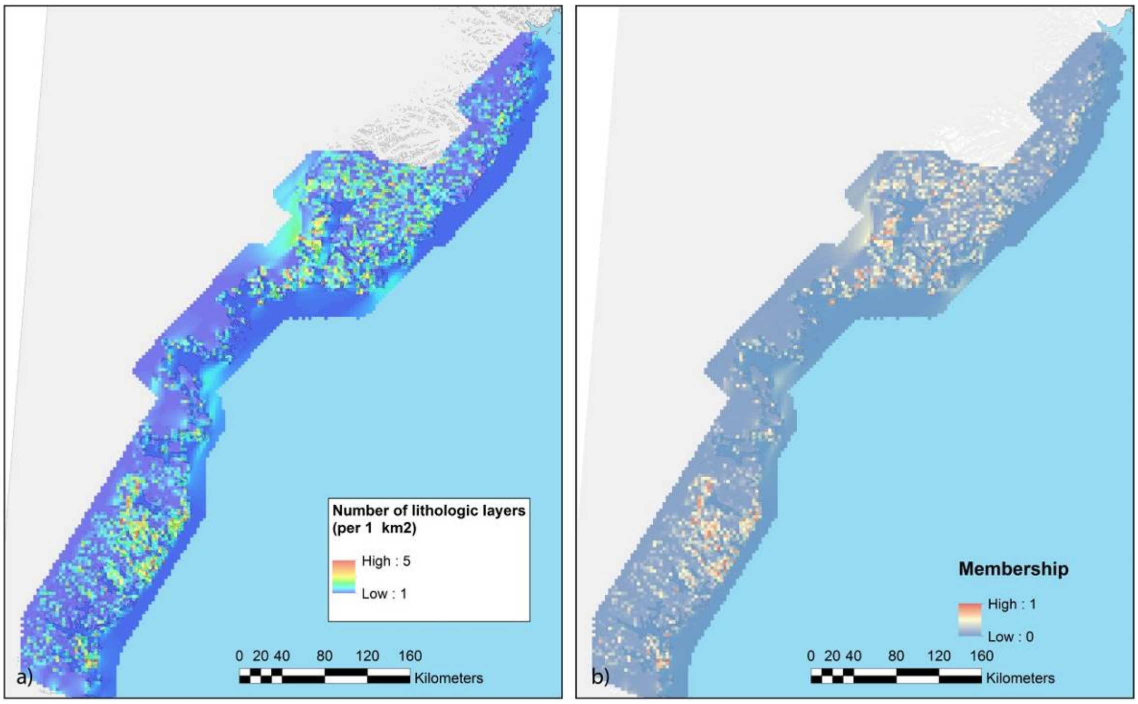

Figure 107 *As an alternative to kriging, natural neighbor interpolation is applied on the numbers of lithologic layers on a 1 x 1 km grid (see Fig. 15a) that is associated with the criterion/proxy element T1e and the target element "Lithological units interface complexity".* ***A*** *shows the grid obtained from the natural neighbor interpolation and* ***B*** *shows the fuzzy evidential map that is determined from A by employing the same fuzzy membership function (see Fig. 100b) as used before for corresponding map obtained by kriging.*

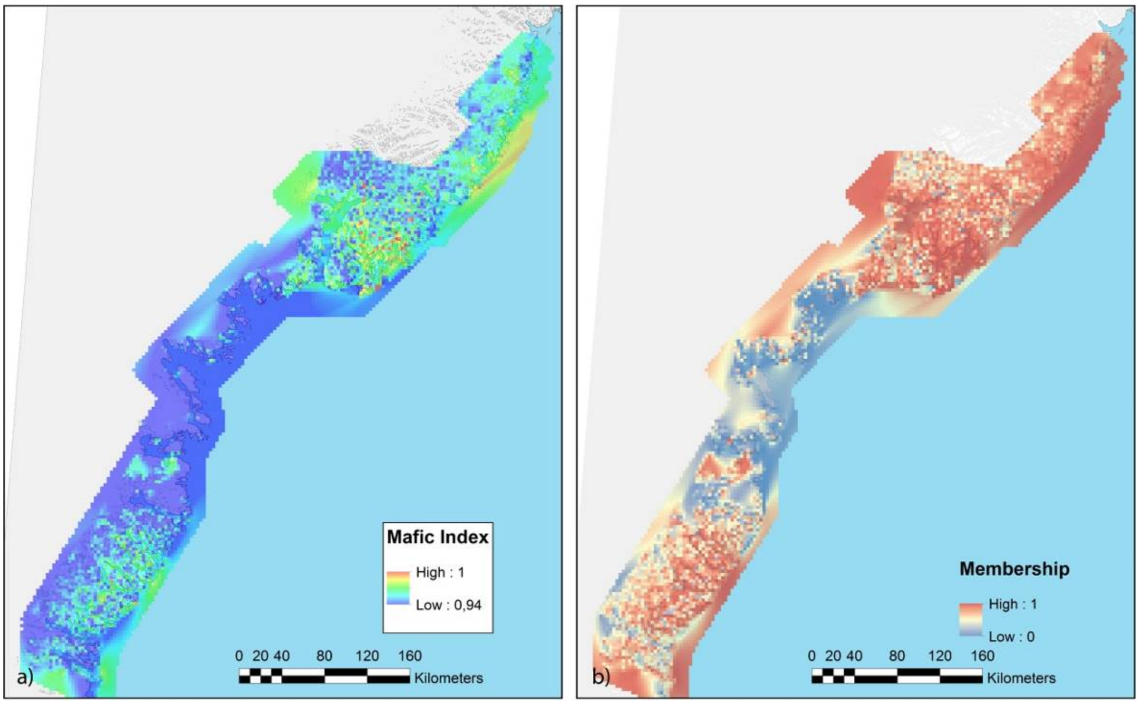

Figure 108. *As an alternative to kriging, natural neighbor interpolation is applied on the mafic index of the pixels from the ASTER satellite data (see Fig. 29a) associated with the criterion/proxy element T2a and the target element "Chemical favorable hosts".* ***A*** *shows the grid obtained from the natural neighbor interpolation and* ***B*** *shows the fuzzy evidential map that is determined from A by employing the same fuzzy membership function (see Fig. 101b) as used before for corresponding map obtained by kriging.*

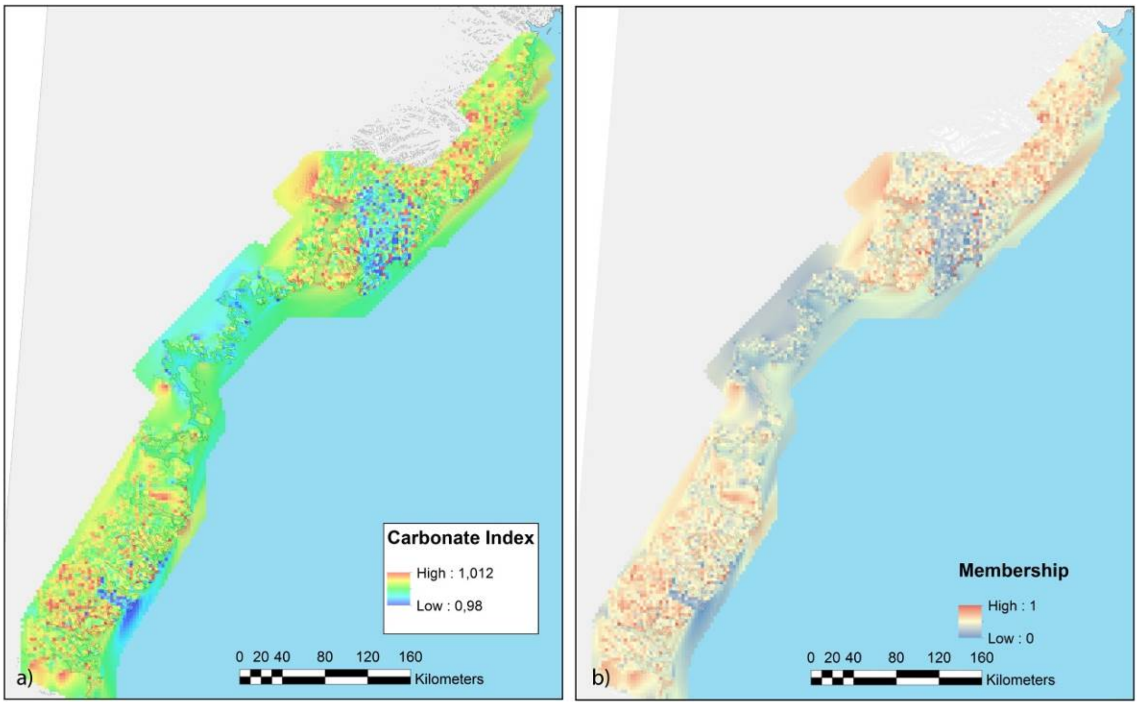

Figure 109. *As an alternative to kriging, natural neighbor interpolation is applied on the carbonate index of the pixels from the ASTER satellite data (see Fig. 30a) associated with the criterion/proxy element T2b and the target element "Chemical favorable hosts".* ***A*** *shows the grid obtained from the natural neighbor interpolation and* ***B*** *shows the fuzzy evidential map that is determined from A by employing the same fuzzy membership function (see Fig. 102b) as used before for corresponding map obtained by kriging.*

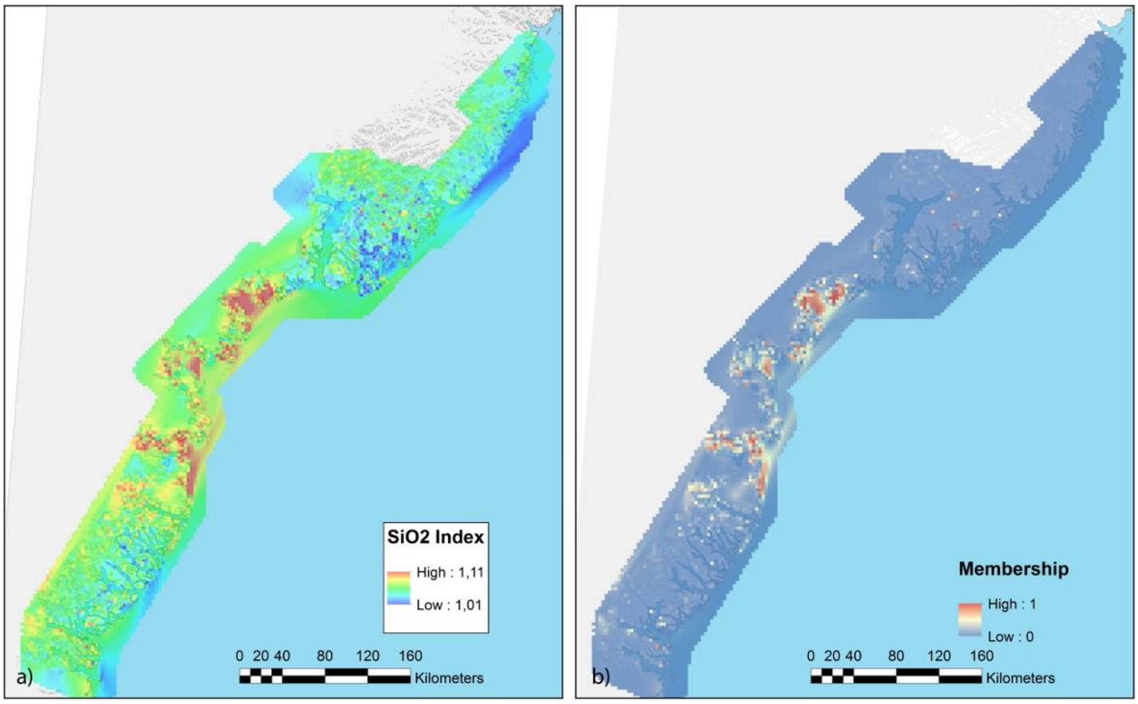

Figure 110. *As an alternative to kriging, natural neighbor interpolation is applied on the SiO2 index of the pixels from the ASTER satellite data (see Fig. 31a) associated with the criterion/proxy element T2c and the target element "Chemical favorable hosts".* ***A*** *shows the grid obtained from the natural neighbor interpolation and* ***B*** *shows the fuzzy evidential map that is determined from A by employing the same fuzzy membership function (Fig. 103b) as used before for corresponding map obtained by kriging.*

Appendix C:
Additional not considered geophysical data

Because East Greenland is a remote area only sparsely covered by other type of geophysical data, they are only of limited use in any kind of statistical approach. However, they provide some valuable information about the deeper structures in the crust and upper mantle and are to some extent able to constrain our model.

Velocity distribution from full-waveform tomography

Low seismic velocities anomalies in the continental crust can be indicative for weakening zones. Due to the remoteness of Greenland, there are very little data available from active deep seismic studies and most knowledge about velocity distribution in the crust and upper mantle is obtained from passive seismic data.

We consider here the global model of the vertically polarized shear velocity “SL20134sv”, which is freely accessible from the internet (http://homepages.dias.ie/aschaeff/Andrew_Schaeffer/SL2013sv.html) and is described in Schaeffer and Lebedev (2013). Their automated multimode inversion (AMI) accounts for full-waveform information of both body and surface waves and an unprecedented large set of seismograms (~3/4 of a million) is used for obtaining this model. Despite the significant improvement in resolution of tomographic inversions using the complete signal in the seismograms, the resolution is probably relatively poor in Greenland due the few local seismic stations and the relatively small number of local seismic events (see Fig. 5 in Schaeffer and Lebedev, 2015).

The model is parameterized on a set of concentric cells and each shell consists of knots on a triangular grid having a constant inter-knot spacing of around 280 km in the lateral directions. In vertical direction, cells are gradually increasing with depths down to 580 km and the first five lower shell borders are at 7, 20, 36, 56 and 80 kilometers.

In Figure 111 velocity perturbations of SV velocities for the depths of 20, 36 and 56 km are shown. In old continental regions, this depth range is approximately associated with the middle crust down to the top of the upper mantle. A 300 kilometer broad, NW-SE striking low velocity anomaly (- $\Delta Vs \approx 50 - 100$ m/s) can be observed, particularly in the 36 and 56 km depths slices in Southern Greenland. Its minimum runs from the Nuuk-Maniitsoq area (65° N) in West Greenland to the area around Skjoldungen (63° N) in East Greenland. SV velocities are generally lower along the East onshore area of Greenland than in the northern central part and in the total south.

After an evaluation of the data was it concluded that the low resolution of the velocity distribution data was insufficient to use the data in the present study.

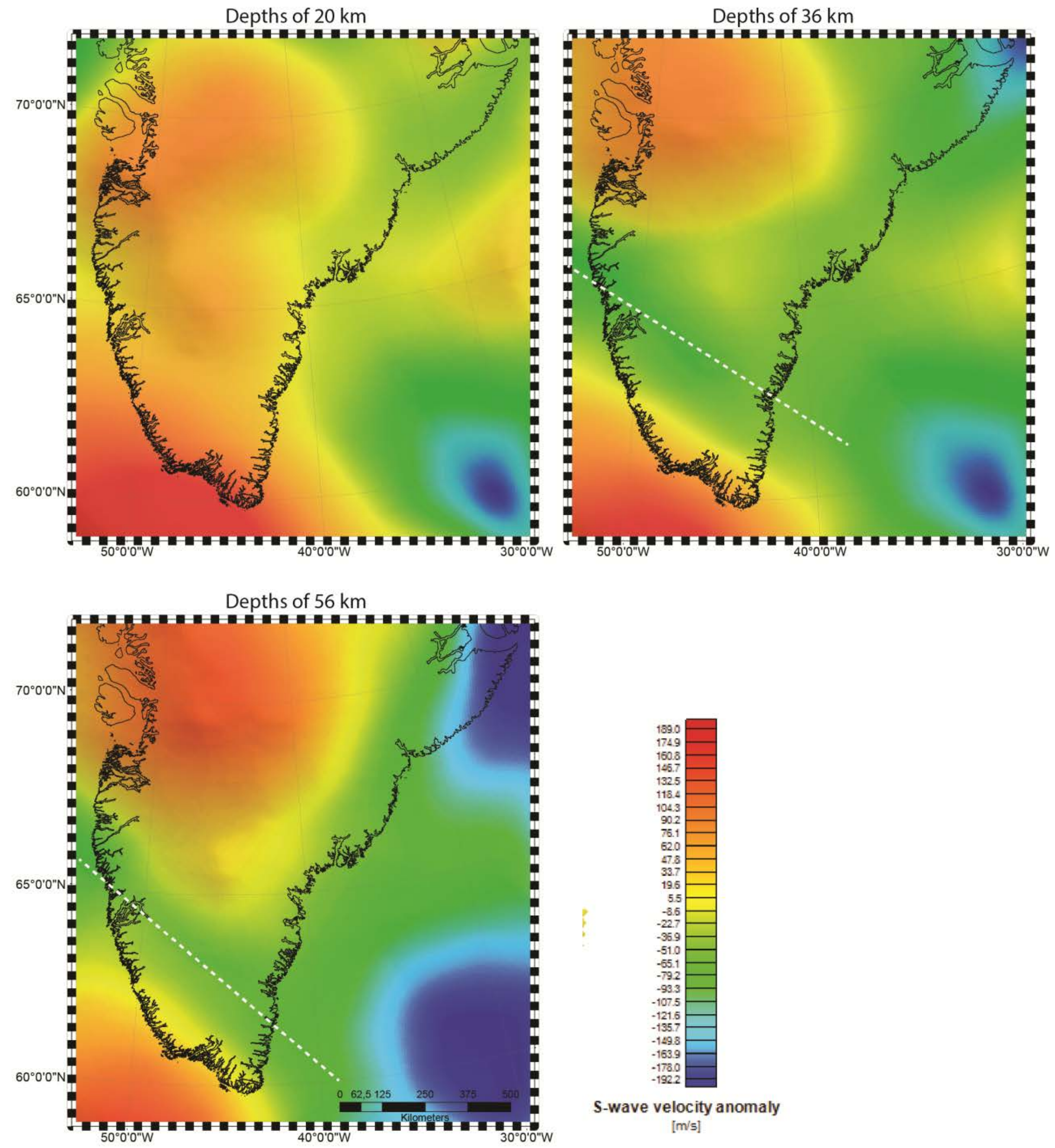

Figure 111. *Depths slices from the global SV velocity model presented by Schaeffer and Lebedev (2013). (Velocities are shown as perturbations relative to standard velocities in the associated depth interval.) The white dashed line indicates a pronounced low velocity zone.*

Earthquake distribution

The Greenland Ice Sheet Monitoring Network (GLISN) is a seismic network (see http://glisn.info) that consists of 32 stations installed in Greenland and on neighboring islands in the arctic. From their catalogue, we extracted events from South East Greenland (Fig. 16). All epicenters are determined from at least three stations and all events are recorded after 1975.

In Figure 112 and Figure 113 the epicenters are plotted together with regional magnetic lineaments as they are determined in the compilation based on CAMP-M. Most seismic activity is observed in the area around Tasiilaq and in the offshore region east of Kap Poul Løvenørn.

The earthquake data provide an interesting dataset but because little investigation have been done to determine the linkage to geological structures/features and as the location of the earthquake is somewhat uncertain was it decided not to use these data.

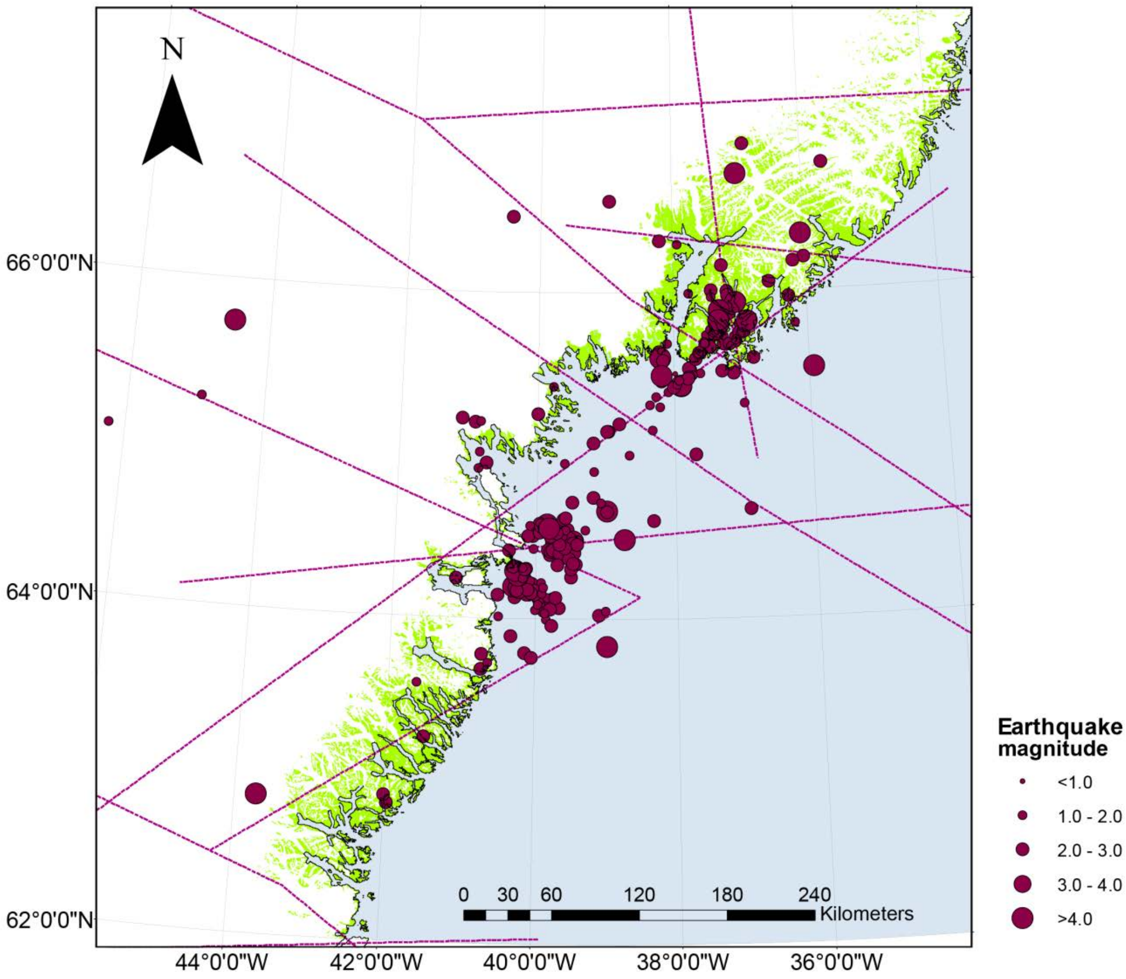

Figure 112. *Magnitudes of earthquakes in South East Greenland. Events are detected by stations of the Greenland Ice Sheet Monitoring Network (GLISN) (see http://glisn.info). Dashed magenta lines indicate regional magnetic lineaments identified from the compilation CAMP-M (see Fig. 51).*

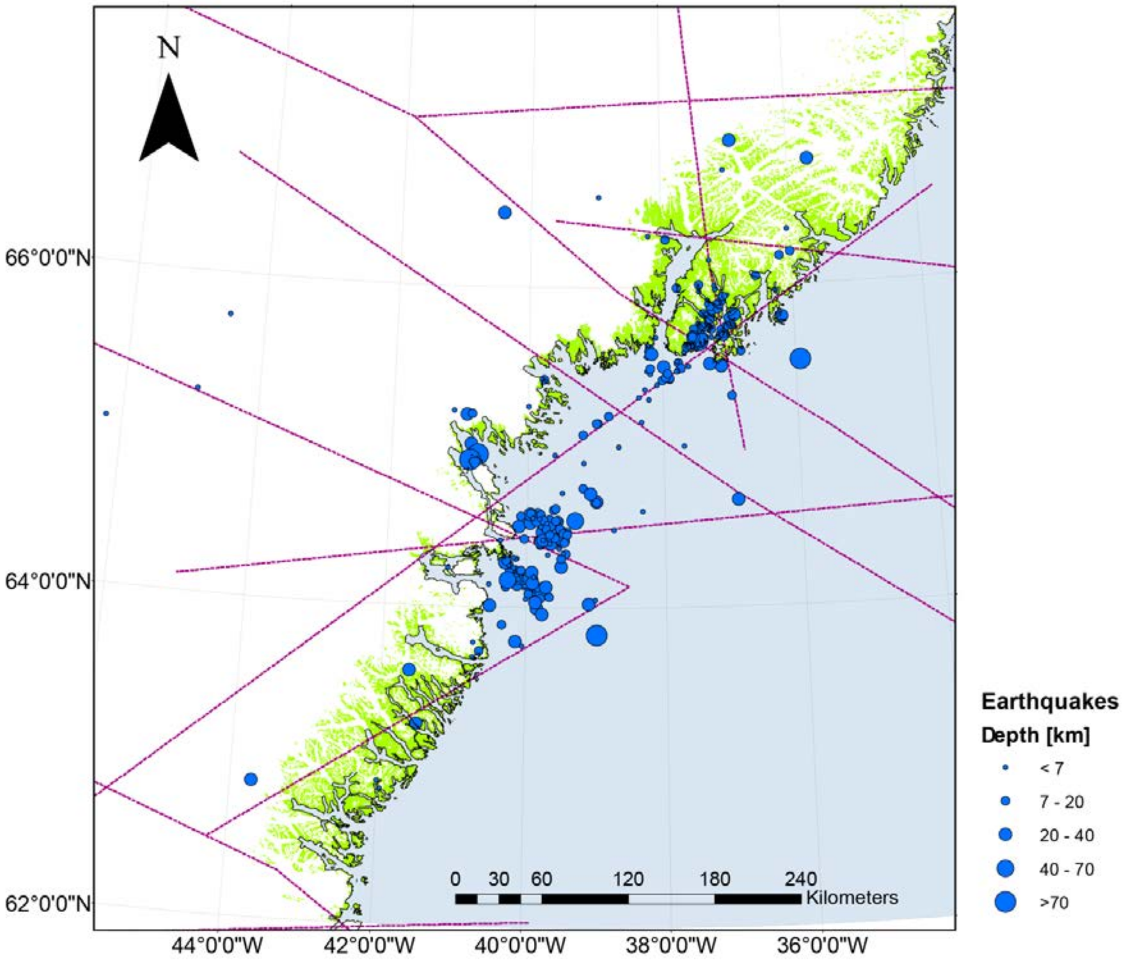

Figure 113. *Depth range of earthquakes in South Greenland.*

Magnetotelluric profile

In the summer 2014 GEUS performed a magnetotelluric (MT) test survey that starts close to the village Isortoq in the south and runs along the southern part of the of the Sermilik Fjord west of the village Tasiilaq (see Heincke *et al.*, 2015). The survey consisted of eight locations arranged mostly along a 2-D line with distances between neighboring stations of 8-15 km. The motivation of the survey was to investigate if it is possible to obtain some information about the Nagssugtoqidian mobile belt fromtheresistivity image.

The fjords and the varying shoreline have a very complex effect on the electromagnetic signals (and the resulting impedances), dominating most of their characteristics. This means that advanced three-dimensional modeling and inversion tests are required to reduce the impact from the seawater before it is possible to draw any reliable conclusions about the resistivity distribution in the subsurface. Such tests have not been done yet and therefore results from the MT measurements are not considered in this study. However, we would like to note that it is may be possible in the future to incorporate this type of information.